

High-resolution investigation of the electronic structure of organic thin films

Dissertation zur Erlangung des
naturwissenschaftlichen Doktorgrades
der Bayerischen Julius-Maximilians-Universität
Würzburg

vorgelegt von

Achim Schöll

aus Kirchheim/Teck

Würzburg, 2003

Eingereicht am 14.10.2003

bei der Fakultät für Physik und Astronomie

Gutachter der Dissertation:

1. Gutachter: Prof. Dr. E. Umbach

2. Gutachter: Prof. Dr. J. Geurts

Prüfer der mündlichen Prüfung:

1. Prüfer: Prof. Dr. E. Umbach

2. Prüfer: Priv. Doz. Dr. G. Reents

Tag der mündlichen Prüfung: 28.10.2003

Promotionsurkunde ausgehändigt am:

1	Introduction	5
2	Theoretical background of applied methods	7
2.1	Photoemission	7
2.2	X-ray absorption	12
2.3	GSCF3 calculations of NEXAFS spectra	17
2.4	Vibronic excitation	18
2.5	LEED	21
3	Experimental	23
3.1	Sample preparation	23
3.2	Investigated molecules and preparation parameters	23
3.3	Beamlines and experimental stations.....	25
3.3.1	U49/1-PGM / UE52-PGM	25
3.3.2	NEXAFS	25
3.3.3	PM-1/SX-700.....	26
3.3.4	STXM	26
3.3.5	XPS	26
3.3.6	SPA-LEED.....	27
4	Results	29
4.1	Energy calibration and intensity normalization in high-resolution NEXAFS spectroscopy.....	29
4.1.1	Motivation.....	29
4.1.2	Energy calibration.....	30
4.1.3	Intensity normalization	34
4.1.4	Conclusions.....	36
4.2	Vibronic finestructure in high-resolution x-ray absorption spectra of organic materials.....	37
4.2.1	Motivation.....	37
4.2.2	The example NTCDA on Ag(111)	39
4.2.2.1	Results and discussion.....	39
4.2.2.2	Conclusion.....	44
4.2.3	Anharmonicity of the core-excited state potential of ANQ.....	45
4.2.3.1	Results and interpretation.....	45
4.2.3.2	Concluding discussion.....	50

4.2.4	A comparison of fine structures in high-resolution x-ray absorption spectra of several condensed organic molecules	52
4.2.4.1	Spectroscopic data and orientation.....	52
4.2.4.2	Franck -Condon (FC) analysis of the NTCDA C-K data.....	55
4.2.4.3	Comparison with PTCDA, NDCA, and BPDCA.....	60
4.2.4.4	Comparison between NDCA and ANQ	62
4.2.4.5	BPDCA.....	66
4.2.4.6	Conclusions	68
4.3	Line shapes and satellites in high-resolution x-ray photoelectron spectra of large π -conjugated organic molecules	71
4.3.1	Motivation.....	71
4.3.2	Results and discussion	71
4.3.3	Concluding discussion	80
4.4	Bonding and screening influences on the line shapes of NTCDA monolayers on Ag(111) as revealed by high-resolution photoemission	81
4.4.1	Motivation.....	81
4.4.2	Results and discussion	82
4.4.3	Conclusion	91
4.5	An order-disorder phase transition upon cooling: NTCDA monolayer on Ag(111).....	93
4.5.1	Motivation.....	93
4.5.2	Results and discussion	94
4.5.3	Concluding remarks	103
4.6	Towards a detailed understanding of the NEXAFS spectra of bulk polyethylene copolymers and related alkanes	105
4.6.1	Motivation.....	105
4.6.2	Experimental	106
4.6.3	Results and discussion	107
4.6.4	Summary	114
5	Appendix	115
5.1	Radiation damage study on PTCDA multilayers.....	115
5.2	Calculated NEXAFS spectra	117
5.2.1	3,4,9,10-perylene-tetracarboxylic acid dianhydride (PTCDA).....	117
5.2.2	Naphthalene	118

5.2.3	Perylene.....	119
5.2.4	Tetracyanochinondimethan (TCNQ)	120
5.3	LEED pictures of additional NTCDA monolayer phases on Ag(111)	123
5.3.1	220 K structure.....	123
5.3.2	180 K structure.....	124
5.3.3	240 K structure.....	125
6	References	127

1 Introduction

Organic materials have attracted steadily increasing attention of researchers over the last two decades. This is mainly due to the highly interesting optical and electronic properties of these materials, which open a wide field of possible applications for electronic devices, such as organic light emitting diodes (OLEDs) [1,2] and displays [3], organic field effect transistors (OFETs) [4,5], or solar cells [6,7].

The properties of these organic thin films can be tailored in a wide range, e.g. by the variation of the structure, size, shape, and functional groups of the molecules, the thin film structure, the choice of differently interacting substrates, such as metals or oxides, or the preparation conditions [8,9]. In many respects, especially π -conjugated organic molecules and polymers have shown very promising properties, such as high charge carrier mobilities [10,11], that are due to their delocalised electronic system. In any case, a detailed understanding of the electronic structure and the influence of intramolecular, intermolecular and interfacial effects is crucial.

Many theoretical and experimental methods, such as photoelectron spectroscopy (PES) [12,13] and near-edge x-ray absorption fine structure spectroscopy (NEXAFS) have been applied to these systems. NEXAFS in particular has proven to be an ideal technique to determine the molecular orientation, interface bonding, and electronic properties (especially of the unoccupied orbitals) of all kind of materials [14-16]. In addition, the high chemical sensitivity of the NEXAFS method is often employed to obtain chemical information, even as contrast in microscopy techniques, such as scanning transmission x-ray microscopy (STXM) [17] and photoemission electron microscopy (PEEM) [18].

Although much information from NEXAFS could already be gained in the past, the advent of high-brilliance and high-resolution undulator beamlines at 3rd generation synchrotron sources enables absorption spectroscopy with unprecedented energy resolution revealing a wealth of additional fine structure which is the major topic of this thesis. This fine structure allows a very detailed analysis of the electronic and chemical state, of vibronic coupling, and of local vibrational properties, and hence yields new information about intermolecular interaction. In addition, it can provide a very detailed fingerprint for the discrimination of chemical substances with subtle differences or in slightly different physical states and surroundings.

In the following, an introduction into the theoretical background of the principally applied spectroscopy techniques (Chapter 2) and their experimental implementation on thin film samples (Chapter 3) will be given. The results presented in Chapter 4 were all published as Journal articles, were recently submitted or are prepared for publication. The corresponding references will be given at the beginning of each section. We will first (Chapter 4.1) address the very important point of energy calibration and intensity normalisation in high-resolution NEXAFS spectroscopy. Chapter 4.2 will then focus on the vibronic fine structure in the high-resolution NEXAFS spectra of organic materials. Chapter 4.3 reports on a high-resolution XPS study of multilayer films of the molecules PTCDA, NTCDA, NDCA, BPDCA and ANQ, focussing on the assignment and interpretation of the various photoemission and satellite lines. In the Chapters 4.4 and 4.5 we will present the XPS, NEXAFS and SPA-LEED data of different NTCDA monolayer phases on the Ag(111) surface, particularly addressing

the differences in the interfacial bonding. A NEXAFS study on matrix effects in bulk polyethylene copolymers will follow in Chapter 4.6.

In the appendix (Chapter 5), additional data will be presented, that were not published so far but might be helpful for future projects. This will include a radiation damage study on PTCDA multilayers, the calculated NEXAFS spectra of PTCDA, naphthalene, perylene, and TCNQ as well as the LEED pictures of additional NTCDA monolayer phases, that were recorded while investigating the phase transition of the relaxed NTCDA monolayer on the Ag(111) surface.

2 Theoretical background of applied methods

2.1 Photoemission

Photoelectron spectroscopy (PES) is a standard technique to analyse the chemical state and electronic structure of surfaces, adsorbates or thin film samples. An energy scheme is plotted in Figure 2.1. The sample is irradiated with photons of energy $h\nu$ (x-rays for XPS, UV-light for UPS), which interact with the electrons in the sample via the photoelectric effect. Thus, photoelectrons are emitted with a specific kinetic energy which is measured by an electron energy analyser. From Figure 2.1 the following relation for the kinetic energy of the photoelectrons can be derived:

$$E_{\text{kin}} = h\nu - E_b - \Phi_S, \quad (2.1)$$

where Φ_S is the work function of the sample and E_b the binding energy of the electron with respect to the Fermi energy. The kinetic energy in the analyser $E_{\text{kin,A}}$ is then

$$E_{\text{kin,A}} = E_{\text{kin}} + \Phi_S - \Phi_A + eU_{\text{bias}} = h\nu - E_b - \Phi_A + eU_{\text{bias}}, \quad (2.2)$$

with Φ_A being the work function of the analyser and U_{bias} the bias voltage. U_{bias} is normally calibrated to fit the analyser work function. Thus, with $U_{\text{bias}} = \Phi_A$, equation (2.2) can be

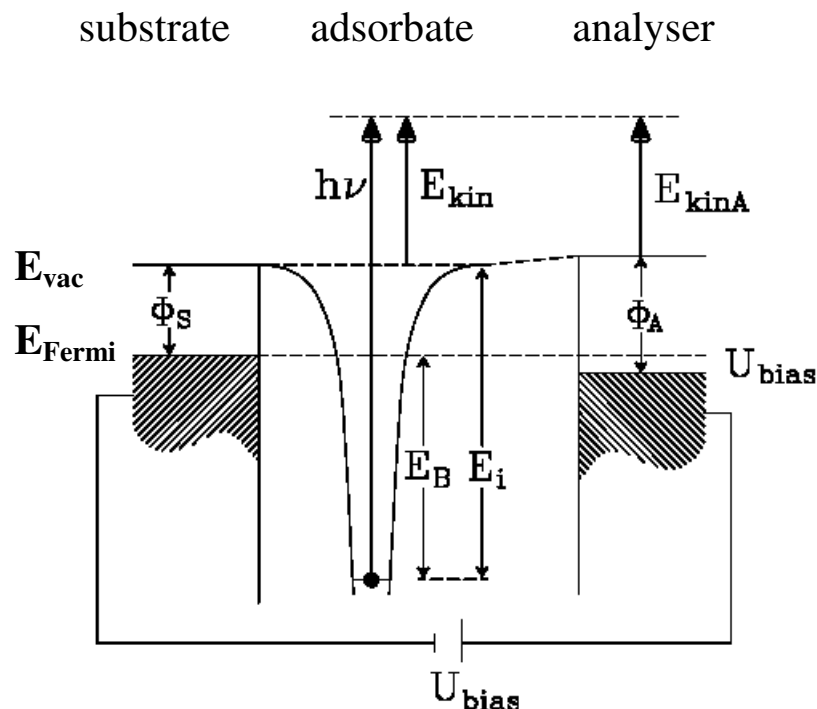


Figure 2.1: Energy scheme for the photoemission process

simplified to:

$$E_{\text{kin}, A} = h\nu - E_b \rightarrow E_b = h\nu - E_{\text{kin}, A}, \quad (2.3)$$

i.e., the binding energy of the electrons can be determined by measuring the kinetic energy of the emitted photoelectrons.

According to their binding energy the electrons can be divided into valence ($E_b < 20$ eV) and stronger bound core electrons. For the investigation of the weaker bound valence electrons UV-light emitting laboratory sources are often used for the excitation, e.g., the He I and He II lines of a He discharge lamp with the energies 21.2 eV and 40.8 eV, respectively. Thus, this method is often referred to as UPS (ultraviolet photoelectron spectroscopy).

Higher energetic excitation in the soft x-ray range is required to analyse the core electrons,

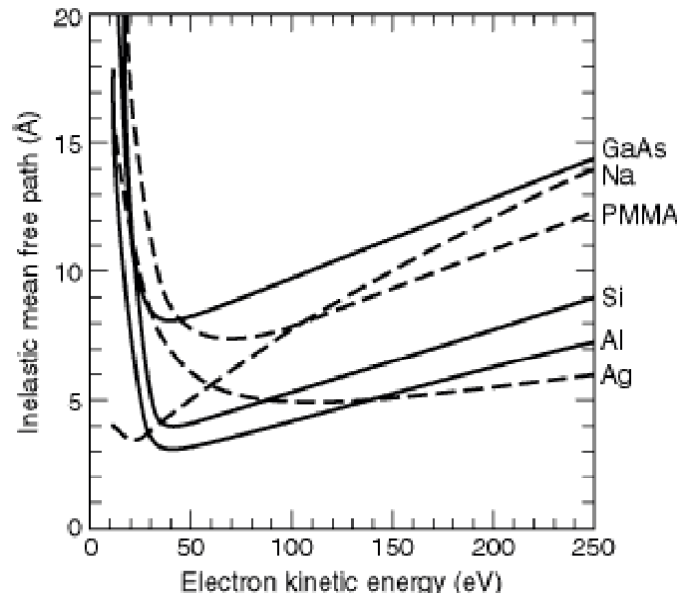


Figure 2.2: Inelastic mean free path of electrons in matter (from Ref. [19])

which lead to the denomination XPS (x-ray photoelectron spectroscopy). In the laboratory this method can be performed with x-ray sources with different anode materials yielding different characteristic $K\alpha$ line energies (e.g., Mg $K\alpha = 1253.56$ eV and Al $K\alpha = 1486.58$ eV).

If a higher brilliance (i.e. higher photon flux density per solid angle and per energy unit) of the excitation line is required, the experiment has to be performed with synchrotron radiation. In addition to the unmatched energy resolution in the soft x-ray range the energy of synchrotron radiation can be adjusted in a wide range (10 eV to keV), thus enabling PES experiments with very high surface sensitivity. In this case the photon energy is tuned to produce photoelectrons with a kinetic energy that corresponds to their minimal inelastic mean free path in the investigated sample (e.g. 7 Å at $E_{\text{kin}} = 60$ eV for PMMA, see Figure 2.2 (from Ref. [19])).

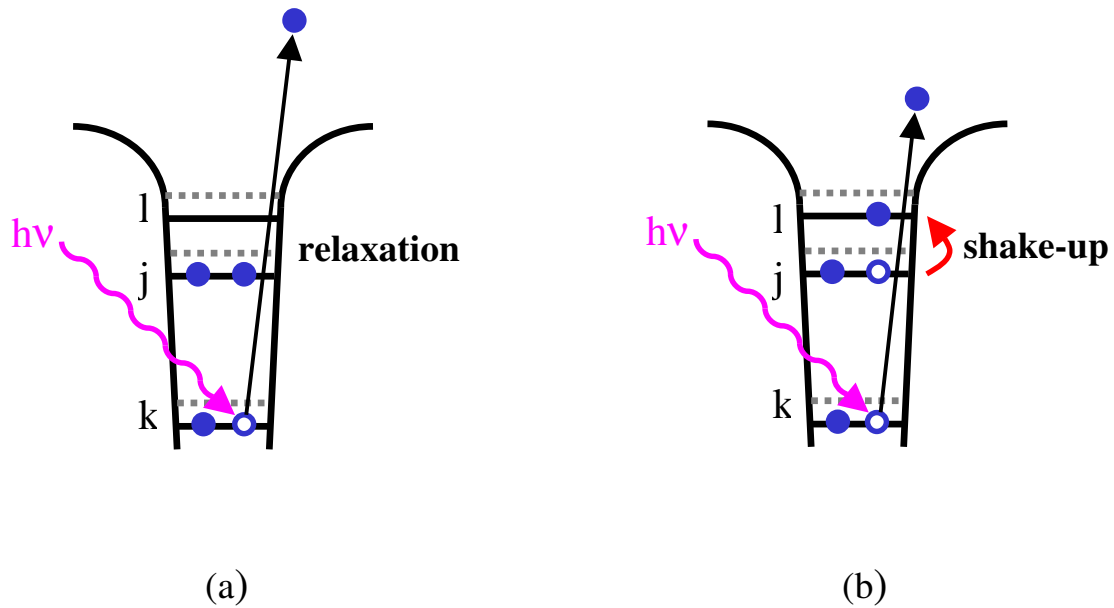


Figure 2.3: Different mechanisms involved in the photoelectron process: (a) intraatomic screening and (b) shake-up excitation.

When studying adsorbates with photoemission spectroscopy, the spectra are often compared to gas phase spectra or calculations. When comparing the binding energies, one has to consider the different reference levels. For gas phase spectra the binding energies are usually referenced to the vacuum level E_{vac} , for solids and adsorbates to the Fermi level E_{Fermi} . Fermi level and vacuum level differ by the work function Φ_S (see also Figure 2.1) that is given by

$$\Phi_S = D + \mu \quad , \quad (2.4)$$

where D is the surface dipole and μ the chemical potential. The dipole part can be explained by electrons that spill out into the vacuum, which shifts the center of gravity of the charge density. This shift generates a dipole layer at the surface which is strong if the electron density at the surface is high. Generally the dipole part of the clean substrate surface is changed by the adsorbate. Thus this effect has to be taken into account, especially for substrate surfaces with a high dipole part (e.g., Ni(111), Pd(111)).

The theory of photoelectron spectroscopy is discussed in detail in many textbooks [20-23] and publications (e.g. Refs. [24-26]), and therefore only a short introduction in the most important relations will be given here.

The binding energy of an electron E_B is influenced by initial and final state effects, that both have to be considered in the description of the photoemission process. In a zero-order approximation only the emitted electron is considered, and it is assumed, that E_B only depends on the energy E_i of the orbital i (Koopman's theory) [27]. All other not participating orbitals are considered as "frozen orbitals", i.e. they are not modified during the emission process. The energy E_i and thus also E_B strongly depend on the chemical environment (chemical shift) [28]. The C 1s binding energy in CF_4 , e.g., is shifted to higher binding energy for about 11 eV if compared to the respective value for CH_4 , which is explained by the strong electronegativity of the fluorine atoms [29]. If the electron density at the carbon atom is reduced, this results in a more positive effective charge at the nucleus and thus a higher binding energy of

the electronic levels. At the same time an opposite shift can be observed for the F core levels. Core levels show the strongest chemical shifts, since they are localised at the atomic core and thus are sensitive to changes of the effective nuclear charge.

Experimental XPS results show, that the photoemission process is not satisfactorily described by this rather simple initial state picture. For a more accurate approach also final state effects have to be considered. Core excitation leads to a reaction of the remaining electrons (see Figure 2.3 a), which try to screen the generated core hole, thus leading to a shift of the observed core level binding energy towards lower energy [30,31]. The reaction of the electronic system can be separated into intraatomic and extraatomic screening. Intraatomic screening delineates the relaxation of the electronic orbitals in the ionised atom to minimize the energy. If the ionised atom is part of a compound (molecule/solid) or adsorbed on a surface, also the electrons of the environment participate in the screening of the core hole (extraatomic screening). This can occur by the generation of an image potential (polarisation interaction) or by charge transfer. Image potential (polarization) screening can be described by the generation of an image charge in the surface (or by a polarization of the neighbouring atoms or molecules in a solid) and the interaction between this image charge (polarization) and the (positive) core hole in the adsorbate [32,33]. Image potential (polarization) screening is the extraatomic screening process for weakly coupled adsorbates (physisorbates) or van-der-Waals bonded solids and is relatively weak (typically $\leq 1\text{eV}$). In the case of chemisorption the image potential (polarization) model is replaced by a charge transfer model. Charge is transferred from the substrate (or from neighbouring atoms) into the strongly coupled adsorbate leading to a very effective screening of the core hole. The resulting screening shifts in the photoemission spectra are much larger than for physisorbed molecules ($\sim 5\text{ eV}$).

In addition to this energy shift of the binding energies, the reaction of the electronic system upon the excitation process leads to the generation of satellites in the photoemission spectra. During the excitation process valence electrons can be excited into unoccupied orbitals (“shake-up”, see Figure 2.3b) [34] or into the continuum (“shake-off”). Due to the energy conservation these excitations reduce the kinetic energy of the emitted electron and lead to satellite lines at higher binding energy in the photoemission spectra.

To describe the peak intensities in PES spectra the photoelectric cross section σ has to be calculated. σ is defined as the probability P_{if} per time unit for the transition of an atom/molecule or solid from an initial state $|\psi_i\rangle$ to a final state $|\psi_f\rangle$ under the influence of electromagnetic radiation. The transition probability P_{if} is given by Fermi’s Golden Rule:

$$P_{if} \sim \left| \langle \psi_f | H' | \psi_i \rangle \right|^2 \delta(E_f - E_i - h\nu) = |M_{if}|^2 \cdot \delta(E_f - E_i - h\nu). \quad (2.5)$$

with the transition matrix elements M_{if}

$$M_{if} = \langle \psi_f | H' | \psi_i \rangle. \quad (2.6)$$

The perturbation operator H' represents the electromagnetic radiation and can be approximated as

$$H' = -\frac{e}{2mc} (\hat{p} \cdot \hat{A} + \hat{A} \cdot \hat{p}), \quad (2.7)$$

where \hat{p} is the momentum operator $-i\hbar\vec{\nabla}$ and $\hat{A}(\vec{r},\vec{t})$ is the vector potential of the electromagnetic field. The factor $\delta(E_f - E_i - h\nu)$ considers the energy conservation where E_f and E_i are the total energies in the final and initial state, respectively. $\hat{A}(\vec{r},\vec{t})$ can be written as

$$\hat{A}(\vec{r},\vec{t}) = \vec{e} \cdot A_o \cdot e^{i(\vec{k}\vec{r} - \omega t)}, \quad (2.8)$$

where \vec{e} describes the polarisation direction of the light. In the vacuum the Coulomb calibration can be applied ($\vec{\nabla} \cdot \hat{A} = 0 \rightarrow \hat{p} \cdot \hat{A} = 0$) and H' can be simplified to $2 \cdot (\hat{A} \cdot \hat{p})$. If further the dipole approximation is applied, i.e. the term $e^{i\vec{k}\vec{r}}$ is written as series expansion and only the first element is taken into account, M_{if} can be written as

$$M_{if} \sim \langle \psi_f | \vec{e} \cdot \hat{p} | \psi_i \rangle, \quad (2.9)$$

which is usually referred to as dipole matrix element (DME). The dipole approximation is valid for $\vec{k} \cdot \vec{r} \ll 1$, which is hardly the case for XPS ($r \approx 1-2 \text{ \AA}$, $k = 2\pi/\lambda$ with $\lambda \approx 10 \text{ \AA}$).

The wave functions can be separated for the initial and final state of the electronic system according to:

$$\psi_i = \hat{C} \cdot \phi_{i,k} \psi_k^R(n-1) \quad \text{and} \quad \psi_f = \hat{C} \cdot \phi_{f,k} \psi_{ijk}^{ion}(n-1), \quad (2.10)$$

where $\Phi_{i,k}$ and $\Phi_{f,k}$ are the wave functions of the excited core electron in the initial and final state, respectively. Ψ_k^R and Ψ_{ijk}^{ion} are the wave functions of the not involved ($n-1$) electrons of the ground state and the ionic final state with a hole in the level k and a valence electron that was excited from a state j to the state l by the photoemission process. \hat{C} is the antisymmetry operator for the wave functions. With these relations the transition matrix element M_{if} can be written as:

$$M_{if} = \langle \psi_f | \vec{e} \cdot \hat{p} | \psi_i \rangle = \langle \phi_{f,k} | \vec{e} \cdot \hat{p} | \phi_{i,k} \rangle \langle \psi_{ijk}^{ion}(n-1) | \psi_k^R(n-1) \rangle. \quad (2.11)$$

In this case only the interaction of the electromagnetic radiation with the electron k is taken into account. The first approximation considers the orbitals, that are not involved in the photoemission process as so-called ‘‘frozen orbitals’’, i.e. unchanged between initial and final state ($\Psi_{ijk}^{ion} = \Psi_k^R$). Now, the second factor is equal to one and the transition matrix element is only the one-electron matrix element. This approximation is called Koopmans’s theory [27]. In this case the core level spectrum of state k consists only of one symmetric peak at the so-called Koopman’s energy. Of course, this approach does not take the intraatomic (intramolecular) core hole screening processes into account. Thus, for a better description the relaxed wave function Ψ_{ijk}^{ion} has to be considered and thus the different integrals are included, that describe the intensity of the main peak and of its satellites. The intensity of each peak is then given by

$$I_{ij} \sim M_{ij}^2 \delta(E_{f,kin} + E_{lj}(n-1) - E_i(n) - h\nu) \quad [35], \quad (2.12)$$

where $E_{lj}(n-1)$ is the energy of the excitation $j \rightarrow l$ and E_i the initial energy in the ground state. The intensity of a particular core level is now split between the main peak [$(l;j) = 0$] and its satellites [$(l;j) \neq 0$] (shake-up), including the excitation into the continuum ($\infty;j$) (shake-off). A very detailed discussion of the theory of the photoemission process can be found in Refs. [20,22-25,27,31,35-38].

2.2 X-ray absorption

Near edge x-ray absorption fine structure spectroscopy (NEXAFS) can provide interesting information on the geometric properties as well as on the electronic structure, in particular the unoccupied states, of all kinds of materials [14]. A schematic illustration of the NEXAFS process is displayed in Figure 2.4 for a diatomic molecule. A very detailed description of the NEXAFS method is given in Refs. [14,24,39]. In the following this chapter will outline the fundamental relations of the NEXAFS theory.

In NEXAFS the x-ray absorption is measured by scanning the photon energy $h\nu$ through an absorption edge. If $h\nu$ exceeds the ionisation energy E_i of the investigated level, the electrons are emitted as photoelectrons, and a high absorption cross section is detected. At $h\nu = E_i$ the well known x-ray absorption edges are observed. However, besides these excitations into continuum states additional, very effective excitations into unoccupied levels can occur. For the diatomic molecule displayed in Figure 2.4 the lowest unoccupied state is a so-called

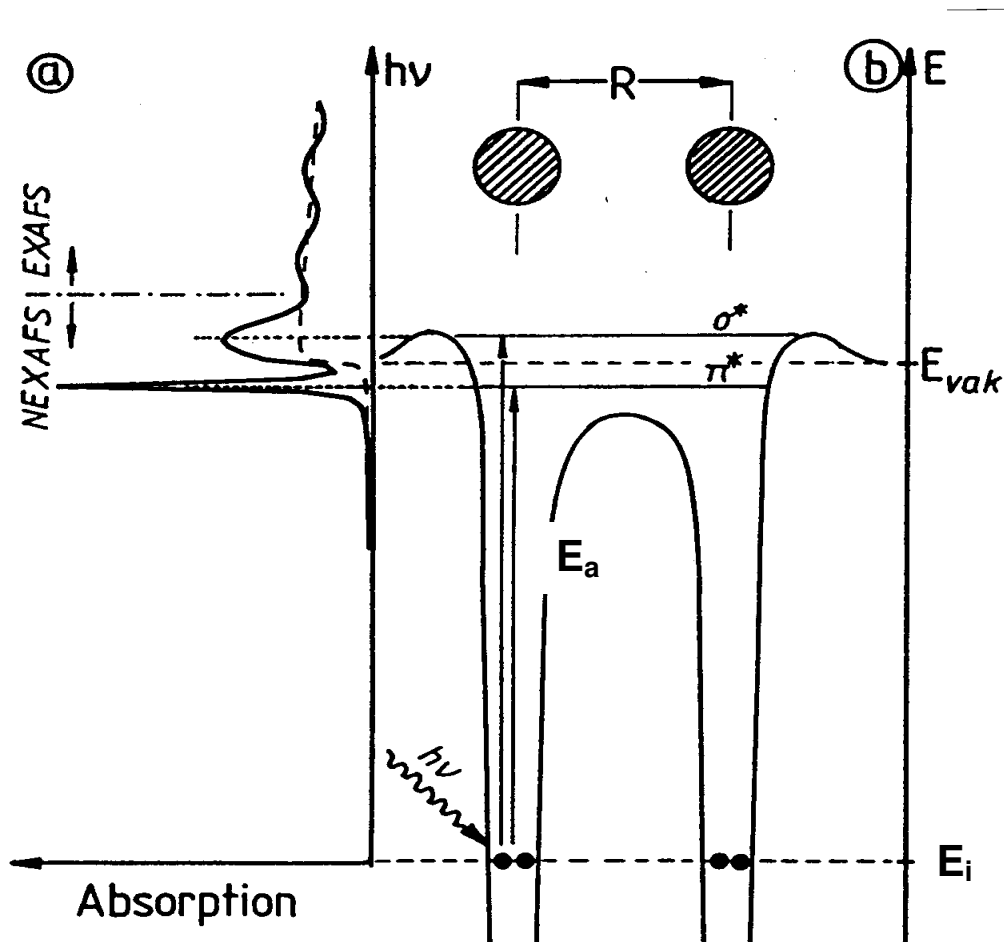


Figure 2.4: Schematic view of the NEXAFS process by the example of a diatomic molecule (from Ref. [14]).

LUMO (lowest unoccupied molecular orbital). As can be derived from Figure 2.4, this level is bound, i.e. below the vacuum level. Other levels may not be bound. The LUMO as well as the HOMO (highest occupied molecular orbital) often have π -symmetry, which is particularly the case for the aromatic organic molecules investigated in this work. Note, that the unoccupied, often non-bonding molecular orbitals are marked by asterisks (*).

The absorption cross section is very high, if the photon energy $h\nu$ is equal to the excitation energy E_a , which is needed to excite a core electron into an unoccupied molecular orbital. The ionisation energy of the unoccupied orbital E^u is then:

$$E^u = E_a - E_i = h\nu - E_i, \quad (2.13)$$

where E_i is the binding energy of the core electron in respect to the vacuum level. In analogy to Koopman's theory in photoelectron spectroscopy (see Chapter 2.1) equation (2.13) is only a rough approximation, since the reaction of the electronic system on the excitation process is not considered. Thus in an accurate approach E_a describes the energy difference between an initial and a final state, that takes the relaxation reaction of the electronic system into account.

Interesting information on the electronic structure can be derived, in particular about the unoccupied (molecular) orbitals. These are very sensitive to both, intramolecular effects, e.g. changes of the chemical bonding within the molecule, to intermolecular influences, e.g. changes in the interaction with the substrate in adsorbate systems, or even small differences in the relatively weak coupling between the molecules in van-der-Waals crystals.

In analogy to the photoelectric cross section σ (Chapter 2.1), the absorption cross section for the x-ray absorption process can be defined as the transition probability P_{if} per time unit for the transition from an initial ($|\psi_i\rangle$) to a final state ($|\psi_f\rangle$) under the influence of electromagnetic radiation. The final state now describes a state with a core hole and an excited electron in a previously unoccupied orbital. The transition probability P_{if} can thus be derived from equations (2.5) and (2.9) to

$$P_{if} \sim |M_{if}|^2 \cdot \delta(h\nu - E_a) = \left| \langle \psi_f | \vec{e} \cdot \hat{p} | \psi_i \rangle \right|^2 \delta(h\nu - E_a). \quad (2.14)$$

A particular problem in the calculation of the transition probabilities P_{if} is the determination of the NEXAFS final state $|\psi_f\rangle$. While several semi empirical [40], *ab initio* and DFT (density functional theory) approaches are well established to calculate the electronic ground state $|\psi_i\rangle$, the calculation of the final state $|\psi_f\rangle$ is more complicated [41,42]. The relaxation time scale does *a priori* not allow to decide, whether an approach in the adiabatic or in the sudden limit has to be applied [14]. In addition, a correct description of the final state demands the consideration of substantially more orbitals than $|\psi_i\rangle$, since the complete absorption spectrum has to be described by various resonances and especially the higher energetic channels strongly interact with the lower ones. For larger systems the numeric effort has to be limited by a calculation in the one-particle picture [42,43]. Multi particle excitations (e.g. π - π^* excitations) can then only be included as corrections.

A Hartree-Fock based *ab initio* method (GSCF3), that was developed by N. Kosugi [44-46] and that was used for the calculation of the low energy resonances (π^* -resonances) of the systems investigated in this work, is described in detail in the next chapter.

A widely used method, that is particularly suited to calculate the higher energetic excitations (σ^* -resonances), is the $X\alpha$ -Scattered-Wave method in combination with the Muffin-Tin

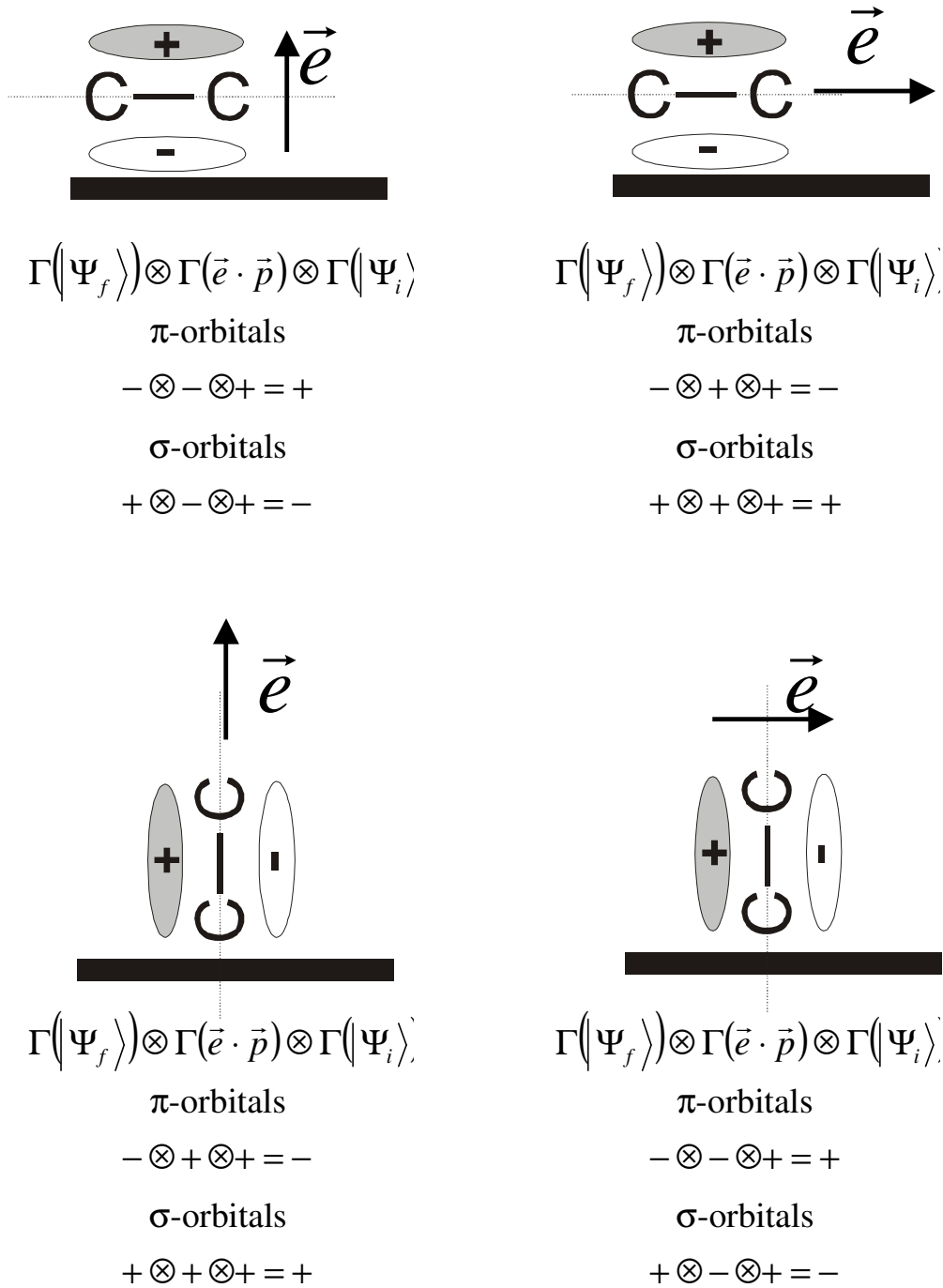


Figure 2.5: Symmetry properties for the NEXAFS process

approximation for the potential. This approach was successfully used for the first time by Dehmer and Dill to calculate the absorption spectrum of N_2 [47,48]. The most limiting approximation for larger molecules is the Muffin-Tin potential, that is divided into spherical symmetric regions around the different atoms, a spherical symmetric region around the entire molecule and a constant intermediate region. Due to this arbitrary choice of the potential this method is often referred to as parameterised *ab initio* method. The $X\alpha$ approximation [49] considers the exchange interaction by a local potential

$$V_{\text{ex}} \sim \alpha \cdot \rho(\vec{r})^{1/3}, \quad (2.15)$$

where $\rho(\vec{r})$ is the local charge density at the position \vec{r} . The parameter α can be determined in the calculation but is often set to a value between 0.7 and 1. Since the resonances are calculated as scattered states, the X α -SW approach provides highly accurate results also for EXAFS-structures, far above the absorption edge.

Due to the angular dependence of the dipole matrix element M_{if} (DME, see equation 2.9), the NEXAFS method can be used to determine the orientation of an adsorbate molecule with respect to the substrate surface. For this purpose the orientation of the \vec{e} -vector of the linearly polarised incident light relative to the surface has to be varied. The DME will only then be different from zero, if the direct product Γ' of the characters of its three elements:

$$\Gamma' = \Gamma(|\psi_f\rangle) \otimes \Gamma(\vec{e} \cdot \hat{p}) \otimes \Gamma(|\psi_i\rangle) \quad (2.16)$$

is totally symmetric (i.e. positive symmetry). If, e.g., the excitation involves a 1s core state (as it is the case for the C K- and O K-edge investigations in this work), the symmetry of the initial state is positive with respect to a reflection at the molecular plane. However, the symmetries of the unoccupied states are different. π -wave functions change the sign upon reflection and thus have negative symmetry, whereas σ -orbitals have positive symmetry. The symmetry character of the transition matrix element also depends on the symmetry of the scalar product $\vec{e} \cdot \hat{p}$. This can be derived from Figure 2.5, where the symmetry properties for π - and σ -orbitals and different polarisation directions are displayed. The combination of flat lying (top) and upright standing (bottom) molecules with perpendicular (left) and parallel polarisation (right) of the light in respect to the surface are considered. For the π -orbitals the symmetry is negative for flat lying molecules and parallel \vec{e} -vector, as well as for upright molecules if the \vec{e} -vector is perpendicular to the surface. In these cases the excitation is not allowed (dipole forbidden). For σ -orbitals the complementary symmetry relations are valid. If the molecules are oriented differently, i.e. if the angle α between the molecular plane and the surface is $0 < \alpha < 90^\circ$, the absorption cross sections and thus the observed resonance intensities are changed accordingly.

The angular dependence of the DME can be calculated for an arbitrary orientation angle α of the adsorbed molecules and an arbitrary direction of the polarisation vector relative to the surface Θ . If the intensity ratio $q = I(\Theta_1)/I(\Theta_2)$ ratio between the intensities of a specific resonance measured with two different polarisation directions Θ_1 and Θ_2 is measured, the orientation angle α can be determined according to

$$\frac{1}{\tan^2 \alpha} = \frac{1}{2 \cdot P} \left(P - \frac{1-q}{\sin^2 \theta_2 - q \cdot \sin^2 \theta_1} \right) \quad [14]. \quad (2.17)$$

Note, that this equation was derived after azimuthal averaging. A non complete polarisation of the synchrotron light is considered by the degree of polarisation P . For perfect linear polarisation ($P=1$) and $\Theta_1 = 0^\circ$, as it will be the case in this work, equation (2.17) can be simplified to

$$\frac{1}{\tan^2 \alpha} = \frac{1}{2} \left(1 - \frac{1-q}{\sin^2 \theta_2} \right). \quad (2.18)$$

Thus, by measuring the angular dependent intensity ratio q of a NEXAFS resonance the average orientation angle α of the corresponding molecular orbital (and therefore the molecule) can be determined.

In the experimental practise the x-ray absorption cross section of a sample is measured as a function of the photon energy. For the excitation of core electrons (e.g., C 1s and O 1s) the required photon energy is typically in the soft x-ray range (100 eV to 1000 eV). Since an x-ray source with variable photon energy and sufficiently high intensity is required, NEXAFS measurements have to be performed with synchrotron radiation. One way to measure the absorption signal is detecting the transmitted photon flux with an x-ray detector (e.g., semiconductor based) behind the sample. However, this method is restricted to samples with optical densities below the total absorption limit, e.g. ultrathin (< 250 nm) polymer films (see Chapter 4.6). The detection of the transmitted radiation is usually not possible for adsorption

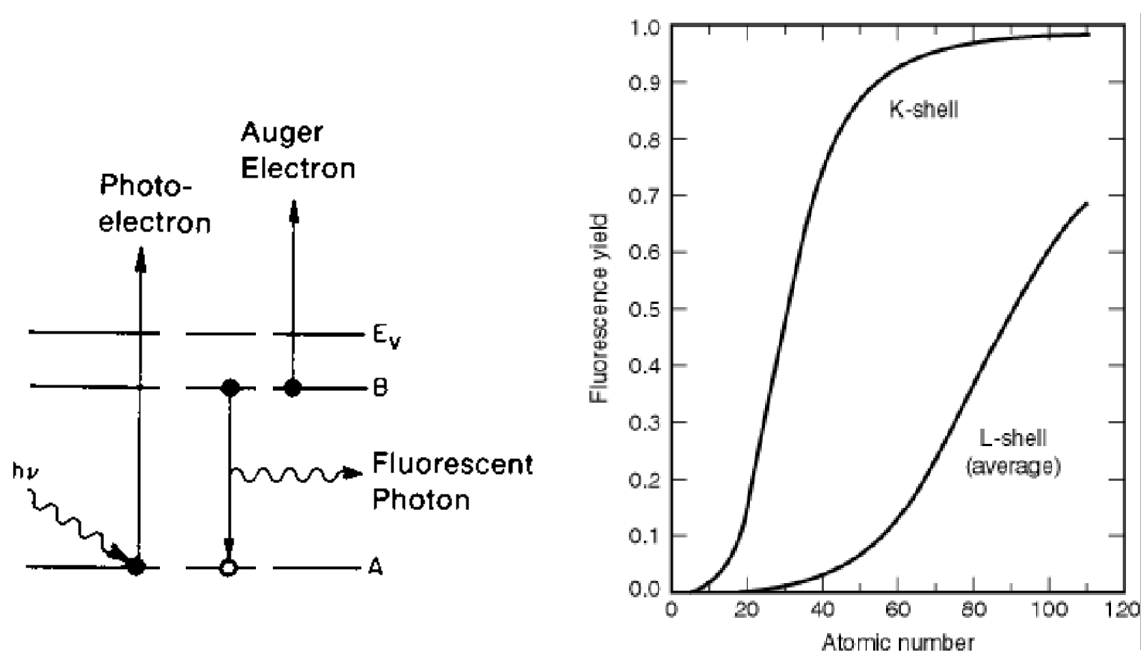


Figure 2.6: (a) Different relaxation processes for a core excited system (from Ref. [14]). The hole is filled by an electron from a higher shell either radiatively by the emission of a fluorescence photon or non-radiatively by emission of an Auger electron. (b) Fluorescence yields represent the probability of core holes in K or L shells that are filled by a radiative process, in competition with non-radiative Auger processes.

systems due to the total absorption of x-rays in the relatively thick substrates and thus secondary effects have to be utilised.

The absorption cross section is proportional to the number of generated core holes. These core holes are refilled with electrons from higher molecular levels. This relaxation is accompanied by two competing processes, the non-radiative Auger decay and the radiative fluorescence decay (see Figure 2.6a). The Auger decay is outweighing the fluorescence channel for small atoms ($Z < 30$ for K-shell excitation, see Figure 2.6b). Thus for thin adsorbed films of organic molecules, where the analysis is mainly focussed on the carbon, oxygen, nitrogen and sulphur K-edges, the Auger decay is the favourable detection method. In addition to the higher signal the NEXAFS method gains surface sensitivity due to the detection of electrons, that have a

relatively small mean free path in matter (typically in the order of several 10 Å, see also Figure 2.2).

Due to various scattering processes within the sample, Auger electrons lead to a spectrum of electrons with smaller kinetic energies. Experimentally one can then choose between three detection modes:

- **Total electron yield (TEY):** in this case all emitted electrons (i.e. Auger plus secondary electrons) are detected. This detection method yields a high signal intensity, though this is paid for with a high background due to low energy electrons. The electrons can be detected with a channeltron or micro channelplate. Alternatively, the sample current, i.e. the current between the sample and ground, can be measured with a nano- or pico amperemeter, which represents the least experimental effort for NEXAFS measurements.
- **Partial electron yield (PEY):** to increase the signal-to-background ratio, a negative retarding field (typically ~50 eV) can be applied to a grid in front of the electron detector (channeltron / channelplate). Thus the background signal from low-energy electrons can be drastically reduced.
- **Auger electron yield (AEY):** the best signal-to-background ratio can be obtained, if only the Auger electrons are detected with an electron energy analyser. This detection mode also enhances the chemical sensitivity, since the analyser energy is tuned to an element specific Auger line (e.g. C-KLL at 266 eV, O-KLL at 512 eV). In addition, NEXAFS has the highest surface sensitivity in the AEY mode, since electrons from deeper layers, that lose energy on their way out of the sample, are not detected.

2.3 GSCF3 calculations of NEXAFS spectra

For the simulation of NEXAFS spectra *ab initio* calculations were performed using Kosugi's GSCF3 package [44-46]. This code is based on the improved virtual orbital approximation (IVO), which explicitly takes into account the effect of the core hole in the Hartree-Fock Hamiltonian and is highly optimised for the calculation of core excited states. These calculations have proven to give good values for the energetic positions and intensities of the π^* -resonances of large compounds, e.g., subunits of polymers [50-52]. For NTCDA, NDCA and ANQ (Chapter 4.2) the ionization potentials, term values, and oscillator strengths for each of the symmetrically inequivalent carbon and oxygen atoms were calculated. In Chapter 4.6 the calculations were performed for one of the middle carbon atoms in butane as a model for polyethylene. The utilized basis set was (621/41) for C and O, (41) for H and (411121/411) for the carbon or oxygen atom with the core hole. An additional polarization function was placed at the atom with the core hole. The ground state geometries were derived from an *ab initio* geometry optimisation at the STO-3G level using the program *GAUSSIAN 98*. To simulate the influence of experimental and intrinsic broadening the calculated NEXAFS spectra were generated by convoluting the GSCF3 results with Gaussian functions of 0.3 eV FWHM for resonances of eigenvalue $\epsilon < 0$ and 1.2 eV for $0 < \epsilon$ at the C K-edge and 0.6 eV for $\epsilon < 0$ and 2.4 eV for $0 < \epsilon$ at the O K-edge, respectively. For this purpose the program *SIMILE* was used.

2.4 Vibronic excitation

Figure 2.7 displays a schematic view of the electronic and vibronic excitations of a diatomic molecule AB. Note, that polyatomic molecules can be discussed in complete analogy. In this case the internuclear distance R has to be understood as a more abstract reaction coordinate of the corresponding vibronic mode.

The lower potential curve belongs to the molecule in the electronic ground state (AB). For the temperature range and the vibronic modes, that are interesting in this work ($T \leq 300 \text{ K} \Rightarrow kT \leq 25 \text{ meV}$, $h\nu \geq 100 \text{ meV}$) the molecule is in its vibronic ground state ($n = 0$).

If during the NEXAFS process a core electron is excited into an unoccupied molecular orbital, an excited molecule with a different potential curve AB^+ is generated. If the final state orbital is, e.g., an anti-bonding π^* -orbital (as it is the case for the π^* -resonances of the organic molecules in this work), the intramolecular bonding is weakened, the potential curve is shifted to higher distances R_0' , and thus the molecule is vibronically excited. As can be derived from Figure 2.7, the photon energy $\hbar\omega$ required to excite the electronic and vibronic state is

$$\hbar\omega = E_A + n \cdot E_{vib}' \quad (2.19)$$

where E_A is the adiabatic energy difference between the vibronic ground states of the initial and final electronic state and $E_{vib}' = h\nu'$ the vibronic energy in the electronic excited (final) state.

To calculate the transition cross section the assumption is generally made, that the nuclear motion is slow ($1/\nu_{vib} \geq 10^{-14} \text{ s}$) compared to the electronic transition. Thus, two approximations can be made. The first is known as *Born-Oppenheimer* approximation [53] and means, that the wave function $\Psi(\vec{R}, \vec{r})$ can be simply written as the product of the electronic wave function $\varphi(\vec{r})$ and the nuclear wave function $\psi(\vec{R})$,

$$|\Psi_i\rangle = |\varphi_i\rangle |\psi_0\rangle \quad \text{and} \quad |\Psi_f\rangle = |\varphi_f\rangle |\psi_n'\rangle, \quad (2.20)$$

where $|\varphi_i\rangle$ and $|\varphi_f\rangle$ are the electron wave functions of the initial and final state, respectively, $|\psi_0\rangle$ is the nuclear wave function of the ground state molecule and $|\psi_n'\rangle$ the nuclear wave function of the excited molecule (i.e. the molecule with a core hole and an electron in the orbital i). The index n denominates the different final states of the nuclear wave function. The electron wave functions are one-particle functions.

The second approximation, the *Franck-Condon principle* [54,55], says, that the nuclear distance R does not change during the excitation process. Thus the transition probability P_{if} (see equation 2.5 and 2.9) can be written as

$$P_{if} \sim \left| \langle \varphi_f | \vec{e} \cdot \hat{p} | \varphi_i \rangle \right|^2 \cdot \left| \langle \psi_0 | \psi_n' \rangle \right|^2 = \left| M_{if} \right|^2 \cdot \left| \langle \psi_0 | \psi_n' \rangle \right|^2, \quad (2.21)$$

since $\vec{e} \cdot \hat{p}$ only effects the electronic wave functions $|\varphi\rangle$. The overlap of the vibronic wave functions $|\langle\psi_0|\psi_n\rangle|^2$ is the so-called Franck-Condon (FC) factor and reflects the excitation cross section P_n for the vibrational level n .

If the FC principle is valid and if a variation of the transition matrix element $M_{fi} = \langle\varphi_f|\vec{e} \cdot \hat{p}|\varphi_i\rangle$ can be neglected in the energy range of the vibrational band (~ 1 eV), the energy distribution $j(\hbar\omega)$ can be simply written as

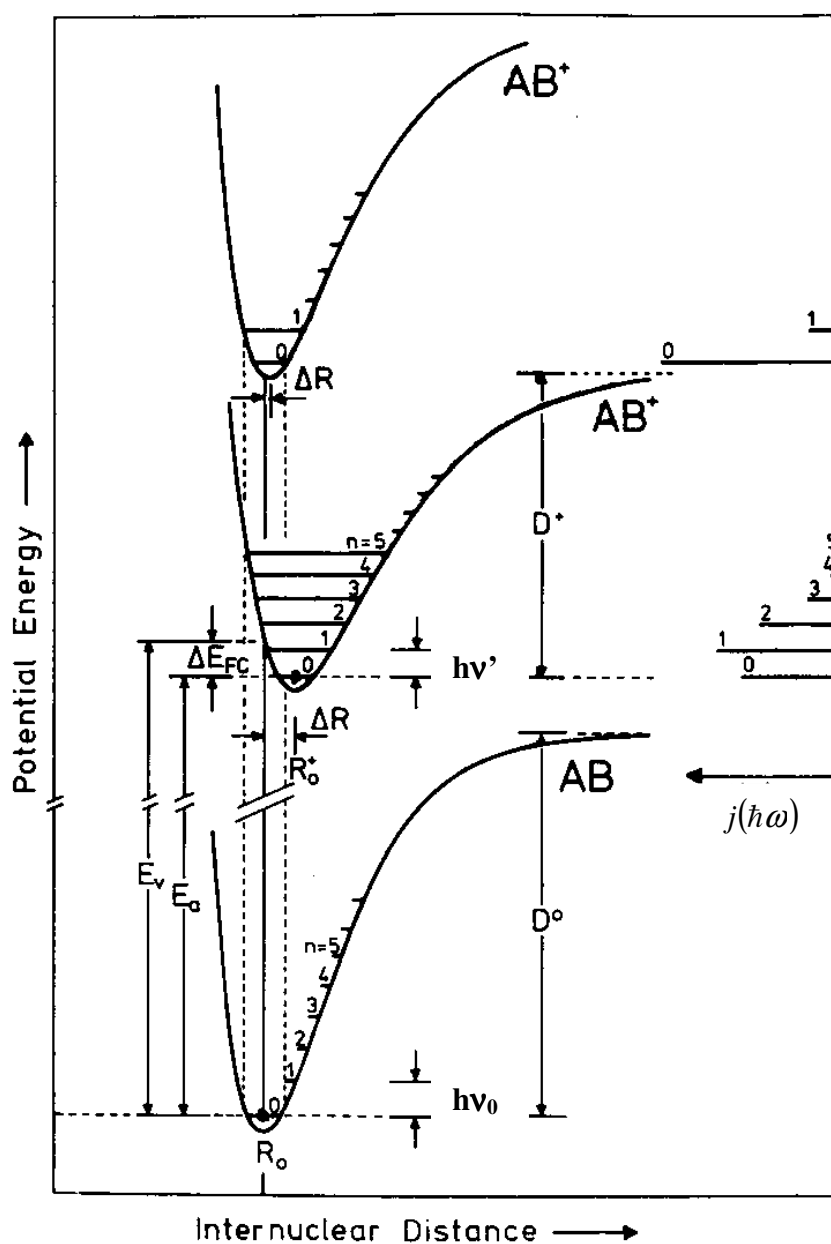


Figure 2.7: Illustration of the potential curves of a molecule to demonstrate the electronic and vibronic excitation in the NEXAFS process (from Ref. [24])

$$j(\hbar\omega) = |M_{fi}|^2 \sum_{n=0}^{\infty} |\langle \psi_0 | \psi_n \rangle|^2 \delta(\hbar\omega - E_a - E_{vib}'). \quad (2.22)$$

A qualitative sight of the resulting spectrum is displayed on the right side of Figure 2.7. A notable overlap of the wave functions only occurs in the range of the dotted vertical lines. If the bonding situation in the molecule does not change significantly upon NEXAFS excitation (i.e. the final state orbital is non-bonding), the equilibrium distance R_0 does practically not change (upper curve) and vibrational excitation does (almost) not occur. If the final state orbital is, e.g., strongly anti-bonding, the equilibrium distance is enhanced to $R_0' = R_0 + \Delta R$, and a wealth of vibronic excitations can be observed in the spectrum. In this case the lowest-energetic transition, the so-called adiabatic threshold E_a , does generally not coincide with the energy of the vertical transition E_v . The energy shift between E_v and E_a is the Franck-Condon shift ΔE_{FC} (see Figure 2.7).

The FC factors can be calculated for the harmonic oscillator potential [56]. It results in a Poisson distribution and thus the spectrum is

$$j(\hbar\omega) = e^{-\beta} \sum_{n=0}^{\infty} \left(\frac{\beta^n}{n!} \right) \delta(\hbar\omega - E_a - E_{vib}'), \quad (2.23)$$

with $\beta = \frac{\Delta E_{FC}}{E_{vib}'}$. More exact theories include second-order coupling terms between electronic

transition and nuclear motion. These result in considerably different values for β but only in very small deviations from the Poisson distribution. For very big β -values the Poisson distribution merges into a Gaussian distribution

$$j(\hbar\omega) \xrightarrow[\substack{\beta \rightarrow \infty \\ E_{vib}' \rightarrow 0}]{\quad} \frac{1}{\sqrt{2\pi\Delta_V}} \exp\left(-\frac{1}{2} \left(\frac{E_v - \hbar\omega}{\Delta_V} \right)^2\right), \quad (2.24)$$

with the full width at half maximum $\Gamma_{1/2} = 2\sqrt{2\ln 2}\Delta_V$, $\Delta_V = \sqrt{\beta} \cdot E_{vib}' = \sqrt{\Delta E_{FC} \cdot E_{vib}'}$. Equation (2.24) is already a good approximation for the envelope of a vibronic progression for $\beta \geq 5$. Note, that the maximum intensity of the vibronic band does only coincide with E_v in the case of (2.24). For small values of β the maximum of the envelope is between E_a and E_v .

Though the harmonic approximation is valid for real molecular excitations only in the vicinity of the potential minimum, various useful relations can be derived from this approach, that can be generally applied with satisfying accuracy [57].

From the potential

$$V = \frac{1}{2} k (R - R_0)^2 \quad (2.25)$$

and the relation for the force constant

$$k = 4\pi^2 \nu^2 \mu \quad (2.26)$$

a simple expression for the change of the nuclear distance $\Delta R = R_0' - R_0$ can be derived:

$$\Delta R = \frac{1}{\pi\nu'} \sqrt{\frac{\Delta E_{FC}}{2\mu}}, \quad (2.27)$$

where $\mu = (1/m_1 + 1/m_2)^{-1}$ is the reduced mass of the (e.g. diatomic) molecule.

For different electronic states of a particular molecule an increase of the equilibrium distance R_0' with decreasing force constant k is expected. A relation, that is fulfilled very well in most cases, was found empirically and leads together with (2.26) to the relation

$$R_0'^2 \cdot \nu = \text{const.} \quad (2.28)$$

Together with (2.27) a correlation of the Franck-Condon shift ΔE_{FC} and the vibronic energy in the electronically excited and in the ground state, $h\nu'$ and $h\nu_0$, respectively, can be derived [58]:

$$\Delta E_{FC} = 1.2eV \left(\frac{h\nu_0}{h\nu'} - 1 \right). \quad (2.29)$$

Thus, with the help of equation (2.29) the measured vibronic energy $h\nu'$ in the NEXAFS excited state can be calculated back to the ground state vibronic energy $h\nu_0$ (and can then be compared to the corresponding values from ground state methods like HREELS and FTIR) if the FC shift is derived from the experimental data.

If higher vibronic levels are excited due to the electronic transition into a strongly anti-bonding or strongly bonding orbital, the harmonic approximation is no longer sufficient to describe the potential shape, since anharmonicity effects have to be taken into account in the potential. A widely used approach, that includes this anharmonicity, is the Morse potential [59]:

$$V = D[1 - \exp(-b(R - R_0))]^2, \quad (2.30)$$

where D is the dissociation energy and b a constant. Both parameters depend on the energy E_n of the vibronic spectrum according to

$$E_n = \left(n + \frac{1}{2} \right) h\nu - \left(n + \frac{1}{2} \right)^2 \frac{(h\nu)^2}{4D}, \quad \text{with } h\nu = \frac{hb\sqrt{\frac{2D}{\mu}}}{2\pi}. \quad (2.31)$$

This equation can be fitted to the experimental data.

Note, that for most simple molecules more exact potential curves are known. These were derived numerically from the experimental gas phase spectra by a method developed by Rydberg [60], Klein [61] and Rees [62].

2.5 LEED

Low-energy electron diffraction (LEED) is a standard technique for the analysis of the geometrical structure of a surface. Due to the small penetration depth of low energy electrons ($E_{\text{kin}} = 10 \text{ eV} - 100 \text{ eV}$) the information comes only from the topmost layers of the investigated sample.

A typical LEED instrument consists of an electron gun, grids and a hemispherical fluorescence screen, that detects the reflected electrons. From the diffraction pattern the symmetry of the surface and information about surface reconstructions and superstructures can directly be derived. A quantitative analysis of the reflex positions yields the geometrical parameters of the two dimensional unit cell. The resolution as well as the dynamic of the measurement can be increased, if an electron gun with a small focal spot and a channeltron as detector are used. This is realised in the SPA-LEED (spot profile analysis low energy electron diffraction).

A detailed discussion of the theory, the experimental procedure and the surface structure determination can be found in Refs. [63-65].

3 Experimental

3.1 Sample preparation

For all studies presented in this work Ag(111) single crystal substrates were used, which were cleaned by repeated cycles of Argon ion sputtering and annealing. Argon ion sputtering (ion energy 600 eV) was performed for 20 minutes at an incidence angle of 45° with respect to the sample surface using ion currents of about 4 μA. The sample was then annealed at 800 K for 15 minutes, and the temperature was then slowly (~ 1 K/s) decreased to 550 K. After this cleaning procedure, the sample was checked by x-ray photoelectron spectroscopy (XPS), low-energy electron diffraction (LEED) and NEXAFS. The sputter/anneal cycles were repeated until no traces of impurities could be detected and sharp LEED-spots indicated a high structural order.

The organic thin films were prepared under UHV conditions (base pressure < 2·10⁻¹⁰ mbar) by organic molecular beam deposition (OMBD). All substances investigated in Chapters 4.2 – 4.5 are available as polycrystalline powders at room temperature and have sufficiently low vapour pressures to allow evaporation from a Knudsen cell connected to the UHV preparation chamber. To check the organic substances for impurities and to control the evaporation rate a quadrupole mass analyser was used. The deposition rate was kept below 1 monolayer per minute in order to prepare structurally well-defined organic films with homogeneous molecular orientation. The substrate temperature was chosen according to the sublimation characteristics of the different molecules. Thus, the PTCDA and BPDCA films were prepared at room temperature, whereas for NTCDA, NDCA and ANQ films the substrate temperature was lowered by LN₂ cooling to approximately 150 K.

The sample temperature was monitored by a NiCr-NiAl thermocouple spot-welded to the sample holder close to the sample. The temperature scale was calibrated before the experiments using the boiling point of LN₂ and the melting point of ice.

3.2 Investigated molecules and preparation parameters

The chemical structure formulae of the investigated organic molecules are displayed in Figure 3.1. The anhydride molecules 1,4,5,8-naphthalene-tetracarboxylic acid dianhydride (NTCDA), 3,4,9,10-perylene-tetracarboxylic acid dianhydride (PTCDA), benzoperylene-(1,2)-dicarboxylic acid anhydride (BPDCA) and 1,8-naphthalene-dicarboxylic acid anhydride (NDCA) all consist of different sized aromatic core systems with one or two functional anhydride groups. NDCA and BPDCA (C_{2v} point group) have an intrinsic dipole moment whereas NTCDA and PTCDA (D_{2h} point group) exhibit an electrostatic quadrupole moment. In addition, we investigated the closely related molecule acenaphthenequinone (ANQ, C_{2v} symmetry), which has a naphthalene core and a quinoic side group.

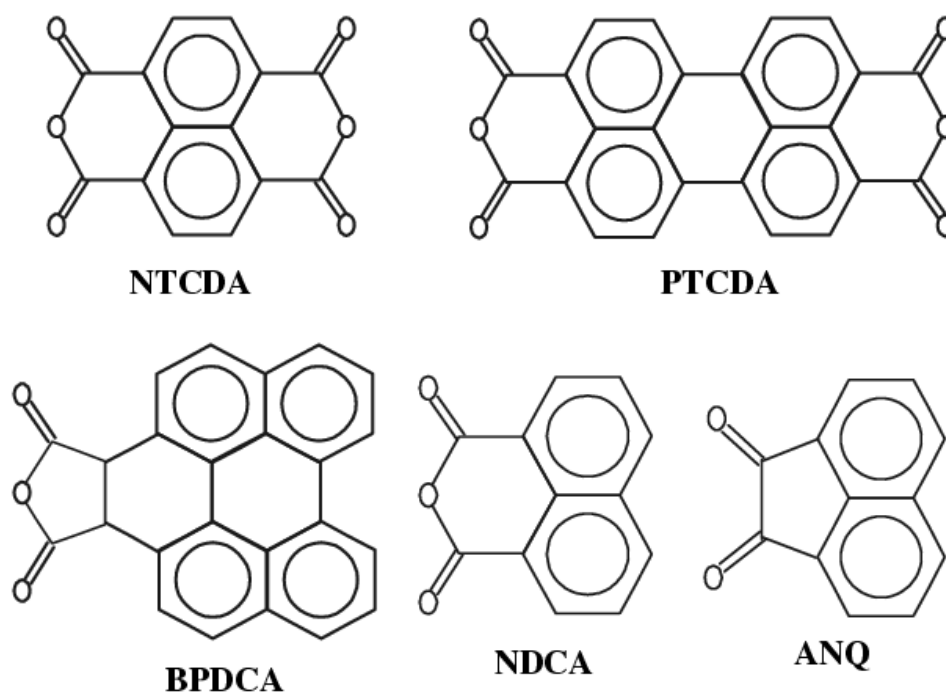


Figure 3.1: Molecular structure formulae of the investigated organic molecules

The molecular masses, the temperatures of the Knudsen cell T_{KC} used for the OMBD film preparation and the multilayer desorption temperatures T_D , as well as some Refs. that give additional information on the thin film preparation for the respective substance are summarised in Table 3.1.

Molecule	NTCDA	PTCDA	NDCA	BPDCA	ANQ
Mass / amu	292	392	198	346	182
T_{KC} / K	450	580	390	500	380
T_D / K	360	530	310	420	300
Refs.	[39,66]	[39,65]	[39,67]	[39]	[67]

Table 3.1: Molecular masses, temperatures of the Knudsen cell T_{KC} used for the OMBD film preparation and multilayer desorption temperatures T_D for the substances investigated in this work. Additional information can be found in the references cited in the last line.

3.3 Beamlines and experimental stations

3.3.1 U49/1-PGM / UE52-PGM

Most of the data presented here were recorded between 02/2001 and 08/2002 at the U49/1-PGM beamline of BESSY II. It consisted of an 84-period undulator of 49 mm period length, a vertically collimating cylindrical mirror (M1), a plane grating monochromator (PGM) with a plane mirror (M2) and a plane grating (G1), two focusing mirrors, i.e. one vertically (cylindrical mirror M3) and one horizontally (spherical mirror M4), and an exit slit [68]. It is noted that the electron beam in the undulator defines the source, i.e. the beamline has no entrance slit and is hence sensitive to the electron beam position. The photon energy ranges from 100 to 1500 eV.

An energy resolving power of $E/\Delta E = 10,500$ was experimentally determined at the N K-edge at 401 eV from the Gaussian contribution to the line width of the vibronic states resolved for the N 1s $\rightarrow \pi^*$ -resonance of gaseous N₂. The corresponding photon flux at the N K-edge was $3 \cdot 10^{10}$ ph/s/100mA (fixed-focus constant $c_{ff} = 10$, exit slit 10 μm).

The spectral resolution can be calculated for the actually employed excitation energies according to $\Delta E \sim E^{3/2}$. The resulting energy resolution for the C K- and O K- NEXAFS spectra presented in this work is thus 24 meV at 300 eV and 56 meV at 530 eV, respectively. The C1s and O1s XPS spectra were recorded with photon energies of 335 eV and 700 eV and a corresponding excitation line width of 26 meV and 88 meV, respectively.

In March 2002 the horizontally polarizing undulator U49/1 was replaced by a new APPLE-II type 79-period undulator with 52 mm period length, which provides either elliptical or linear polarization with variable direction of the polarization plane.

The beamline has a spectroscopy end station which consists of a two chamber ultra-high vacuum system. It allows in-situ film preparation in a preparation chamber (equipped with a sputter gun, low-energy electron diffraction (LEED) optics, and a Knudsen cell for the evaporation of organic substances) and direct sample transfer into the analysis chamber equipped with a SCIENTA SES200 electron energy analyser [69] for high quality photoemission experiments as well as a retarding field detector for partial electron yield (PEY) NEXAFS.

3.3.2 NEXAFS

For all PEY NEXAFS data presented in this work a retarding voltage of 50 V was applied. During NEXAFS scans also the total electron yield (TEY) signal was recorded by measuring the sample current. Energy scans in a large window (generally 40 eV) around the absorption edges were performed with an energy step width of 20 meV. For the high-resolution data the photon energy was scanned in 2 meV steps to exploit the full monochromator resolution.

3.3.3 PM-1/SX-700

The NTCDA monolayer NEXAFS spectra presented in Chapter 4.5 were recorded at the PM-1 dipole (bending magnet) beamline at BESSY-II. This beamline uses a Petersen-type SX-700 monochromator to select photon energies in the range from 20 to 2000 eV with an energy resolving power of about $E/\Delta E = 3000$ and a photon flux of about $1 \cdot 10^{10}$ ph/s/100mA at 400 eV ($c_{ff} = 2.08$, exit slit 50 μm). Also this beamline has no entrance slit. A detailed description of the beamline and its performance can be found in Refs. [39,70]. The absorption signal was measured by detecting the C- and O-KLL Auger electron yield (AEY) with a VG CLAM-II analyser. The experimental set-up of the UHV system used for the PM-1 measurements is described in detail in Refs. [39,66,71].

3.3.4 STXM

All NEXAFS data presented in Chapter 4.6 were recorded in 02/2000 and 03/2000 using the Stony-Brook scanning transmission x-ray microscope (STXM) [72] at the National Synchrotron Light Source (NSLS). The resolving power was $E/\Delta E = 2500$ [73]. To calibrate the energy scale, absorption spectra of gaseous CO_2 and of the investigated samples were recorded simultaneously [17]. For in-situ heating of thin film samples in the STXM, a special sample holder was built that allowed resistive heating of TEM (transition electron microscopy) grids.

A very detailed description of the experimental procedure of x-ray spectro-microscopy at the NSLS beamline X1A can be found in Ref. [17].

3.3.5 XPS

The utilized SCIENTA SES200 electron energy analyser [69] at the BESSY U49/1-PGM (now UE52-PGM) beamline has a possible energy resolution of $\Delta E < 5$ meV at a pass energy of 2 eV. For all XPS data a constant pass energy of 40 eV was applied which corresponds to an analyser resolution of $\Delta E = 80$ meV. Together with the excitation line width of 26 meV and 88 meV (see above) at a photon energy of 335 eV and 700 eV, respectively, the overall experimental resolution (analyser plus beamline) can thus be calculated to 84 meV for the C 1s and 119 meV for the O 1s photoemission data in the Chapters 4.3, 4.4, and 4.5. All spectra were recorded with normal emission of the photoelectrons and a 60° angle between the (horizontally polarized) synchrotron beam and the sample surface normal.

The XPS spectra were background corrected by subtracting the sum of an exponential curve and a Shirley function thus eliminating the influence of secondary and multiply scattered electrons.

All samples were checked carefully for possible radiation damage during the data acquisition and no signs of degradation on the time scale of the presented XPS and NEXAFS experiments (~ 1 hour) were observed. For PTCDA multilayers we explicitly performed a radiation damage study, yielding significant damage only for much higher radiation doses. (see Appendix 5.1)

3.3.6 SPA-LEED

The LEED pictures were recorded with an Omicron SPA-LEED (spot-profile analysis low-energy electron diffraction) with an electron energy of 28 eV. The utilized SPA-LEED apparatus is characterised by a high resolving power and a high dynamic, which lead to a high transfer width of 1000 Å. It utilises an electron gun with a small focus and a channeltron (instead of a fluorescence screen) to detect the reflected electrons. In the Omicron set-up, that was developed by M. Henzler and co-workers [74], the electron gun and the channeltron are fixed and the reciprocal space is scanned by electrostatic deflection. A more detailed description is given in Ref. [65].

4 Results

4.1 Energy calibration and intensity normalization in high-resolution NEXAFS spectroscopy

4.1.1 Motivation

The near-edge x-ray absorption fine structure (NEXAFS) technique has become a powerful technique to analyse interesting new materials, adsorbates, and thin films [14]. This method is particularly useful for the investigation of organic substances, for at least three reasons. First, the excitation of core electrons into unoccupied molecular orbitals yields important information on the electronic structure involving chemical shifts of the core levels as well as significant fine structure in the unoccupied valence states. Both are sensitive to the chemical bonding and the latter are responsible for electron transport [75-78]. Secondly, NEXAFS is a local probe that monitors the local distribution of valence states at the different core hole sites that can be selected by the energy dependence of the absorption cross section [52]. Thirdly, NEXAFS is ideally suited to investigate the molecular orientation based on the linear NEXAFS dichroism [76,79-81]. A detailed understanding of the rich fine structure is backed by appropriate calculations [14,44,82-84]. These advantages of NEXAFS are best illustrated by the example presented in Chapter 4.2, the observation of detailed fine structure in highly-ordered thin films of various organic substances which is due to various electronic transitions and their coupling to vibrations [85]. It is emphasized that such fine structures can only be observed by using a high-brilliance beamline with a high energy resolution monochromator at a 3rd generation synchrotron source.

It is obvious that energy calibration and intensity normalization become more important as more fine structure is resolved. Of course, a beamline, i.e. the monochromator, has to be energy-calibrated before being used. It is less well known that the energy calibration should be checked routinely – e.g. twice during each fill - , in particular when a very accurate energy scale is required. The reason is that mechanical movements, positions of optical elements, the position of the electron beam after each refill, and changes of the heat load on optical elements and hence thermally induced deformations frequently lead to changes of the photon energy scale. Most experimenters hence rely on typical structures in the transmission or flux (I_0) curve for a routine recalibration of their data since the I_0 signal is usually recorded simultaneously. This is particularly the case for the C 1s edge at which two very prominent “dips” in the flux curve appear at about 284 and 291 eV (see Figure 4.1.1). However, as we will show in the following, there are severe problems with this procedure since the I_0 structures also may change and since it may be impossible to record a useful I_0 signal simultaneously, e.g. when using a high-brilliance beamline with a very small focal spot.

Such changes of the I_0 curve may also be disastrous for the intensity normalization of the spectra which is required because the primary photon flux usually has a significant energy dependence. This intensity variation as a function of the photon energy can be as much as 98 %, at the C 1s edge due to the absorption by photolytically dissociated carbon impurities on the optical elements. In such a case the intensity normalization will fail even if only small changes in the I_0 curve occur.

In the following we will give examples how large these effects can be and by which means these problems can be solved. Thus, after a short experimental section, we will first discuss the energy calibration and will then move on to the intensity normalization problem. This work has been published in *the Journal of Electron Spectroscopy and Related Phenomena* (see Ref. [86]).

4.1.2 Energy calibration

The energy scale of a monochromator has to be calibrated at several points, even if a good description of the energy /wavelength dependence on mechanical parameters (e.g. angle of the grating) is available. Of course, the energy scale depends on all mechanical parameters like positions and angles of the grating, the various mirrors, and the exit slit, and therefore has to be calibrated carefully. The calibration, once established, can be influenced by mechanical

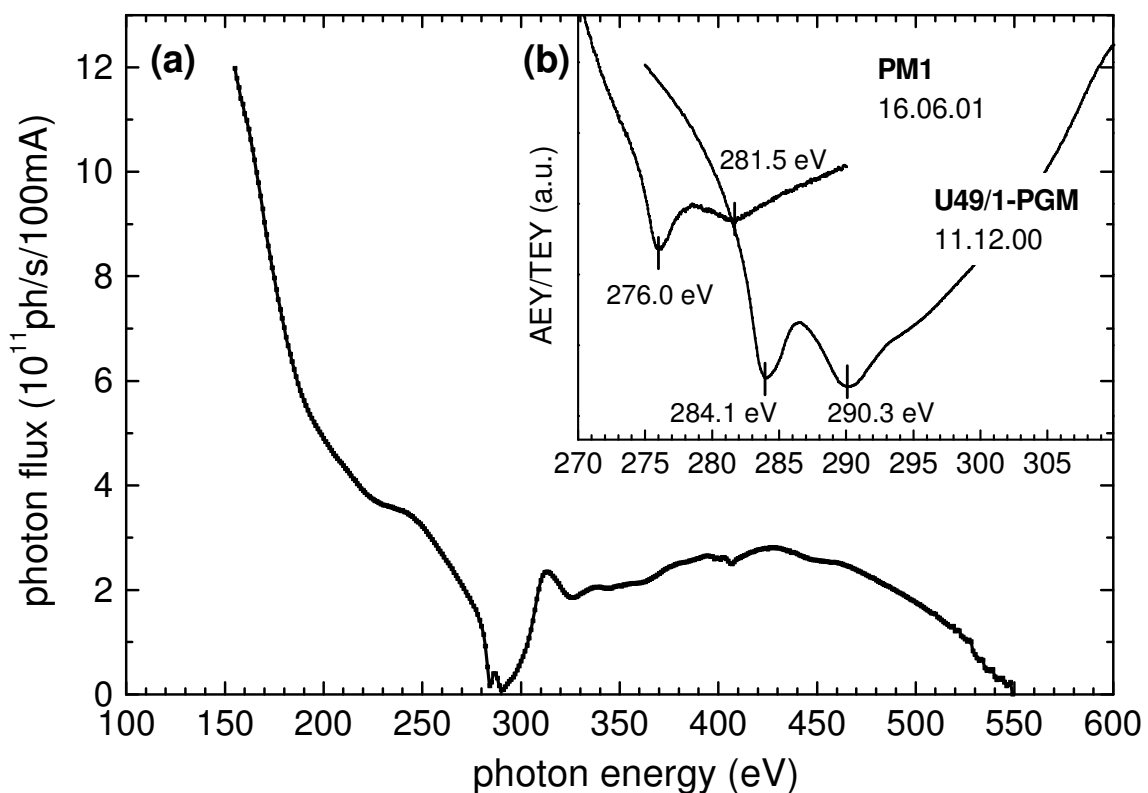


Figure 4.1.1: (a) Photon flux of the U49/1-PGM beamline at BESSY II recorded by a photodiode using the first undulator harmonic (monochromator settings: fix focus constant $c_{ff} = 2.25$; exit slit: $30 \mu\text{m}$). (b) (Inset): Comparison of the flux curves of the PM1 and U49/1-PGM beamlines at BESSY II around the carbon K-edge plotted on nominal (not recalibrated) energy scales.

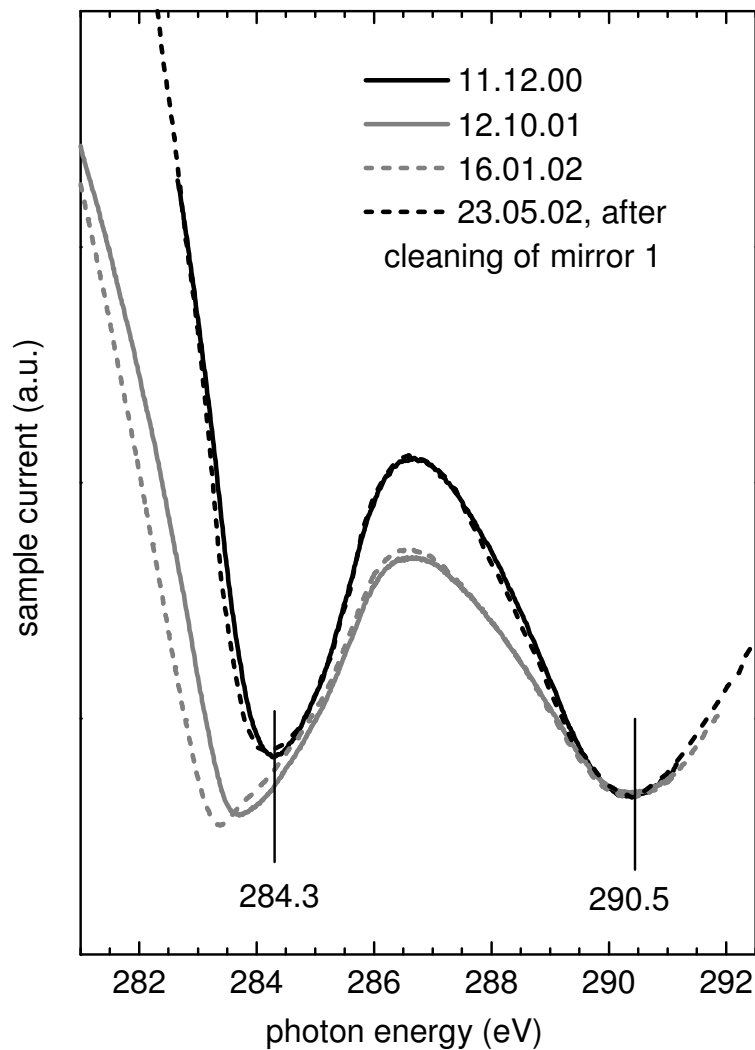


Figure 4.1.2: Comparison of flux curves using the current from a clean Ag sample (total electron yield) recorded at the U49/I-PGM (three older data) and the UE52/PGM (latest spectrum), respectively. The energy scales were recalibrated, and the intensities were adjusted at the second dip in the flux curve.

clearance of the monochromator drives, faults of the angle decoders, mechanical shocks, exchange of gratings, bake-outs of the UHV chambers, and even by the temperature increase of optical elements in the high photon flux after injection. The energy scale also depends on the position of the electron beam, especially for beamlines without entrance slit. This position may change after modifications of the storage ring or of the orbit parameters, and it may vary from run to run, after new injections, or even during data recording. Hence it is important to check the energy calibration routinely, i.e. at the beginning of each beamtime, after each refill, and perhaps even before and after each new experiment (see below).

There are at least three different approaches for this calibration check. 1) The most accurate and most general method is the use of very precisely known photoemission lines and an accurately calibrated photoelectron spectrometer. 2) If standard samples have been previously measured by NEXAFS using a calibrated beamline their NEXAFS spectra can be used as calibration standards in the future. Using gaseous samples with well known absorption

spectra, e.g. He, Ar, N₂, Ne and Xe, this is a common way of energy calibration. Relatively simple experimental requirements, sharp absorption features and a wide energy range (10 – >103 eV) make it the most popular method for beamline commissioning in the VUV and soft x-ray range [87]. For in-situ calibration near the carbon edge carbonaceous gases such as CO₂, CO and acetylene can also be applied [17]. 3) Similarly, if the flux (transmission) vs. energy curve of the monochromator, usually called I₀ curve, has sharp and stable structures, these can also be used as calibration points. This third method is commonly applied near the C 1s edge at which the I₀ curve always has two very pronounced dips. It is well established – though very dangerous (see below) – to set the photon energy at these dips to 284.7 and 291.0 eV, respectively [14].

The last point is illustrated in Figure 4.1.1a which shows a typical transmission (I₀) curve of a soft X-ray beamline (U49/1-PGM at BESSY II) with the dominant double-dip at about 290 eV. This dip is due to absorption by carbon contaminants deposited on the optical elements by photolytical processes. In the case of the U49/1-PGM with five optical elements the photon flux drops from about $4.1 \cdot 10^{11}$ ph/s/100mA at 230 eV to $8.1 \cdot 10^9$ ph/s/100mA at 290 eV. Of course, such a pronounced structure in the I₀ curve is disadvantageous because of the intensity loss (factor 50) and the problem of normalization (see below). However, it is commonly believed that the dips can be used for routine and accurate energy calibration. The inset (Figure 4.1.1b) provides a zoomed view of the dip region of two different monochromators using their nominal energy scale. It demonstrates that the flux curves can differ in both, energy and shape for these different beamlines (here: PM1 and U49/1-PGM). As mentioned, the common way of (re)calibration would be to set the energies of the dips to 284.7 eV and 291.0 eV, respectively [14]. However, it can be derived from the inset of Figure 4.1.1b that this method is not sufficient since not only the energy positions but even the energy separation of both dips may vary, for instance between 5.5 and 6.3 eV in the present case.

Moreover, the shape, the energy separation, and in particular the energy positions of the dips of a calibrated beamline may change as a function of time. This is shown in Figure 4.1.2 which displays the I₀ curves taken at three different runs (continuous black line and grey lines) within about one year using the same U49/1-PGM monochromator. The monochromator was carefully calibrated each time according to the procedure given below. While the second (because of its shallow shape less suited) dip remained constant in energy, the first sharp I₀ dip shifted from 284.3 to 283.4 eV, i.e. by nearly 1 eV ! The deviation of 1.3 eV of the here measured first dip (dashed grey curve) from the literature value is unacceptable and nearly two orders of magnitude worse than the possible accuracy of calibration. We note that the origin of this shift is a proceeding contamination of the first mirror, since a cleaning of this mirror in March 2002 brought the shape of the flux curve and hence also the dip positions almost completely back to the initial state of December 2000 (compare black curves in Figure 4.1.2). This result also shows, that the applied cleaning procedure of mixed oxygen/argon plasma etching [88] is an appropriate method to remove contaminants. Note also, that the replacement of the undulator U49/1 by the new UE52 in March 2002 had no significant effect on the shape of the flux curve.

Now we briefly describe an accurate calibration method that can be used as standard procedure. In a first step this requires the accurate calibration of an electron spectrometer. By using the well-known energies of a laboratory X-ray source and of prominent photoemission or Auger lines of clean noble metals (see Table 4.1.1) [89,90] one can exactly determine the deviation Δ of the used spectrometer over the full range of kinetic energies. This is done by recording at least two peaks that are as far as possible apart from each other on the kinetic energy scale. Their energy positions are carefully evaluated yielding $E_{\text{Kin}}^{\text{meas}}$ and subtracted from the corresponding calibration values ($E_{\text{Kin}}^{\text{cal}}$ or $E_{\text{B}}^{\text{cal}}$, see Table 4.1.1) according to

Cu		Ag		Au		Ni		Ru	
PES line	E_B (eV)	PES line	E_B (eV)	PES line	E_B (eV)	PES line	E_B (eV)	PES line	E_B (eV)
2s	1097.05	3d _{3/2}	374.27	4f _{7/2}	83.98*	2s	1008.31	3s	586.37
2p _{1/2}	952.48	3d _{5/2}	368.26*			2p _{1/2}	869.99	3p _{1/2}	483.77
2p _{3/2}	932.67*					2p _{3/2}	852.75	3p _{3/2}	461.54
3s	122.48					3s	110.77	3d _{3/2}	284.30
3p _{3/2}	75.14*					3p _{1/2}	66.98	3d _{5/2}	280.13
						3p _{3/2}	66.30	4s	75.25
								4p _{3/2}	43.40
Auger	E_K (eV)	Auger	E_K (eV)			Auger	E_K (eV)		
L ₃ VV	918.62*	M ₄ VV	357.80*			L ₃ VV	846.00		
						L ₃ M _{2,3} V	774.42		
excitation energies of common laboratory sources									
AlK α = 1486.58 \pm 0.03 eV*					MgK α = 1253.56 \pm 0.03 eV*				

Table 4.1.1: Calibration values for some photoemission binding energies and Auger kinetic energies of the clean metals Cu, Ag, Au, Ni, and Ru using Al and Mg K α excitation and calibrated energies of the Al and Mg K α excitation lines. The data indicated by asterisks (*) were taken from Refs. [89] and [90] (accuracy = 0.02 eV). The other data (unpublished) were acquired by Höfer, Hudeczek, Wurth and Umbach using a calibrated VG ESCALAB Mk I (accuracy < 0.05 eV).

$$\Delta = E_{\text{Kin}}^{\text{cal}} - E_{\text{Kin}}^{\text{meas}} = (h\nu - E_B^{\text{cal}}) - E_{\text{Kin}}^{\text{meas}}. \quad (4.1.1)$$

The deviation Δ is then plotted versus the real kinetic energy resulting in a straight line (a non-linear behaviour of the spectrometer is usually not found [89,90]) which can then be used as calibration curve for this particular spectrometer. This calibration should be checked routinely, say at least twice a year or – better – for each run. With our SCIENTA XES200 analyzer at the U49/1-PGM we measured the 3d_{5/2} and M₄VV lines of a carefully cleaned Ag(111) sample with Mg K α and Al K α excitation (to cover a sufficiently wide kinetic energy range, 350 – 1120 eV) and obtained a constant deviation (offset) of $\Delta = 0.22$ eV. Of course, the Fermi edge of s-metals (e.g. Cu, Ag, Au) is also a good calibration point.

In the next step the photon energy scale of the monochromator is calibrated by recording photoemission lines with accurately known binding energies, for instance those of Table 1, using photon energies in the energy range of interest. For example, for the spectral range of the C 1s NEXAFS measurements we recorded the Ag Fermi edge using the nominal photon energies $h\nu = 270$ and 320 eV, respectively, and determined the exact values of $h\nu$ by taking

the analyser deviation Δ at 270 (320) eV kinetic energy into account. In this way an accuracy of the absolute energy scale of <50 meV can be obtained. The error bar mainly depends on the quality of the calibration values and on the evaluation of the measured photoemission/Auger lines. Of course, the relative accuracy is significantly better, for instance better than 10 meV, depending on the resolution of analyser and monochromator. This relative accuracy turned out to be of prime importance also for the intensity normalization as discussed in the next section.

The experimenters should be aware, that a recalibration by simply shifting the energy might lead to a distorted energy scale. This is because the energy is inversely proportional to the wavelength, and for most monochromators the miscalibration is typically due to an offset in wavelength. However, for small recalibrations within a small energy range, e.g. 100 meV in the range 270 to 320 eV, non-linearity effects in the energy scale are negligible. For larger deviations one has to recalibrate the wavelength and recalculate the energy scale to maintain linearity.

We note, that in addition to the energy calibration procedures described above a new method, that can be utilized for plane-grating monochromators with the freedom to change the fixed-focus constant c_{ff} , has been developed by BESSY [91]. In combination with the in-vacuum angular encoders of the new BESSY PGM generation, that allow highly accurate measurements of the mirror and grating angles [92], this method shows an absolute accuracy of the calibrated energy of $\Delta E/E \sim 10^{-4}$.

4.1.3 Intensity normalization

As mentioned above, NEXAFS spectra have to be normalized since the photon flux varies as a function of energy and time. This normalization is often performed by dividing the sample signal $I_{\text{sample}}(h\nu)$ simply by the flux curve $I_0(h\nu)$. A better normalization procedure which applies to very thin films or adsorbates takes the substrate signal $I_{\text{substrate}}(h\nu)$ into account, according to

$$\begin{aligned} I(h\nu) &= [I_{\text{sample}}(h\nu) - f \cdot I_{\text{substrate}}(h\nu)] / I_0(h\nu) = \\ &= I_{\text{sample}}(h\nu) / I_0(h\nu) - f \cdot I_{\text{substrate}}(h\nu) / I_0(h\nu). \end{aligned} \quad (4.1.2)$$

Here I_{sample} contains the photon energy dependent signals from the adsorbate (or deposited thin film) and from the (attenuated) substrate, while $I_{\text{substrate}}$ stems from the clean substrate. When this is subtracted one has to consider that $I_{\text{substrate}}$ is attenuated by the overlayer resulting in a material, coverage, angle and energy dependent factor $f < 1$. The sample and substrate signals may be recorded in total, partial or Auger yield mode [14] which should be chosen according to the experimental requirements and available equipment. It is emphasized that for each method different offsets due to higher-order contributions, dark currents, stray light, secondary electrons, etc. may occur which also have to be taken into account by subtracting offsets from both signals. The attenuation factor f is usually not sufficiently known and hence is used as a free parameter.

The measurement of the I_0 curve is the central issue for the normalization routine. Conventionally, I_0 is detected by measuring the photocurrent from a Au grid mounted behind the exit slit of the monochromator [14]. In order to avoid problems with contaminations on the I_0 detector one can regularly evaporate a fresh gold film onto the grid before data recording. However, monitoring the I_0 intensity of a state-of-the-art high-brilliance undulator

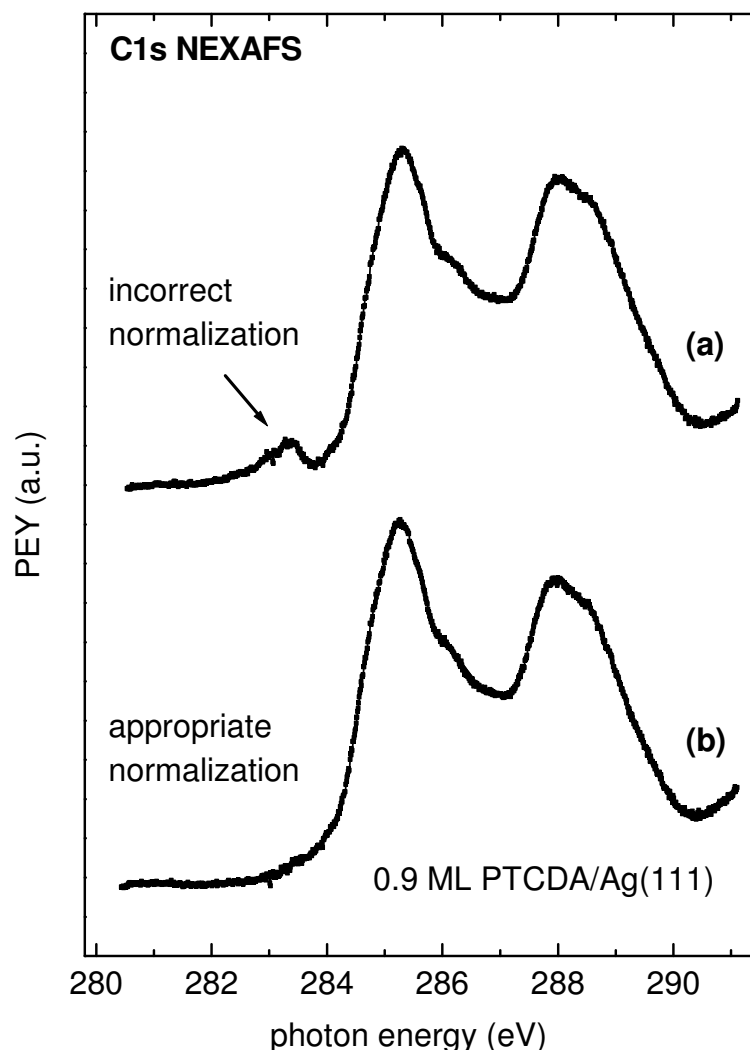


Figure 4.1.3: C 1s NEXAFS spectrum of 0.9 monolayers of PTCDA/Ag(111), (a) normalized by a clean substrate spectrum, as recorded; (b) after proper energy recalibration of sample and I_0 spectra (see text).

beamline is more difficult since this may provide a much smaller beam size ($< 100 \mu\text{m}$). Therefore the use of a conventional gold grid with a mesh size in the order of the magnitude of the beam size is not appropriate since even minor movements of the experimental chamber or the beam will drastically change the I_0 photocurrent signal from the grid and will hence make a correct normalization impossible. Also, measuring the photocurrent with a photodiode is not suitable, at least not for C-K NEXAFS experiments on thin films or monolayers, since the effect of carbon contaminations on the diode will lead to artifacts. In principle, one could use a gas cell inserted between exit slit and sample to record the I_0 curve. This has not been tried by us so far.

A proper alternative is to use the clean substrate spectrum for normalization, i.e.

$$I_0(h\nu) \sim I_{\text{substrate}}(h\nu). \quad (4.1.3)$$

This is possible if the substrate does not show any specific absorption structures in the interesting energy range. Equation (2) can then be reduced to

$$I(h\nu) = c \cdot (I_{\text{sample}}(h\nu) / I_{\text{substrate}}(h\nu) - f) \quad (4.1.4)$$

Of course, I_{sample} and $I_{\text{substrate}}$ (from the clean substrate!) can only be recorded sequentially. In this case the energy calibration has to be monitored carefully, since small changes in the electron orbit, that can occur, e.g., during injection, can slightly shift the photon energy scale, as discussed above. At the U49/1-PGM beamline we observed energy shifts of up to 100 meV between two subsequent injections.

In Figure 4.1.3 it is shown what happens if this effect is not carefully taken into account. The figure displays the C 1s NEXAFS spectrum of a 0.9 ML thick PTCDA (3,4,9,10-perylene-tetracarboxylicacid-dianhydride) film on Ag(111) after it was normalized to (a) a substrate spectrum as measured and (b) to an energy-corrected substrate spectrum. Actually both, the monolayer and the substrate spectrum, were calibrated to the correct energy in this latter case leading to a relative shift of both by 50 meV. It is emphasized that such an energy shift can already lead to strong artifacts in the final spectrum (compare spectrum (a) to spectrum (b) in Figure 4.1.3), particularly in the region of the first sharp I_0 -dip. Since the lowest π^* -resonances of many organic molecules appear exactly in this energy range, a very careful check of all structures in this particular energy range is advisable. In the present case the appearance or non-appearance of (a) structure(s) around 283.5 eV would have major implications since it provides information about the involvement of the lowest unoccupied molecular orbital (LUMO) in the bonding to the substrate. We further note that the (properly corrected) structures in this energy range are very different for similar molecules (e.g. PTCDA and NTCDA) in different bonding situations (e.g. different states or on different substrate surfaces) (see Chapter 4.5 or, e.g., Ref. [93]) indicating the great importance of an accurate energy calibration and intensity normalization.

4.1.4 Conclusions

High-brilliance, high-resolution undulator beamlines enable NEXAFS measurements with very distinct fine structures that are due to various electronic transitions and their coupling to vibrations. This detailed structure contains a variety of information about electronic, chemical and structural properties provided that both, the energy calibration as well as the normalization are carried out with great care.

In this chapter we discussed some of the problems that can arise at such beamlines and gave some procedures how to avoid them. Energy calibrations are easy to perform routinely thus achieving an accuracy of absolute energies of less than 50 meV and of relative energies of about 10 meV. Also, the normalization requires accurate energy scales for both, the sample spectra and the corresponding normalization curves. Otherwise artifacts may arise that lead to incorrect interpretations. Of course, artifacts are particularly large for small signal-to-background ratios, e.g. for signals from monolayers. Thus for a proper normalization, it is strongly recommended to take energy calibration spectra (e.g. of the substrate Fermi edge or of a clean Au foil mounted on the sample holder) directly before or after each sample NEXAFS spectrum.

4.2 Vibronic finestructure in high-resolution x-ray absorption spectra of organic materials

4.2.1 Motivation

Probing the vibronic fine structure in the NEXAFS spectra of large molecules is very promising, since, next to a detailed analysis of the electronic structure, interesting additional information may be expected, e.g., about the coupling to the various vibrational modes, or about polaronic and excitonic effects. A comprehensive understanding of the electron-vibron coupling is also of fundamental relevance for the further development of organic superconductors (SC), since the coupling of electronic and vibronic excitations may be decisive for the SC mechanism in these materials [94,95].

Vibrational fine structure due to the coupling of electronic transitions to vibronic excitations is well established in optical spectroscopy, and it has been observed in several electron spectroscopic experiments such as photoemission or NEXAFS, especially for small molecules and in the gas phase. Most previous NEXAFS experiments with vibrational fine structure hence have been performed on small molecules in the gas phase, e.g., N₂ [96], O₂ [97], CO [98,99], CO₂ [98,100], ethylene [98,101,102], formaldehyde [103], alkanes [104] or one-ring aromates [105-107]. Their spectra could satisfactorily be described by a coupling of electronic transitions to vibronic excitations. Upon adsorption, though, one has to deal with additional broadening of the observed structures due to inhomogeneities within the condensed layers and intermolecular screening effects. High-resolution NEXAFS investigations at the C K-edge in some cases still allow the observation of vibronic features in the C 1s excitation data of physisorbed molecules, such as butadiene [108], hexatriene [108], or butene and similar small hydrocarbons with ethylene building blocks [109] and subunits of polymers [77]. Also, very few photoemission results with vibrational fine structure have been published for small adsorbates or condensates on single-crystalline surfaces [110-112]. Due to the usually lower spectral resolution at the O1s edge the vibronic fine structure in the O K-edge data of condensed species is often degraded below the resolution limit [99].

The prospects for resolving such features have partly been overcome by the high-brilliance third-generation synchrotron sources, which have proven resolving powers of up to $E/\Delta E = 100.000$ in the vacuum-ultraviolet range [113]. An additional problem when probing larger polyatomic molecules is that one has to deal with a large number of normal modes that can be excited. These can wash out the fine structure by superposition of multiple vibronic states. Vibronic fine structure will then only be resolved, if the electronic transition couples preferentially to one or only to a small number of normal modes. In all cases, the energy difference between vibronic states must be greater than the intrinsic lifetime broadening, otherwise the fine structure will not be resolved.

In the following three chapters (4.2.2 – 4.2.4) the results of high-resolution NEXAFS investigations of condensed multilayers of some organic molecules with extended π -conjugated ring systems are presented, focusing on the vibronic features and their dependence on intra- and intermolecular properties.

We emphasize that we also obtained highly resolved NEXAFS spectra with similar fine structures for a number of other systems, such as some acenes which will be published elsewhere [114]. In all cases, we found distinct vibronic absorption fine structures which can be analysed and understood in the same way as will be discussed below thus demonstrating the general validity of the present approach.

4.2.2 The example NTCDA on Ag(111)

This chapter will address the fine structure in the high-resolution C 1s NEXAFS data of the anhydride molecule 1,4,5,8-naphthalene-tetracarboxylic acid dianhydride (NTCDA), focusing on the vibronic features and their dependence on the crystal structure. This work has been submitted to *Physical Review Letters* (see Ref. [85]).

4.2.2.1 Results and discussion

Figure 4.2.2.1 displays the C K-edge NEXAFS data for NTCDA multilayers prepared at a substrate temperature of 160 K (spectra (a) and (c)) and after annealing at 260 K (spectra (b) and (d)). On the left-hand side, spectra are shown on an extended energy scale. Three prominent sharp peaks are detected for $284 < hv < 290$ eV, which all are identified as π^* -resonances. From their dependence on the polarization of the incident x-rays, the molecular orientation can be deduced [14]. The orientation depends on the film preparation: for in-situ prepared low-T films the molecular planes are essentially coplanar oriented with respect to the

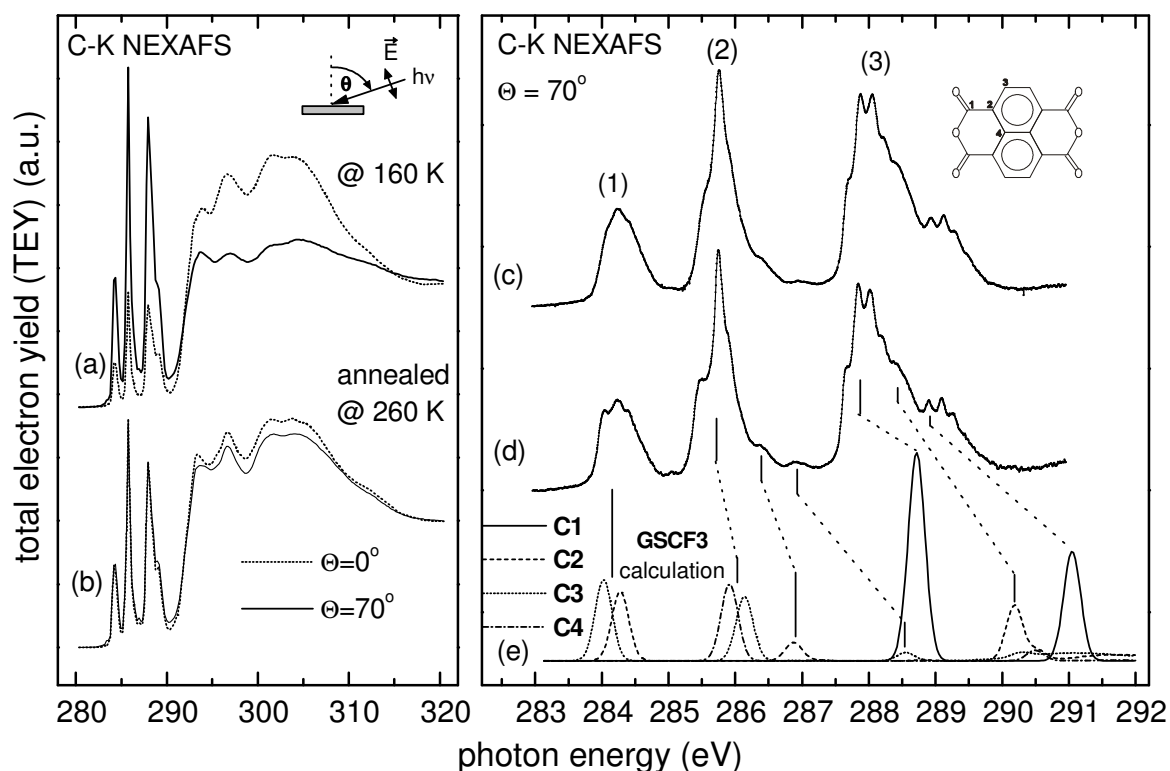


Figure 4.2.2.1: Left: C K-edge NEXAFS spectra on an extended energy scale for (a) NTCDA multilayers (about 15 layers) deposited at 160 K and (b) after annealing at 260 K, for grazing ($\Theta=70^\circ$) and normal ($\Theta=0^\circ$) x-ray incidence. Right: (c)+(d): π^* -region of the C K-NEXAFS spectra of both NTCDA films recorded at $\Theta = 70^\circ$; (e): calculated NEXAFS resonances using the GSF3 code [44-46]. The electronic transitions involving different C atoms C1-C4 (as indicated in the inset) are attributed to the peaks by guidelines.

surface (spectra (a)). After annealing at 260 K crystallites with an average molecular angle of about 45° with respect to the substrate are formed, probably with the geometric structure of NTCDA single crystals [115] (spectra (b) and (d)). This is in complete accordance with recent spectromicroscopic results proving the existence of differently oriented micro crystallites [116].

On the right-hand side of Figure 4.2.2.1 the π^* -resonances of the two preparations are plotted on an expanded energy scale (spectra (c) and (d)). For these spectra the energy resolution has been improved using optimum monochromator settings and small photon energy steps (5 meV). A rich fine structure with numerous well-resolved peaks and shoulders is visible, especially for peak (3). A closer comparison of the two spectra, however, reveals significant differences, best observed on the low energy side of peaks (1) and (2), where the shoulder gets more pronounced upon annealing. Spectrum (e) represents the result of the GSCF3-calculations for NTCDA yielding the electronic transitions which are compared with spectrum (d). (The “stretching” of the energy scale of the calculated spectra is a well known effect observed also for similar ab initio methods.) This comparison clearly yields two electronic transitions for peak (1) and major contributions from three transitions for peaks (2) and (3), respectively. The peak assignment is indicated in Figure 4.2.2.1. Peaks (1) and (2) mainly correspond to excitations of C 1s initial states located at naphthalene carbon atoms C2, C3 and C4 into LUMO and LUMO+1 final states. The major contributions to peak (3) are the anhydride (C1) C 1s \rightarrow LUMO and LUMO+1 transitions and a C 1s (C2) \rightarrow LUMO+4 transition. The present GSCF3-calculation completely agrees with an earlier $X\alpha$ -SW calculation for the similar NDCA molecule (naphthalene-dicarboxylic anhydride) [82].

The highly-resolved absorption fine structures in spectra (c) and (d) of Figure 4.2.2.1 are undoubtedly interpreted as coupling of the electronic transitions to vibronic excitations in the core-excited final state, in agreement with the above cited publications on vibronic fine structures of small molecules. In the following, these multiple structures are analysed in detail using least-square fitting of vibronic progressions taking the Franck-Condon (FC) principle into consideration. For this purpose we assume parabolic potential curves for the electronic ground and core-excited state described by

$$V_{pot} = \alpha \cdot (R - R_E)^2 \quad \text{and} \quad V'_{pot} = \alpha' \cdot (R - R'_E)^2, \quad (4.2.2.1)$$

respectively, with R being the normal coordinate of the observed vibrational mode, R_E the equilibrium distance and α the harmonicity (parameters with ' refer to the core-excited state). The FC factors $f^2_{(vv')} = |\langle v | v' \rangle|^2$ (v and v': vibrational wave functions of the initial and final state, respectively), which describe the relative intensities of the various lines of each progression, are computed simultaneously during fitting. Since we deal with vibronic modes above ~ 100 meV we only have to consider the vibronic ground state in the electronic initial state. Thus only five fit parameters are required to describe each vibronic progression: $a = \alpha' / \alpha$, $\Delta R = R'_E - R_E$, $h\nu'$, the energy of the adiabatic transition E_0 , and the intensity I. For all vibronic progressions Voigt profiles with identical line widths (Gaussian and Lorentzian) were used. Note, that this is the minimum number of fit parameters necessary to describe a vibronic progression.

Figure 4.2.2.2 shows the fitting sequence of peak (3) of the annealed multilayer film (spectrum (d) in Figure 4.2.2.1), that has the best-resolved vibronic fine structure. In Figure 4.2.2.2 (a) the experimental curve is fitted with three electronic transitions and their coupling to one vibronic mode each, according to the calculations shown in Figure 4.2.2.2. The experimental data is reproduced reasonably well. However, the very high quality (resolution

and statistics) of our experimental data allows an even closer inspection. Especially the leading edge of the first two vibronic peaks of peak (3) (indicated by the grey background in Figure 4.2.2.2) still shows an insufficient agreement between fit and data, as can be derived from the oscillations in the residuum. Such an oscillation at the leading edge cannot result from the neglect of a second or third progression coupled to the same electronic transition since these progressions all start at the same E_0 . We thus tried to reproduce this part of the spectrum with highest accuracy.

We started to fit the leading edge to determine the line shape. The Lorentzian contribution was determined to $\Gamma_L = 83(3)$ meV which is in excellent agreement with literature data, e.g.

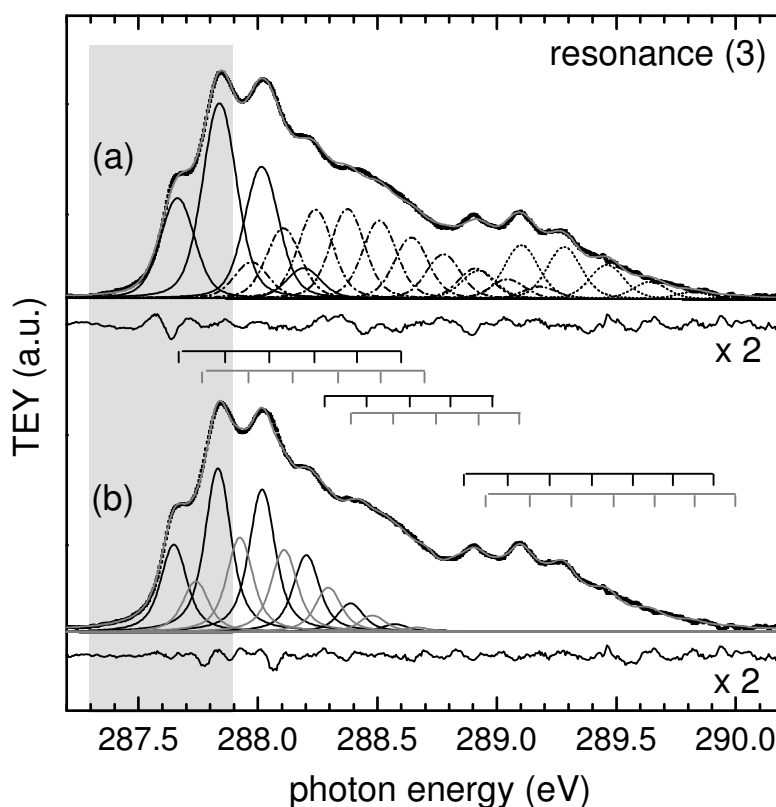


Figure 4.2.2.2: Comparison of resonance (3) of the annealed NTCDA film (see spectrum (d) in Figure 4.2.2.1) with curve fits of vibronic progressions taking numerically calculated Franck-Condon factors into account for three electronic transitions (a) without and (b) including Davydov splitting. For clarity only the two Davydov components of the first electronic transition are plotted. Corresponding vibronic progressions are indicated as bar graphs. The residua are multiplied by 2. The energy range used for the leading edge analysis is shaded grey.

for CO [117]. This parameter was fixed in the further analysis. The Gaussian line width, containing contributions from experimental resolution, inhomogeneities within the investigated layer, and low-energy phonons, was determined to $76(3)$ meV and fixed for all Voigt profiles used in Figure 4.2.2.2(b). We then thoroughly refitted the spectrum in the grey shaded range (see Figure 4.2.2.2(b)). A satisfying result could only be obtained by using an

additional peak *between* the first vibronic structures which, of course, needs a reasonable explanation.

Since the above mentioned *ab initio* calculations predict major contributions in this range only from three electronic transitions which are already included in Figure 4.2.2.2a, we must consider other effects. For example, one could think of a coupling of a second or further vibronic excitations to the same electronic transition. This *does not* lead to a significant improvement of the fit, since it cannot describe the lack of intensity between the peaks of the first progression. Thus, also the fit quality expressed by χ^2 ($\chi^2 = \sum_n (I_{\text{exp}} - I_{\text{fit}})^2 / I_{\text{exp}}$) in the energy range between 287.25 and 288.85 eV changed only slightly from 0.046 to 0.041 although we used four more fit parameters. As only remaining alternative we considered a possible energy splitting of the excited electronic state which is well established as Davydov splitting [118] in optical spectroscopy in the visible range [119]. It occurs for two (or more) molecules per unit cell, as for crystalline NTCDA. To comprise the splitting in our theory

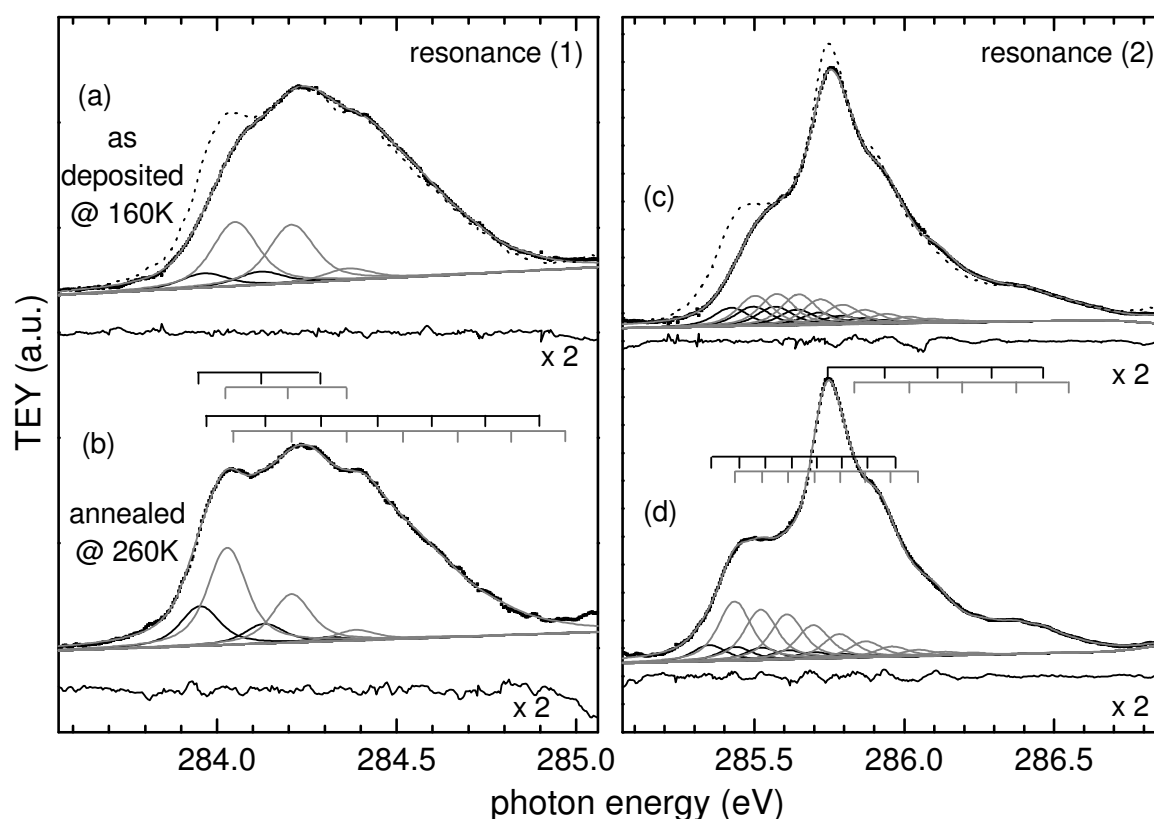


Figure 4.2.2.3: Details of NEXAFS resonances (1) (left) and (2) (right) of the NTCDA multilayer films of Figure 4.2.2.1. Top: as deposited @ 160 K. Bottom: after annealing @ 260 K. To underline the differences, the bottom spectra are also plotted as dashed lines in the upper part. The residua are multiplied by a factor 2; corresponding vibronic progressions are indicated as bar graphs. For clarity only the two Davydov components of the first electronic transition are plotted.

		As deposited @ 160 K					Annealed @ 260 K				
resonance	assignment	E_o (eV)	$h\nu'$ (meV)	Γ_G (meV)	E_{DV} (meV)	$h\nu_o$ (meV)	E_o (eV)	$h\nu'$ (meV)	Γ_G (meV)	E_{DV} (meV)	$h\nu_o$ (meV)
1	C3 1s → LUMO	283.97	158	100	87	179	283.95	179	75	76	247
	C2 1s → LUMO	284.05	161			245	284.03	150			212
2	C4 1s → LUMO+1	285.42	73	86	80	78	285.35	87	76	85	93
	C3 1s → LUMO+1	285.50	182			196	285.43	177			189
	C2 1s → LUMO+1	286.25	-			-	286.28	-			-
3	C1 1s → LUMO	287.68	188	93	94	244	287.65	185	76	95	238
	C2 1s → LUMO+4	288.28	177			221	288.26	174			218
	C1 1s → LUMO+1	288.86	179			219	288.83	179			216

Table 4.2.2.1: Results of the least-square curve fitting of resonances (1) – (3) of NTCDA films as deposited @ 160 K and after annealing @ 260 K: energy of the 00-transition E_o , Gaussian width Γ_G , vibronic energy in the excited state $h\nu'$, Davydov splitting E_{DV} and vibronic energy in the ground state $h\nu_o$.

function we included one more progression per electronic transition, i.e. only two more fit parameters, the (constant) Davydov splitting E_{DV} of the core-excited electronic levels and the intensity I of the shifted progression, while α' , R_E' , and $h\nu'$ were kept as for the unshifted progression. Indeed, the fit improves very significantly with a Davydov splitting of $E_{DV} = 92(3)$ meV, as derived from the strong reduction of χ^2 from 0.046 to 0.018 (see also residuum around 287.6 eV). Such a value for E_{DV} is reasonable considering Davydov splittings found in the VIS range, e.g. 300 meV for oligothiényls [120]. The remaining ripples in the residuum at higher energy are due to additional but less strongly coupled vibrations which were not fitted to keep the number of fit parameters as small as possible.

All parameters derived from the fits are summarized in Table 4.2.2.1. For a comparison of the obtained vibrational frequencies for the core-excited state with data from vibrational spectroscopies, the *ground-state* vibronic energies $h\nu_o$ can be calculated using the empiric formula

$$h\nu_o = h\nu'(\Delta E_{FC} / 1.2 + 1) \quad (4.2.2.2)$$

involving the FC shift

$$\Delta E_{FC} = 0.5 \cdot h\nu'(\Delta R)^2 \quad [121]. \quad (4.2.2.3)$$

These values are also listed in Table 4.2.2.1. The agreement between our data for peak (3) (probing the C1 excitations; 238 and 216 meV) with the C=O stretching mode (229 meV) in condensed NTCDA [122] is very good. The same conclusion can be drawn for peak (2) – and to some extent also for peak (1) - which are shown in Figure 4.2.2.3 and briefly discussed below. Also in these cases the obtained ground state frequencies fit very well to ring (88 - 94 meV) and C-H modes (~190 meV) [122]. Of course, NEXAFS cannot compete with the established vibrational spectroscopies in terms of energy resolution. However, it provides via the localized core-excitation a *local* probe of the vibrational structure.

The analysis of peaks (1) and (2) is indicated in Figure 4.2.2.3. We particularly address the effect of different local geometric structures in NTCDA films comparing the upper and lower spectra. As discussed above, NTCDA films prepared at low substrate temperature form a metastable phase with almost coplanar molecular orientation (spectra (a) and (c)) whereas they transform into the single crystal structure upon annealing ((b) and (d)) [79]. The changes in the NEXAFS fine structure are most obvious at the leading edge of both peaks.

Such modifications of the electronic structure upon structural changes in weakly bound molecular solids have not been observed so far. What is their origin? Interestingly, the analysis of the vibronic progressions yields the same peak positions for both structural modifications. Of course, the Gaussian line width is reduced – but only little - upon annealing due to reduced inhomogeneous broadening (see Table 4.2.2.1), whereas the Lorentzian broadening remains constant. However, the FC factors change significantly which must be due to changes of the potential curves in the ground and/or excited electronic state. This indicates significant changes of the intermolecular interaction in the condensed layer and thus raises the question, whether the bonding mechanism in NTCDA films is adequately described by mere van-der-Waals and electrostatic interaction.

4.2.2.2 Conclusion

In conclusion, we have shown that the very high spectral resolution at 3rd generation synchrotron sources enables new insight into the electronic structure of large organic molecules. We present high-resolution NEXAFS data of condensed NTCDA films that clearly show vibronic fine structure. This has not yet been observed for aromatic molecules with delocalised π -systems larger than benzene. The spectra can be described by a strong coupling of each electronic transition to predominantly one vibronic mode, which for the excitation of the anhydride carbon atoms can unambiguously be identified as C=O stretching mode. Furthermore, the analysis of the present high-quality data gives first experimental evidence for a Davydov splitting in core-excitations and indicates rather different interactions between the NTCDA molecules in different structural phases.

4.2.3 Anharmonicity of the core-excited state potential of ANQ

In this chapter we investigate the closely related molecule acenaphthenequinone (ANQ), which has a naphthalene core and a quinoic functional group. ANQ is particularly interesting because it is to our knowledge the largest aromatic molecule which shows well-resolved vibronic fine structure in the O K-edge spectra in the condensed phase. This work has been submitted to the *Chemical Physics Letters* (see Ref. [123]).

4.2.3.1 Results and interpretation

Figure 4.2.3.1 displays the C 1s (Figure 4.2.3.1a) and O 1s (Figure 4.2.3.1b) NEXAFS spectra of condensed multilayers (thickness ~ 20 ML) of ANQ on a Ag(111) surface. The spectra

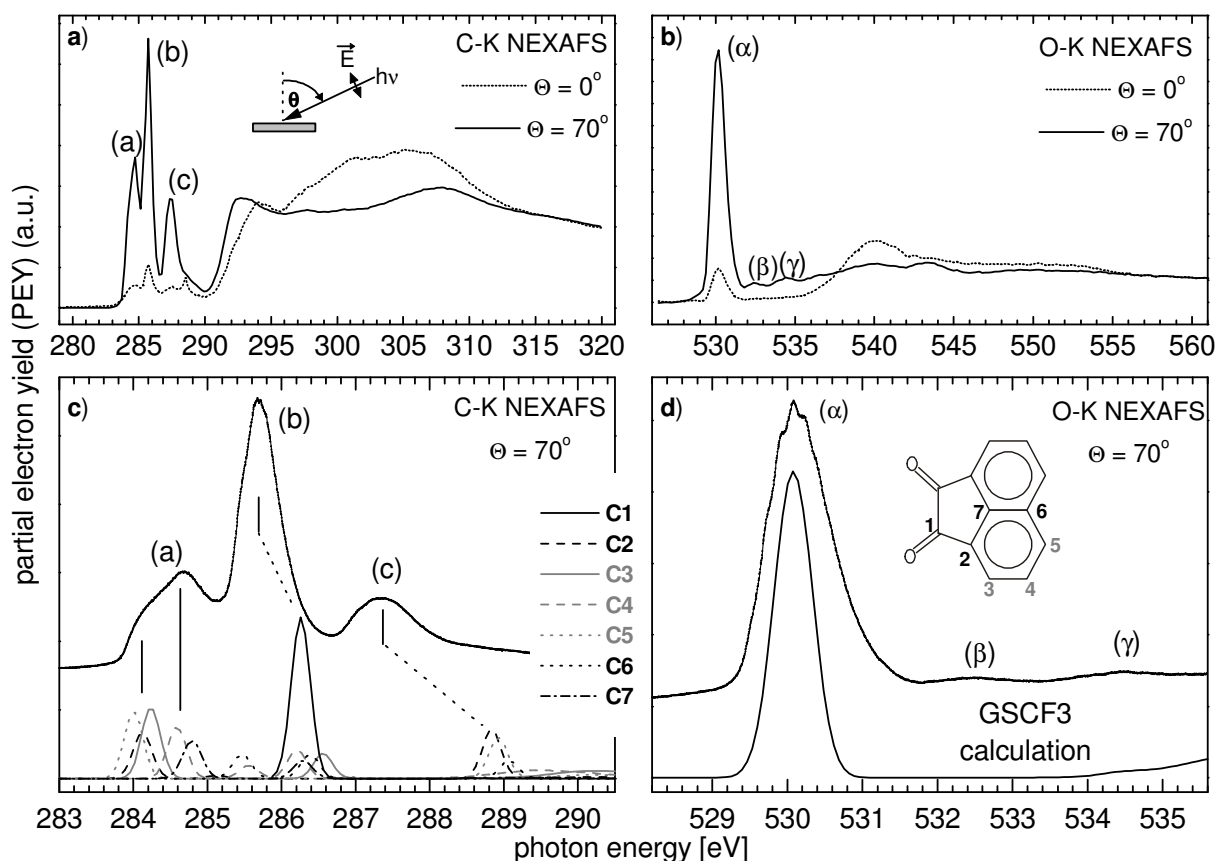


Figure 4.2.3.1: (a) C K- and (b) O K-NEXAFS spectra of multilayer films of ANQ recorded at grazing ($\Theta = 70^\circ$) and normal ($\Theta = 0^\circ$) incidence. As inset in figure (d) the molecular structure of ANQ is depicted. The π^* -regions of the (c) C K- and (d) O K-NEXAFS spectra are shown on expanded scales recorded at $\Theta = 70^\circ$ with optimised monochromator resolution. In frames (c) and (d) the calculated term energies for the lowest energy transitions are plotted. The calculated energies were shifted by -2.3 eV and -1.0 eV at the C K- and O K-edge, respectively, to align the first experimental and theoretical transition.

were recorded with normal ($\Theta = 0^\circ$) and grazing ($\Theta = 70^\circ$) incidence of the synchrotron light with respect to the surface, as illustrated in Figure 4.2.3.1a. The polarization was adjusted by changing the angular position of the sample relative to the incoming, horizontally polarized synchrotron beam. The molecular structure of ANQ is plotted as inset in Figure 4.2.3.1d.

Three prominent sharp peaks, denominated (a), (b) and (c), are observed in Figure 4.2.3.1a for $283 \text{ eV} < h\nu < 290 \text{ eV}$, which all are identified as π^* -resonances because of their dichroic behaviour (Figure 4.2.3.1a and 1b). At the O K-edge (Figure 4.2.3.1b) one intense π^* -resonance, denominated (α), at 530 eV dominates the spectrum for $\Theta = 70^\circ$. Two small peaks (β , γ) are found at 532.5 eV and 534.4 eV. From the dependence of the π^* -intensities in the O K- and C K-data on the polarization of the incident x-rays, the average orientation of the molecular plane can be deduced [14] as $\phi = 28(3)^\circ$ with respect to the surface plane. Though in principle the NEXAFS dichroism can only provide an average angle for the molecular orientation, this result strongly suggests a crystalline growth, because the crystal structure of ANQ shows four molecules in an orthorhombic unit cell which are tilt an angle of 28.9° against the (001) plane [124]. Our NEXAFS data thus clearly indicate a (poly-)crystalline order in the film with the (001) direction aligned with the surface normal. Although significant fine structure and angular changes also occur for the features above 290 eV and 535 eV, respectively, we will focus here on the energy range below the threshold, for reasons that will become clear in the following.

In Figure 4.2.3.1 the π^* -resonances at the C K- (Figure 4.2.3.1c) and O K-edge (Figure 4.2.3.1d) are plotted on an expanded energy scale and compared with the results of GSCF3-calculations. Both experimental spectra were recorded at grazing incidence ($\Theta = 70^\circ$), and the spectral resolution was improved using optimum monochromator settings; in addition, much smaller photon energy steps (5 meV) have been employed. The calculated energies were shifted by -2.3 eV and -1.0 eV at the C K- and O K-edge, respectively, to align the first experimental and theoretical transition.

The π^* -resonances at the C K-edge (Figure 4.2.3.1c) show further structure as indicated, e.g., by the low-energy shoulders of peaks (a) and (b), but no vibronic features as for NTCDA [85] are explicitly resolved. The experimental spectrum is reproduced well by the calculations and can be explained by the various contributions of electronic transitions from C 1s initial states at the seven chemically different carbon atoms into the lowest molecular orbitals (LUMO – LUMO +3). The assignment of the different electronic transitions to the observed peaks is indicated by guidelines in Figure 4.2.3.1c. Note, that the apparent stretch of the calculated energy scale is well known for this and similar *ab initio* methods and depends on the applied basis set.

In the O K-data, however, a number of fine structure peaks and shoulders, which are assigned to vibrational progressions, is resolved for peak (α), which is unambiguously interpreted as O 1s \rightarrow LUMO transition. This is particularly corroborated by the results of the *ab initio* calculation in Figure 4.2.3.1d, that shows only one electronic transition being responsible for peak (α).

To extract the information about the vibronic properties from the fine structure of peak (α) we performed a detailed least-square peak fitting analysis. In a first step we assumed *parabolic* potential curves for the electronic ground and core-excited states described by

$$V_{pot} = \alpha \cdot (R - R_E)^2 \quad \text{and} \quad V_{pot}' = \alpha' \cdot (R - R_E')^2, \quad (4.2.3.1)$$

respectively, with R being the normal coordinate of the observed vibrational mode, R_E the equilibrium distance and α the harmonicity (parameters with ' refer to the core-excited state). The Franck-Condon factors

$$f_{(v v')}^2 = |\langle v | v' \rangle|^2 \quad (4.2.3.2)$$

(v and v' : vibrational wave functions of the initial and final state, respectively), that determine the envelope of the fitted vibronic progression, are computed simultaneously during the fit. Since at 150 K only the $v = 0$ mode is significantly populated in the electronic ground state, only seven fit parameters have to be utilized to describe a vibronic progression: $a = \alpha'/\alpha$, ΔR

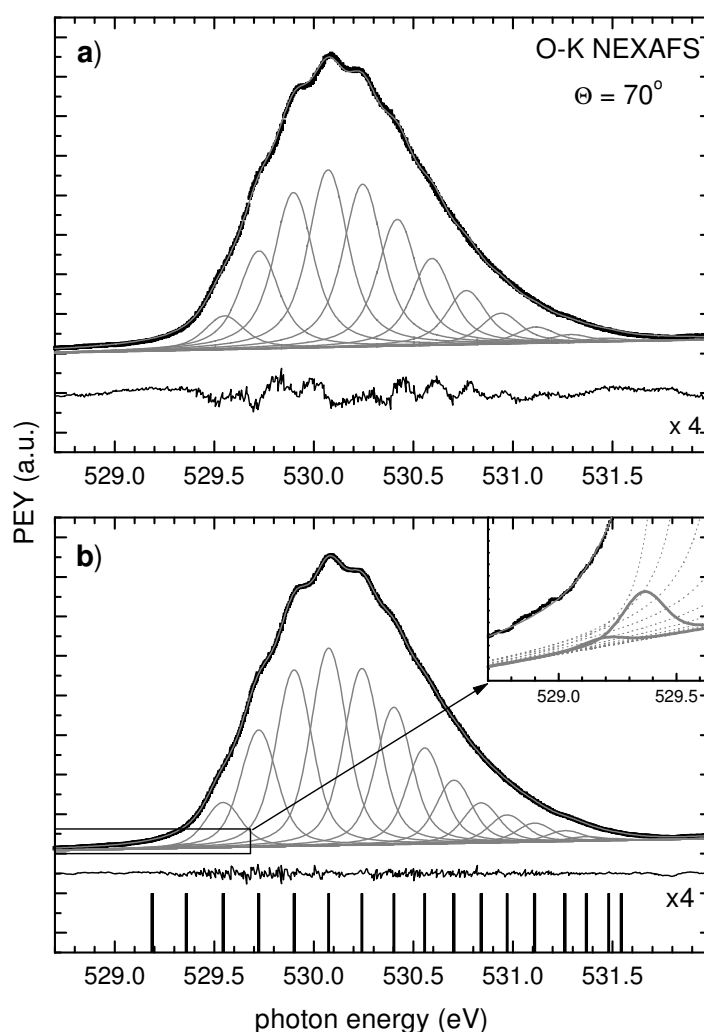


Figure 4.2.3.2: (a) Comparison of the experimental data (dots) for the O K-NEXAFS resonance (α) (see Figure 4.2.3.1d) of ANQ multilayers with the least-square curve fit result of one vibronic progression taking into account numerically calculated Franck-Condon factors and a harmonic potential (see text). (b) Fit result for resonance (α) with 17 Voigt profiles with identical lineshape. The energy positions and intensities were fitted independently but with optimized start values from the harmonic fit (Figure 4.2.3.2a). For clarity the residua in (a) and (b) were multiplied by a factor 4 in both pictures. At the bottom of Figure 4.2.3.2b the resulting energy positions of the vibronic states are plotted as bar graphs.

$= R_E' - R_E$, $h\nu'$, the energy of the adiabatic transition E_A , the intensity I and the Gaussian and Lorentzian contributions to the Voigt line shape, that was kept equal for all vibronic states.

Figure 4.2.3.2a shows the so-obtained fit result for one vibronic progression assuming a harmonic potential. The overall agreement is good, though the residuum, i.e. the difference between measured spectrum and fit result (magnified by a factor 4 in Figure 4.2.3.2a and 2b, for clarity), still shows significant fine structure that, together with the high statistical quality of our data, challenges this interpretation.

A possible explanation for the misfit could be a coupling of the electronic transition to two (or more) normal modes. For our fit procedure this means of course, that the adiabatic electronic transitions have to be constrained to the same energy E_A . However, a refit with this approach did not increase the fit result satisfactorily, because in all possible cases the vibrational fine structure, which is most pronounced for the 4th - 8th vibration, became smeared out.

Since especially on the high-energy side the periodic oscillations of the residuum plot indicate an increasing misfit of the vibronic energy positions, an influence of the anharmonicity of the excited state potential is suggested, that leads to smaller energetic distances of the vibronic peaks at higher energy. In the next step, we thus fitted the experimental data with 17 Voigt profiles of identical line shape but free intensities and energy positions. As start values of the fit the parameters derived from the harmonic fit were utilized. The fit result is plotted in Figure 4.2.3.2b. In the inset in Figure 4.2.3.2b, that provides a zoomed view of the low energy onset of peak (α), the first two fitted peaks can be recognized. The O 1s lifetime broadening was determined to 97 meV and the corresponding Gaussian width of the fitted Voigt profiles to 156 meV.

We now see an excellent match of the fitted and the experimental curve as shown by the residuum. This is, of course, not surprising if one considers the much higher number of free fit parameters that are now applied (36) in comparison to Figure 4.2.3.2a (7 fit parameters). Nevertheless, we still get an evident result. On the bottom of Figure 4.2.3.2b the energy positions of the fitted peaks are displayed as bar graphs. We clearly see the anharmonicity effect of the potential in the core-excited state, that decreases the spacing of the vibronic states for increasing term values.

Anharmonic potentials can generally be described by the Morse potential

$$E(R) = E_D \left[1 - e^{-a(R-R_E)} \right]^2 \quad (4.2.3.3)$$

in good approximation. If one takes the quadratic term of the series expansion of the exponential function into account one obtains a second energy term in addition to the harmonic energy $E_n = h\nu' \cdot (n + 1/2)$ (resulting from the linear expansion term) such that the energies become

$$E_n = h\nu' \cdot (n + 1/2) - \chi h\nu' \cdot (n + 1/2)^2. \quad (4.2.3.4)$$

$\chi h\nu'$ can be derived from Figure 4.2.3.3 where the measured term energies are plotted versus the term values, and a curve according to equation (4.2.3.4) is adapted. The resulting anharmonicity of $\chi h\nu' = 2.6(1)$ meV has the same order of magnitude as, e.g., the corresponding value for CO (1.7 meV) [97]. The excellent accordance of the experimental energy values with the anharmonic approach (Figure 4.2.3.3) is a clear evidence for our interpretation, that we observe a progression in an anharmonic potential.

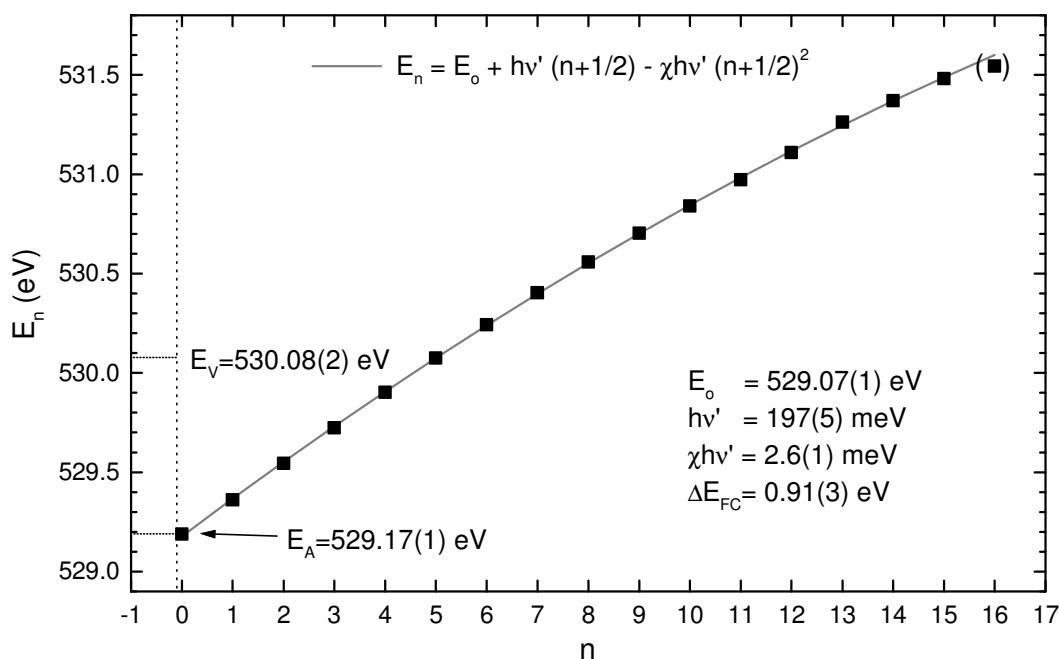


Figure 4.2.3.3: Plot of the energy positions E_n of the vibronic states as derived from Figure 4.2.3.2b versus the term value n . From the fitted curve $E_n = E_o + hv' (n+1/2) - \chi hv' (n+1/2)^2$ (grey line) the parameters E_o (the potential minimum in the electronically excited state), hv' , and the anharmonicity $\chi hv'$ of the core-excited potential as well as E_A can be deduced. For the shown curve the first fitted peak in Figure 4.2.3.2b was assigned to the vibronic quantum number $n = 0$ (see text). The energy of the vertical transition E_V is also indicated.

In addition, the vibronic energy $hv' = 197(5)$ meV in the excited state can be derived from the fit curve in Figure 4.2.3.3. From this, the vibronic energy in the ground state hv_o can be calculated according to the empiric formula [58]

$$hv_o = hv' \cdot (\Delta E_{FC} / 1.2 + 1), \quad (4.2.3.5)$$

if the Franck-Condon shift, i.e. the energy difference between the adiabatic (E_A) and the vertical transition (E_V) is known. E_V can be determined to 530.08(2) eV from the maximum of the measured envelope of the vibronic progression in Figure 4.2.3.2b. If we assign the adiabatic transition ($n = 0$) to the first fitted peak in Figure 4.2.3.2b (see inset) at 529.17(1) eV, the Franck-Condon shift can be determined to $\Delta E_{FC} = 0.91(3)$ eV. The respective ground state vibronic energy is then calculated to $hv_o = 346(10)$ meV. If this result is compared to the corresponding ground state vibronic spectra of ANQ, as derived by FTIR measurements [125,126], it strongly suggests the assignment of the observed vibronic mode to modes that involve a high amplitude of C-H stretch vibrations, observed with FTIR between 381 - 386 meV. No other modes exist in the ground state between 220 meV and 500 meV, as also known from DFT calculations.

The deviation of about 35 meV between our value and the value determined by FTIR can be explained by a wrong assignment of the adiabatic transition. If the first fitted peak in Figure 4.2.3.2b is associated with the quantum number $n = 1$ (instead of $n = 0$) and we further assume, that the peak belonging to $n = 0$ has very low intensity and thus can not be observed in Figure 4.2.3.2b, the resulting values for the adiabatic transition and the Franck-Condon

shift are $E_A = 528.98(1)$ eV and $\Delta E_{FC} = 1.10(3)$ eV, respectively. A fit, analog to the analysis presented in Figure 4.2.3.3, now yields an excited state vibronic energy $h\nu' = 200(5)$ meV and the resulting ground state vibronic energy can be calculated to $h\nu_o = 383(10)$ eV. This value is in excellent agreement with the FTIR values for C-H vibronic modes of ANQ in the electronic ground state. The parameters derived from our analysis of the O 1s $\rightarrow \pi^*$ -resonance in Figure 4.2.3.2b and Figure 4.2.3.3 are summarized in Table 4.2.3.1.

assignment of first peak	Γ_L (meV)	Γ_G (meV)	E_A (eV)	E_V (eV)	ΔE_{FC} (eV)	$\chi h\nu'$ (meV)	$h\nu'$ (meV)	$h\nu_o$ (meV)
n = 0	97	156	529.17(1)	530.08(1)	0.91(2)	2.6(1)	197(2)	346(10)
n = 1	97	156	528.98(1)	530.08(1)	1.10(2)	2.6(1)	200(2)	383(10)

Table 4.2.3.1: Parameters derived from the analysis of the O 1s $\rightarrow \pi^*$ -resonance in Figure 4.2.3.2b and Figure 4.2.3.3 for the two possible assignments of the first fitted peak ($n = 0$ and $n = 1$): Lorentzian (Γ_L) and Gaussian (Γ_G) line widths, energies of the adiabatic (E_A) and vertical (E_V) transition, Franck-Condon shift (ΔE_{FC}), anharmonicity ($\chi h\nu'$) and vibronic energy ($h\nu'$) in the core excited state as well as the calculated ground state ($h\nu_o$).

4.2.3.2 Concluding discussion

In this chapter we presented highly-resolved C K- and O K-NEXAFS spectra of acenaphthenequinone, that, for the first time, show well resolved vibronic fine structure upon O 1s excitation of a relatively large organic molecule in the condensed phase. The data indicate a very pronounced sensitivity of the electron-vibron coupling to the localization of the core-hole. Whereas the large number of significantly intense electronic transitions and probably also the coupling of various vibronic progressions to different C 1s excitations leads to a smearing of the vibronic fine structure of the C 1s NEXAFS data, the O 1s $\rightarrow \pi^*$ -transition shows well-resolved fine structure that is due to the excitation of one vibration mode. According to our data, this mode is a C-H stretching mode and not a C=O mode. This example shows, that NEXAFS can very selectively excite molecular vibrations that not necessarily are located at the absorbing atom

The reason for this – at first glance surprising – result can be qualitatively understood. The final state orbital, that becomes occupied in the NEXAFS process, plays an important role in the electron-vibron coupling. The spatial distribution of the molecular π -system and its reaction on excitation leads to changes in the molecular bonding, that can either be local or distributed over the entire molecule. Thus bonds that are quite distant from the excited atom may be affected, which can lead to a high cross section for the coupling of a particular vibronic mode, e.g. the C-H stretching mode at 197 meV in the present case, corresponding to 346 meV in the ground state.

If the orbital structure is altered, e.g. by changing the functional group from the quinoidic (ANQ) to an anhydride group (NDCA), strong differences in the electron-vibron coupling can

be observed: the anhydride C 1s $\rightarrow \pi^*$ transition now shows fine structure, whereas the vibronic structure at the O K-edge is smeared out [127]. Similar results were obtained for other anhydride molecules, e.g. NTCDA [85]. In these cases the evaluation of the C 1s absorption fine structures indicates a coupling to C=O stretching vibration taking the derived ΔE_{FC} values and assuming the same formula (4.2.3.5) to be valid.

Of course, vibronic fine structure can only be observed if both, the experimental resolution and, particularly, the film quality is sufficient. In our experiment we determined the Gaussian width of the utilized Voigt profiles to 156 meV. Together with the known experimental resolution of 56 meV we can estimate the contribution of inhomogeneous broadening and additional, non-resolved low-frequency vibronic modes, i.e. phonons, to about 146 meV.

Finally we like to emphasize that – to our knowledge for the first time – the anharmonicity of the potential of a relatively large core-excited molecule could be determined. The obtained value for the anharmonicity parameter $\chi = 0.013$ is rather large and indicates that anharmonic potentials have to be taken into account for a careful analysis of highly-resolved NEXAFS spectra. Furthermore the adiabatic O 1s \rightarrow LUMO electronic transition energy (00-transition) has been derived as 529.18 (10) eV which is significantly different from the commonly taken peak maximum or centre of gravity which is 530.1 eV here.

4.2.4 A comparison of fine structures in high-resolution x-ray absorption spectra of several condensed organic molecules

In this chapter a comparative analysis of the C K- and O K-NEXAFS spectra of the anhydride molecules NTCDA, PTCDA, BPDCA, and NDCA (see Figure 3.1 for the chemical structures of the investigated molecules), that consist of differently sized aromatic core systems with one or two functional anhydride groups, and ANQ will be presented. We will focus on the vibronic fine structures in the high-resolution spectra and the mechanism of electron-vibron coupling. This work is prepared for publication in *Surface Science* (see also Ref. [128]). Note, that parts of the following chapter are similar to the previous chapters 4.2.2 and 4.2.3, since it is designed to be a comprehensive review as a separate journal article.

4.2.4.1 Spectroscopic data and orientation

Figure 4.2.4.1 shows the C-K and O-K NEXAFS spectra of condensed multilayer films of the anhydride molecules 1,4,5,8-naphthalene-tetracarboxylic acid dianhydride (NTCDA), 3,4,9,10-perylene-tetracarboxylic acid dianhydride (PTCDA), benzoperylene-(1,2)-dicarboxylic acid anhydride (BPDCA) and 1,8-naphthalene-dicarboxylic acid anhydride (NDCA), and the quinoic acenaphthenequinone (ANQ). The spectra were taken with s- (dotted) and p-polarization (solid) of the incident synchrotron light, respectively. The polarization was adjusted either by changing the angular position of the sample relative to the incoming, horizontally polarized light from the U49/1-PGM beamline from perpendicular (0°) to grazing (70°) incidence or, after installation of the UE52-undulator, by changing the polarization vector from horizontal to vertical polarization while maintaining the grazing incidence geometry. Note, that for BPDCA the O-K spectrum with s-polarisation could not be recorded due to experimental difficulties.

All C-K spectra show three distinct π^* - derived features on the low energy side of the absorption edge between 283 eV and 290 eV. At the O-K absorption edge the spectra are dominated by an intense peak between 530 eV and 532 eV.

From the angular-dependent linear dichroism [14] of the NEXAFS spectra interesting information about the morphology of the investigated organic thin films can be obtained. For NTCDA the molecular orientation can be manipulated by the choice of the substrate temperature [79]: after preparation at a substrate temperature of 160 K the multilayer film shows preferentially flat lying molecules, as derived from the dependence of the π^* -intensities on the polarization of the incident x-rays. This dependence can be evaluated quantitatively and yields an average tilt angle of the molecules of $35(5)^\circ$ with respect to the surface. Annealing the sample at 260 K (spectra (1.2)) leads to distinct changes in the linear dichroism: the C-K NEXAFS data show an average tilt angle of the molecules of $50(5)^\circ$, and hence we cannot conclude any preferential orientation. Nevertheless, recent spectromicroscopic investigations of our group [116] clearly demonstrate the existence of differently oriented NTCDA micro-crystallites for these preparation conditions, which explain our (laterally averaging) spectroscopic observation. We further believe, that after multilayer deposition at 160 K the film consists of a mixture of crystallites and of a phase with flat lying molecules. Almost perfectly flat lying molecules after deposition at low temperature and

almost perpendicular molecules after annealing could be demonstrated by Gador *et al.* [79] using smaller deposition rates and slightly different temperatures. The morphological differences between the two NTCDA multilayer modifications lead to distinct changes in the fine structure of the C 1s NEXAFS spectra, as will be discussed in detail in Chapter 4.2.4.2

For PTCDA films (spectra (1.3) and (1.8)) we see a homogeneous orientation with perfectly

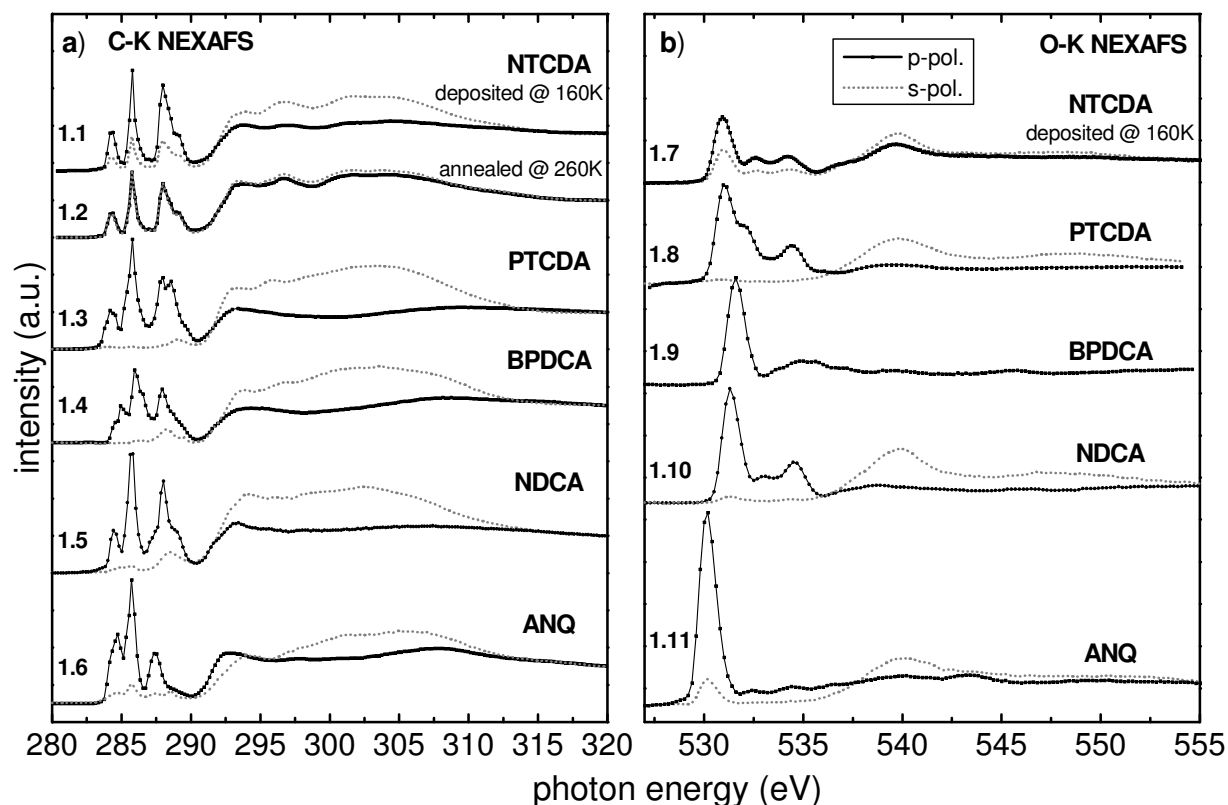


Figure 4.2.4.1: C-K (left) and O-K (right) NEXAFS spectra of multilayer films (film thicknesses 10-30 ML) of the molecules NTCDA (spectra 1.1, 1.2 and 1.7), PTCDA (spectra 1.3 and 1.8), BPDCA (spectra 1.4 and 1.9), NDCA (spectra 1.5 and 1.10), and ANQ (spectra 1.6 and 1.11) condensed on Ag(111). The spectra displayed as solid lines were recorded with p-polarisation, the dotted curves with s-polarisation of the incident X-ray beam. For BPDCA the O-K spectrum with s-polarisation could not be recorded due to experimental difficulties. For NTCDA, spectra 1.1 and 1.7 were recorded after multilayer deposition at a substrate temperature of 160 K, and spectrum 1.2 after the sample was annealed at 260 K.

flat-lying molecules. This is well-known and was observed before for film thicknesses of up to 1000 ML [129]. PTCDA grows almost epitaxially on the Ag(111) surface and forms multilayer films with low stress and high structural order. The molecules BPDCA (spectra (1.4) and (1.9)) and NDCA (spectra (1.5) and (1.10)) also form multilayer films with flat-lying molecules under the applied preparation conditions, as can be derived from our data within the accuracy of the evaluation of the NEXAFS dichroism.

For ANQ (spectra (1.6) and (1.11)) we observe a small deviation from a flat lying orientation ($\varphi = 28(3)^\circ$ with respect to the surface plane). Though our NEXAFS experiments can only provide an average value for the tilt angle, this result corresponds very well to the structural

configuration in an ANQ single crystal. The crystal structure of ANQ shows four molecules in an orthorhombic unit cell that are all tilted 28.9° against the (001) plane [124]. Our NEXAFS data thus indicate a crystalline film structure with the (001) direction aligned with the substrate surface normal. A very homogeneous, possibly crystal-like order with low stress is also indicated by the high-resolution NEXAFS results presented in the following.

Although significant fine structure and angular changes also occur for the features above 290 eV and 535 eV, respectively, we will focus here on the energy range of the sharp π^* -resonances on the low energy side of the absorption edge.

Figure 4.2.4.2 shows the region of the π^* -resonances at the C 1s edge between 283 eV and 291 eV (Figure 4.2.4.2a) and at the O 1s edge between 528.5 eV and 536.5 eV (Figure 4.2.4.2b) on an expanded energy scale. The spectra were recorded at grazing incidence ($\Theta = 70^\circ$) with horizontal polarization of the incident synchrotron radiation, and the spectral resolution was improved using optimum monochromator settings; in addition, much smaller photon energy steps (5 meV) have been employed (see experimental section) for these energy scans. To allow a better comparison of the data the intensities were normalized to the peak with highest intensity, i.e. peak (b) in the C-K and peak (α) in the O-K data.

For all anhydride molecules a rich fine structure with various peaks and shoulders can be observed in the C-K data (Figure 4.2.4.2a). Especially for the region of the peaks denoted by (c) these multiple structures are undoubtedly interpreted as coupling of the electronic transitions to vibronic excitations in the core-excited final state, in agreement with the above

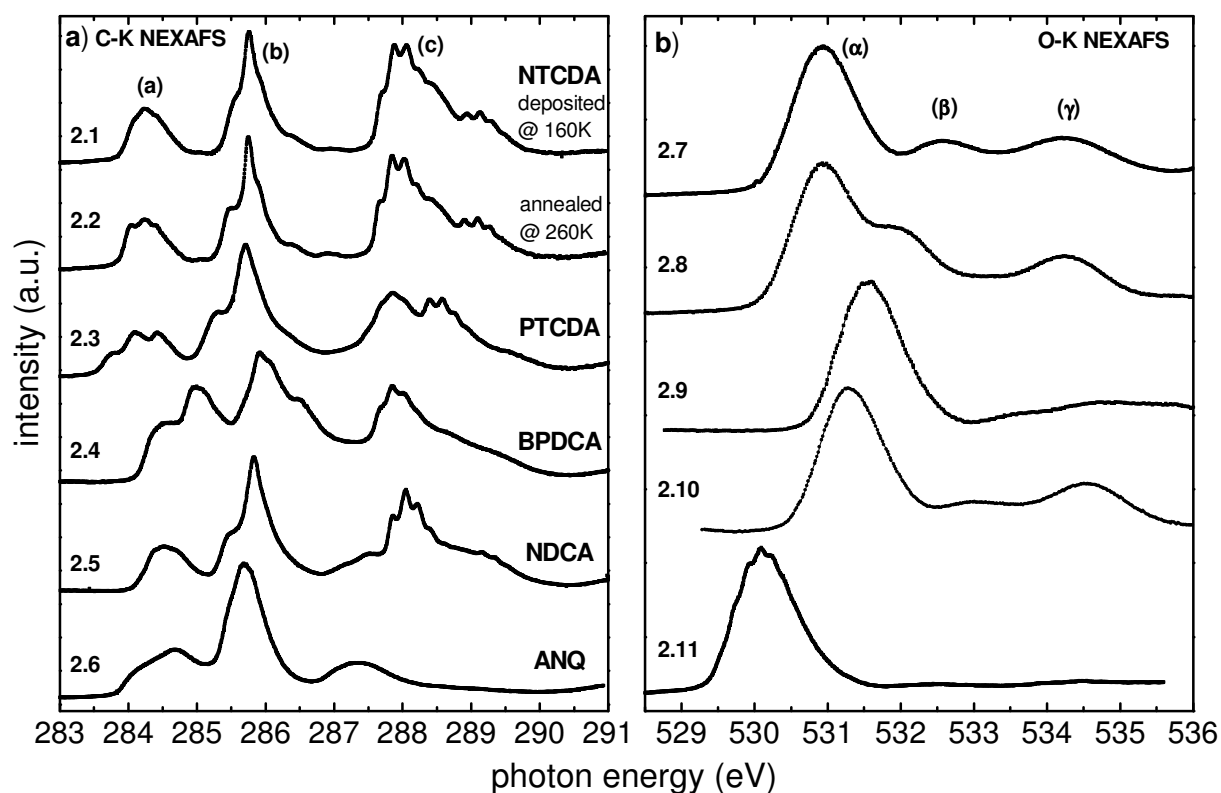


Figure 4.2.4.2: Enlarged view of the π^* -region of the C-K (left) and O-K (right) NEXAFS spectra of Figure 4.2.4.1. All spectra were recorded with *p*-polarisation of the incident X-ray beam and with maximum energy resolution. The spectra were normalised to the intensity of resonances (c) and (α), respectively.

cited publications on vibronic fine structures of small molecules and with the results of the preceding chapters.

The well-resolved, characteristic fine structure allows to clearly differentiate between the rather similar anhydride molecules. Especially for the molecules PTCDA and NTCDA, which only differ in the size of their aromatic cores, the spectra recorded with low energy resolution so far could only be distinguished by the relative intensities of the peaks (a) and (b), that are due to excitations at the ring carbon atoms, with respect to peak (c), that is mainly due to excitations of the anhydride carbon atoms. Due to the increased energy resolution of our present data the corresponding spectra (2.2) and (2.3) show distinct differences in the fine structure throughout the entire spectra. This can be observed, for example, for peak (a), which seems to consist of three contributions in both cases, but with obviously different energy positions and different relative intensities. Also peak (c) shows strong differences in the vibronic fine structure for the two molecules. Just from the comparison of the two closely related molecules NTCDA and PTCDA we can conclude, that high-resolution NEXAFS can be utilized as a sensitive tool to provide a very detailed fingerprint for the precise identification of organic substances.

Moreover, the high-resolution NEXAFS data clearly resolve the influence of different layer morphologies on the electronic structure. For instance, if we compare spectra (2.1) and (2.2), which belong to the two different NTCDA modifications described above, we see distinct differences in the fine structure. This can best be observed for the two ring peaks (a) and (b): after deposition at a substrate temperature of 160 K spectrum 3.1 shows less clearly discernible low-energy shoulders for peaks (a) and (b). After annealing at 260 K, leading to a different crystalline order, these shoulders become more pronounced. We will address this aspect in a detailed analysis later.

In the O-K NEXAFS spectra (Figure 4.2.4.2b) three peaks, denominated (α), (β) and (γ), can be observed for all 5 molecules. The spectra are dominated by peak (α), followed by the two peaks (β) and (γ) with lower intensity. For ANQ (spectrum 2.11) the two latter peaks are only hardly visible at 532.5 eV and 534.5 eV. Whereas the O-K NEXAFS data of NTCDA (2.7), PTCDA (2.8) and NDCA (2.10) do not show any fine structure, peak (α) of ANQ (spectrum 2.11) shows a distinct vibronic structure with various nearly equidistant shoulders on both sides of the peak maximum at 530.1 eV. These features have an intensity distribution that resembles that of a vibronic progression. Furthermore, from the shape of the vibronic envelope, which clearly shows more than three vibronic states on the lower energetic side of the peak maximum, the NEXAFS final state orbital can be assigned as strongly antibonding. In the corresponding ANQ C-K data (spectrum 2.6) the vibronic fine structure is not visible for peak (c) as it is for the anhydride molecules. This finding indicates strong differences in the electron-vibron coupling due to differences in the local electronic structure of the functional group, which we will discuss in detail later. For BPDCA (2.9) we also observe a similar, but not as well resolved vibronic fine structure for the O-K peak (α). This is the only molecule that shows vibronic coupling upon both, O 1s and C 1s excitations into molecular orbitals which are located on the functional subunit.

4.2.4.2 Franck -Condon (FC) analysis of the NTCDA C-K data

In Figure 4.2.4.3 the result of a GSCF3-calculation for NTCDA is plotted together with the experimental spectra. The calculated energies were shifted by -2.3 eV and -0.9 eV at the C-K and O-K edge, respectively, to align the first experimental and theoretical transitions. A

comparison of the experimental and calculated data reveals a “stretching” of the calculated energy scale, which is well known for this and similar *ab initio* methods and depends on the applied basis set. Nevertheless, if the “energy stretch” is taken into account, the calculated spectra fit the experimental data very well and help to assign the different electronic transitions contributing to the observed peaks.

In the upper right corner of Figure 4.2.4.3b the molecular structure of NTCDA is plotted, and the non-equivalent atoms C1-C4 and O1/O2 are denominated. The NEXAFS spectra consist of a superposition of transitions from different initial states with the core hole at the symmetrically non-equivalent carbon and oxygen atoms (C1 – C4 and O1/O2, respectively) into the lowest unoccupied molecular orbitals LUMO – LUMO+4. The assignment of the various calculated transitions to the different features in the experimental spectra is indicated

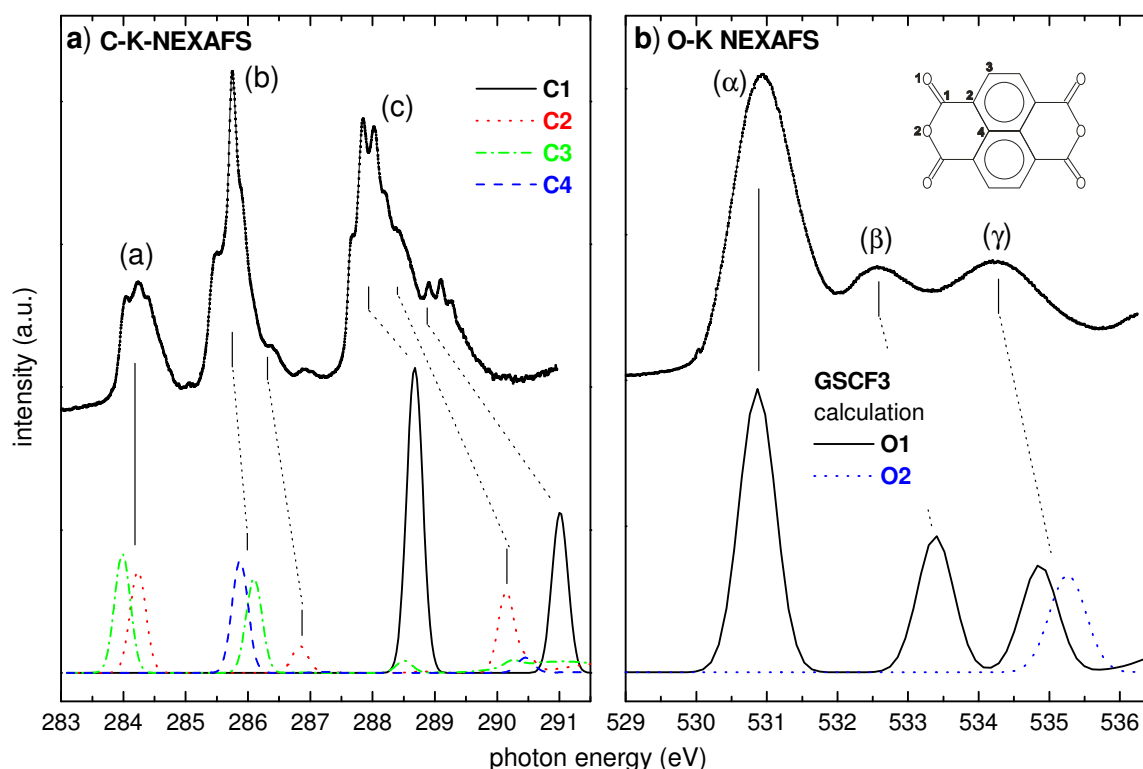


Figure 4.2.4.3: π^* -region of the experimental C-K (left) and O-K (right) NEXAFS data of NTCDA compared with corresponding GSCF3-calculations (bottom). The calculated spectra were shifted in energy to align the first transitions (see also text). The inequivalent carbon and oxygen atoms distinguished in the calculation are indicated in the inset.

in Figure 4.2.4.3. It clearly yields two electronic transitions for peak (a) and major contributions from three transitions to peaks (b) and (c) in the C-K NEXAFS spectra. Peaks (a) and (b) mainly correspond to excitations of C 1s initial states located at naphthalene carbon atoms C2, C3 and C4 into LUMO and LUMO+1 final states, whereas peak (c) can be attributed to anhydride (C1) C 1s \rightarrow LUMO and LUMO+1 transitions plus a C 1s (C2) \rightarrow LUMO+4 transition.

We performed a detailed least-square peak-fit analysis of the fine structure in the C-K NEXAFS spectra of NTCDA, which was already reported in chapter 4.2.2.1, and hence we

will on briefly outline the results here. Vibronic progressions were fitted to the experimental data taking the Franck-Condon principle into account and assuming parabolic potential curves for the electronic ground and core-excited state described by

$$V_{pot} = \alpha \cdot (R - R_E)^2 \text{ and } V_{pot}' = \alpha' \cdot (R - R_E')^2, \quad (4.2.4.1)$$

respectively, with R being the normal coordinate of the observed vibrational mode, R_E the equilibrium distance and α the harmonicity (parameters with ' refer to the core-excited state). The Franck-Condon factors

$$f_{(v v')}^2 = |\langle v | v' \rangle|^2 \quad (4.2.4.2)$$

(v and v': vibrational wave functions of the initial and final state, respectively) are computed simultaneously during the fit. Since we mainly deal with vibronic modes above ~ 100 meV (see below) no vibronic excitation in the electronic ground state has to be considered at room temperature. Thus, only five fit parameters are required to describe each vibronic progression: $a = \alpha'/\alpha$, $\Delta R = R_E' - R_E$, $h\nu'$, the energy of the adiabatic transition E_0 , and the intensity I. For all vibronic progressions Voigt profiles with identical line widths (Gaussian and Lorentzian) were used. Note, that this is the *minimum* number of fit parameters necessary to describe a vibronic progression.

Figure 4.2.4.4 shows a least-square fit sequence of peak (c) of the annealed NTCDA multilayer film (see Figure 4.2.4.3a), which exhibits the best-resolved vibronic fine structure.

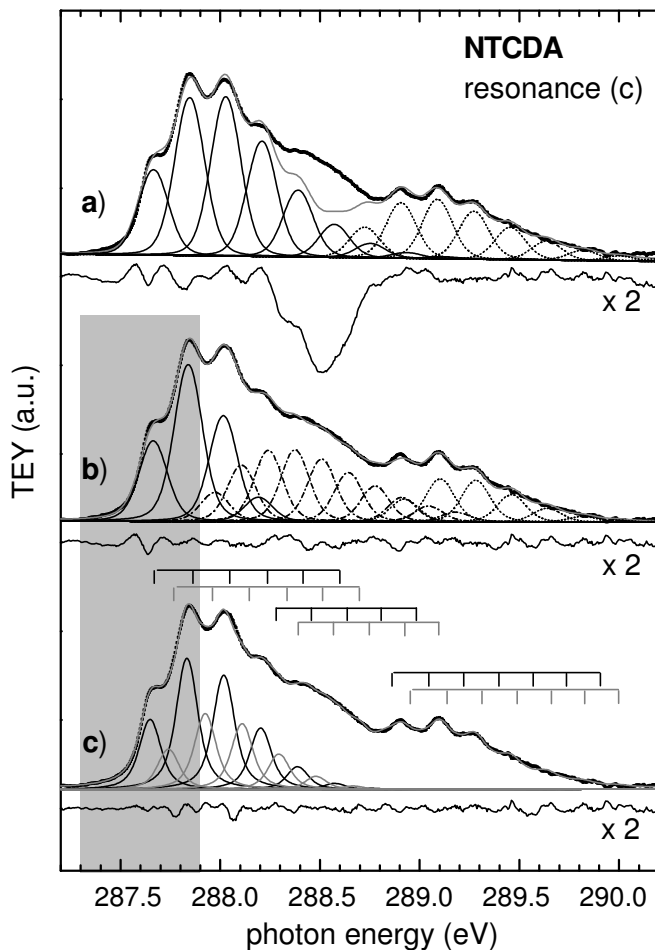


Figure 4.2.4.4: Comparison of the experimental data for NEXAFS resonance (c) of NTCDA multilayers annealed at 260 K (see Figure 4.2.4.3a) with least-square curve fits of vibronic progressions taking numerically calculated Franck-Condon factors into account, for two electronic transitions (a), for three electronic transitions (b), and for three electronic transitions including Davydov splitting (c). For clarity only the two Davydov components of the first electronic transition are plotted. Corresponding vibronic progressions are indicated as bar graphs above the spectra. The residua displayed below each data set are multiplied by a factor 2. The grey-shaded area represents the energy range used for the leading edge analysis. The χ^2 in the shaded region decreases from 0.046 (fit (b)) to 0.018 (fit (c)) by employing the Davydov model.

Figure 4.2.4.4a clearly demonstrates that two electronic transitions and their coupling to one vibronic mode in each case (which is suggested by the two sets of “ripples” in the measured curve) are not sufficient to reproduce the experimental spectrum. Taking into account a third electronic state (shown in Figure 4.2.4.4b) definitely improves the agreement between fit and experimental curve. This is in full agreement with the calculations which result in three major transitions in this range (see Figure 4.2.4.3a). However, the very high quality (resolution and statistics) of our experimental data allows an even closer inspection. Especially the leading edge of the first two vibronic features of peak (c) (indicated by the grey background in Figure 4.2.4.4) still shows an insufficient agreement between fit and data (see the oscillations in the residuum below each spectrum in Figure 4.2.4.4). As we described in detail in Chapter 4.2.2.1 the misfit at the leading edge does not result from the neglect of a second or third progression coupled to the same electronic transition. Also, possible artifacts from the flux normalization (see Chapter 4.1) can be excluded. Since the leading edge in all such experiments has an outstanding significance for the description by fits we tried to reproduce this part with highest accuracy.

We started to fit the leading edge to determine the two contributions to the line shape to $\Gamma_L = 83(3)$ meV (Lorentzian contribution) and $\Gamma_L = 76(3)$ meV (Gaussian contribution). Γ_L was fixed in the further analysis, since no significant differences of the life time broadening are expected and could be observed for the other electronic transitions. The Gaussian line width, which contains contributions from experimental resolution, inhomogeneities within the investigated layer, and low-energy phonons, was determined to 76(3) meV and also fixed for all Voigt profiles displayed in Figure 4.2.4.4c. We thoroughly refitted the spectrum in the grey shaded range (see Figure 4.2.4.4c). A satisfying result could only be obtained by using an additional peak *between* the first two vibronic peaks, which can only be explained by a possible energy splitting of the excited state. Such a splitting is expected to occur also in NEXAFS since it is well established as Davydov splitting in optical spectroscopy in the visible range [119,130]. It occurs if the unit cell contains two or more chemically and physically equal molecules, which is true for NTCDA in crystalline layers [115]. The splitting was comprised in the theory function by including one more progression per electronic transition shifted by a constant (fitted) value E_{DV} . The vibronic envelope (α' , R_E') and the vibronic energy ($h\nu'$) were kept the same for both progressions, and thus only the three intensities of the shifted progressions had to be added as fit parameters. The corresponding fit result is presented in Figure 4.2.4.4c. Indeed, the fit improves significantly for a Davydov splitting of $E_{DV} = 92(3)$ meV, as derived from the strong reduction of χ^2 from 0.046 to 0.018 (see also the residuum around 287.6 eV in Figure 4.2.4.4c). Such a value for E_{DV} is conceivable considering Davydov splittings found in the VIS range (e.g. 300 meV for oligothiényls [120]).

The fit parameters are summarized in Table 4.2.2.1 (Chapter 4.2.2). For a comparison of the obtained vibrational frequencies of the core-excited state with data from other spectroscopies probing the ground state (e.g. high-resolution electron energy loss spectroscopy (HREELS) or infrared spectroscopy), the ground-state vibronic energy can be derived from the vibronic energy in the excited state and the Franck-Condon shift ΔE_{FC} by the empiric formula

$$h\nu_o = h\nu' \cdot (\Delta E_{FC} / 1.2 + 1) \quad (4.2.4.3)$$

using the FC shift

$$\Delta E_{FC} = 0.5 \cdot h\nu' \cdot (\Delta R)^2 \quad [121]. \quad (4.2.4.4)$$

The corresponding values for $h\nu_0$ are also listed in Table 4.2.2.1. The agreement between our data for peak (3) (probing the C1 excitations, i.e. 238 and 216 meV) with the C=O stretching mode (229 meV) in condensed NTCDA as determined by HREELS [122] is very good. The same conclusion can be drawn for peak (b) – and to some extent also for peak (a) – which are shown in Figure 4.2.4.5 and briefly discussed below. Also in this case the ground state frequencies obtained here fit very well to the ring (88 - 94 meV) and C-H modes (~190 meV) [122].

Figure 4.2.4.5 presents the analysis of peaks (a) and (b). We particularly address the effect of different layer morphologies and local geometric structures in the NTCDA films comparing the upper and lower spectra. As derived from the polarization dependence [14] and already discussed above, NTCDA films prepared at low substrate temperature form a metastable phase with almost coplanar molecular orientation (Figures 4.2.4.5a and c) whereas they transform into the single crystal structure upon annealing at 260 K (Figures 4.2.4.5b and d). The most obvious changes in the NEXAFS fine structure occur at the leading edge of both peaks. Such modifications of the electronic structure upon morphological changes in weakly bound molecular solids have not been observed and described so far. Interestingly, the

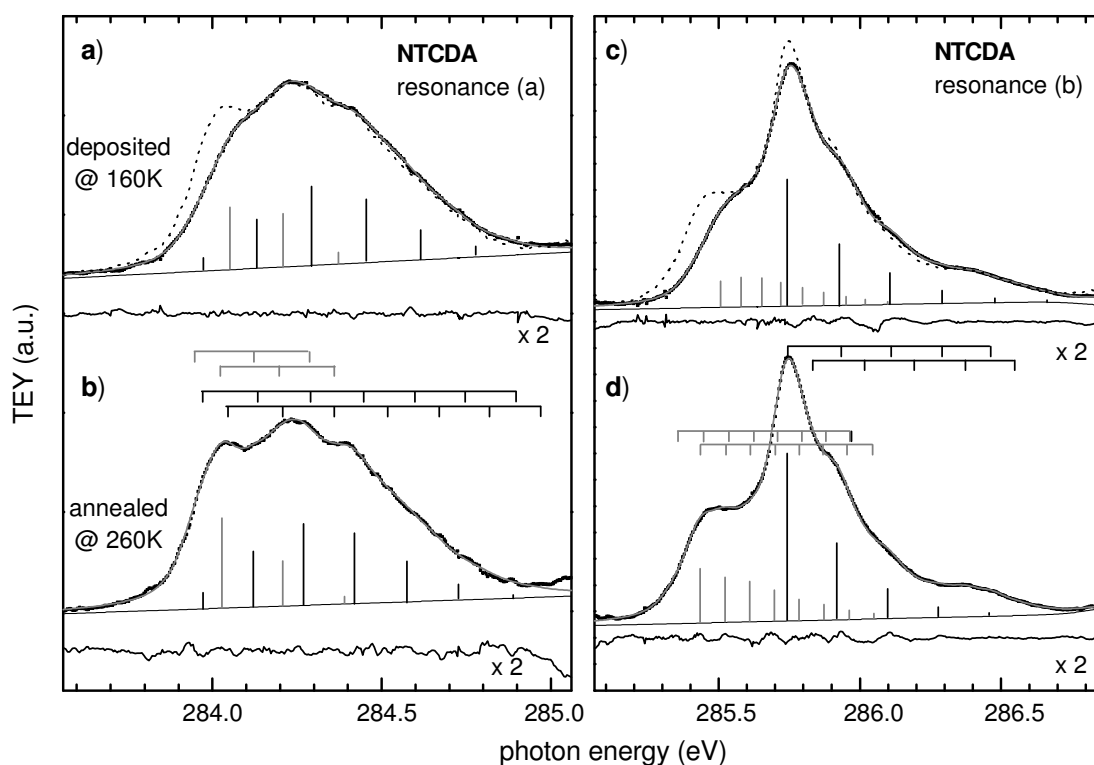


Figure 4.2.4.5: High-resolution NEXAFS spectra showing details of the resonances (a) (left) and (b) (right) of the NTCDA multilayer films of Figure 4.2.4.2 (spectra 2.1 and 2.2). Top: as deposited at 160 K; bottom: after annealing at 260 K. To underline the differences, the bottom spectra are also plotted as dashed lines in the upper part. The residua are multiplied by a factor 2. For clarity only one Davydov component of each electronic transition is plotted as bar graph. The corresponding progressions are indicated on top of the experimental curves b and d.

(independent) fit analyses of the vibronic progressions yield the same peak positions for both structural modifications. Of course, the Gaussian line width is reduced upon annealing due to reduced inhomogeneous broadening, but only by about 20% (see Table 4.2.2.1), whereas the Lorentzian broadening remains constant. However, the FC factors and especially the ΔR values change significantly which must be due to changes of the potential curves in the ground and/or excited electronic state. In fact, in the annealed layer the difference ΔR between the minima of the potential curves in the ground and excited state, respectively, is significantly smaller than in the layer deposited at 160 K (e.g., $\Delta R = 2.57$ instead of $\Delta R = 2.79$ for the first progression of peak (a) and $\Delta R = 1.41$ instead of $\Delta R = 1.57$ for the first progression of peak (b)). This indicates significant changes of the intermolecular interaction in the condensed layer and thus raises the question, whether the bonding mechanism in NTCDA films is adequately described by mere van-der-Waals and electrostatic interaction.

4.2.4.3 Comparison with PTCDA, NDCA, and BPDCA

As seen in Figure 4.2.4.2, vibronic fine structures similar to those of NTCDA are also observed for peak (c) in the C-K NEXAFS spectra of the other anhydride molecules PTCDA, BPDCA, and NDCA. In Figure 4.2.4.6 these peaks (c) are plotted on an expanded energy scale to allow an easier comparison with the above discussed NTCDA data. For NTCDA the spectrum of the annealed film, which shows the best-resolved fine structure, is plotted.

For PTCDA vibronic progressions can easily be recognized for the anhydride C 1s \rightarrow LUMO and C 1s \rightarrow LUMO+1 transitions at 287.8 eV and 288.4 eV, respectively, though the C 1s \rightarrow LUMO transition is not as well resolved for PTCDA as for NTCDA. This is not due to a significantly increased inhomogeneous broadening, since the transition at 288.4 eV shows sharp lines. However, a superposition of additional electronic transitions and vibrational excitations is believed to cause the observed smeared structures. In the BPDCA data only the anhydride C 1s \rightarrow LUMO transition at 287.8 eV shows strong vibronic coupling. For NDCA a very clear vibronic progression is resolved for the C 1s \rightarrow LUMO transition around 288.0 eV. In addition, the regular structures around 289.2 eV belong to the vibronic fine structure of the anhydride C 1s \rightarrow LUMO+1 transition, though they are superposed by the vibronic states with high term value of the C 1s \rightarrow LUMO resonance and other electronic transitions (see GSCF3-calculations in Figure 4.2.4.7).

For PTCDA, BPDCA and NDCA the larger number (if compared with NTCDA) of symmetrically inequivalent carbon atoms (4 for NTCDA, 7 for PTCDA and NDCA, 12 for BPDCA), due to the larger size of the aromatic ring system and/or the lower symmetry leads to additional electronic transitions within the energy region of peak (c) (see, e.g., GSCF3-calculations for NDCA in Figure 4.2.4.7). Thus, a detailed peak fit analysis is more difficult than for NTCDA. Especially the determination of the line shape is complicated by transitions derived from the ring system, that lead to intensity contributions at the leading edge of the first vibronic progression. Nevertheless, a determination of the vibronic parameters is still possible with satisfying accuracy. In this analysis the electronic transitions, that do not show a distinct vibronic splitting, were accounted for just by additional Gaussian peaks in the fit function.

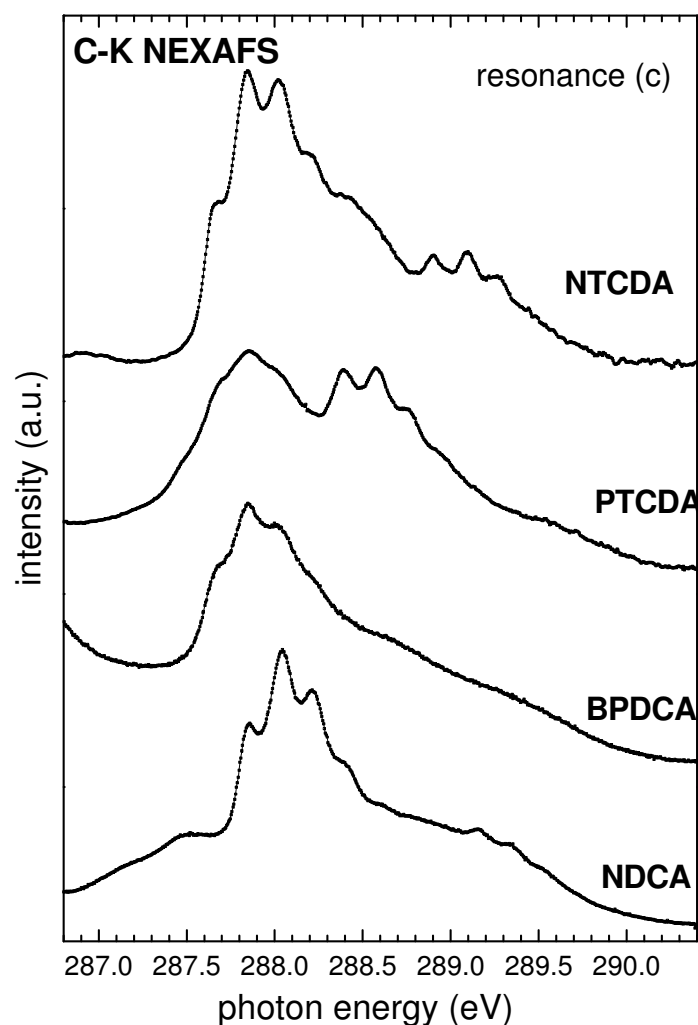


Figure 4.2.4.6: Comparison of the vibronic fine structure of C K-NEXAFS resonance (c) of the different anhydride molecules NTCDA, PTCDA, BPDCA, and NDCA (enlarged parts of spectra 2.2 – 2.5 of Figure 4.2.4.2).

The assignment of the electronic transitions, the energy of the adiabatic transitions E_A , the vibronic energies $h\nu'$ and $h\nu_0$ as well as the Franck-Condon shift ΔE_{FC} are summarized in Table 4.2.4.1. The vibronic parameters for all investigated anhydride molecules are similar; the ground state vibronic energies fit the C=O stretching mode very well in all cases. The ground state vibronic spectra for PTCDA and NDCA were obtained by HREELS [131] and FTIR [126], respectively; the corresponding values for the C=O stretching mode are 222 meV for PTCDA and 221 meV for NDCA (see Table 4.2.4.1). The striking analogy of the electron-vibron coupling for the different anhydride molecules reflects the similarity of the local electronic structure of the anhydride group. If the anhydride C $1s \rightarrow$ LUMO and C $1s \rightarrow$ LUMO +1 transitions are excited, the core hole creation and the occupation of the final state orbitals lead to a reaction of the electronic system. This reaction of the electronic system induces changes in the C=O bonding within the functional group. For all investigated anhydride molecules this process is apparently very similar and hence we see the same strong coupling to the C=O stretching mode. Moreover, for NTCDA our detailed analysis allows to detect also a preferential coupling to C-H and ring modes, if the core hole is created at ring carbon sites. This indicates the sensitivity of the electronic system to the localization of the

core hole. Thus, upon ring C 1s excitation the changes in the molecular bonding situation mainly influence the ring system and the attached hydrogen atoms.

	PTCDA		BPDCA	NDCA	
assignment	$C_{\text{anhyd.}} 1s \rightarrow$ LUMO	$C_{\text{anhyd.}} 1s \rightarrow$ LUMO+1	$C_{\text{anhyd.}} 1s \rightarrow$ LUMO	$C_{\text{anhyd.}} 1s \rightarrow$ LUMO	$C_{\text{anhyd.}} 1s \rightarrow$ LUMO+1
E_A (eV)	287.68(1)	288.73(1)	287.68(1)	287.86(1)	-
$h\nu'$ (meV)	186(5)	184(5)	173(5)	183(5)	185(5)
ΔE_{FC} (eV)	0.29(1)	0.24(1)	0.23(1)	0.23(1)	-
$h\nu_o$ (meV)	230(10)	226(10)	206(10)	218(5)	-
C=O stretch (meV)	222 [131]		-	221 [126]	

Table 4.2.4.1: Results of the vibronic analysis of resonances (c) of the PTCDA, BPDCA and NDCA films. The assignment of the various transitions and the vibronic parameters are explained in the text. In the bottom line literature values for the vibronic energy of the C=O stretch mode in the ground state are listed for PTCDA and NDCA.

4.2.4.4 Comparison between NDCA and ANQ

Figure 4.2.4.7 compares the π^* -regions of the C-K (Figure 4.2.4.7a) and O-K (Figure 4.2.4.7b) NEXAFS spectra of NDCA and ANQ. The two molecules have the same naphthalene core but ANQ has a quinoic functional group with only two terminal oxygen atoms, while NDCA has one additional bridging oxygen atom. In this figure also the results of GSCF3-calculations are plotted. In all cases the calculated energy scale was aligned to fit the first experimental peak. Thus, the theoretical C-K and O-K spectra of NDCA had to be shifted by -2.3 eV and -0.7 eV, and the ANQ spectra by -2.3 eV and -1.0 eV, respectively. The assignment of the different electronic transitions to the observed peaks is indicated by guidelines.

For NDCA the experimental peak (a) in the C-K spectra is due to transitions with the core hole at the ring atoms C4 and C5 (both bonding to hydrogen atoms) into the LUMO, whereas peak (b) has contributions from different ring C 1s \rightarrow LUMO and LUMO+1 transitions. Peak (c) results from two major transitions from the anhydride C 1s levels into the LUMO and LUMO+1. Both transitions show distinct coupling to the C=O stretching vibration as discussed earlier. If only the functional group is changed, i.e. in present case for ANQ the anhydride group with three oxygen atoms is replaced by the quinoic group with two oxygen atoms, strong differences in the NEXAFS spectra occur. In the C-K NEXAFS data peak (c) is strongly decreased in intensity whereas peaks (a) and (b) are broadened and slightly shifted towards lower energy. The broadening is not due to inhomogeneities in the layer as can be

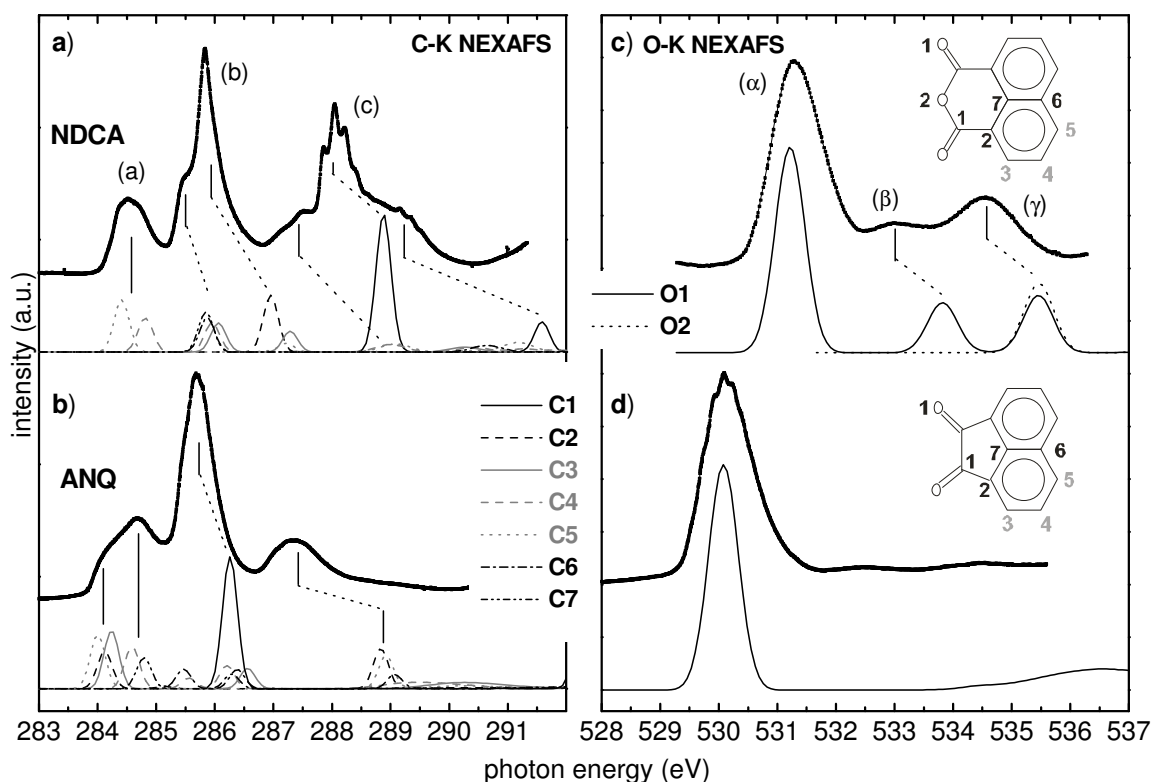


Figure 4.2.4.7: π^* -region of the experimental C-K (left) and O-K (right) NEXAFS spectra of NDCA and ANQ compared with corresponding GSCF3-calculations. The calculated spectra were shifted in energy to align the first peaks (see also text). The inequivalent carbon and oxygen atoms distinguished in the calculation are indicated in the chemical formulae depicted as insets in Figure 4.2.4.7b and d.

derived from the ANQ O 1s data, as discussed in Chapter 4.2.3 and below. By comparison with the *ab initio* calculations we find that the changes of peak (c) are mainly caused by a strong shift of the anhydride C 1s (C1) \rightarrow LUMO transition towards lower energy. This excitation now contributes to peak (b) for ANQ instead to feature (c) for NDCA. A closer inspection of the calculated data reveals strong shifts towards lower energy also for the transitions from C2, C3 and C7 atoms. Now at least 5 transitions contribute to peak (a), leading to the observed broadening.

The experimental O-K spectra are also very well reproduced by the calculations. The NDCA peaks (α) and (β) are due to O 1s (O1) \rightarrow LUMO and LUMO+1 transitions, respectively, whereas peak (γ) is a superposition of an O 1s (O1) \rightarrow LUMO+3 and an O 1s (O2) \rightarrow LUMO excitation. For all three NDCA peaks no vibronic fine structure can be resolved. In the functional group of the ANQ molecule the bridging oxygen O2 is missing, and thus the O-K spectra are not superposed. In addition, the O 1s (O1) \rightarrow LUMO+1 and LUMO+3 transitions are strongly decreased in intensity. The O-K NEXAFS spectrum is thus dominated by peak (α), that has only the contribution of one electronic transition from the O1 1s core state into the LUMO. The interesting result is here, that this NEXAFS resonance shows a very well resolved vibronic progression, whereas no vibronic fine structure is visible in the C-K NEXAFS data of the ANQ molecule. This is, of course, an uncommon observation, since the life time broadening is lower (e.g. 79 meV for the C 1s and 157 meV for the O 1s level in CO [117]) and the experimental resolution is much better at the C-K edge than at the O-K edge (24 meV and 56 meV, respectively), whereas the inhomogeneous broadening influences the

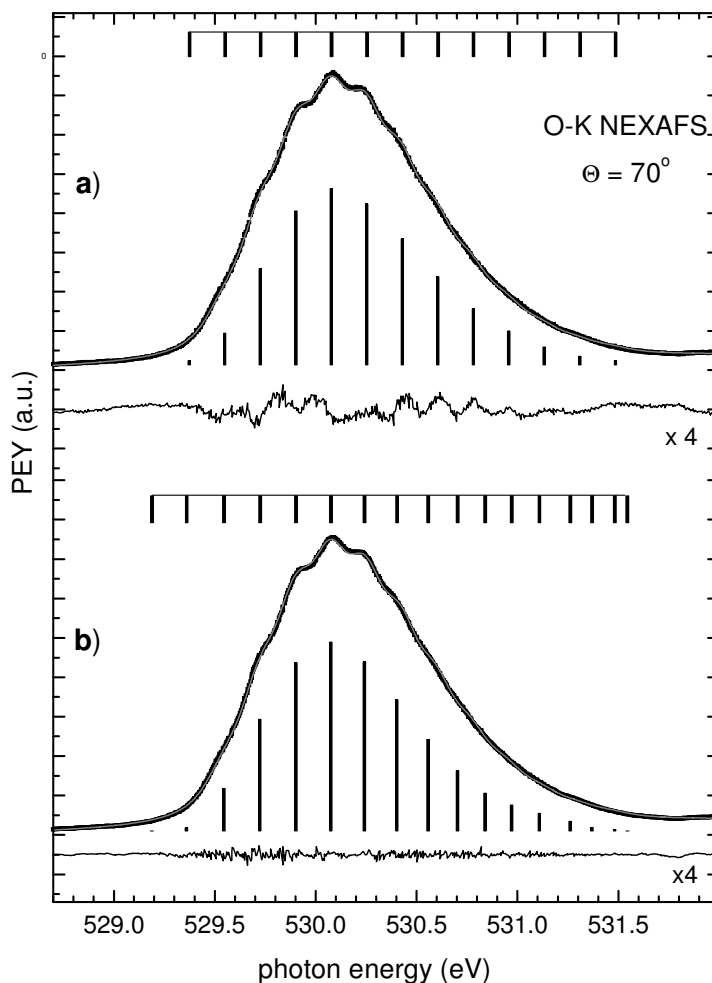


Figure 4.2.4.8: (a) Comparison of the experimental data (dots) for the O K-NEXAFS resonance (α) (see Figure 4.2.4.2, spectrum 2.11) of ANQ multilayers with the least-square curve fit result of one vibronic progression (plotted as bargraph underneath the experimental curve) taking into account numerically calculated Franck-Condon factors and a harmonic potential (see text). (b) Fit result for resonance (α) with 17 Voigt profiles with identical line shape implicitly assuming an anharmonic potential. The progression is plotted as bargraph underneath the experimental curve. The energy positions and intensities were fitted independently but with optimised start values from the harmonic fit displayed in the upper part. For clarity the residua in (a) and (b) were multiplied by a factor 4. Above Figures a) and b) the resulting energy positions of the vibronic states are plotted to clarify the harmonic and anharmonic distribution, respectively.

observed structures in both regimes in the same way. Thus, this result cannot be explained by experimental reasons but must be an intrinsic effect.

We have analysed this effect in Chapter 4.2.2 and hence will only briefly report the result here. To gain more information about the electron-vibron coupling mechanism we performed a detailed peak fit analysis of the ANQ peak (α). In a first step we assumed parabolic potential curves for the electronic ground and core-excited states (in analogy to the analysis of the anhydride C-K spectra that was discussed above) and fitted the experimental data with one vibronic progression. The overall agreement is good as can be derived from Figure 4.2.4.8a, though the residuum (plotted underneath the corresponding spectra, magnified by a factor 4)

still shows some significant structure that, together with the high statistical quality of our spectra, challenges this interpretation. The coupling of the electronic transition to two (or more) normal modes can not explain the misfit, as explained in detail in Chapter 4.2.3. However, the increasing deviation of the harmonic fit at the higher energy side strongly points towards the influence of an anharmonicity of the excited state potential. A refit with 17 Voigt profiles of identical line shape but free intensities and energy positions, presented in Figure 4.2.4.8b, clearly shows the effect of the potential anharmonicity in the core-excited state, that decreases the spacing of the vibronic states for increasing term values. This is clarified by the bar graphs on top of the experimental curve in Figure 4.2.4.8b, that displays the energy positions of the fitted peaks. From the line shape of the fitted Voigt profiles the O 1s lifetime broadening was determined to 97 meV and the corresponding Gaussian width to 156 meV.

Using the Morse potential

$$E(R) = E_D \left[1 - e^{-a(R-R_E)} \right]^2 \quad (4.2.4.5)$$

as description of the anharmonic potential and taking the quadratic approximation (i.e. by expanding the exponential function to the third, quadratic term) one obtains the term energies E_n

$$E_n = hv'(n+1/2) - \chi hv'(n+1/2)^2. \quad (4.2.4.6)$$

The anharmonicity $\chi hv'$ can be derived to 2.6(1) meV from Figure 4.2.4.9 (see also Chapter 4.2.3), where the term energies are plotted versus the term values n , and a curve according to equation (4.2.4.6) is adapted.

Furthermore, the vibronic energy $hv' = 197(5)$ meV in the excited state can be derived from the fit curve in Figure 4.2.4.9. From this, the vibronic energy in the ground state hv_0 can be calculated according to equation (3) if the Franck-Condon shift, i.e. the energy difference

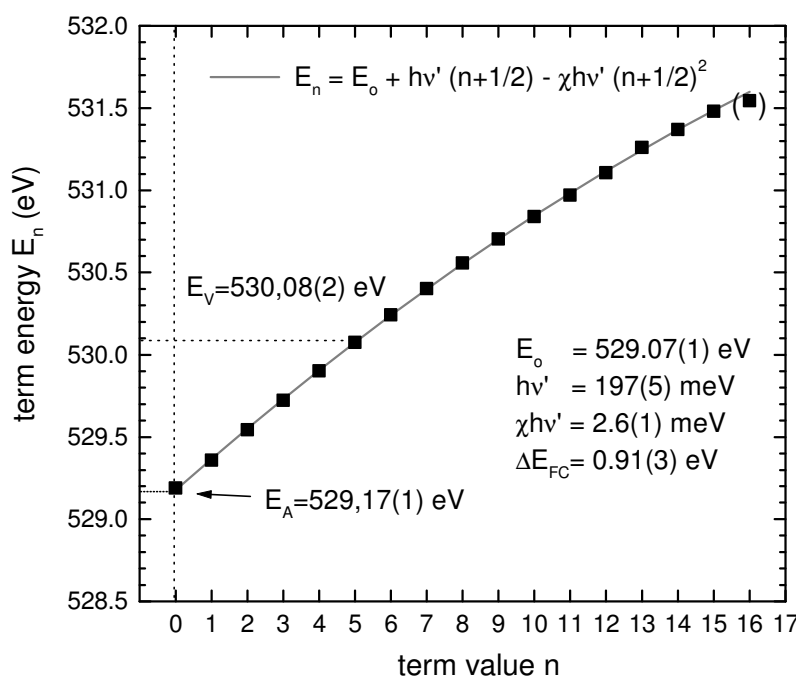


Figure 4.2.4.9: Plot of the energy positions E_n of the vibronic states as derived from Figure 4.2.4.8b versus the term value n . From the fitted curve $E_n = E_0 + hv'(n+1/2) - \chi hv'(n+1/2)^2$ (grey line) the parameters E_0 (the energy of the potential minimum of the electronically excited state), hv' , and the anharmonicity $\chi hv'$ of the core-excited potential as well as E_A can be deduced. For the shown curve the first fitted peak in Figure 4.2.4.8b was assigned to the vibronic quantum number $n = 0$ (see text). The energy of the vertical transition E_V is also indicated (see also Chapter 4.2.3).

between the adiabatic (E_A) and the vertical transition (E_V) is known. E_V (the maximum of the vibronic progression in Figure 4.2.4.8b) can be determined to 530.08(2) eV. If the adiabatic transition ($n = 0$) is assigned to the first fitted peak in Figure 4.2.4.8b at 529.17(1) eV, the resulting Franck-Condon shift is $\Delta E_{FC} = 0.91(3)$ eV and the respective ground state vibronic energy is calculated as $h\nu_o = 346(10)$ eV. If this result is compared to the corresponding ground state vibronic energies of ANQ, as derived from FTIR measurements [125,126], the observed vibronic mode must be assigned to modes involving a high amplitude of C-H stretch vibrations, observed with FTIR between 381 - 386 meV. No other modes exist in the ground state between 220 meV and 500 meV, as also known from DFT calculations.

The deviation of about 35 meV of our value from the value determined by FTIR can be explained by an incorrect assignment of the adiabatic transition. If the first fitted peak in Figure 4.2.4.8b is associated with the quantum number $n = 1$ (instead of $n = 0$) the resulting vibronic parameters are $E_A = 528.98(1)$ eV and $\Delta E_{FC} = 1.10(3)$ eV (see Figure 4.2.4.9), and the ground state vibronic energy is $h\nu_o = 383(10)$ eV. This value is in excellent agreement with the FTIR values for C-H vibronic modes of ANQ in the electronic ground state. We hence believe, that the latter assignment is the correct one as shown in Figure 4.2.4.9, but due to the used approximation the alternative assignment can not be excluded.

The parameters derived from our analysis of the $O\ 1s \rightarrow \pi^*$ -resonance in Figure 4.2.4.8b and Figure 4.2.4.9 are summarized in Table 4.2.4.2 (for an assignment of the first fitted peak to $n = 0$).

Comparing the rather similar molecules NDCA and ANQ we see, that the changes in the electronic structure, induced by the two different functional groups, lead to strong changes in the electronic transitions as well as in the electron-vibron coupling. For ANQ we do not observe the coupling of the C=O stretching mode to excitations of the carbon atom of the functional group, but that an excitation of the $O\ 1s \rightarrow LUMO$ transition reorganizes the electronic system in such a way, that it has a strong effect on the C-H bonds.

	Γ_L [meV]	Γ_G [meV]	E_A [eV]	ΔE_{FC} [eV]	$\chi h\nu'$ [meV]	$h\nu'$ [meV]	$h\nu_o$ [meV]
ANQ	97(5)	156(5)	529.17(1)	0.91(2)	2.6(1)	197(2)	346(10)
BPDCA	100(10)	181(10)	530.6(1)	0.9(1)	-	171(3)	300(10)

Table 4.2.4.2: Parameters derived from the analysis of the vibronic fine structure of the ANQ and BPDCA $O\ 1s (O1) \rightarrow LUMO$ resonances in Figures 4.2.4.8b, 4.2.4.9 and 4.2.4.10. For the ANQ data the results corresponding to an assignment of the first fitted peak to $n = 0$ are plotted (see text).

4.2.4.5 BPDCA

As could already be seen in Figure 4.2.4.2, BPDCA is the only here investigated molecule, for which vibronic fine structure is resolved for both, the C-K (see, e.g., spectrum 2.4) and the O-K NEXAFS data (see spectrum 2.9). In both cases this occurs upon excitations from $1s$ orbitals into molecular orbitals localized on the functional group. BPDCA is thus a very

interesting model molecule for the investigation of local differences of the electron-vibron coupling within the anhydride group. Upon excitation of the anhydride C 1s \rightarrow LUMO transition, we clearly observe a coupling to the C=O stretching vibration (see Table 3.2.4.1).

In the O-K data vibronic fine structure is resolved for peak (α), the O 1s (O1) \rightarrow LUMO transition, indicated by equally spaced shoulders on both sides of the peak maximum at 531.5 eV. This can be clearly seen in Figure 4.2.4.10, presenting an enlarged view of the BPDCA peak (α). The result of a peak fit analysis with one vibronic progression is also displayed in

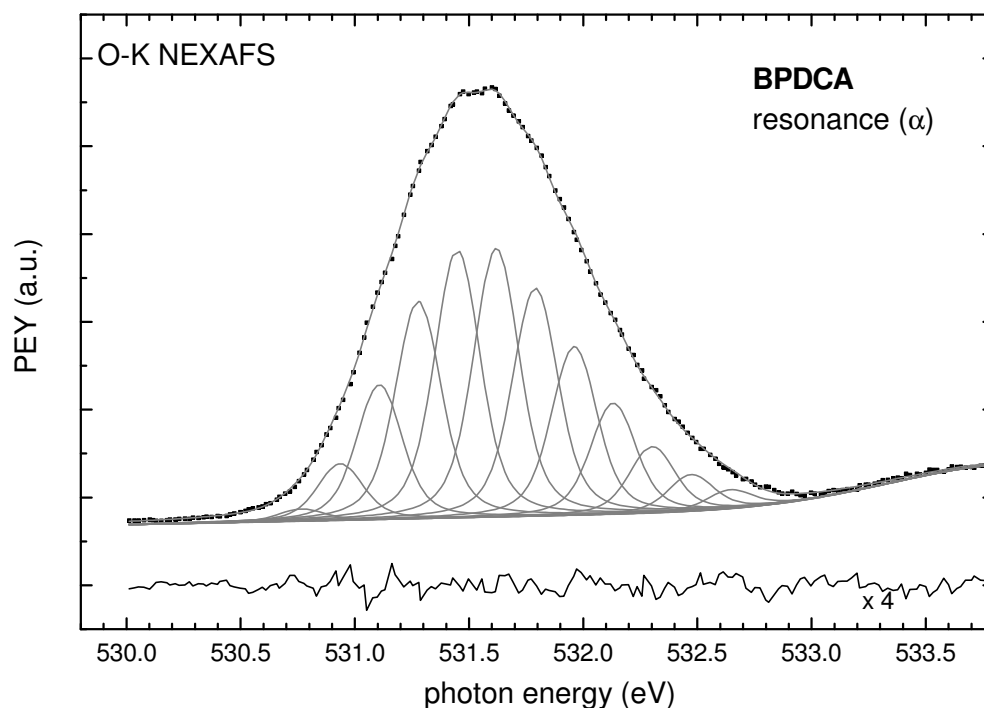


Figure 4.2.4.10: Peak fit analysis of BPDCA resonance (α) using harmonic potentials and numerically calculated FC-factors.

Figure 4.2.4.10. The fit result utilizing a harmonic potential is satisfying, as can be derived from the residuum (plotted below the experimental and fit data in Figure 4.2.4.10). However, the fine structure is not as clearly resolved as for the ANQ peak (α) and thus does not allow such a detailed analysis. Nevertheless, the parameters, that describe the excited and ground state vibronic properties, can be determined. The vibronic energy in the core excited state $h\nu' = 171$ meV is significantly smaller than for ANQ and, in addition, the Gaussian width of 181 meV is larger, most likely due to a larger inhomogeneous broadening. These two parameters are apparently responsible for the reduced resolution of the fine structure in the BPDCA case. Our analysis reveals a ground state vibronic energy of about 300 meV. At the time of this work no ground state vibronic data for BPDCA was available, but a comparison with the well-known FTIR [126] and HREELS [122,131] data of other large anhydride molecules points towards the excitation of a C-H mode. C-H stretching modes are usually observed around 380 meV and are generally the only modes appearing in the energy range between 220 meV and 500 meV. The deviation of our value can, in analogy to the interpretation of the ANQ data, be attributed to an incorrect assignment of the first visible peak in the fitted data to the adiabatic transition. However, in the BPDCA case a predominant coupling to more than

one vibrational mode cannot be excluded, which would then lead to rather different values for the vibrational energies.

4.2.4.6 Conclusions

We have shown that the now available very high spectral resolution at 3rd generation synchrotron radiation sources enables new insight into the electronic structure of large organic molecules using near-edge x-ray absorption fine structure spectroscopy. We present high-resolution NEXAFS data of condensed organic molecules that clearly show vibronic fine structure. This had not yet been observed for aromatic molecules with delocalised π -systems larger than benzene. A detailed peak fit analysis based on the Franck-Condon principle succeeds and yields interesting information on the vibronic coupling in the NEXAFS process. Though the relatively large molecules possess a large number of vibrational modes, their NEXAFS spectra can be described by a predominant coupling of one vibronic mode to each electronic transition. If the NEXAFS excitation takes place at the anhydride carbon atoms this mode can unambiguously be identified as C=O stretching mode for all anhydride molecules investigated in this work (NTCDA, PTCDA, NDCA and BPDCA). Furthermore, the analysis of the present high-quality data of NTCDA gives first experimental evidence for a Davydov splitting in core-excitations. The Davydov splitting could be determined as 94 meV for the C 1s \rightarrow LUMO and C 1s \rightarrow LUMO+1 transition, respectively. For NTCDA samples with different layer morphology we observe a significant difference in the potential curves indicating a different intermolecular bonding between the molecules in the condensed phase. This significant change challenges the common bonding picture of weakly, van-der-Waals-like interacting molecules.

The vibronic fine structure is very similar for the anhydride molecules with different sizes of the ring system. However, a change of the functional group from an anhydride (e.g., NDCA) to a quinoic group (ANQ), leads to strong differences in the electron-vibron coupling: now the C 1s \rightarrow π^* -transition in the functional group does not show vibronic coupling, whereas a vibronic structure is visible in the O-K edge data. The O 1s \rightarrow π^* -transition of ANQ (acenaphthenequinone) shows the so far best-resolved fine structure of an O 1s excitation of a large organic molecule in the condensed phase. The large number of relatively intense electronic transitions and probably also the coupling of two or more vibronic progressions to the different C 1s excitations leads to a smearing of the vibronic fine structure in the C K-edge data. Our detailed analysis of the O K-edge spectra shows, that the O 1s \rightarrow π^* excitation couples to one vibration mode, which is a C-H stretching mode and not a C=O mode. This example shows, that NEXAFS may very selectively excite molecular vibrations which not necessarily have to be located on the absorbing atom.

This seems surprising, at first glance. Nevertheless, the result can be qualitatively understood in a simple picture. By the NEXAFS excitation process the electronic structure of the molecule is significantly changed: an additional positive charge is localized on the ionized atom and an additional negative charge is filled into a previously unoccupied orbital. Since unoccupied orbitals often have antibonding character with respect to particular intermolecular bonds depending on their spatial distribution, the “new” π^* electron may lead to a significant bond lengthening of these bonds or this bond and hence the corresponding vibration(s) may strongly couple to the electronic excitation. The unoccupied orbital (in the presence of the core hole) can be localized around the excited atom, e.g. in a functional group like the anhydride group, or delocalised over the entire molecule. The former situation apparently occurs for the anhydride molecules leading to a predominant coupling of the C=O stretching

vibration if at least the anhydride carbon atoms are excited. The latter situation is apparently valid for ANQ for which the O-excitation leads to a coupling to the C-H stretching mode at 197 meV with high cross section, corresponding to about 385 meV (as measured with FTIR [125,126]) in the ground state. Of course, this picture is oversimplified because the excitation process not only involves one core state and one unoccupied orbital but may also influence and rearrange the entire electronic system.

This interpretation is corroborated by the NEXAFS spectra of BPDCA. In this case we observe both, the C=O stretching mode upon C 1s and the C-H stretching mode upon O 1s excitation of the functional group atoms. This clearly shows the sensitivity of the molecular electronic system, that reacts very differently if the hole is created at different core sites within one molecule although the different excitations involve the same previously unoccupied orbital, e.g. the LUMO. Thus in the first case (C 1s excitation) the C=O bonds, and in the second case (O 1s excitation) the C-H bonds are affected strongest leading to a coupling to the corresponding vibronic modes.

An additional interesting result of the analysis of the ANQ O K-edge NEXAFS data is the determination of the anharmonicity of the potential in the core-excited state. The obtained value for the anharmonicity parameter $\chi = 0.013$ is rather large and indicates that anharmonic potentials have to be taken into account for a careful analysis of highly-resolved NEXAFS spectra. Their neglect in the other curve fit analyses (to keep the number of free fit parameters as low as possible) may be the reason for the remaining “wiggles” in the residua of Figures 4.2.4.4, 4.2.4.5 and 4.2.4.10.

4.3 Line shapes and satellites in high-resolution x-ray photoelectron spectra of large π -conjugated organic molecules

4.3.1 Motivation

In this chapter, that will be submitted to the *Journal of Chemical Physics* (see Ref. [132]), we present a high-resolution x-ray photoemission study on condensed multilayer films of large, aromatic π -conjugated molecules on a Ag(111) surface. The photoemission spectra of the rather similar, systematically varied molecules show distinct differences and thus provide very useful fingerprints. The high quality of the data enables us to determine binding energy differences in the x-ray photoelectron (XPS) spectra for the different carbon sites within the ring system, which are usually only resolved in the gas phase [133]. Additional, well-resolved finestructure in the spectra can be assigned to shake-up satellites. These satellite structures have been intensely studied for organic molecules in the gas phase and the solid state by both, experimental [134,135] and theoretical methods [136,137] and allow further insight into the intramolecular and intermolecular reactions of the electronic system upon the excitation process.

The model molecules presented in this chapter, 3,4,9,10-perylene-tetracarboxylic acid dianhydride (PTCDA), 1,4,5,8-naphthalene-tetracarboxylic acid dianhydride (NTCDA), 1,8-naphthalene-dicarboxylic acid anhydride (NDCA), acenaphthenquinone (ANQ) and benzoperylene-(1,2)-dicarboxylic acid anhydride (BPDCA), all have delocalised aromatic electronic systems, which have a major influence on their chemical and physical properties. The corresponding molecular structures are plotted in Figure 4.3.1. The molecules were chosen in order to systematically vary the size of the aromatic ring system (naphthalene – perylene – benzoperylene), the functional group (anhydride-quinone; NDCA – ANQ) and the polarity (NTCDA – NDCA, BPDCA – NDCA). The C_{2v} -symmetric molecules BPDCA, NDCA and ANQ are polar with differently strong dipole moments of different strengths, whereas PTCDA and NTCDA (D_{2h} symmetry) have electrostatic quadrupole moments.

In all molecules the functional group acts as an electron acceptor, with the anhydride group (three oxygen atoms) being the stronger acceptor as compared to the quinone group (two oxygen atoms). The part of the electron donor is played by the aromatic ring system and here the donor strength increases with the size of the aromatic system. Therefore we have a systematic variation of the donor-acceptor strength and the polarity, which will help us to explain experimental observations.

4.3.2 Results and discussion

Figure 4.3.1 shows the C1s (a) and O1s (b) XPS spectra of condensed multilayers of the 5 different molecules PTCDA, NTCDA, NDCA, ANQ and BPDCA together with schemes of the corresponding molecular structures. To allow a better comparison the integral intensities

were normalized. The differences in the energy positions and relative intensities of the photoemission lines of the relatively similar molecules are striking. We emphasize, that the measured energies were calibrated very carefully according to Chapter 4.1, resulting in an absolute accuracy of the energy scale of about 50 meV.

For all five molecules the peak corresponding to the carbon atoms of the functional group is shifted to higher binding energies and clearly separated from the most prominent peak which is attributed to the ring carbon atoms. The higher binding energy of the functional group carbon can be understood in a simple initial state picture: the highly electronegative oxygen atoms in the functional groups withdraw electrons and thus reduce the charge density particularly on the covalently bound carbon atoms of the functional group. The core level binding energies are thus increased. In addition, there might be a difference between both carbon species in the dynamic response of the multi-electron system to the creation of the core hole (screening effect). Both effects are usually referred to as chemical shift [138].

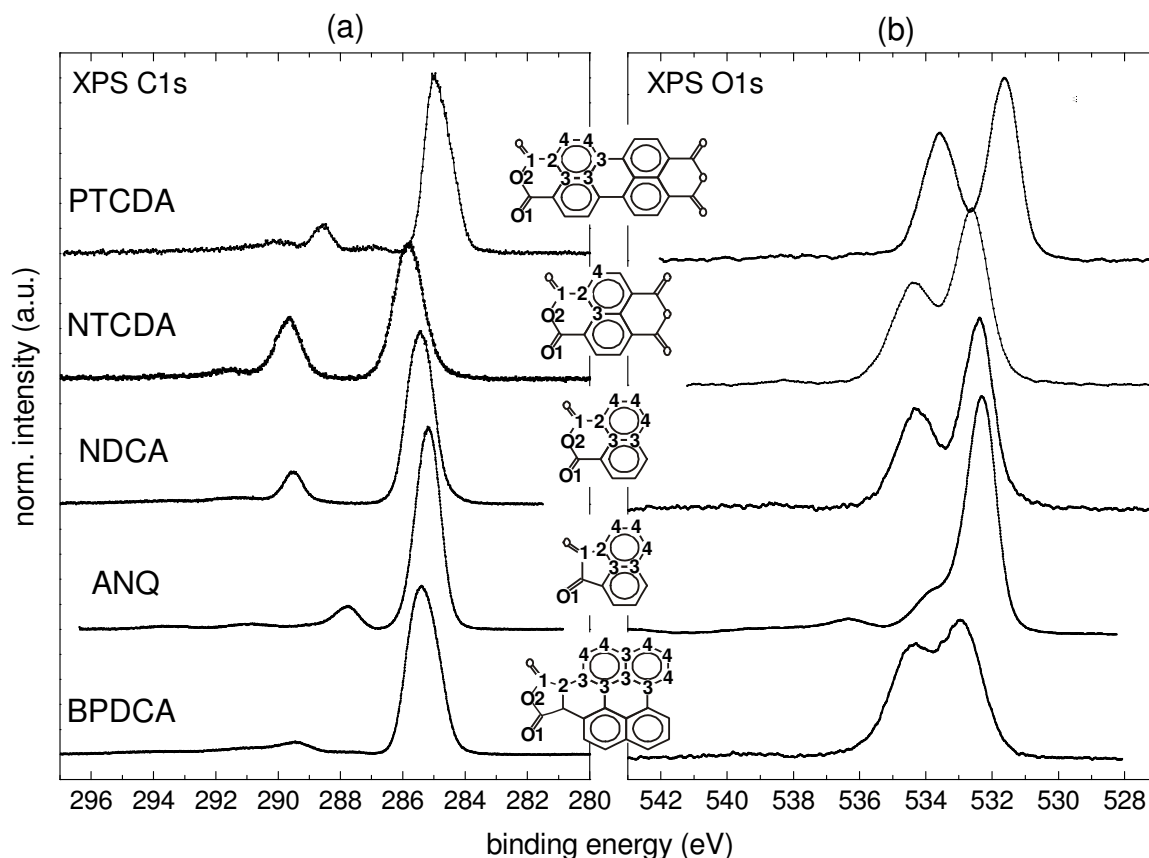


Figure 4.3.1: C 1s (a) and O 1s (b) XPS data from multilayer films of the molecules PTCDA, NTCDA, NDCA, ANQ and BPDCA. The spectra were taken with excitation energies of 335 eV (C 1s) and 700 eV (O 1s) and a constant analyser pass energy of 40 eV. The molecular structures are plotted in the middle, and the different carbon and oxygen sites are marked (see text).

The shift between the anhydride carbon (NDCA: 289.54 eV) and the quinone carbon (ANQ: 287.79 eV) is due to the different number of oxygen atoms (3 and 2, respectively) in the corresponding functional groups.

In the O1s spectra (Figure 4.3.1b) the two clearly separated peaks of the anhydrides can be assigned to the two chemically different oxygen atoms in the anhydride functional group. The energy separation of the two peaks varies between 1.56 eV in BPDCA and 1.76 eV in PTCDA. The peak at lower binding energy belongs to the double bonded terminal oxygen (O1), the peak at higher binding energy to the bridging oxygen atom (O2) as can be judged from their relative intensities. For ANQ only the O1 peak is visible. All other structures are due to satellites and will be discussed in detail below.

The different binding energies of the photoemission lines provide interesting information on the delocalisation of the electronic system and the resulting ability to screen the core hole:

For the molecules with the same naphthalene core (ANQ \rightarrow NDCA \rightarrow NTCDA) the change of the C1s peak energies shows the expected chemical shift towards higher binding energies when the number of oxygen atoms in the functional groups is increased, in agreement with the role of the aromatic part as electron donor. The same tendency can be observed in the O1s spectra. However, in this case the trend should be reversed due to the role of the oxygen atoms as electron acceptors. Thus a mere initial state picture for the explanation may not be sufficient. This is underlined by the strong energy shift of up to 1 eV towards lower binding energy of the PTCDA C 1s and O 1s levels. Since the stoichiometric ratio of oxygen and carbon atoms for PTCDA is the same as for NDCA, we would (in first approximation) expect very similar core level binding energies. Thus, we explain this energy shift to differences in the final state screening for these two molecules: in PTCDA we observe a very effective screening mechanism of the large, strongly delocalised electronic π -system, that can very flexibly react upon core hole creation and can transfer charge to stabilize the core ionised atom. A very strong support of this explanation comes from the fact that both, the C 1s and the O 1s holes of PTCDA are shifted by 1-2 eV to lower binding energy. Additional influence by intermolecular screening is indicated by the strong influence of the neighbouring molecules on the satellite structures, as will be discussed below.

It is interesting to note, that we observe the opposite effect for BPDCA: the binding energies of both, O 1s and C 1s levels are rather high as compared to those of the other molecules. By simple initial state considerations we would expect the lowest C 1s binding energy for this molecule (benzoperylene core with only one anhydride group), and by mere final state (screening) consideration the lowest O 1s binding energy (because of the large π -electron system needed for effective screening). However, the mechanisms are more complicated. The benzo group apparently “decouples” the anhydride group from the perylene part, thus reducing the size of the screening effect significantly. Thus, in spite of the relatively large size of the aromatic part, initial state effects dominate the relative peak positions for BPDCA.

Peak fit analysis:

In the C 1s spectra the different contributions from the ring carbon atoms are not easily discernible, but some internal structure of the peaks is indicated by the strongly asymmetric peak shapes. Thus, to further interpret the XPS data we performed a *comparative*, for the whole spectra series *consistent* simultaneous least-square peak fit analysis. This allows to resolve the contributions of the chemically different ring carbon atoms, define their positions and to distinguish and assign photoemission lines and satellite structures in the C1s and O1s data.

We applied linear constraints that reflect the corresponding stoichiometry and physical considerations. For the photoemission lines Voigt profiles were used with constant Lorentzian (life time) widths of 80 meV (C 1s) and 100 meV (O 1s), respectively. The values for the intrinsic lifetime broadening of the core states were derived from high resolution NEXAFS

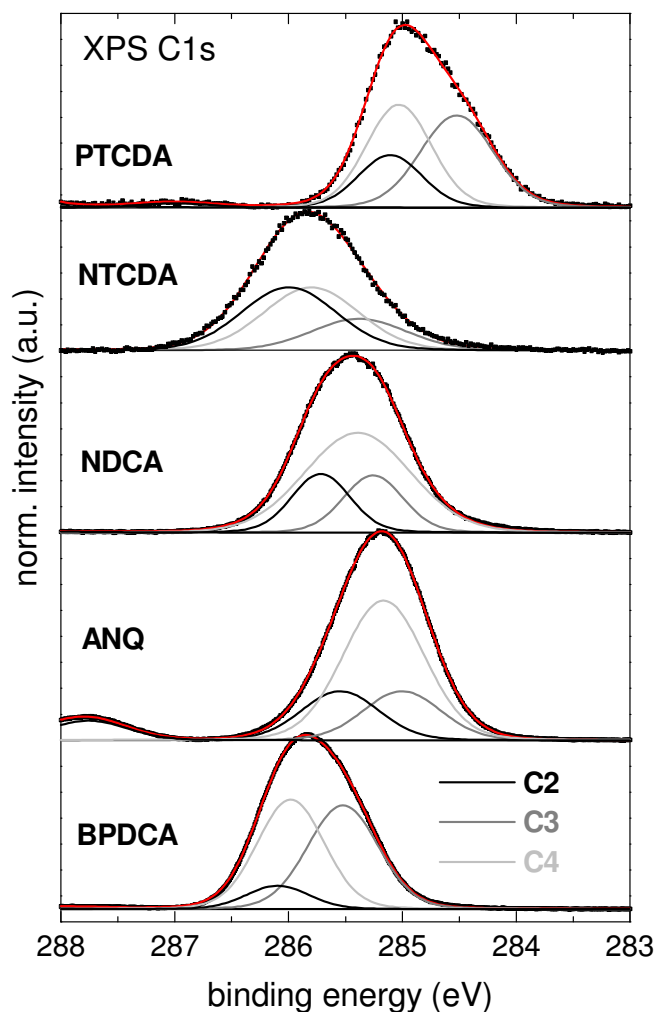


Figure 4.3.2: Results of the peak fitting analysis of the ring carbon peaks in the C 1s spectra. 3 Voigt profiles were used that refer to the atoms C2 – C4 as specified in the legend. Experimental data is displayed as points, fitted peaks as straight lines.

sequence) of the three different ring carbon atoms (C2–C3) were defined by comparison of the 5 molecules with different stoichiometric ratio of (ring) carbon atoms. Assuming that the relative energy positions of the 3 different carbon atoms are the same for the 5 similar molecules, the XPS ring carbon peaks were fitted with 3 Voigt profiles with a fixed area ratio C2:C3:C4 according to the stoichiometric ratio of the corresponding molecules (PTCDA: 4:8:8; NTCDA: 4:2:4; NDCA: 2:2:6; ANQ: 2:2:6; BPDCA: 2:10:10). The Gaussian width was fitted and linear constraints were used, that reflect the further inhomogeneity within the classified groups. Thus, e.g. for NTCDA the Gaussian width has to be the same for all 3 contributions of the carbon atoms C2–C4, but e.g., for NDCA the width of the C3 peak could be larger than the width of the C2 peak, since all C2 atoms are equal, whereas for symmetry reasons, there are 3 different C3 atoms.

The six possible relative positions (i.e. the possible sequences of the three peak binding energies) were now tested to describe the different ring carbon spectra simultaneously, and

measurements on these molecules, as described in Chapter 4.2. The Gaussian width, containing contributions from experimental resolution and inhomogeneities, was fitted respecting constraints as we will specify later. For all satellite peaks Gaussian peak shapes were used.

The ratio of the peak areas was fixed according to the stoichiometric ratios, e.g. for the anhydride O1s spectra:

$$\text{area (peak O1 + satellites)} : \text{area (peak O2 + satellites)} = 2 : 1.$$

The carbon atoms can be classified into 4 categories as specified by the chemical structure displayed in Figure 4.3.1: the carbon atoms of the functional groups (C1) with bonds to carbon and oxygen atoms, the connecting C atoms between the functional groups and the ring systems (C2), carbon atoms of the aromatic core that are bonded to 3 other ring carbons (C3) and carbon atoms that are bonded to two carbons and one hydrogen (C4). This is, of course, a simplified approach, since for all molecules except NTCDA there are further differences in the chemical environment of the C3 and C4 species, which are beyond the resolving power of our experiment, though.

In a first step the relative energy positions (i.e. the binding energy

the sum of the χ^2 ($\chi^2 = \sum_n (I_{\text{exp}} - I_{\text{fit}})^2 / I_{\text{exp}}$) was minimized to obtain the best fit result. This result yielded the following energetic order: the C3 peak at the lowest binding energy,

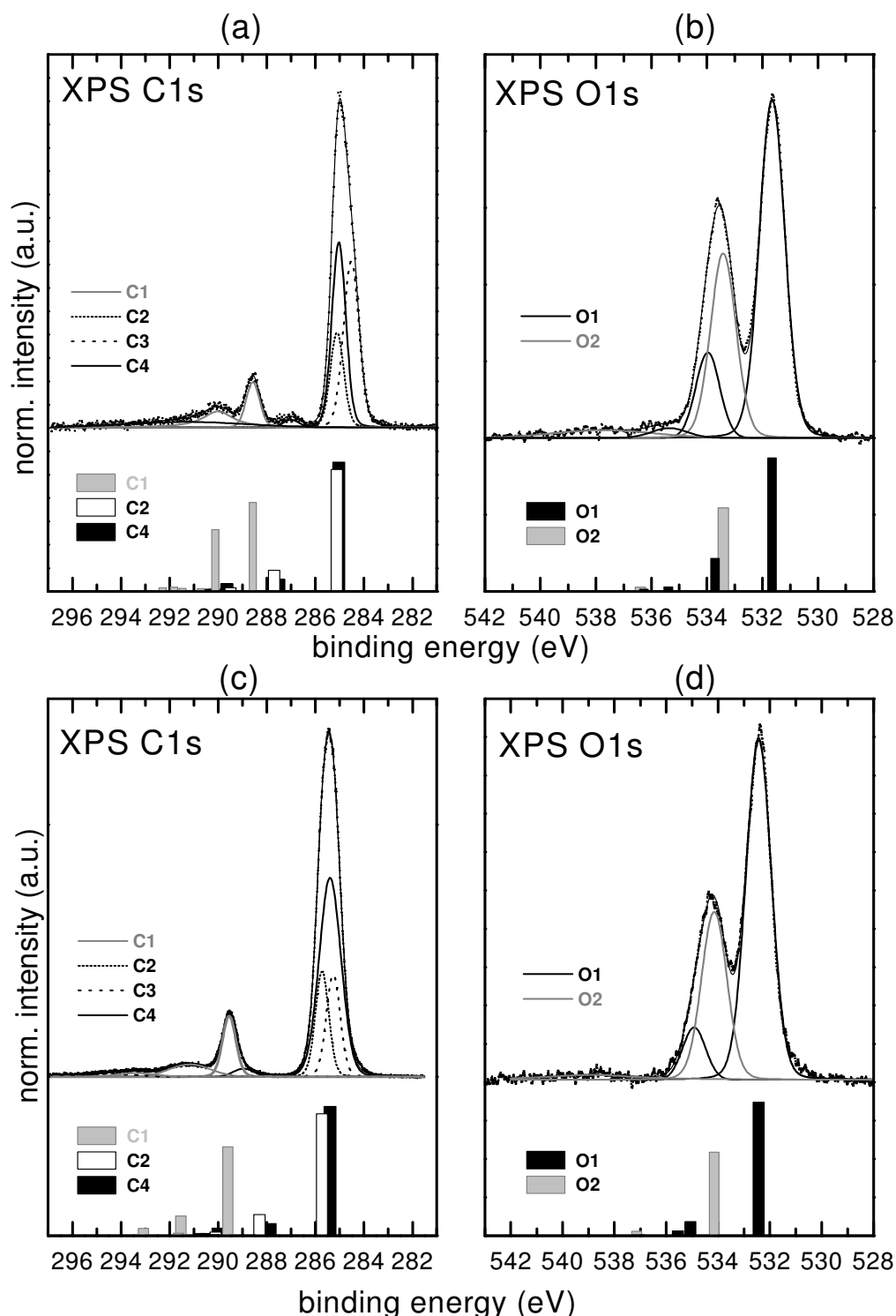


Figure 4.3.3: Comparison of experimental XPS data with peak fit results for PTCDA ((a): C 1s, (b): O 1s) and NDCA ((c): C 1s, (d): O 1s) and with SDCI calculations by Jung et al. [137]. The calculated spectra were obtained for molecules with two adjacent neighbours, thus simulating the condensed phase. They were shifted in energy to adjust the calculated to the experimental energies for the ionic ground state (at lowest binding energy) and are plotted as bar graphs in the lower part of each frame. For C 1s excitation the C3 atoms do not show significant satellite intensities.

followed by C4 and C2. The corresponding fit and experimental spectra are plotted in Figure 4.3.2. The ionisation potentials of the various ring carbon species of the five molecules are summarized in Table 4.3.1.

The different core binding energies are the result of local differences in the charge density in the initial (and perhaps also final) state. The electron withdrawing effect of the oxygen atoms of the functional group does not only lead to a strongly decreased electronic density and therefore higher binding energy of the functional group carbon C1, but apparently also affects the C2 atoms, which link the functional groups to the aromatic core. These show the highest C 1s binding energy of the ring carbons. This effect seems to be smallest for the C4 atoms in the middle of the aromatic system. Our results of the different C1s binding energies are in good agreement with similar experiments in literature, e.g. on various polymers in Ref. [139].

Satellite features:

Satellites can easily be distinguished in the spectra of Figure 4.3.1. These can be assigned to shake-up processes that are caused by (additional) excitations of valence electrons upon the sudden creation of a core hole. They are thus described by two-hole-one-particle states (2hp).

The shake-up process is usually described in the so-called sudden approximation, i.e. the photoemission process is considered to be so fast ($\tau \sim 10^{-17}$ s) that no significant changes of the initial state wave functions occur on that timescale. The transition matrix elements M_{if} for the photoemission process can then be written as (see also Chapter 2.1, equation (2.11)):

$$M_{if} = \langle \psi_f | \vec{e} \cdot \hat{p} | \psi_i \rangle = \langle \phi_{f,k} | \vec{e} \cdot \hat{p} | \phi_{i,k} \rangle \langle \psi_{ijk}^{ion}(n-1) | \psi_k^R(n-1) \rangle \quad [25] \quad (4.3.1)$$

The first factor on the right hand side is a one-electron transition matrix element that describes the transition of electron k to a continuum state (ionisation). The shake-up intensity is governed by the second factor, the projection of the created 2hp-ion state ψ_f onto the frozen hole state ψ_i . If the overlap of the frozen core hole state and the ionic ground state is high, most of the intensity will go into the main (unshifted) photoemission line. However, if this overlap is low we can expect relatively high intensities of excited ionic final states, that appear as shake-up satellites in the photoemission spectra at higher binding energies. For an exact determination of the satellite positions and intensities additional information, e.g. from SDCI calculations [137], is very helpful. This semi empirical approach considers up to doubly excited states by a CNDO/S-CI or INDO/S-CI calculation.

Figure 4.3.3 shows the calculated XPS C1s and O1s satellite spectra for PTCDA (Figures 4.3.3a + b) and NDCA (Figures 4.3.3c + d) from Jung et al. [137] together with the peak fit results for the experimental data. The calculated spectra, plotted as bar graphs, were shifted in energy to align calculated and experimental energies of the peaks with lowest binding energy.

For the O 1s spectra of the anhydrides (Figures 4.3.3b + d) the calculations show clearly, that shake up satellites of the O1 peak are buried under the O2 photoemission peak. In complete agreement, a fit of the experimental data with only two peaks does not lead to an acceptable result, since the ratio of the peak areas is far from the demanded value of 2:1. Thus the good fit results presented in Figures 4.3.3b and f were obtained by fits with 5 and 4 peaks for PTCDA and NDCA, respectively, according to the main contributions (main peaks and satellites) predicted by the calculations. For PTCDA two satellites for O1 and 1 satellite for O2 were used, and the constraints were set to reflect the stoichiometry as mentioned above (O1 + satellites : O2 + satellite = 2:1). For NDCA one satellite peak was allowed for each photoemission line.

Backed by the information of the very accurate calculations, a detailed peak fit analysis is possible in this case. In Figure 4.3.4 the peak fit results for the O 1s data of all 5 molecules can be compared. The results are also given in Table 4.3.1. For all molecules, the spectra contain relatively intense shake-up lines for both oxygen atoms, which are due to HOMO-LUMO shake-up excitations. The high intensity of the O1 satellite allows a particularly good fit result and provides good energy values for the HOMO – LUMO transition upon O1

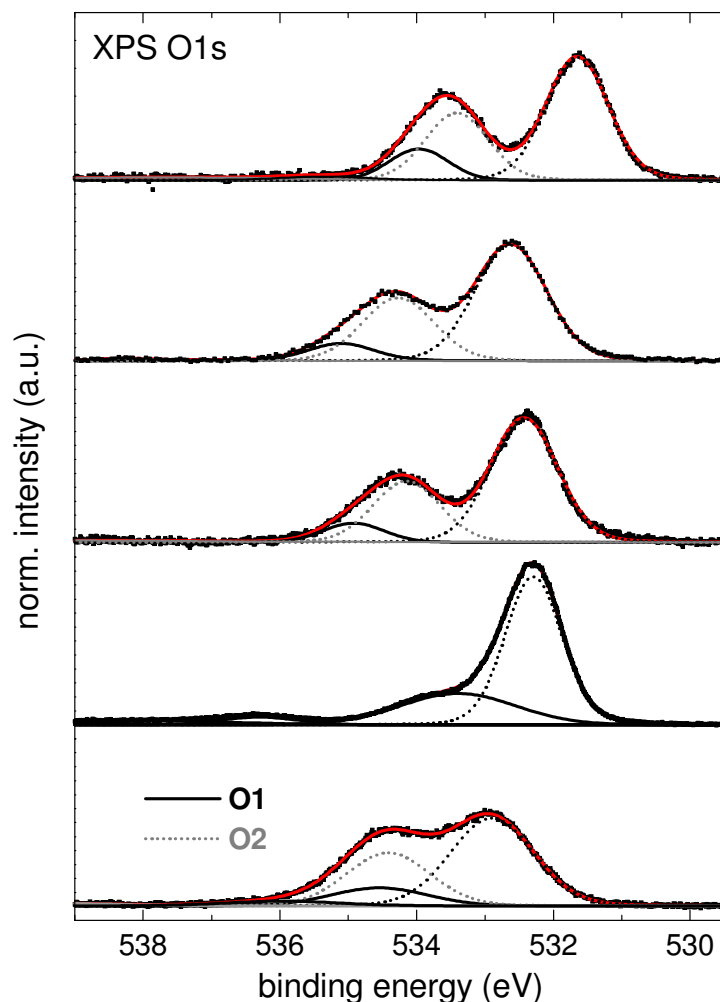


Figure 4.3.4: Results of the peak fitting analysis of the O 1s spectra. Experimental data is displayed as points, the fitted main lines as dotted lines, and fitted satellite peaks as straight lines.

excitation for all investigated molecules. The values are very similar for the molecules PTCDA (2.32 eV), NTCDA (2.48 eV) and NDCA (2.50 eV) since for these molecules the local electronic environment of the anhydride group is very similar.

For BPDCA the rather low value of 1.65 eV must be the result of the more localized nature of the electronic system at the functional group, as derived above from the relative binding energies.

For ANQ we find the first satellite at 1.11 eV higher binding energy relative to the main line and with a relatively high intensity if compared to its anhydride counterparts. Additional satellites are clearly visible for this molecule at 4.01 and 5.95 eV higher binding energy, that can also be attributed to shake-up excitations. As expected, the local electronic structure seems to be very different for this functional group. A more detailed assignment of the satellite spectra would require information from appropriate calculations.

For the C 1s spectra (Figures 4.3.3a + c) it is an interesting result of the calculations, that the C3 atoms do not show a significant satellite intensity. This is the result of a rather big overlap of the wave function of the frozen core hole state with that of the ionic ground state as discussed earlier. Thus most of the spectral intensity appears in the main photoemission line. In other words this means, that the response of the electronic system upon core hole creation is rather small or equally distributed over the entire molecule.

The shake-up excitation of an electron into an unoccupied state will be very favourable if it helps to transfer charge as to screen the core hole and thus to stabilize the created ion.

Therefore an intense shake-up satellite indicates a favourable charge redistribution in the corresponding excited ionic state for an optimum core hole screening. Satellite intensities hence are very sensitive to the donor-acceptor strength in the investigated molecule. Roughly speaking, a satellite will be very intense if a part of the molecule can act as a strong electron donor, thus helping to stabilize the ion by charge transfer towards the core hole [134].

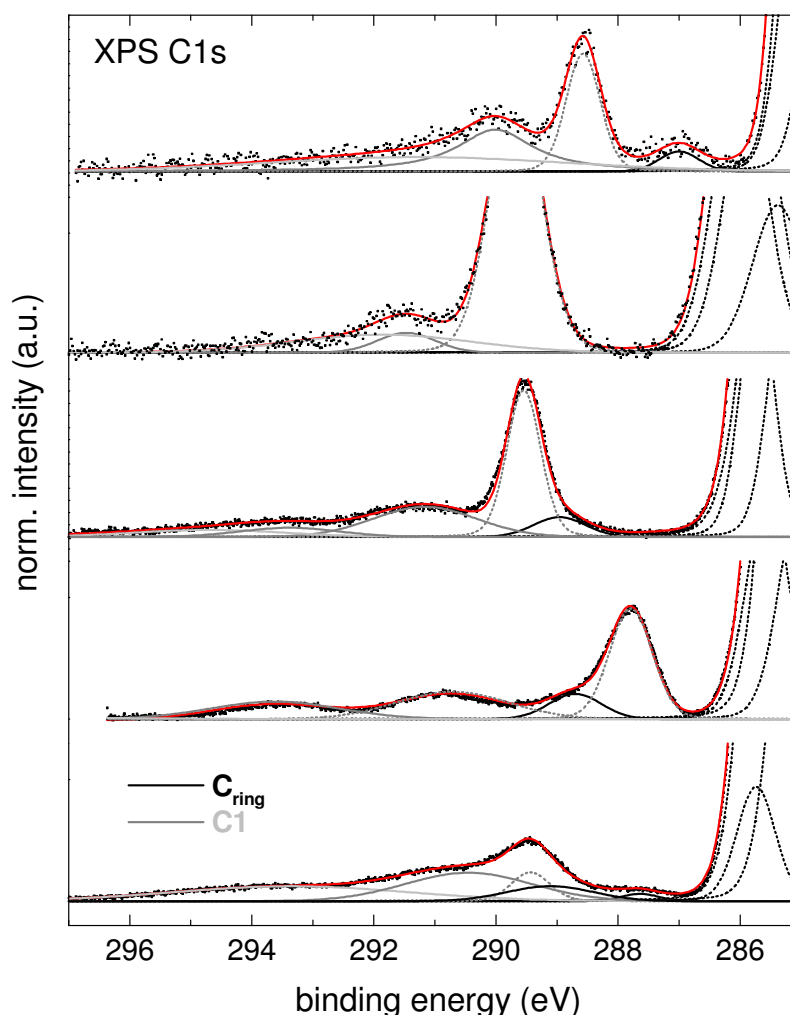


Figure 4.3.5: Peak fitting analysis of the satellite region of the C 1s spectra. The spectra were magnified by a factor of 4 to allow a better view of the low-intensity structures. Experimental data is displayed as points, fitted photoemission lines as dotted lines, and fitted satellite peaks as straight lines.

This well described effect can be observed in our experimental data if we compare, e.g., the C 1s shake-up satellite intensities for PTCDA and NTCDA in Figure 4.3.5: both, the anhydride and the ring carbon peaks have more intense satellites for the PTCDA molecule due to the higher donor strength of the perylene core.

If we keep the same aromatic naphthalene system and compare NTCDA and NDCA (Figure 4.3.5) we observe a relative increase of satellite intensity for the NDCA molecule. This effect has to be attributed to the polarity of the NDCA molecule and was observed for similar

organic compounds in the condensed phase before. Freund *et al.* [134] explained their equivalent observations for para-nitroaniline (PNA) and nitroso-benzene with particularly strong intermolecular screening effects for polar molecules in the solid state.

The SDCI calculations of Jung *et al.* [137] showed considerable intermolecular contributions to the shake-up satellite intensities also for PTCDA. For PTCDA as well as for NDCA the calculations only fit the experimental data if the molecular surrounding was taken into account by a sandwich geometry of 3 molecules. This observation indicates, that the interaction of these molecules in the condensed phase is beyond a pure van-der-Waals type.

	PTCDA			NTCDA			NDCA			ANQ			BPDCA		
	E _B (eV)	W _G (eV)	I _{rel.}	E _B (eV)	W _G (eV)	I _{rel.}	E _B (eV)	W _G (eV)	I _{rel.}	E _B (eV)	W _G (eV)	I _{rel.}	E _B (eV)	W _G (eV)	I _{rel.}
C1 (C=O)	288,57	0,61	0,07	289,67	0,94	0,24	289,54	0,56	0,09	287,79	0,76	0,08	289,43	0,70	0,02
C2 (C-CO)	285,11	0,61	0,15	286,00	0,94	0,26	285,72	0,56	0,15	285,55	0,76	0,17	285,74	0,70	0,08
C3 (C-C)	284,52	0,71	0,30	285,38	0,94	0,13	285,26	0,58	0,15	285,01	0,76	0,17	285,03	0,84	0,39
C4 (C-H)	285,03	0,63	0,30	285,80	0,94	0,26	285,39	1,05	0,46	285,17	0,80	0,50	285,57	0,79	0,39
Sat_{ring}	287,00		0,01	-	-	0	289,54		0,09	288,70		0,02	287,64 289,11		0,005 0,02
Sat_{C1}	290,01		0,08	291,47		0,02	291,17 293,38		0,05 0,02	290,71 293,62		0,05 0,04	290,45		0,06
Chi²	4,19 · 10 ⁻⁶			3,04 · 10 ⁻⁵			1,04 · 10 ⁻⁵			5,39 · 10 ⁻⁶			3,64 · 10 ⁻⁶		
O1 (O=C)	531,65	1,03	0,53	532,63	1,19	0,57	532,43	1,10	0,57	532,29	0,92	0,58	532,90	1,38	0,49
O2 (C-O-C)	533,41	1,03	0,29	534,27	1,19	0,31	534,15	1,10	0,28	-	-	-	534,41	1,38	0,30
Sat_{O1}	533,97 535,35		0,12 0,02	535,11		0,08	534,93		0,08	533,40 536,30 538,24		0,24 0,04 0,06	534,55 535,97		0,11 0,03
Sat_{O2}	537,72		0,05	538,24		0,02	538,88		0,04	-	-	-	539,41		0,02
Chi²	5,20 · 10 ⁻⁵			2,38 · 10 ⁻⁵			6,07 · 10 ⁻⁵			7,62 · 10 ⁻⁶			2,14 · 10 ⁻⁵		

Table 4.3.1: Fit results for the energy positions, relative intensities and linewidths of the photoemission and satellite lines in the C1s and O1s XPS spectra of PTCDA, NTCDA, NDCA, ANQ and BPDCA.

4.3.3 Concluding discussion

The XPS data presented here show distinct systematic differences for the rather similar molecules PTCDA, NTCDA, NDCA, ANC and BPDCA. The spectra therefore provide unambiguous fingerprints for the corresponding substances.

The high quality of the photoemission data and a detailed peak fit analysis enabled us to determine the binding energies of the chemically different ring carbon atoms and the assignment of additional satellite structures. Thereby, these five molecules represent ideal model systems to study fundamental aspects of core-level spectroscopy, such as initial and final state effects as well as satellites that arise from the influence of the intramolecular and intermolecular electronic density distribution in both, the ground state and the core-ionized excited state.

Thus, the reaction of the electronic system upon ionisation leads not only to remarkable peak shifts but also to further excitations among the electrons of the valence levels, which appear in the spectra as shake-up satellites. There are various influences on the satellite intensities, that can be divided into two groups: firstly intramolecular contributions, that determine the ability of the molecular electronic system to react on the core-hole creation, such as the donor-acceptor strength, and secondly intermolecular contributions, that are responsible for the influence of the molecular surrounding on the electronic response in the condensed phase.

Finally, we emphasize that the present results prove the importance of taking satellites into account if a quantitative analysis of organic compounds is attempted because otherwise the stoichiometry would come out incorrect and inconsistent. Furthermore, an understanding of relative peak shifts and satellite intensities for organic molecules in different chemical or physical environment is needed to arrive at correct qualitative and quantitative conclusions if, e.g., molecules are brought into contact with each other, with other molecules, with surfaces or with solutions. Moreover, subtle changes within a large molecule due to environmental influences may be used for further insight into structural or electronic details, but such conclusions require a detailed fine structure analysis as provided here.

4.4 Bonding and screening influences on the line shapes of NTCDA monolayers on Ag(111) as revealed by high-resolution photoemission

4.4.1 Motivation

The interactions between organic molecules and inorganic substrates or contacts is of basic interest due to their influences on the interface properties of hybrid systems, which are used in many different applications or electronic devices like, e.g., organic light emitting diodes (OLEDs) [1], displays, organic field effect transistors (OFETs) [4] and organic based sensors [140]. Charge-carrier injection from metal contacts into the organic semiconductor plays a crucial role, and thus the electronic structure of these systems is essential and has attracted the attention of many researchers over the last decades [12,13]. Numerous studies have been performed for various metal-organic combinations with particular emphasis on the chemical bond and the electronic properties, e.g. the formation of an electric dipole layer, the so-called interface dipole [141-145].

The major advantage in using organic thin films is the possibility to tailor the properties in a wide range by the proper choice of the molecule, the inorganic material and the preparation conditions [8]. In the present stage, model systems play a key role in the understanding of the interface properties. We have chosen the heteroaromatic molecule NTCDA (1,4,5,8-naphthalene-tetracarboxylic acid dianhydride) adsorbed on a (111)-oriented Ag single crystal to learn more about the model interface and especially on the potential of high-resolution x-ray photoelectron spectroscopy for such studies. Previous experiments in our group have shown the possibility of a temperature-induced manipulation of the molecular orientation for NTCDA (films from flat-lying to an almost perpendicular orientation with respect to the surface plane [146] and the influence of the changed layer morphology on the electronic structure [147]). Also, a strong dependence of the substrate – adsorbate bonding on the substrate material and the orientation of the substrate surface could be demonstrated for NTCDA monolayers on various Ag, Cu and Ni surfaces using UV-photoemission spectroscopy (UPS) and near-edge x-ray absorption fine structure (NEXAFS) [148].

NTCDA on Ag(111) is particularly interesting since at room temperature three different NTCDA monolayer structures are known: depending on the molecular density within the monolayer a compressed and a relaxed structure, denominated CM and RM in the following, could be identified by LEED and STM measurements [66,149]. The RM refers to a commensurate superstructure with the superstructure matrix $\begin{pmatrix} 4 & 0 \\ 3 & 6 \end{pmatrix}$ and two molecules per unit cell and exists for coverages of $\theta < 0.8$ ($\theta = 1$ refers to saturation coverage). For higher coverages ($\theta > 0.8$) the compressed monolayer is built and was identified as point-on-line superstructure with the matrix $\begin{pmatrix} 3.97 & 6.52 \\ -2.98 & 0.58 \end{pmatrix}$ by recent SPA-LEED measurements [65]. An

intermediate structure (RM₂) can be observed for $\theta \approx 0.8$, that is similar to the RM structure, but has one unit cell vector that is 4 % shorter. The corresponding superstructure matrix is $\begin{pmatrix} 3.83 & 0 \\ 3 & 6 \end{pmatrix}$ [65]. An additional monolayer modification, denominated LT in the following, can be prepared if the RM is cooled down to low temperatures ($T < 160$ K). For this LT structure, which was first observed by L. Kilian [65], no LEED spots can be observed. Also for the CM structure an analog low temperature phase exists (C-LT), that does not show any LEED spots. The monolayer structures can be reversibly transformed by adsorption or desorption of molecules (RM/CM or CM/RM) or by changing the sample temperature (RM/LT or CM/C-LT). The latter phase transition will be discussed in detail in Chapter 4.5. Furthermore, it is noteworthy for the discussion below, which will particularly address the interfacial bonding of NTCDA on Ag(111), that intact molecules are desorbed if the sample is heated to 440 K [66].

In this chapter (submitted for publication in the *Journal of Physical Chemistry* [150]) we present a high-resolution x-ray photoemission study on different NTCDA monolayer films on the Ag(111) surface. It is most interesting that the photoemission spectra of the molecules chemisorbed in different structural modifications (RM, CM or LT) which are interrelated by a reversible structural phase transition only, show distinct differences. The high quality of the data and a detailed peak fit analysis enable us to determine the energetic positions of all different carbon and oxygen atoms as well as a number of intense satellites, that are due to intramolecular multi-electron relaxations (shake-up satellites) and/or due to charge-transfer screening between the substrate and the adsorbed molecule. Shake-up satellites have been investigated and classified for molecules in the gas phase [151-154] and various adsorbates in detail [155-160]. Also for organic molecules, these satellites have been intensely studied in the gas phase and the solid state by both, experimental [134,135] and theoretical methods [136,137]. They allow further insight into the intramolecular and interfacial reactions of the electronic system during the excitation process. Strong differences of the intensities of these features between the different atoms and between the different monolayer modifications indicate differences of the local charge-transfer screening within the molecule and provide interesting information on the bonding mechanism for the different films.

4.4.2 Results and discussion

Figure 4.4.1 shows the C 1s (a) and O 1s (b) XPS spectra of condensed NTCDA multilayers (thickness ~ 20 layers) compared to the three different monolayer films mentioned before. In Figure 4.4.1b the molecular structure of the NTCDA molecule is displayed and the chemically different oxygen (O1 and O2) and carbon atoms (C1 – C4) are indicated.

The C 1s and O 1s multilayer spectra were multiplied with a factor of 0.33 and 0.06, respectively, to allow a better comparison with the monolayer data. A detailed analysis of the multilayer spectra was presented in Chapter 4.3. In the C 1s data (spectrum 1.1), the low energy peak belongs to the ring carbon atoms (C2 – C4) and the peak at 289.7 eV to the anhydride carbon C1. The small peak at 291.7 eV is a HOMO – LUMO shake-up satellite of the C1 peak. The O 1s data (spectrum 1.5) show two peaks that can be attributed to the O1 (532.6 eV) and the O2 oxygen atoms (534.4 eV). A O1 HOMO – LUMO shake-up satellite at 535.1 eV is buried underneath the O2 peak.

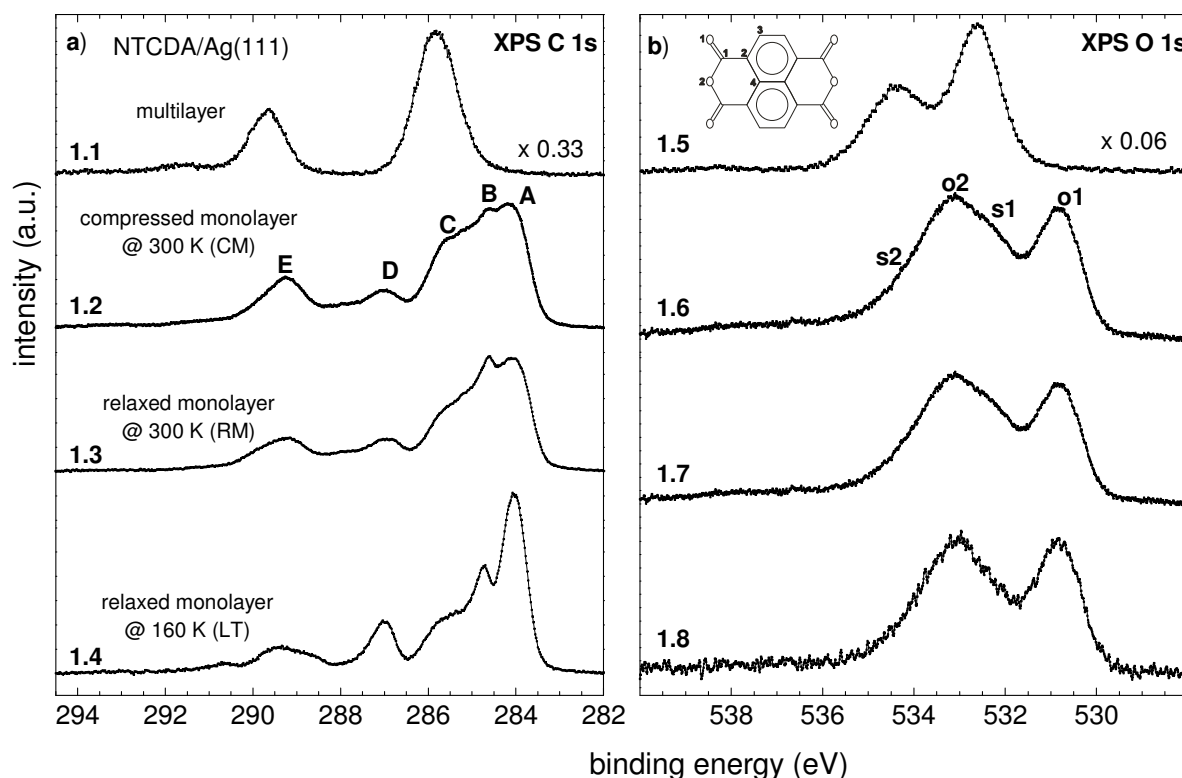


Figure 4.4.1: (a) C 1s and (b) O 1s XPS spectra of NTCDA monolayers on Ag (111), recorded with a photon energy of 335 eV (C 1s) and 700 eV (O 1s), respectively (analyser pass energy 40 eV in all cases). The spectra of three different monolayer structures are presented: compressed monolayer CM (spectra 1.2. and 1.6), relaxed monolayer RM (spectra 1.3 and 1.7) and the low temperature (LT) modification of the RM layer (spectra 1.4 and 1.8). For details on the preparation and the structure of the films (see text). Top (spectra 1.1 and 1.5): the multilayer spectra from Chapter 4.3 are plotted, multiplied by a factor of 0.33 and 0.06, respectively, for comparison. In Figure 4.4.1b a scheme of the NTCDA molecule is displayed and the chemically different oxygen (O1 and O2) and carbon atoms (C1 to C4) are labelled.

For all monolayers we observe strong changes of the spectra as compared to the weakly coupled multilayers due to the interaction with the Ag(111) surface. Thus we must in each case conclude a distinct chemisorptive character of the substrate – adsorbate bonding. This finding is consistent with all other spectroscopic data, e.g. from UPS [65,66], NEXAFS [161] (see also Chapter 4.5) and HREELS [162].

A strong shift of the ring carbon peak towards lower binding energy from multilayer to monolayer is visible in the C 1s spectra in Figure 4.4.1a. This shift (about 2 eV from 286 eV to 284 eV for the peak maximum) is mostly due to the additional screening of the core hole by charge transfer from the metal substrate. The ring carbon peak shows further fine structure for all monolayers, namely two well resolved peaks, denominated (A) at 284 eV and (B) at 285 eV, that can be attributed to different ring carbon atoms, and a broad shoulder (C) at the high energy side.

The peak (D) at 287 eV can be attributed to the anhydride carbon and is shifted by nearly 3 eV with respect to the multilayer. This relatively big shift indicates, that the functional group carbon, which is least screened in the molecule due to the strong electronegativity of the oxygen atoms in the anhydride group, profits most from the additional screening channel in

the interfacial state. At higher energies a wealth of satellite peaks, e.g. peak (E) at 289 eV, is resolved, that will be analysed and assigned later. It will also be shown that (E) is not the remnant of the anhydride peak at 289.5 eV in the multilayer.

Interestingly, the spectra of all monolayers basically show the same spectral features at similar energetic positions, but with drastically different intensities. If we compare the RM with the CM species, the about 20 % lower coverage mainly leads to a lower intensity of the shoulder (C) at 286 eV and the satellite peak (E) at 289.5 eV.

If the RM film is cooled down to 160 K, resulting in the LT structure, the relative intensities in the C 1s data change drastically. Again, the 286 eV shoulder (C) and the 289.5 eV peak (E) decrease, but at the same time the photoemission lines (A) at 284 eV and (D) at 287 eV strongly increase. These striking differences in the core level spectra indicate strong differences in the bonding mechanism to the substrate for the monolayers at different substrate temperatures (RM – LT).

The O 1s data (Figure 4.4.1b) of the NTCDA monolayers are dominated by two peaks, that can be attributed to the two oxygen atoms in different bonding situations in the functional group, in analogy to the multilayer. As observed before in the C 1s data (Figure 4.4.1a), the monolayer lines are shifted towards lower binding energies. However, within the functional group the screening effect on the oxygen core states is smaller as compared to the anhydride carbon, indicated by the smaller energy shift of 2 eV and 1.5 eV for the O1 (o1 line) and O2 oxygen atoms (o2 line), respectively.

For all monolayers the intensity ratio between the O1 and the O2 peak is far from the stoichiometric value of 2 : 1. This is easily explained by an intense satellite of the O1 peak that contributes to the intensity of the peak at 533 eV. This satellite is responsible for the shoulder (s1) at 532.5 eV, that is clearly visible in the CM and RM data (spectra 1.6 and 1.7, respectively). The shape of the O2 peak at the higher energy side indicates, that at least one further satellite (s2) has to be considered around 534 eV.

The differences in the O 1s data between the monolayers are in complete analogy to what we observed for the C 1s spectra. The energetic positions of the spectral features for the different monolayer states are almost unchanged, whereas a decrease of the intensity of the satellite peak (s1) at 532.5 eV from CM to RM and from RM to LT mainly accounts for the changes in the O 1s spectra of the different monolayer films.

Peak fit analysis:

To further analyse the various spectroscopic features, i.e. to distinguish and assign the photoemission lines and satellite structures and to define their energetic positions, a detailed least-square peak fit analysis was performed for the C 1s and O 1s spectra of Figure 4.4.1.

O 1s spectra:

The smaller number of spectral features that originate from only two chemically different oxygen species makes the O 1s data easier to interpret. Spectrum 2.1 in Figure 4.4.2 shows the fit result of the multilayer O 1s spectrum (see Chapter 4.3, Figure 4.3.2). The peaks at 532.6 eV and at 534.2 eV can be attributed to the photoemission lines of the O1 and O2 atoms. At 535.2 eV an intense HOMO-LUMO shake-up satellite of the O1 peak is visible. An additional Gaussian function was applied to account for the background at about 538 eV, that is due to various shake-up losses of both photoemission lines.

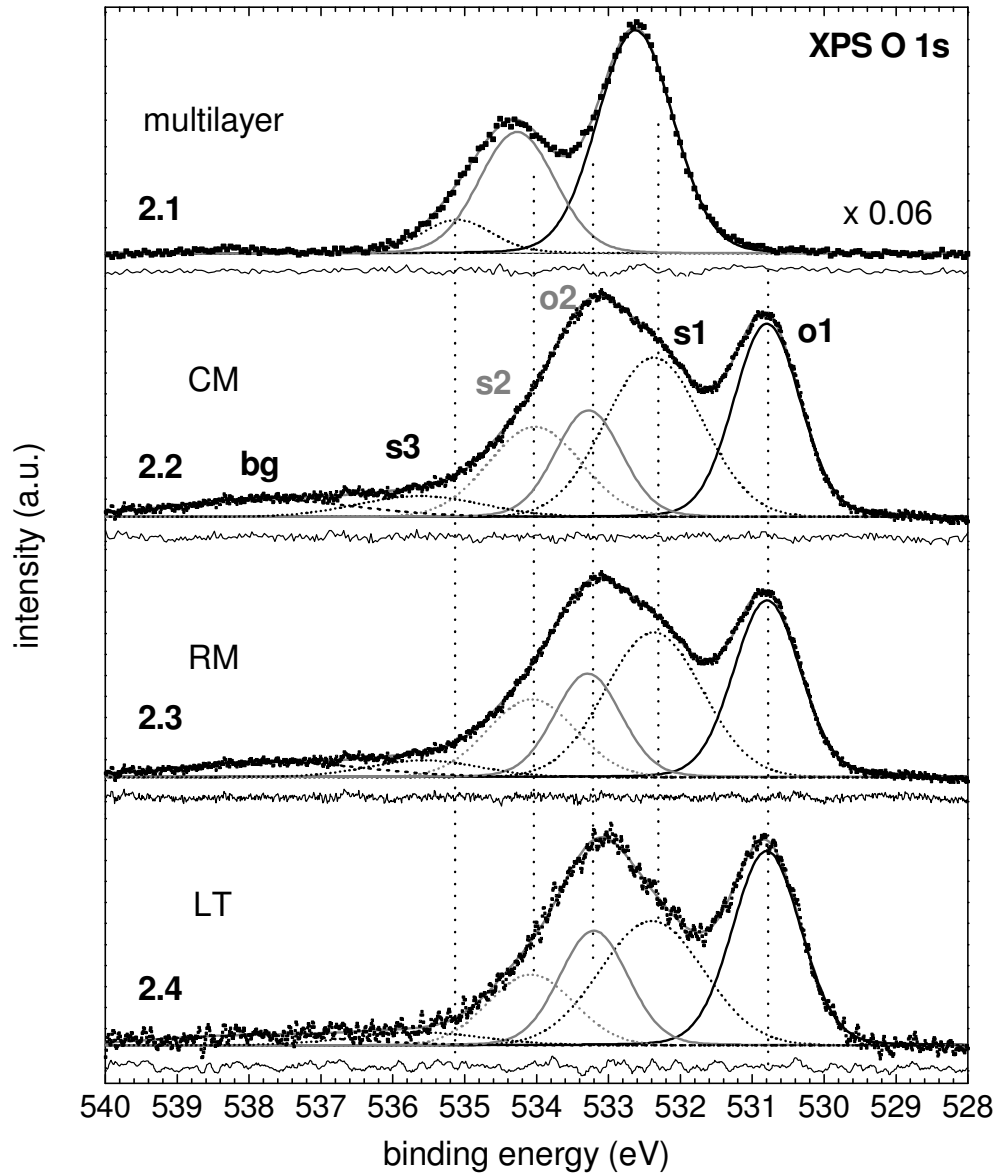


Figure 4.4.2: Result of the peak fit analysis of the O 1s spectra of the NTCDA compressed monolayer (CM, spectrum 2.2), relaxed monolayer (RM, spectrum 2.3) and low-temperature monolayer (LT, spectrum 2.4). The multilayer fit (spectrum 2.1) from Figure 4.3.2 is plotted for comparison. For the main peaks (o1) and (o2) Voigt functions with fixed Lorentzian width of 0.1 eV and equal Gaussian width were used. The satellites (s1), (s2) and (s3) as well as the background (bg) are accounted for by Gaussian peaks. The intensities are constrained by the stoichiometry of atoms in NTCDA to $(o1 + s1 + s3 + \frac{2}{3}bg) : (o2 + s2 + \frac{1}{3}bg) = 2$. The residua are plotted below the spectra.

A minimum number of six peaks is needed to satisfyingly reproduce the monolayer O 1s spectra, as can be directly concluded from the experimental data: the O1 photoemission line at 530.8 eV (o1), the O1 satellite (s1), that due to intensity reasons can be attributed to the intense shoulder at 532.4 eV, the O2 photoemission line at 533 eV (o2), a satellite peak at 534 eV (s2), that for stoichiometric reasons has to be attributed to the O2 peak, plus two more peaks between 535 eV (s3) and 538 eV (bg), that generate the line shape of the spectra at higher energies.

Thus various constraints can be used to reduce the number of free parameters in the fit function. For the main lines Voigt profiles are used with a constant Lorentzian line width of 0.1 eV^{*} and equal (fitted) Gaussian line widths. All satellite peaks are represented by Gaussian functions. Stoichiometry demands, that the intensity ratio of the O1 and O2 main lines plus their satellites has to be equal to two ($(o1 + s1 + s3 + \frac{2}{3}bg) : (o2 + s2 + \frac{1}{3}bg) = 2$).

Note, that the satellite s3 can be attributed to O1, as will become clear later. The area of the background Gaussian peak (bg) is included in the intensity ratio of O1 and O2 with a fraction of 2:1 since no detailed knowledge is available on the origin. However, from shake-up calculations [137] it is known that several weak satellites from both oxygen atoms arise in this energy range.

	CM			RM			LT		
	E _B (eV)	A	Γ _G (eV)	E _B (eV)	A	Γ _G (eV)	E _B (eV)	A	Γ _G (eV)
o1	530.80	0.28	1.03	530.79	0.25	1.04	530.80	0.28	1.06
o2	533.29	0.15	1.03	533.29	0.15	1.04	533.20	0.17	1.06
s1	532.37	0.32	1.59	532.37	0.29	1.58	532.40	0.27	1.69
s2	534.03	0.17	1.52	534.07	0.14	1.45	534.08	0.12	1.40
s3	535.62	0.05	2.04	535.57	0.04	1.82	535.66	0.03	2.15
bg	537.84	0.07	3.01	537.71	0.06	3.01	537.96	0.04	3.01
χ²	1.23*10 ⁻⁵			1.23*10 ⁻⁵			1.92*10 ⁻⁵		

Table 4.4.1: Results of the least-square peak fit analysis of the NTCDA O 1s monolayer spectra from Figure 4.4.2. The parameters are the binding energy E_B, the peak area A, the Gaussian width Γ_G of the fitted peaks as well as the fit quality χ². For a detailed peak assignment see text.

In Figure 4.4.2 the result of a peak fit deconvolution of the monolayer O 1s data using these constraints is displayed. The corresponding residua (plotted underneath each spectrum) show the excellent quality of the fit results. The energy positions, intensities and line widths of the fitted peaks are summarized in Table 4.4.1 together with the χ² values ($\chi^2 = \sum_n (I_{\text{exp}} - I_{\text{fit}})^2 / I_{\text{exp}}$) of the corresponding optimal fit which are a measure of the fit quality. The dotted guidelines in Figure 4.4.2 indicate, that between the different monolayer

* Values of 0.1 eV for the lifetime broadening of the O 1s and 0.08 meV for the C 1s core hole were determined from the NEXAFS data of NTCDA and the similar molecules ANQ and BPDCA in Chapter 4.2. No indications for a different lifetime for the 1s states in the NTCDA monolayers were found in this work and previous XPS experiments on NTCDA and similar molecules (see Chapter 4.3).

structures only minor changes of the energy positions of the spectral features occur. Note that the similarities of the peak energies of the different adsorbate states are an indicator for both, the correctness of the fit result, since the peak energies were optimised independently in the fit, and the similarity of the chemical state.

The chemisorption process involves the hybridisation of the delocalised molecular π -system with metal states. The resulting hybrid-orbitals differ in their character; they may have more metal or more adsorbate character. The latter can more effectively screen the adsorbate core hole, since they have a stronger electron density on the molecule. This results in a lower binding energy of the observed photoemission line. Thus, we can assume that the same orbitals are involved in the screening process for all monolayer modifications, resulting in generally the same binding energies of the spectral features.

The very intense satellites (s1) and (s2) are typical for the photoemission spectra of weakly chemisorbed molecules and are well understood, e.g. for CO on metal substrates [155]. Different theoretical approaches have been used to explain these features, e.g. by Bagus, Hermann and Seel (BHS) [163-167], by Messmer et al. [30] and by Schönhammer and Gunnarsson (SG) [168-170]. It is commonly agreed, that the charge transfer from the substrate, that follows the core excitation to screen the core hole, leads to different lines in the photoemission spectra. The line at lowest binding energy belongs to the well- or fully screened core state (sometimes also referred to as “shake-down” satellite), whereas the lines at higher binding energies can be attributed to unscreened or poorly screened final states. The latter can be observed with very high intensities if the photoemission process and the charge transfer from the substrate occur on the same timescale [155,171], which is the case for weak chemisorption or physisorption. The energy of the poorly screened lines is very similar to the energy of the multilayer peaks, since in both cases only intramolecular screening processes are important. In the following, we will refer to the well- or fully screened lines at lowest

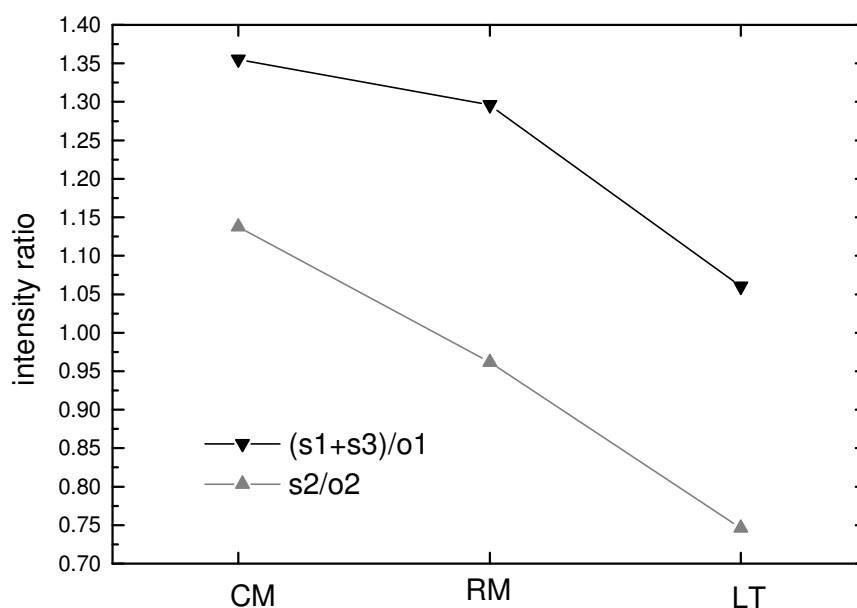


Figure 4.4.3: Intensity ratio of the satellite and main lines of the two different oxygen atoms O1 and O2, $(s1+s3)/o1$ and $s2/o2$, respectively, for the three different monolayers CM, RM and LT.

binding energy as main lines, since for the present example these lines are generally most intense.

The assignment of (s1) and (s2) to poorly screened core states strongly suggests the interpretation of (s3) as shake-up satellite of the poorly screened O1 state (s1), in analogy to the multilayer spectra. This was anticipated in the intensity constraints for the fit analysis of the O 1s data but even if this tentative assignment was incorrect, the final result would hardly be changed.

It is very interesting, that the relative intensities of the main and satellite peaks show distinct changes for the different monolayers. This is demonstrated by Figure 4.4.3, where the intensity ratios of the O1 and O2 main lines (o1 and o2, respectively) and their satellites (s1+s3 and s2, respectively) are plotted for the three preparations. The satellites are more intense than the main lines for the CM structure, but their relative intensity decreases for the RM structure. For the LT layer the satellite intensities are about equal to the main line for O1 and smaller than the main line for O2.

The changes of the satellite intensities can be explained by changes in the timescale of the charge transfer of the screening process from the Ag substrate and hence by subtle changes in the strength of the interface coupling. The time that is needed to transfer substrate electrons to the NTCDA molecule, or more accurately to reorganize the whole electronic system, to screen the core hole is apparently shortest for the LT structure, resulting in a relatively small intensity of the poorly screened compared to the well-screened states. A significant increase of the adsorbate-substrate coupling must be responsible for this observation.

C 1s spectra:

A complete analysis of the more complicated C 1s data is not as easy and straightforward as for the O 1s data. A number of 4 distinguishable carbon atoms (labelled C1-C4 in the inset in Figure 4.4.1) causing different C 1s main lines and satellites has to be considered, leading to the rich spectra 1.2-1.4 with various peaks and shoulders presented in Figure 4.4.1. We will try in the following to understand and assign the most prominent features in the C 1s data by a comparison of the different monolayer spectra and the pre-information from the analysis of the O 1s data.

We will start with the LT spectrum (4.4 in Figure 4.4.4), which shows the best resolved lines. If we integrate all the peaks in spectrum 4.4 on the right (A1) or left side (A2) of the minimum at 286.5 eV and calculate the intensity ratio A1/A2 we find 2.47, which is very close to the stoichiometric ratio of 2.5 between naphthalene ring (10) and functional group carbon atoms (4). Thus the assumption appears obviously justified, that the intensity between 283 eV and 286.5 eV can be attributed to the ring carbon atoms C2 – C4, i.e. their main and satellite lines, whereas all features above 286.5 eV belong to the anhydride atoms (C4). The small deviation from the stoichiometric ratio is most likely due to additional weak satellites of the naphthalene carbon atoms that are buried underneath the anhydride peaks. These are less important and will not change the results significantly, and hence are omitted in the fit analysis. We can further assume the same line shape for all main lines, since firstly, previous XPS [132] and NEXAFS [85,128] experiments on NTCDA and similar molecules showed the same lifetime broadening for the different carbon atoms, and secondly there is no obvious reason for differences in the Gaussian line widths, since the experimental resolution and inhomogeneous broadening should be equal.

Thus, for the naphthalene part the peaks (A) at 284 eV and (B) at 285 eV have to be attributed to the main lines of the atoms C2 – C4, the broad shoulder (C) at 286 eV to their satellites. On

the higher energetic side of the spectrum we can identify the anhydride C1 photoemission line at 287 eV followed by several anhydride satellites at higher energy.

As mentioned earlier, a comparison of the C 1s monolayer spectra clearly shows the strong

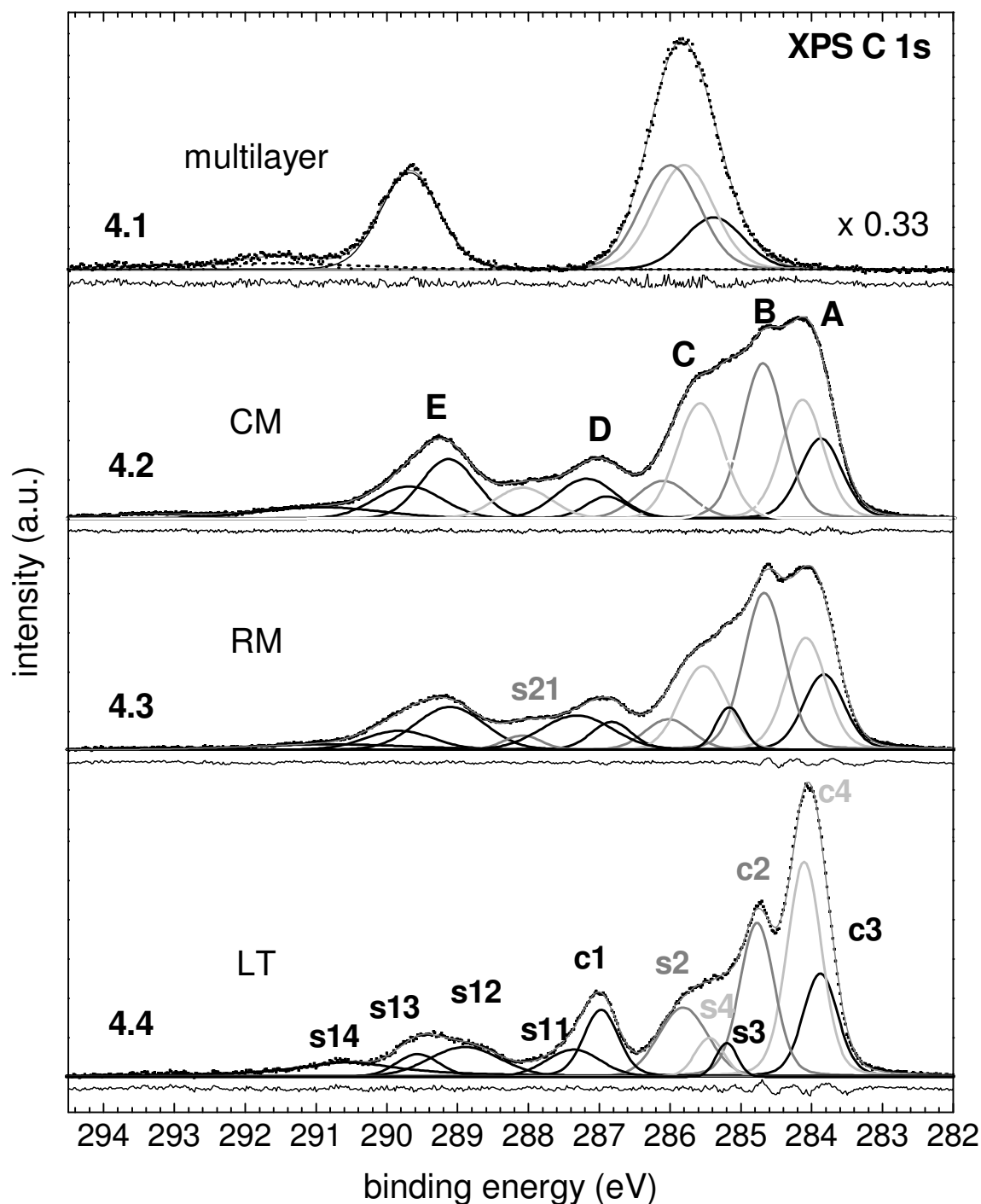


Figure 4.4.4: Results of the peak fit analysis of the C 1s spectra of the NTCDA compressed monolayer (CM, spectrum 4.2), relaxed monolayer (RM, spectrum 4.3) and low-temperature monolayer (LT, spectrum 4.4) in comparison to the multilayer fit (spectrum 4.1) from Figure 4.3.2 (Chapter 4.3). For the main lines (c1 - c4) Voigt functions with fixed Lorentzian width of 0.08 eV and identical Gaussian widths were used. All satellite peaks (s11 - s14 and s2 - s4) are represented by Gaussian peaks. See text for detailed information about the constraints used. The residua are plotted below the spectra.

decrease of the satellite peaks (C) and (E) from CM to RM and especially from RM to LT. This is in complete analogy with the result for the satellites in the O 1s analysis. Since the satellites (C) and (E) also coincide energetically very well with the multilayer ring and anhydride carbon lines at 286 eV and 289 eV, respectively, their assignment as poorly screened C 1s states of the ring and anhydride carbon atoms is evident.

With these preconditions a peak fit “deconvolution” of the LT spectrum can be performed. The result is displayed in Figure 4.4.4, spectrum 4.4. The fit parameters were constrained as follows: for the main lines (c1) – (c4) Voigt profiles were utilized with constant Lorentzian line width of 80 meV and equal but fitted Gaussian width. For all satellite peaks Gaussian functions with variable widths were used. For each ring carbon one satellite was allowed (s2 – s4), for the anhydride carbon four satellites have to be used (s11 - s14). The latter are obvious from the shape of the spectrum above 287 eV. The ratio of the peak areas was constrained according to the NTCDA stoichiometry:

$$(c1 + \text{satellites}) : (c2 + s2) : (c3 + s3) : (c4 + s4) = 4 : 4 : 2 : 4 .$$

As starting values the satellite peaks (s2) – (s4) were set in the same relative energetic order as the main lines (c2) – (c4). An excellent fit result is obtained with these assumptions, as can be derived from the residuum plotted below spectrum 4.4. All parameters resulting from this peak fit analysis and those of the other C 1s spectra are summarized in Table 4.4.2. We see, that the photoemission lines (c3) and (c4) contribute to peak (A), whereas peak (B) is generated by (c2). The main contribution to the shoulder (C) is satellite (s2), that represents the poorly screened C 1s core state of the carbon atom C2 while the carbon atoms C3 and C4 have much weaker satellites. On the anhydride side, peak (D) is mainly due to the (c1) line. (s12) can again be attributed to the C1 poorly screened core state and (s14) to an additional shake-up satellite, as in the multilayer data. Peaks (s11) and (s13) are most likely also due to shake-up losses of the (c1) line. Note, however, that the distinction between “shake-up” peaks and “poorly screened final states” is artificial since both belong to the same type of final state, namely an excited ionic state, and would be described by the same means in any theoretical approach [155].

If the same fit function is applied to the RM spectrum 4.3, the most important changes between the two structures become very clear. The fit result is also displayed in Figure 4.4.4 (spectrum 4.3). The (c1)- and (c3)-lines are strongly reduced, whereas the respective satellites (s12), (s3) and (s4) strongly gain intensity. Only, the (c2)-line is increased while the (s2)-satellite is decreased. The same trend is followed if we compare the fit of the RM data (spectrum 4.3) with the fit of the CM data (spectrum 4.2).

The strong changes in the relative intensities of the signals from well- and poorly screened core states especially between the LT and RM structure also indicate local differences in the charge transfer, that occurs for the core hole screening. Whereas the C3 and C4 core holes seem to be better screened for the LT layer, the charge transfer to screen the C2 and C1 holes is less effective. For the RM and CM layers, the C1 and C3 screening is even worse, whereas C2 is now screened more effectively.

These local changes of the charge-transfer rates on the time scale of the ionisation process for different core sites within the same molecule are most likely due to differences in the geometric distribution of the molecular orbital system, especially of the frontier orbitals that participate in the adsorbate-substrate bonding. Interestingly, the intensity ratio A1/A2 is decreased significantly for the RM (2.19) and CM (1.95) data, indicating, that satellites from the ring carbon atoms now contribute more to the anhydride side of the spectra. To take this observation into account, a satellite peak s21 had to be included in the fit, that can be

	CM			RM			LT		
	E_B (eV)	A	Γ_G (eV)	E_B (eV)	A	Γ_G (eV)	E_B (eV)	A	Γ_G (eV)
c1	286.89	0.44	0.64	286.83	0.53	0.62	286.97	1.11	0.52
c2	284.69	3.11	0.64	284.67	3.03	0.62	284.77	2.56	0.52
c3	283.87	1.60	0.64	283.83	1.45	0.62	283.88	1.71	0.52
c4	284.13	2.38	0.64	284.08	2.15	0.62	284.11	3.58	0.52
S11	287.18	1.07	0.99	287.32	1.08	1.18	287.37	0.63	0.88
S12	289.13	1.48	0.92	289.11	1.32	1.15	288.90	0.92	1.16
S13	289.69	0.97	1.12	289.83	0.58	1.13	289.56	0.42	0.70
S14	290.94	0.63	2.06	290.78	0.38	2.62	290.56	0.98	1.77
s2	286.10	0.90	0.89	286.02	0.63	0.77	285.81	1.51	0.81
S21	288.08	0.78	0.94	288.09	0.24	0.63	-	-	-
s3	285.15	0.79	0.50	285.16	0.50	0.43	285.20	0.32	0.35
s4	285.57	2.41	0.77	285.53	1.74	0.77	285.44	0.49	0.47
χ^2	7.65*10 ⁻⁴			9.19*10 ⁻⁴			1.84*10 ⁻³		

Table 4.4.2: Results of the least-square peak fit analysis of the NTCDA C 1s monolayer spectra from Figure 4.4.4. The parameters are the binding energy E_B , the area A, the Gaussian width Γ_G of the fitted peaks as well as the fit quality χ^2 . For a detailed peak assignment see text.

interpreted as representative for shake-up satellites from naphthalene carbon atoms. Since SDCI calculations on the similar molecules PTCDA, NDCA and PTCDI show the strongest shake-up intensity from the aromatic system for the C2 carbon atoms, we assign this peak as C2 shake-up satellite s21. The intensity of peak s21 was also included in the fit constraints.

4.4.3 Conclusion

We present high-resolution C 1s and O 1s XPS spectra of NTCDA monolayers on the Ag(111) surface for three different adsorbate states interrelated by reversible structural phase transitions. If the spectra are compared to the well-known spectra of weakly interacting NTCDA molecules in multilayers, we see strong differences, that clearly demonstrate the chemisorptive bond of NTCDA to the Ag(111) surface. The additional screening by charge transfer from the substrate shifts the monolayer photoemission lines towards lower binding energy by 1.5 eV to 3 eV. Due to the high energy resolution and the high structural quality of the three different monolayer configurations a rich fine-structure can be observed (especially in the C 1s data) that is due to the main lines of the carbon and oxygen atoms in different

bonding situations and various satellites. A careful peak fit analysis helps us to assign the various spectral features in the XPS spectra and gives the binding energies of the chemically different oxygen and carbon atoms. The strongest satellite lines are explained by poorly screened core states, that occur especially for weakly chemisorbed adsorbates by an incomplete charge-transfer screening process. Our analysis yields distinct differences for these satellites in the various adsorbate states, that indicate local differences for the charge-transfer screening within the molecule. This points towards subtle differences in the adsorbate-substrate coupling for the different NTCDA monolayer species. However, for a detailed understanding additional information from calculations, especially on the geometrical distribution of the NTCDA-metal hybrid orbitals, that participate in the adsorbate-substrate bonding, and their reaction upon creation of a core hole is needed. We emphasise that this is the first detailed XPS line shape analysis of a monolayer of a large organic molecule on a well-defined substrate.

4.5 An order-disorder phase transition upon cooling: NTCDA monolayer on Ag(111)

4.5.1 Motivation

A conventional first-order melting process that converts a crystalline solid into an isotropic liquid at constant pressure requires the supply of heat to the system. Consequently, the entropy of the liquid phase exceeds that of the crystal. In most cases – one exception is ice under normal pressure conditions – volume expansion occurs upon melting, i.e., the liquid is less dense than the crystal. The opposite process, a first-order transition from the crystal to liquid phase upon cooling (described as “inverse melting”) is rare but it exists in nature [172]. In such a case adding heat to the liquid at constant pressure causes the liquid to freeze into a crystalline solid. This is for instance the case for He-3 below about 0.3 K in a pressure range of about 30 kbar [173]. Another example is the organic polymer P4MP1 (isotactic poly(4-methylpentene-1)) which exhibits inverse melting behaviour around 150 – 200 K [174]. These phenomena can be described in Tammann’s universal pressure and temperature phase diagram in which the melting curve separates the crystalline phase from the melt region, which is further subdivided into liquid and amorphous phases [175-177]. Tammann noted that $T_m/dp = 0$ when $\Delta V = 0$, and that $T_m/dp = \infty$ when $\Delta H = \Delta S = 0$ (T_m denotes the melting temperature, V is the specific volume, H the enthalpy and S the entropy). There is one region below the $\Delta H = \Delta S = 0$ line in which inverse melting can be observed. Inverse melting in bimetallic alloys (e.g. Ti-Cr, Nb-Cr, Ta-Cr, Zr-Mo, or Fe-W) is described in terms of an under cooled melt in which the chemical order energetically stabilizes the melt compared to the mixed crystalline phases [178,179]. In all these cases, high pressures are involved.

We have investigated such an “inverse melting” structural phase transition in a pure 2D system, i.e. within a molecular monolayer – in our case 1,4,5,8 naphthalene-tetracarboxylic acid-dianhydride (NTCDA) - chemisorbed on a Ag(111) single crystal. NTCDA is an ideal model system to investigate interface properties, in particular those which are related to substrate induced structural modifications (see also Chapter 4.4): NTCDA monolayers are found to form three coverage-dependent superstructures on Ag(111) at room temperature [65,146,149]: for coverages below 80 % of saturation, a commensurate superstructure is formed (in the following denoted “relaxed monolayer” – RM). For saturation coverage a point-on-line superstructure (denoted by CM – “compressed monolayer”) is detected in high-resolution low-energy electron diffraction experiments. An additional intermediate structure (RM₂) was found by L. Kilian for a coverage of about 80 % [65]. The RM₂ is similar to the RM structure but has one unit cell vector that is 4 % shorter. The monolayer structures can be reversibly transformed by adsorption or desorption of molecules (RM/CM or CM/RM). In both superstructures the molecules are aligned in 1D chains as confirmed by scanning tunnelling microscopy (STM) [148,149]. L. Kilian found, that upon cooling to about 160 K the long-range ordered monolayers undergo an order-disorder transition. Annealing at about 190 K recovers the long-range ordered phase [65,180].

In order to clarify the underlying mechanism and driving force of the phase transition we investigated the molecule-substrate interaction for the ordered and disordered phases by

various electron spectroscopy methods. The emphasis of the previous chapter (Chapter 4.4) was set on high-resolution x-ray photoemission data of the different NTCDA monolayer films RM, CM and LT on the Ag(111) surface. The detailed analysis of the XPS spectra revealed distinct differences of the core hole screening due to substrate-adsorbate charge transfer for the different structural modifications, especially between the RM and LT phase. The spectra of the LT monolayer showed the highest intensities (compared to RM and CM) for the well-screened photoemission lines, which has to be explained by a strong charge transfer from the Ag(111) substrate to the adsorbate molecule upon core excitation. Those findings are supported by near-edge x-ray absorption fine structure (NEXAFS) and UV photoelectron spectroscopy data presented in this chapter, that show the filling of unoccupied molecular orbitals in the LT phase.

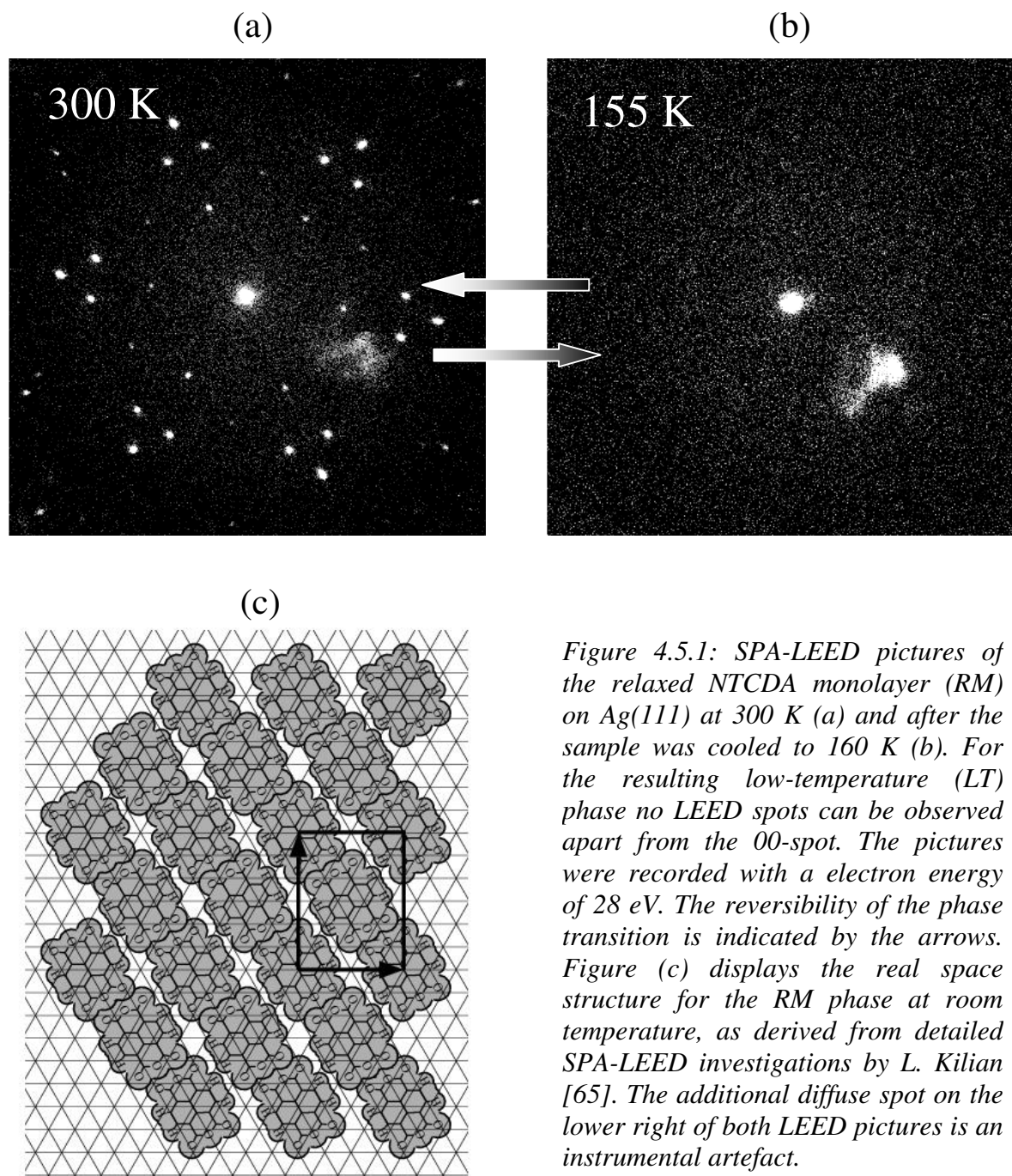
From these results the long-range ordered RM and CM phases can be characterized as weakly chemisorbed due to the π -interaction with the metal substrate, in complete agreement with previous publications [146,161,181]. In the LT phase NTCDA is more strongly bound to the substrate which on first hand seems to be contradictory. However, a stronger bonding increases the adsorption energy which in terms of the Gibbs free enthalpy ΔG means that the enthalpy ΔH becomes more negative (compared to the entropic term $-T \cdot \Delta S$). Thus, we obtain experimental evidence that the observed phase transition is governed by the enthalpy and hence the molecule-substrate interaction is extremely crucial.

4.5.2 Results and discussion

Figure 4.5.1a shows the LEED picture of a relaxed monolayer (denominated RM in the following) of NTCDA on the Ag(111) surface. The coverage is $\Theta = 0.75$ ($\Theta = 1$ refers to saturation coverage). The structure is well-known due to previous LEED and STM investigations [66,149]. It refers to a commensurate superstructure with the superstructure matrix $\begin{pmatrix} 4 & 0 \\ 3 & 6 \end{pmatrix}$, has two molecules per unit cell, and exists for coverages of $\Theta < 0.8$. The intense and sharp LEED spots indicate a high degree of lateral order and large domain sizes. The real space structure of the RM monolayer, suggested by L. Kilian from the detailed analysis of SPA-LEED data [65], is displayed in Figure 4.5.1c. The molecules are densely packed in one direction and build rows, touching each other with their short sides. The structure is relatively open perpendicular to the rows.

If the relaxed monolayer is cooled down to $T < 160$ K, the LEED spots completely disappear resulting in the LEED picture of Figure 4.5.1b, that only shows the 00-spot. Thus no long range lateral order exists for this low-temperature monolayer structure (denominated LT in the following). Furthermore, the slightly more diffuse 00-spot indicates some roughening of the sample surface. If the sample is annealed, the LEED spots reappear, and at a substrate temperature of $T \sim 200$ K the RM LEED pattern is completely restored, which proves the complete reversibility of the RM – LT phase transition.

Figure 4.5.2 shows the C 1s (a) and O 1s (b) XPS spectra of the RM and LT phases together with the results of a least-square peak fit deconvolution. A detailed discussion of the XPS data on the basis of a peak fit analysis was described in Chapter 4.4. The differences in the spectra of the two phases are enormous, especially in the C 1s data, where, e.g., the peaks at 284 eV and 287 eV are much more intense for the LT phase.



The peaks in the C 1s data can be assigned as indicated in Figure 4.5.2a. The peaks (c1) – (c4) are the main lines of the 4 chemically different carbon atoms (see also Figure 4.3.1) which stem from well-screened final states of the ionised atoms. The anhydride carbon line (c1) is clearly separated from the ring carbon peaks (c2) – (c4) due to the strong electronegativity of the three oxygen atoms in the functional group. The satellites (s12), (s2), (s3) and (s4) can be assigned to poorly screened final states of the carbon lines (c1) – (c4). These satellites are observed if the photoemission process and the screening charge transfer from the substrate occur on the same timescale, which may be the case for weak chemisorption. Thus both, the well-screened and the poorly screened photoemission lines, are visible in the XPS spectra.

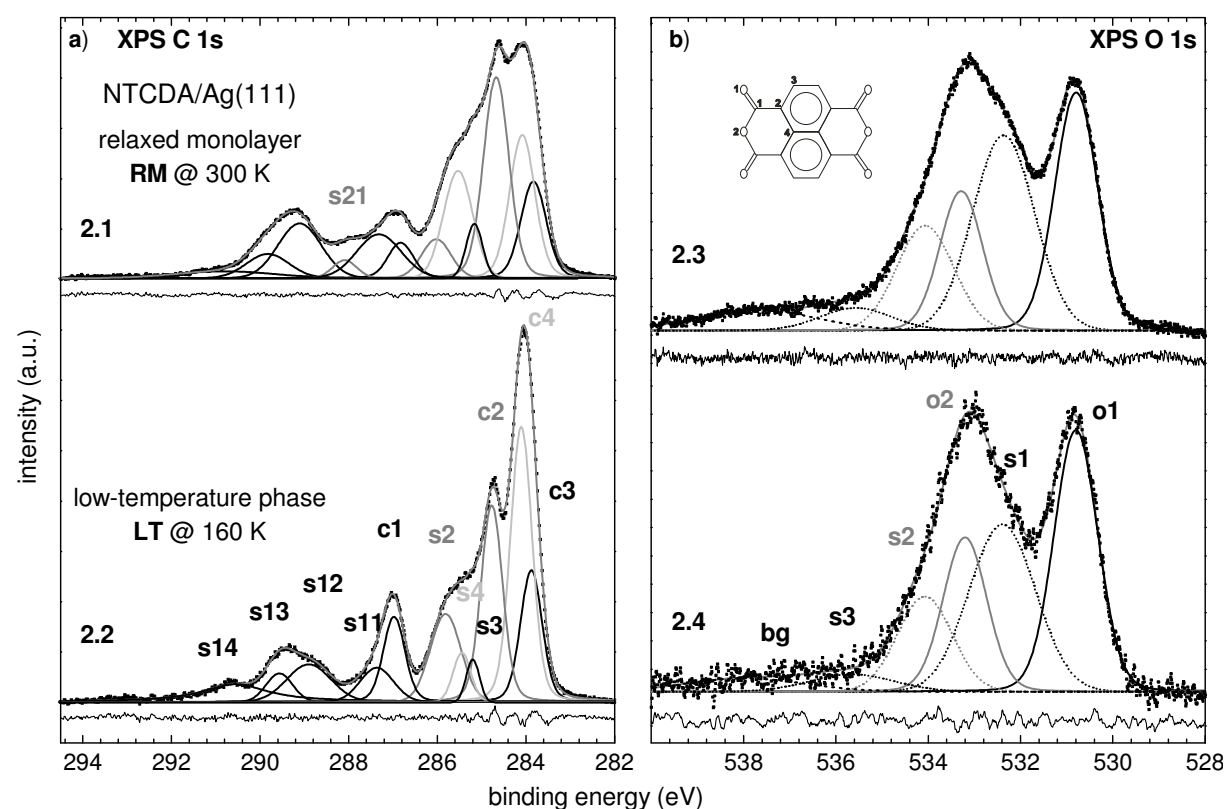


Figure 4.5.2: C 1s (a) and O 1s XPS spectra (b) of the RM (spectra 2.1 and 2.3) and LT phases (spectra 2.2 and 2.4). The spectra were recorded with photon energies of 335 eV and 700 eV, respectively, and a constant analyser pass energy of 40 eV. Together with the spectra the peak fit results from Chapter 4.4 are plotted.

The satellites (s11), (s13) and (s14) can be attributed to additional shake-up losses of the (c1) and (s12) lines. A similar assignment can be made for the O 1s data in Figure 4.5.2b. Here the two photoemission lines (o1) and (o2) of the two chemically different oxygen atoms O1 and O2 (see Figure 4.3.1) are clearly separated. The satellites (s1) and (s2) are again attributed to the poorly screened O1 1s and O2 1s core states, and (s3) to a HOMO-LUMO shake-up satellite of (s1).

The analysis of the O 1s data shows, that the intensities of the (s1) and (s2) satellites relative to the (o1) and (o2) main lines clearly decrease from the RM to the LT structure, whereas the energy positions of the spectral features show almost no energy shift. The analogue observation can be made for the C 1s data, where the satellites (s3), (s4) and (s12) decrease for the benefit of an increase of the intensity of the corresponding main lines. Also here the energy positions are almost unchanged. This clearly indicates changes in the effectiveness of the charge transfer on the time scale of the photoemission process, i.e. the probability that metal electrons are transported to the adsorbate to screen the core hole during the excitation process. The experimental result thus points towards an increased probability for this screening process for the LT structure, which indicates a stronger coupling between the Ag substrate and the NTCDA molecule for the low-temperature phase.

In Figure 4.5.3 the UPS spectra of the NTCDA RM and LT phase from Ref. [65] are plotted. The spectra were recorded with He I excitation (21.22 eV) and normal emission of the photoelectrons. On the bottom of Figure 4.5.3a the valence spectrum of the clean Ag(111) sample is plotted for comparison and helps to identify the substrate peaks in the monolayer

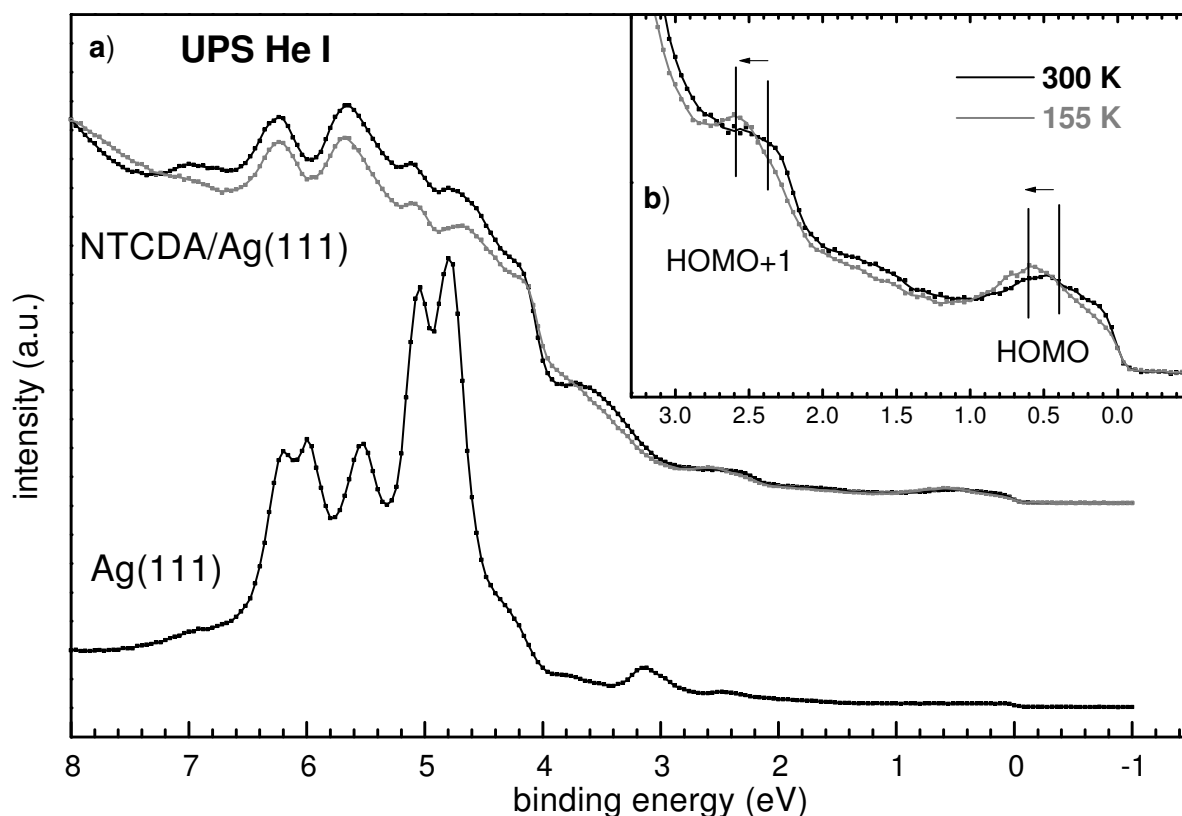


Figure 4.5.3: (a) UPS data of the clean Ag(111) substrate (bottom) and the RM (black curve) and LT (grey curve) phases from Ref. [65]. The spectra were recorded with He I excitation (21.22 eV) and normal emission. In the inset (b) the low energy region of the RM (black curve) and LT (grey curve) spectra is plotted on an expanded energy scale. The lines indicate the shift of the HOMO and HOMO+1 peaks towards higher binding energy.

spectra. The most intense structures in the Ag spectrum are the Ag d-bands between 4.5 eV and 6.5 eV. The peaks at 0.5 eV and 2.5 eV in the NTCDA monolayer spectra can be attributed to the new HOMO and HOMO+1 that form upon bonding. Both are metal-NTCDA hybrid states, the former has mostly NTCDA LUMO and Ag 5s, the latter NTCDA HOMO and Ag 4d contributions [182]. The new HOMO as well as the HOMO+1 clearly shift towards higher binding energies by about 0.2 eV if the RM phase is transformed into the low-temperature phase. This is clarified by the inset in Figure 4.5.3 (Figure 4.5.3b), where this part of the spectra is plotted on an expanded energy scale. This energy shift of the hybrid orbitals, that play an important role in the NTCDA-metal bonding, indicates remarkable changes of the bonding for the phase transition and thus corroborates the interpretation of the core level spectra.

Additional information about the electronic system, especially on the unoccupied orbitals, and the orientation of the molecules in the different films can be gained from NEXAFS experiments [14]. In Figure 4.5.4 the C K- (Figure 4.5.4a) and O K-edge (Figure 4.5.4b) NEXAFS spectra are displayed for the two monolayer phases (RM at 300 K and LT at 155 K). The spectra were recorded with normal ($\Theta = 0^\circ$, grey curves) and grazing incidence ($\Theta = 70^\circ$, black curves) of the horizontally polarised photon beam, respectively, as illustrated by the sketch in Figure 4.5.4b. The latter case comprises a high \vec{E} component perpendicular to the sample surface and thus leads to high intensities of transitions into the unoccupied molecular π^* -system for flat lying NTCDA molecules, whereas for normal incidence and flat

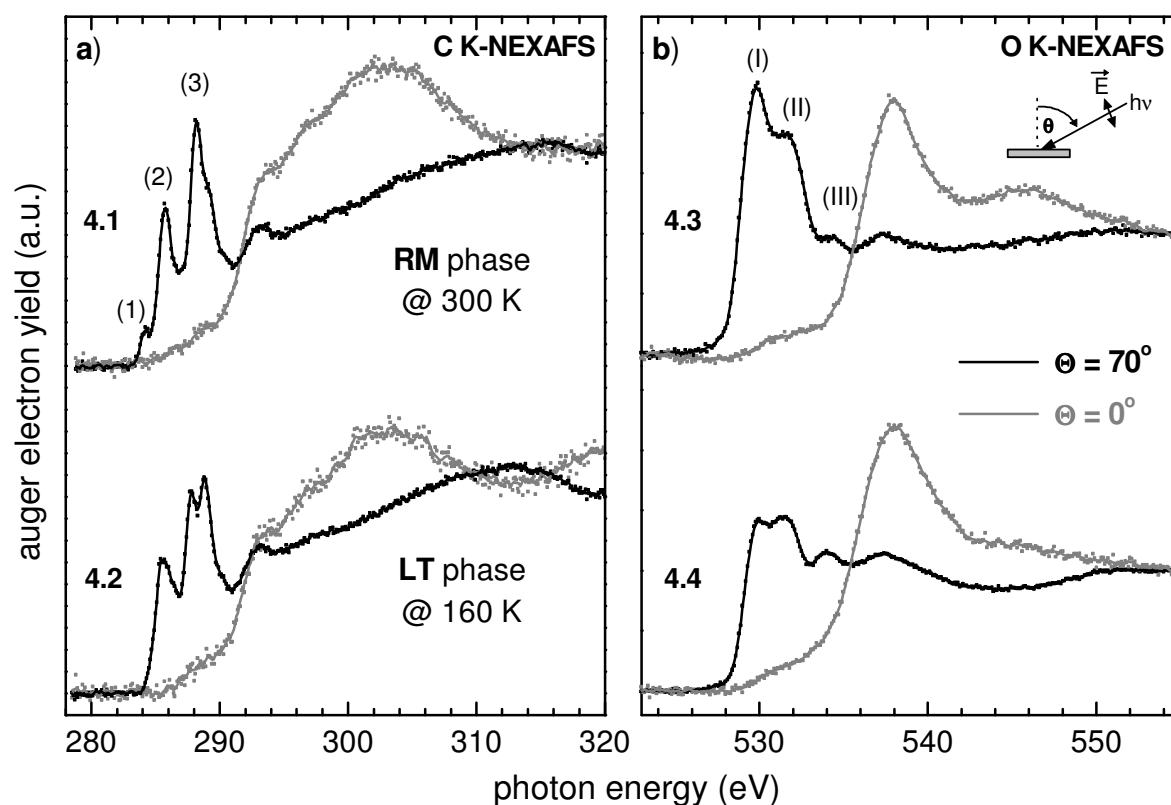


Figure 4.5.4: C K- (a) and O K-NEXAFS spectra (b) of the RM (spectra 4.1 and 4.3) and LT phase (spectra 4.2 and 4.4). The spectra were recorded in the auger electron yield (AEY) mode and with normal ($\Theta = 0^\circ$, grey curves) and grazing ($\Theta = 70^\circ$, black curves) incidence of the horizontally polarised synchrotron light, as illustrated in Figure 4.5.4b.

lying molecules no π^* -intensity is expected. Thus, the observed NEXAFS linear dichroism of the π^* -resonances, i.e., the peaks between 284 eV and 290 eV at the C K-edge and the peaks between 528 eV and 536 eV at the O K-edge in Figure 4.5.4, indicates almost perfectly flat lying molecules for both, the RM and the LT film. Within the accuracy of the method ($\sim 3^\circ$) no changes of the flat lying orientation of the NTCDA molecules can be detected for the phase transition. This result is particularly interesting since it excludes a change of the flat lying molecular orientation due to stress in the monolayer film when the sample is cooled down. Thus the observed loss of long-range order is caused by purely lateral changes in the overlayer structure.

Nevertheless, if we compare the π^* -resonances of the two phases in detail, strong differences can be observed. This is confirmed by the Figures 4.5.5c and 4.5.5d, where the π^* -regions of the C K- (Figure 4.5.5c) and O K-data (Figure 4.4.5d) of the RM (black curves) and LT phases (grey curves) are plotted on expanded energy scales. At the C K-edge (Figure 4.4.5c) peak (1) almost completely disappears if the sample is cooled down. The intensities of peak (2) and (3) also decrease while the shoulder on the high energy side of peak (3) gains intensity, leading to a doublet for the LT film. Furthermore peak (3) shifts towards lower energy by about 0.3 eV. At the same time peaks (I) and (II) at the O K-edge (Figure 4.5.5d) are strongly decreased in intensity, whereas peak (III) is slightly increased. Here the strong changes in the NEXAFS data unambiguously point to changes in the NTCDA-Ag bonding upon the phase transition.

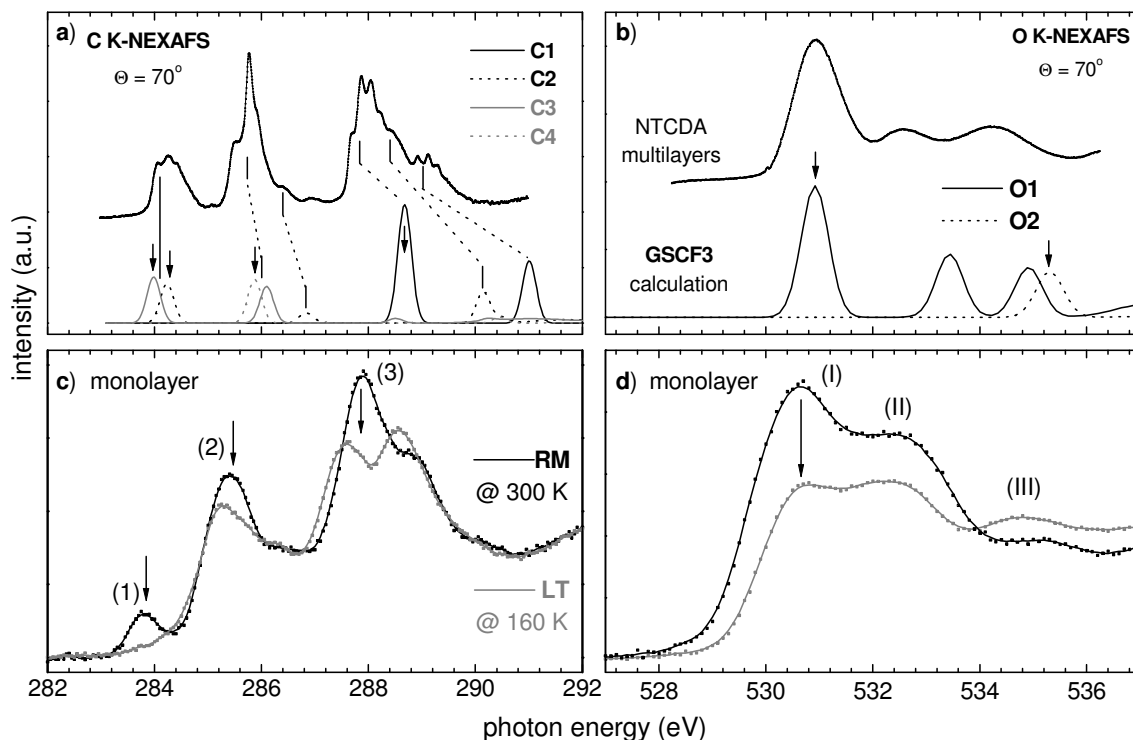


Figure 4.5.5: π^* -region of the experimental C K- (Figure 4.5.5a, top) and O K- (Figure 4.5.5b, top) NEXAFS data of NTCDA multilayers compared to *ab initio* calculations (Figures 4.5.5a and b, bottom) for the free NTCDA molecule (see also Chapter 4.2.4). The calculated spectra were shifted in energy to align the first transitions (see text). The inequivalent carbon (C1-C4) and oxygen atoms (O1/O2) taken into account in the calculation are indicated in the structural image in Figure 4.4.1. The assignment of the calculated transitions to the experimental resonances is indicated by the guidelines in Figure 4.5.5a. Transitions into the LUMO are marked by arrows in Figures 4.5.5a and b. The π^* -regions of the C K- (Figure 4.5.5c) and O K-NEXAFS (Figure 4.5.5d) spectra of the RM (black curves) and the LT (grey curves) phases are compared in the bottom panels of Figure 4.5.5. The arrows indicate the most prominent changes in the spectra.

To get further insight into the origin of these differences of the chemisorptive bonding on the unoccupied levels, a detailed interpretation of the NTCDA NEXAFS data on the basis of *ab initio* calculations is very helpful. In Figure 4.5.5a and 4.5.5b the results of an *ab initio* calculation (GSCF3 program package [44,45]) for isolated NTCDA is presented. Since the calculations were performed for the free molecule, they can be best compared to the experimental spectra of (weakly interacting) NTCDA multilayers, that are plotted in the upper part of Figures 4.5.5a and 4.5.6b. For details on the calculations and the interpretation of the multilayer data see Chapters 4.2.2 and 4.2.4.

The NEXAFS spectra consist of a superposition of transitions from different initial states with the core hole at the symmetrically non-equivalent carbon and oxygen atoms (C1 – C4 and O1/O2, respectively, see Figure 4.4.1) into the lowest unoccupied molecular orbitals LUMO – LUMO+4. The attribution of the various calculated transitions to the different features in the experimental spectra is indicated by the guidelines in Figures 4.5.5a and b. This clearly yields two electronic transitions for peak (1) and major contributions from three transitions for peaks (2) and (3) in the C-K NEXAFS spectra, respectively. Peaks (1) and (2) mainly correspond to excitations of C 1s initial states located at naphthalene carbon atoms C2, C3 and C4 into

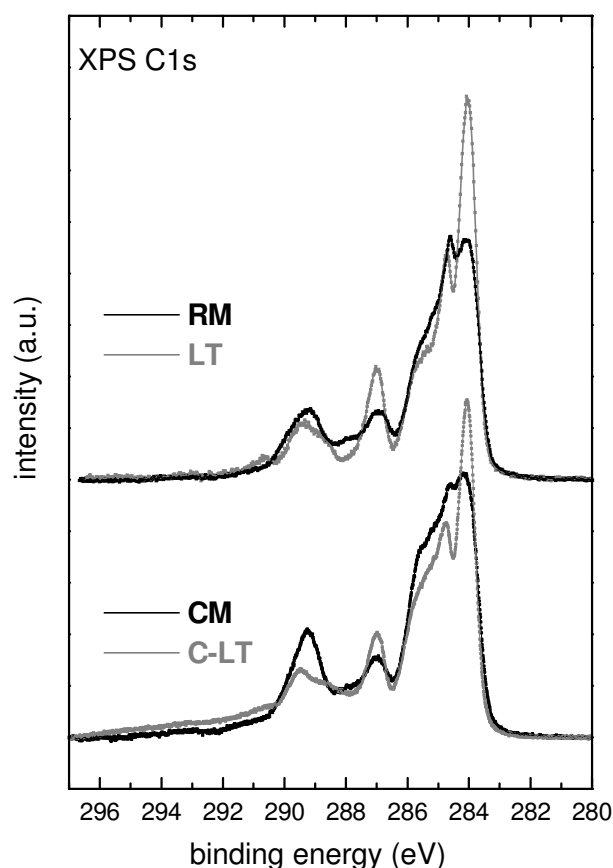


Figure 4.5.6: Comparison of the C 1s XPS spectra of the RM (top, black line) and LT phase (top, grey line), with the corresponding data for the CM (bottom, black line) and C-LT phase (bottom, grey line).

LUMO and LUMO+1 final states, whereas the highest intensity in peak (3) can be attributed to anhydride (C1) C 1s \rightarrow LUMO and LUMO+1 transitions plus a C 1s (C2) \rightarrow LUMO+4 transition. The multilayer O K-NEXAFS spectrum can be interpreted as a superposition of O1 \rightarrow LUMO, LUMO+1 and LUMO +2 and O2 \rightarrow LUMO transitions.

The NEXAFS spectra of the RM film show basically the same spectral features as the NTCDA multilayer, namely the peaks (1)-(3) at the C K-edge (Figure 4.5.5c) and the peaks (I)-(III) at the O K-edge (Figure 4.5.5d). The general shift of the monolayer spectra towards lower energies upon cooling has to be attributed to additional, substrate related screening and bonding effects. The occurrence of substrate excitations (e.g. phonons) in the monolayer data and life time/bonding effects may explain, why the well resolved vibronic fine structure of the multilayer C 1s spectra (Figure 4.5.5a) is smeared out. Thus, if these general differences are considered, the calculated electronic transitions of Figures 4.5.5a and b can

be accommodated with the NEXAFS spectra of the RM phase in good analogy to the multilayer data.

Under consideration of the *ab initio* calculations the comparison of the NEXAFS data of the two monolayer phases reveals, that the strongest changes upon the phase transition occur for spectral features, that have strong contributions of transitions into LUMO final states. The corresponding transitions (C1-C4 \rightarrow LUMO and O1/O2 \rightarrow LUMO) are marked by arrows in the calculated spectra in Figures 4.5.5a and b. All these transition are strongly decreased in intensity if the RM film is transformed into the LT phase. This can be interpreted as additional charge, that is transferred from the Ag substrate to the NTCDA molecule in the stronger coupled LT phase. Thus the LUMO gets completely occupied, and the respective NEXAFS transitions are decreased in intensity. This interpretation is in complete accordance with the photoemission spectra, that indicate a stronger substrate-adsorbate interaction for the LT phase. Especially the UPS data show that the former LUMO, that is pulled below the Fermi level and partly filled in the RM state, shifts further down in energy and becomes completely filled.

Figure 4.5.6 compares the C 1s XPS spectra of the RM and LT phases, which were analysed in detail in the discussion of Figure 4.5.2, with the corresponding data of the compressed monolayer (CM) at room temperature and the low temperature phase of the compressed monolayer (C-LT). The analogy of the RM/LT and CM/C-LT phase transitions can clearly be

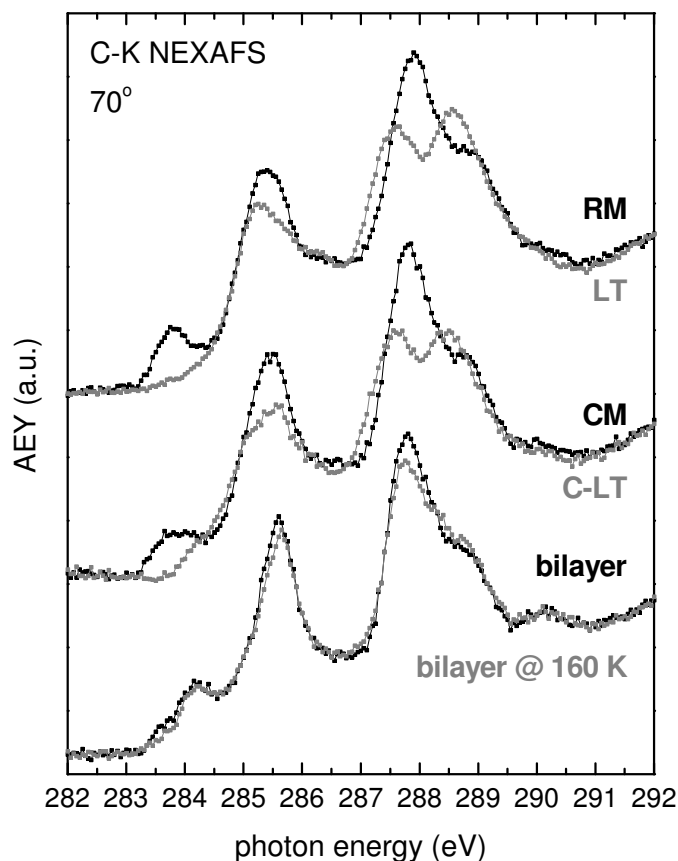


Figure 4.5.7: Comparison of the C K-NEXAFS spectra of the RM (top, black line) and LT phase (top, grey line), with the corresponding data for the CM (middle, black line) and C-LT phase (middle, grey line) and a NTCDA bilayer at 300 K (bottom, black line) and at 160 K (bottom, grey line).

observed. The most important changes, that occur in the C 1s XPS spectra upon the CM/C-LT phase transition, can be explained by the decrease of the relative intensities of poorly screened core states due to the stronger interface bonding in the C-LT phase, in complete accordance with the interpretation of the XPS data of the RM/LT transition. The analogy of the transitions is corroborated by Figure 4.5.7, that compares the C K-edge NEXAFS spectra of the RM and LT phases (top) from Figure 4.5.5c with the spectra of the CM and C-LT phases (middle). Also in the C-LT phase the NEXAFS transitions into LUMO final states are suppressed due to the increased metal-to-LUMO charge transfer. The small differences between the NEXAFS spectra of the NTCDA bilayer at 300 K and at 160 K, that are displayed on the bottom of Figure 4.5.7, can be explained by the co-existence of regions with monolayer coverage (most likely with CM structure at 300 K), that transform into the corresponding low temperature phase upon

cooling. This assumption appears justified, since NTCDA multilayers are known to grow laterally in a rather inhomogeneous fashion at room temperature, forming islands with crystalline order with only one or two layers between these islands [116].

Figure 4.5.8 displays a series of C K-NEXAFS scans that were recorded at various temperatures in the region of the phase transition. Starting with the RM phase the sample was cooled down (Figure 4.5.8a) until the LT phase was reached and subsequently annealed (Figure 4.5.8b) until the RM structure was recovered. The cooling and heating rates were ± 0.1 K/s, respectively. The spectra gradually change when the sample is cooled down (Figure 4.5.8a), starting with the RM spectrum at 210 K. Note, that cooling to temperatures below 160 K does not lead to further changes in the spectra. The strongest changes occur between 165 K and 162.5 eV. Also upon annealing, the spectra change gradually from the LT to the RM spectrum between 170 K and 187.5 K. Here the strongest changes can be observed between 180 K and 183 K.

The indicated hysteresis behaviour of the phase transition is clearly demonstrated by Figure 4.5.9. The data points plotted as black squares were obtained by fitting the transition spectra in Figure 4.5.8 to a linear combination of the RM and LT spectra (i.e. $\text{spectrum}(T) = c \cdot \text{RM spectrum}(210 \text{ K}) + (1-c) \cdot \text{LT spectrum}(160 \text{ K})$). The fit parameters c were then plotted for the different temperatures and constitute the hysteresis curve of the RM-LT phase transition. A

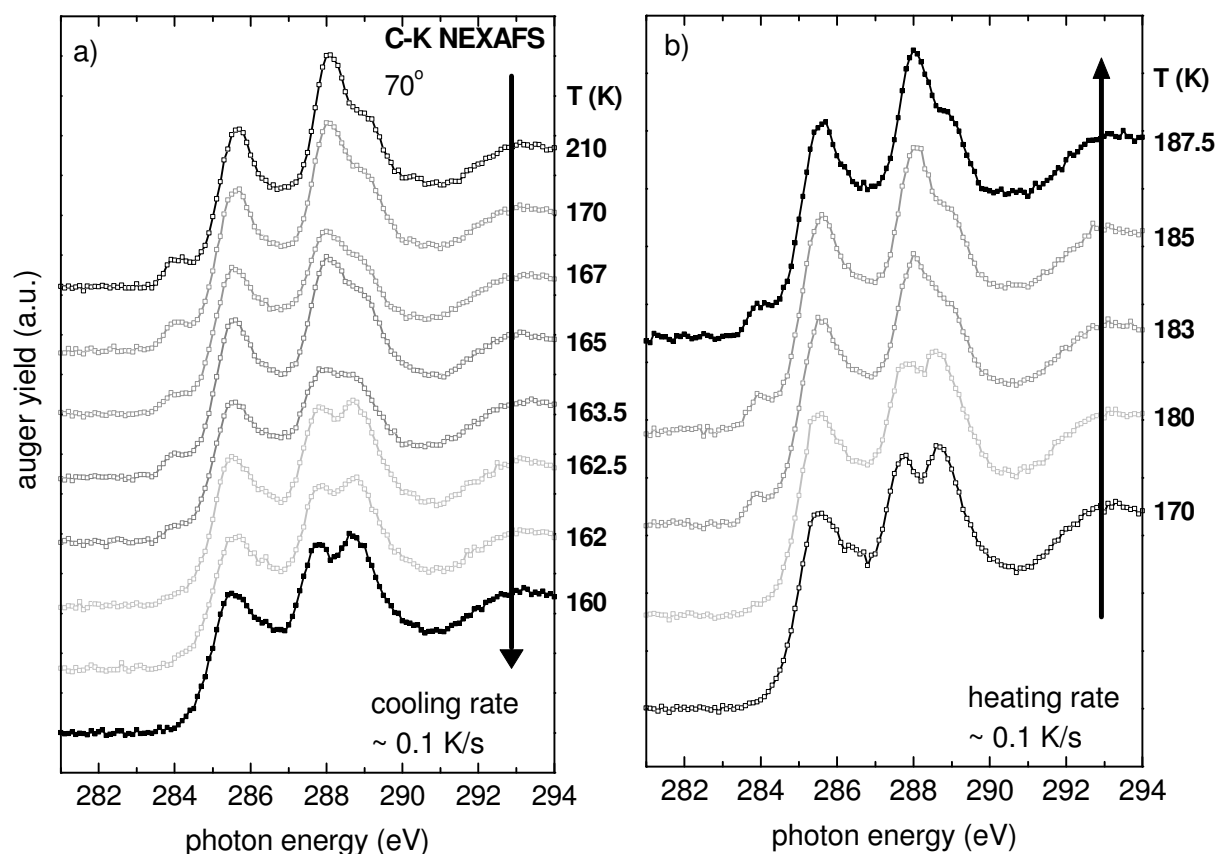


Figure 4.5.8: C 1s NEXAFS scans recorded while the sample was cooled down from 210 K to 160 K (Figure 4.5.8a) and subsequently annealed from 170 to 187.5 K (Figure 4.5.8b). The cooling and heating rates were ~ 0.1 K/s, respectively. The scan times were about 15 s, thus the temperatures plotted on the right side of the Figures are the average temperatures during the corresponding scans.

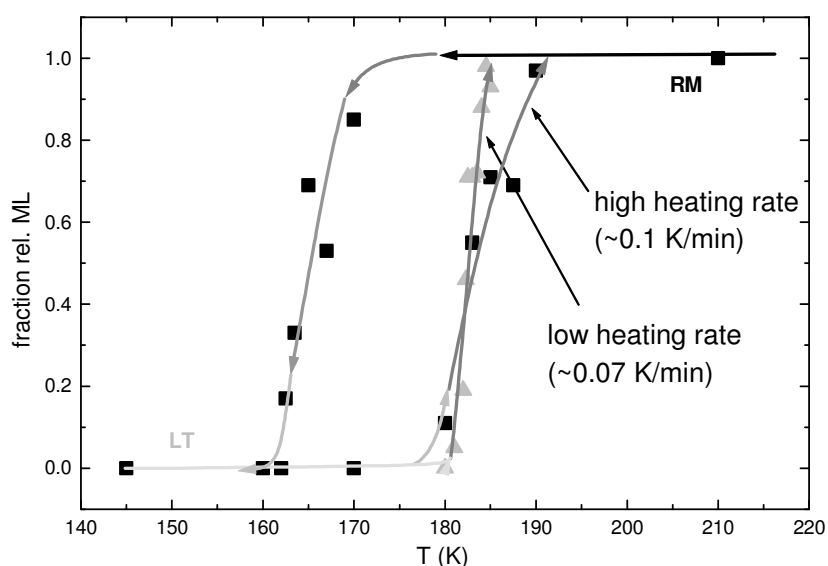


Figure 4.5.9: Hysteresis curve derived from a fit of the phase transition C 1s NEXAFS spectra (see Figures 4.5.8a and b) to a linear combination of the RM and LT spectra (see text). The data points plotted as grey triangles were obtained from an additional heating cycle with a heating rate of 0.07 K/s. The arrows were drawn as guidelines to demonstrate the direction of the transition.

solid line is drawn in Figure 4.5.9 to guide the eye. The data points displayed as grey triangles were derived from an additional heating cycle with lower heating rate (~ 0.07 K/s) and result in a steeper slope of the hysteresis curve. The hysteresis behaviour clearly indicates, that the phase transition is a thermally activated first order transition.

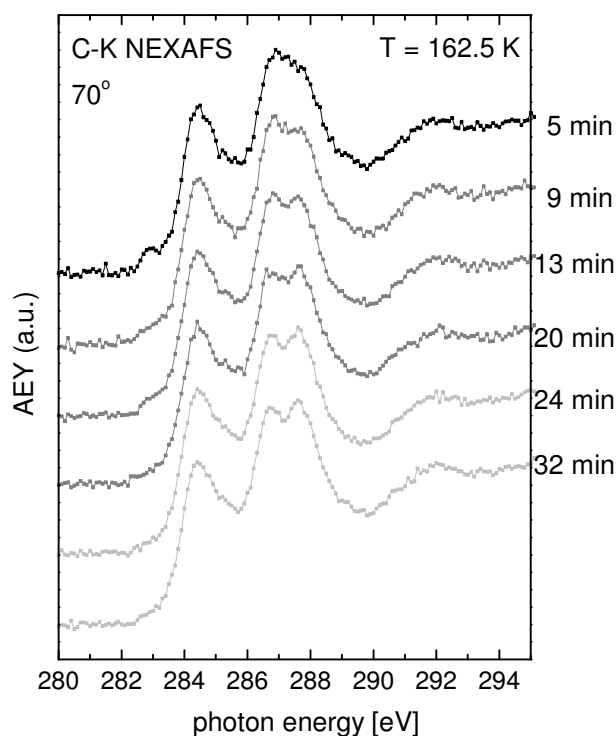


Figure 4.5.10: C 1s NEXAFS scans that were recorded after the RM sample was cooled to 162.5 K for the time specified on the right side of the spectra. The scan times were about 15 s.

Figure 4.5.10 displays repeated C K-NEXAFS scans (scan time ca. 15 s) that were recorded after the RM sample was cooled to 162.5 K for the time specified on the right side of the corresponding spectrum. The time dependent transformation of the topmost spectrum, that still shows mainly the RM signature after 5 min at 162.5 K, into the spectrum with complete LT signature on the bottom (after 32 min at 162.5 K) proves the thermal activation of the phase transition, that occurs on the time scale of 0.5 h. The activation energy was determined to $E_A = 60(5)$ meV for the RM \rightarrow LT phase transition from the time dependence of the transition at various temperatures between 140 K and 160 K by SPA-LEED measurements.

4.5.3 Concluding remarks

In this chapter an extensive electron spectroscopic study of the order-disorder phase transition that occurs for a NTCDA monolayer on the Ag(111) surface is presented. This phase transition is very uncommon since the long-range ordered adsorbate layer transforms into a disordered phase if the sample temperature is *decreased* to 160 K. Therefore this phase transition can be regarded as inverse melting process. A hysteresis of about 20 K for the transition temperature was found. Thus, the transition can be characterised as a thermally activated first order phase transition. This is also corroborated by the fact, that the RM phase can be frozen by rapidly cooling to LHe temperatures.

Combining XPS, UPS and NEXAFS results yields an interesting picture of the changes in the electronic structure at the interface during the phase transition: In the NEXAFS data the transitions into the LUMO are suppressed for the LT phase, which is attributed to a complete occupation of the LUMO due to charge transfer from the substrate. Thus, the remaining NEXAFS resonances are shifted towards lower energy by about 0.3 eV due to the missing LUMO. The UPS data clearly show a shift of the new HOMO and HOMO+1 signals to higher binding energy by 0.2 eV, whereas in the XPS spectra the C 1s and O 1s core level binding energies are not effected by the phase transition. However, a strong decrease of the XPS

satellite structures indicates a marked increase of the screening charge transfer rate on the time scale of the photoionization process for the LT phase.

The results show consistently, that the bonding between the NTCDA molecules and the Ag(111) substrate is significantly stronger in the LT phase. The frontier orbitals are shifted towards higher binding energy and additional charge is transferred to the LUMO. The increased charge density in the LUMO may also explain the more effective charge transfer observed for the screening process of the XPS core hole. This interpretation is supported by very recent HREELS results [162], that, in addition to strong differences in the vibronic signature of the NTCDA molecules in the two phases, indicate that the electronic occupation of the LUMO is strongly increased in the LT phase.

These findings are consistent with the above discussed scenario of an enthalpy-driven phase transition. The increasing strength of the molecular bonding to the substrate upon cooling to the LT phase is consistent with lowering the enthalpy ΔH which is obviously overriding the entropic $T\Delta S$ term in the free enthalpy. Nevertheless we may also have to take other aspects into account which are the topic of present investigations like, e.g., the intralayer interactions. For instance, the fact that the inverse melting is not observed for NTCDA monolayers adsorbed on Ag(100) may be due to the fact that the molecular density within the NTCDA monolayer is higher for the Ag(111) than for the Ag(100) system. Another aspect not investigated so far is the possible influence of the coverage of the surface. A different behaviour of the phase transition at coverages below $\Theta = 0.7$ could shine light on the effect of second layer adsorption. Therefore, some open questions remain.

4.6 Towards a detailed understanding of the NEXAFS spectra of bulk polyethylene copolymers and related alkanes

4.6.1 Motivation

The interpretation and use of Near Edge X-ray Absorption Fine Structure spectra of macromolecules is often based on molecular analogues, a semi-quantitative building block or finger print approach, as well as calculations based on isolated small molecules [14,183]. Implicit in this approach is the assumption that the character of the bonding and antibonding orbitals in single molecules are the most fundamental aspect, while intermolecular interactions and matrix effects are generally considered to be negligible. Occasionally, band structure approaches have been used, but generally they are poor guides to the interpretation of NEXAFS spectra due to the effect of the core hole on the electronic structure [184].

In contrast, the small molecule analogue approach (“building-block principle”) in combination with calculations has yielded considerable insight [185-188]. However, success has been elusive in some instances. For example, the interpretation of the low energy C 1s NEXAFS features near ~288 eV in various saturated hydrocarbons continues to pose experimental and theoretical challenges. A unified interpretation has not yet emerged. Initially, the low energy peak of polyethylene (PE) and long-chain alkanes was assigned to a mixed $\sigma^*/$ Rydberg character based on $X\alpha$ scattered wave ($X\alpha$ SW) calculations [189]. The existence of Rydberg states in the bulk has been questioned in general [190]. Pronounced dichroic signals in both the low energy C 1s \rightarrow $\sigma^*_{\text{C-H}}$ /Rydberg region near 288 eV and higher energy C 1s \rightarrow $\sigma^*_{\text{C-C}}$ region at 290-295 eV could be observed from oriented and ordered materials, qualitatively supporting assignments to molecular orbitals that reflected the C-H and C-C bonding character of the materials [191,192]. Based on primarily theoretical work, Bagus et al. challenged previous interpretations by assigning the low energy features to three states of purely Rydberg character with vibrational overtones [193]. Väterlein et al. subsequently re-affirmed the mixed $\sigma^*/$ Rydberg character through very detailed $X\alpha$ -SW calculations [194].

In this chapter, we present experimental data, supported by theoretical calculations, that result in a detailed understanding of the NEXAFS spectroscopy of saturated hydrocarbons. The fractional disorder and crystallinity in ethylene-1-alkene copolymers has been systematically changed by controlling the frequency and length of the side-chains. This results in ideal model systems with systematic changes in the fraction and size of the crystallites as well as their unit cell dimensions [195,196]. In turn, a systematic experimental investigation of intermolecular interactions in the bulk of these materials was possible. Pronounced and systematic variations for both the low energy features near 288 eV, as well as the σ^* features in the 290-295 eV region have been observed. Ab initio calculations are in accordance with the observations and reproduce the systematic trend in spectral intensities as a function of material composition. Our work shows unambiguously, based on experimental data, that intermolecular interactions are essential in understanding the NEXAFS spectra of some polymers. These results also clarify the spectral assignments of polyethylene and related

materials and specifically rule out that the two most prominent low energy features in ordered alkanes and related polymers are dominated by Rydberg character. This work has been published in the *Chemical Physics Letters* (see Ref. [197]).

4.6.2 Experimental

All samples were synthesized at DOW Chemical using constrained geometry catalyst technology. The co-polymerization process results in non-crystallizable short chain branches of well defined length at random locations along the chains in the otherwise crystallizable polymer (linear polyethylene). We have chosen comonomers for which the resulting short chain branches do not participate in crystallite formation [195]. Samples were sectioned from bulk pellets into ultrathin films of about 150 nm thickness by cryo-microtomy at -100°C and mounted on TEM grids. A list of all comonomer samples investigated in this chapter, their content in weight- and mol-percent, the resulting average number of branches per 1000 backbone carbon atoms, their density, molecular weight, and degree of crystallinity is provided in Table 4.6.1.

All NEXAFS data were recorded using the Stony-Brook Scanning Transmission X-ray Microscope (STXM) [72] at the National Synchrotron Light Source (NSLS). The resolving power was 2500 [73]. To calibrate the energy scale, absorption spectra of gaseous CO_2 and of the samples were recorded simultaneously [17]. For in-situ heating of thin film samples in the STXM, a special sample holder was built that allowed resistive heating of TEM grids.

Ab initio calculations were performed using N. Kosugi's GSCF3 package [44], which uses the Improved Virtual Orbital approximation [198] for accurate calculation of core excitation spectra [199]. We calculated the ionization potentials, term values, and oscillator strengths for one of the middle carbon atoms in butane as a model for polyethylene. The basis set was (621/41) for C, (41) for H and (4111/311/*) for the carbon atom with the core hole. The ground state geometries were prepared by an ab initio geometry optimization at the STO-3G level. Gaussian line widths used in generating the simulated spectra from the ab initio results were 0.3 eV FWHM for orbitals of eigenvalue $\epsilon < 1$, 1.2 eV for $1 < \epsilon$.

Co-monomer	Designation	Weight-%	Mol-%	Branches per 1000 backbone atoms	Density (g/cm^3)	Molecular weight	Degree of crystallinity (after [196])
butene	EB-37	6.8	3.7	21	0.917 ^{a)}	119,300	0.45
	EB-69	12.8	6.9	38	0.901 ^{a)}	154,300	0.35
	EB-79	14.6	7.9	44	0.897	105,600	0.32
	EB-100	18.2	10.0	56	0.8873	96,300	0.27
octene	EO-20	7.4	2.0	11	0.8664	197,100	0.52

Table 4.6.1: Parameters of samples investigated.

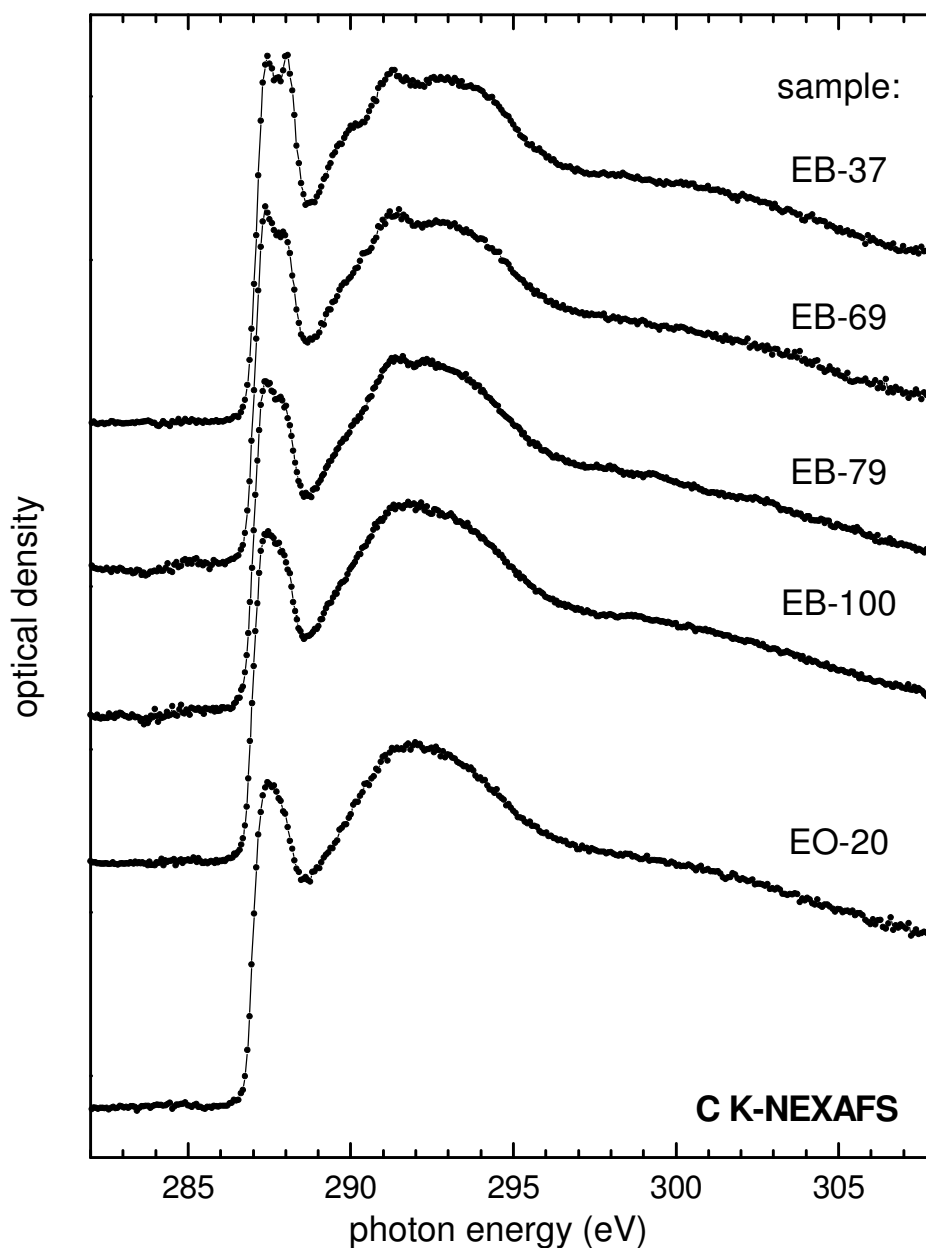


Figure 4.6.1: High energy resolution C 1s NEXAFS spectra of the copolymers listed in Table 4.6.1. The edge-jump was normalized identically for each spectrum, and the spectra are offset for clarity.

4.6.3 Results and discussion

Figure 4.6.1 presents the transmission C 1s NEXAFS spectra of the copolymer samples specified in Table 4.6.1. It can be readily observed that for low branching ratio and short branch length (ethylene-1-butene EB-37, EB-69) a predominant double peak at 287.4 eV and 288.0 eV is visible, whereas for high branching ratio (EB-100) or long branch length (EO-20) the feature reduces to a broad single peak with a high energy shoulder. A corresponding, similar behaviour can be seen in the σ^*_{C-C} region. Three features are visible at 290.1 eV,

291.3 eV and 292.9 eV for the EB samples with low comonomer content, but progressively disappear into a broad structure for higher branching ratios. The ethylene-1-octene (EO) sample shows only broad features.

The qualitative behaviour of the 1-butene sequence is readily understood. It is well known that the volume fraction of the crystalline phase of ethylene-1-alkene copolymers, i.e. the degree of crystallinity, is strongly dependent on the comonomer content [196]. The degree of crystallinity ranges from 0.7 for the homopolymer, and, after an initial drop to about 0.55 for 2 mol% comonomer content, shows an almost linear decrease with increasing copolymer content to about 0.2 for 15 mol% copolymer. For comonomers larger than C₃, the crystallinity does not depend on the length of the non-crystallizable comonomer, but is rather determined by the comonomer content, i.e. the branching ratio, which controls the length of the crystallizable chain between branches [196].

To confirm the influence of crystallinity, we heated an EB-37 sample progressively to higher temperature. Results by Alizadeh et al. using calorimetric methods have shown that at about 40°C below the melting point, the degree of crystallinity starts to decrease substantially from

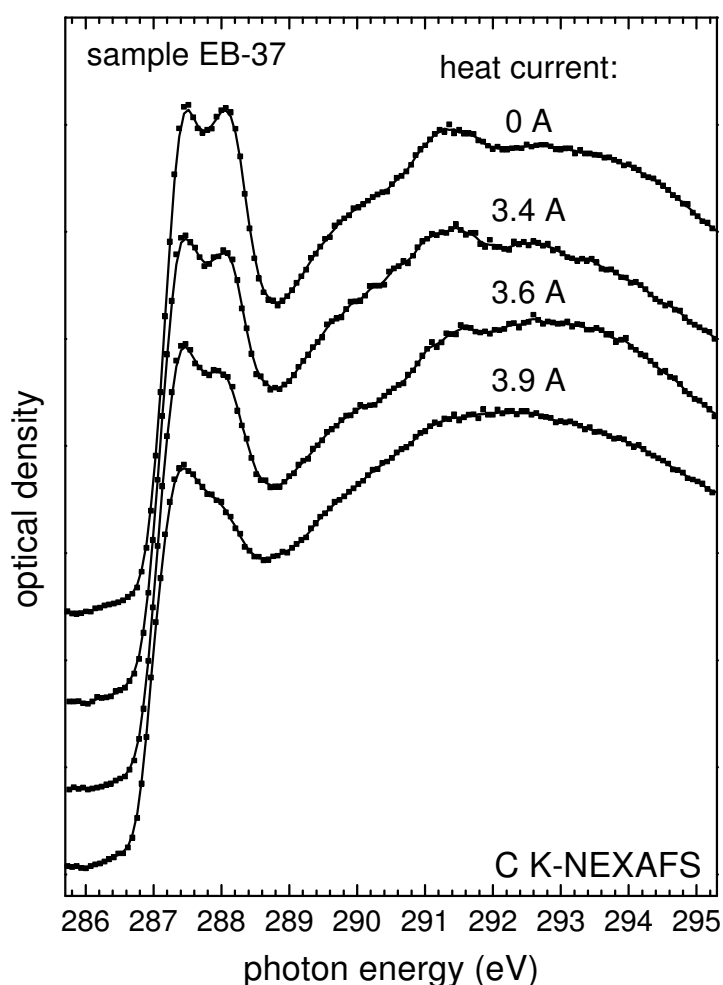


Figure 4.6.2: High energy resolution C 1s NEXAFS spectra of heated EB-37. Sample currents as indicated are an indirect measure of temperature. The sample melted and was destroyed for $I > 3.9$ A. The edge-jump was normalized identically for each spectrum, and the spectra are offset for clarity.

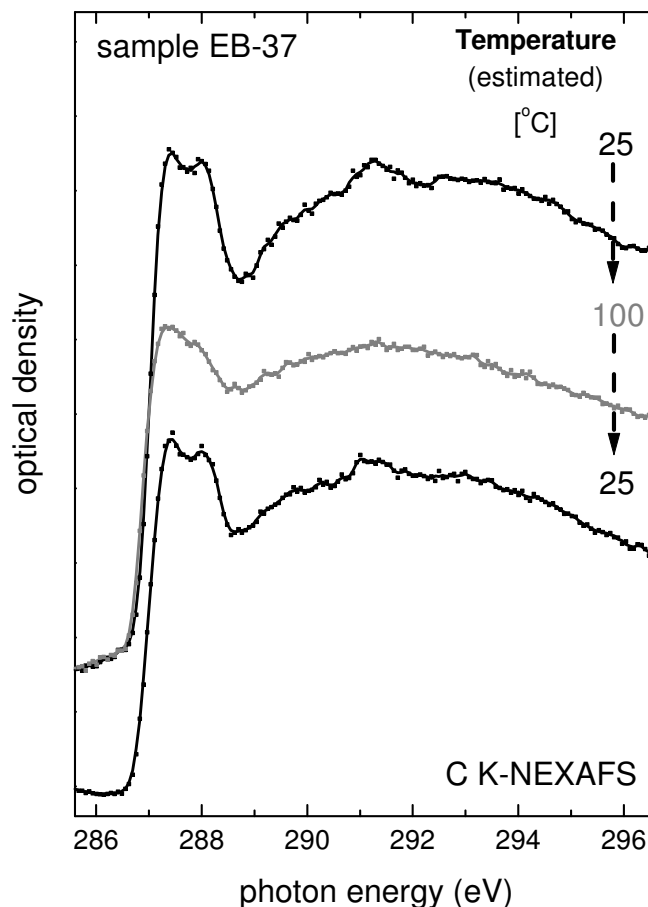


Figure 4.6.3: C K-NEXAFS spectra recorded while the EB-37 sample was heated from room temperature close to the melting point (estimated temperature 100°C) and subsequently cooled off to RT. The spectra clearly prove the reversibility of the crystalline amorphous phase transition.

the low temperature asymptotic limit [196]. Thus, another sequence of samples covering a range of crystallinity could be produced. The results of these heating experiments are presented in Figure 4.6.2, with the TEM grid heated with a current of 0, 3.4, 3.6 and 3.9 A, respectively. Unfortunately, no direct temperature measurement was possible given the tight space constraints of the x-ray microscope. Since the sample was destroyed above 3.9A, we conclude that at this current the melting temperature of about 110°C has been reached or exceeded. For a different EB-37 sample we confirmed the reversibility of the crystalline-amorphous phase transition, which is illustrated by Figure 4.6.3. The sample was heated to approximately 100°C until the double peak disappeared. The heating current was then turned off and the sample cooled off to room temperature, clearly yielding the same spectral signature as the EB-37 sample before the heat cycle.

For a semi-quantitative analysis, we fitted the spectra to the smallest number of peaks that resulted in good fits. We achieved excellent fits in the 287-298 eV range with 3 Voigt functions constrained to the same width. The number of fitted peaks can be mapped onto prior theoretical calculations [194] as well as onto our own calculations (see below). The fit of EB-69 is shown as an example in Figure 4.6.4. The extracted spectral intensities of all ethylene-1-alkene copolymers are plotted in Figure 4.6.5 against the degree of crystallinity.

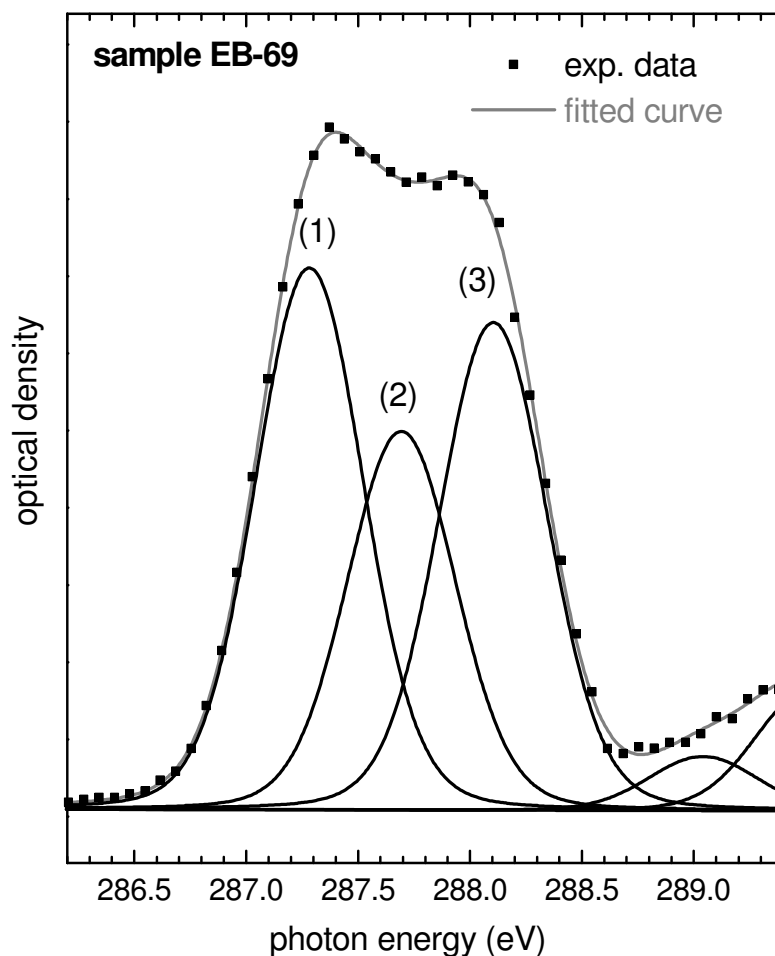


Figure 4.6.4: Three-peak fit of the low-energy features in the NEXAFS spectrum of sample EB-69. To eliminate background influence a step function was subtracted and two more peaks at higher energies were fitted

Within experimental error, a systematic, essentially linear trend can be observed for the EB samples. The peak energies of the EB samples also show systematic, monotonic trends: peaks (1) and (2) shift slightly to lower energies for smaller crystallinity, while the energy of peak (3) remains the same. The values for EB-37 and EB-100 are summarized in Table 4.6.2. The observed changes in the spectra of the EB sequence can be qualitatively explained by spectral contributions of two phases, amorphous and crystalline, which each have different spectra. As the crystallinity decreases, and hence the average density, the double peak structure vanishes. Hence, the 287.4 eV and 288.2 eV peaks (labelled (1) and (3) in Figure 4.6.4) are signature features of high density crystallites.

In contrast to the low comonomer EB samples, the EO-20 material has a markedly different spectrum; rather featureless broad peaks that, at first sight, appear to be from a totally amorphous, low-density copolymer. However, the crystallinity of EO-20 is about 52%, and thus higher than the crystallinity of EB-37 [196]. The explanation for the observed spectral difference can thus not be due to differences in crystallinity or to differences in conformation populations. The crystallites in both samples consist of planar all-trans chain segments; samples with the same crystallinity have similar trans and gauche populations. Rather, wide-angle x-ray scattering and electron microscopy have shown that the EO has smaller

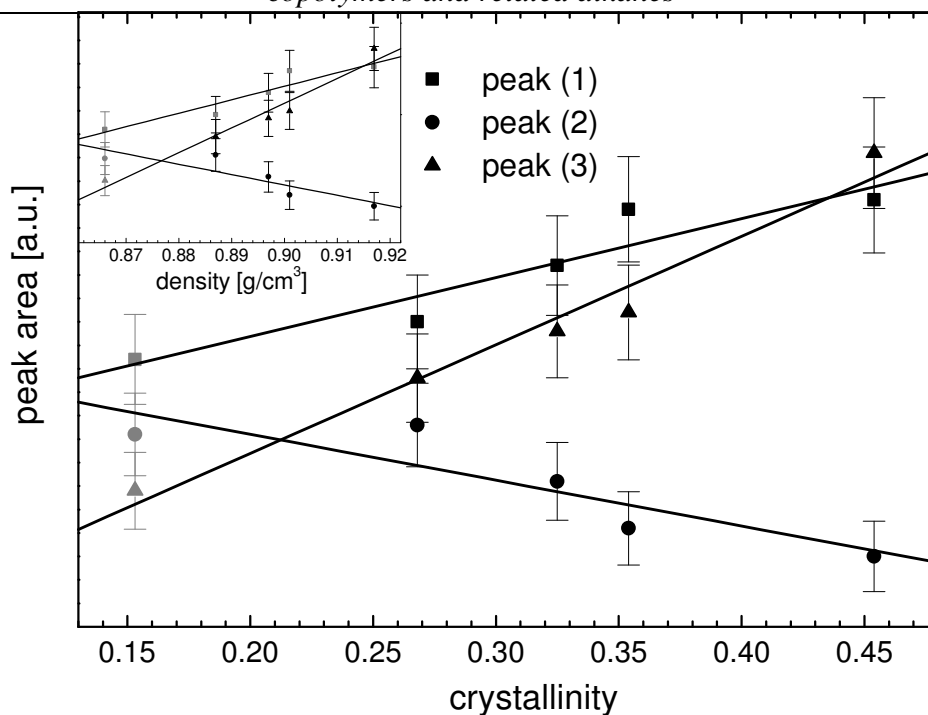


Figure 4.6.5: Spectral intensities of EB and EO samples plotted against degree of crystallinity. The dark symbols represent EB-samples, the grey symbols the EO-20 sample. Inset: NEXAFS intensities plotted against polymer density

crystallites than EB in which the lattice, particularly the a-axis of the orthorhombic unit cell, is expanded due to differences in interfacial stress [195]. The increased lattice spacing results in larger intermolecular distances in the crystallites, changing the intermolecular interaction and, as we are forced to conclude, the spectra: Peaks (1) and (3) are greatly decreased compared to EB-37, while peak (2) is relatively pronounced, as derived from the fit analysis. The low density of EO-20 (see Table 4.6.1) is a reflection of the expanded crystal structure. When plotting the peak intensities of the EO and EB samples against density (see inset to Figure 4.6.5), we can see that the peak intensities of the EO sample fit well with a picture in which the average intermolecular distances and hence the material density determines the NEXAFS spectra.

In order to confirm the origin of these spectral changes, we explored the sensitivity of the spectra to various geometries with ab initio calculations. Virtually no differences were found between all-trans, all-gauche conformations and a combination of trans and gauche conformations. Similarly, the sensitivity to chain length and branching was explored, but only very small changes could be observed. Only intermolecular interaction resulted in significant changes. Figure 4.6.6 shows the calculated C-K NEXAFS spectra for two butane molecules in two different geometries: on the left hand side of Figure 4.6.6, the butane molecules are parallel (see sketch on the upper left; the planes represent the C-C planes), on the right hand side of Figure 4.6.6, the butane chains are crossed. The resonances numbered 1, 2a, 2b, and 3 contribute to the energy region that we fitted. (Note, that we refer to peaks derived from fitted data as (1), (2), (3) and to peaks in the calculation as 1, 2, 3.) The predicted energies are about 2 eV higher than those of the experiment.

If the distance between the molecule centers is decreased from 3.8 Å to 3.2 Å (Figure 4.6.6a) or 3.4 Å (Figure 4.6.6b), respectively, resonances 2a and 2b are significantly reduced,

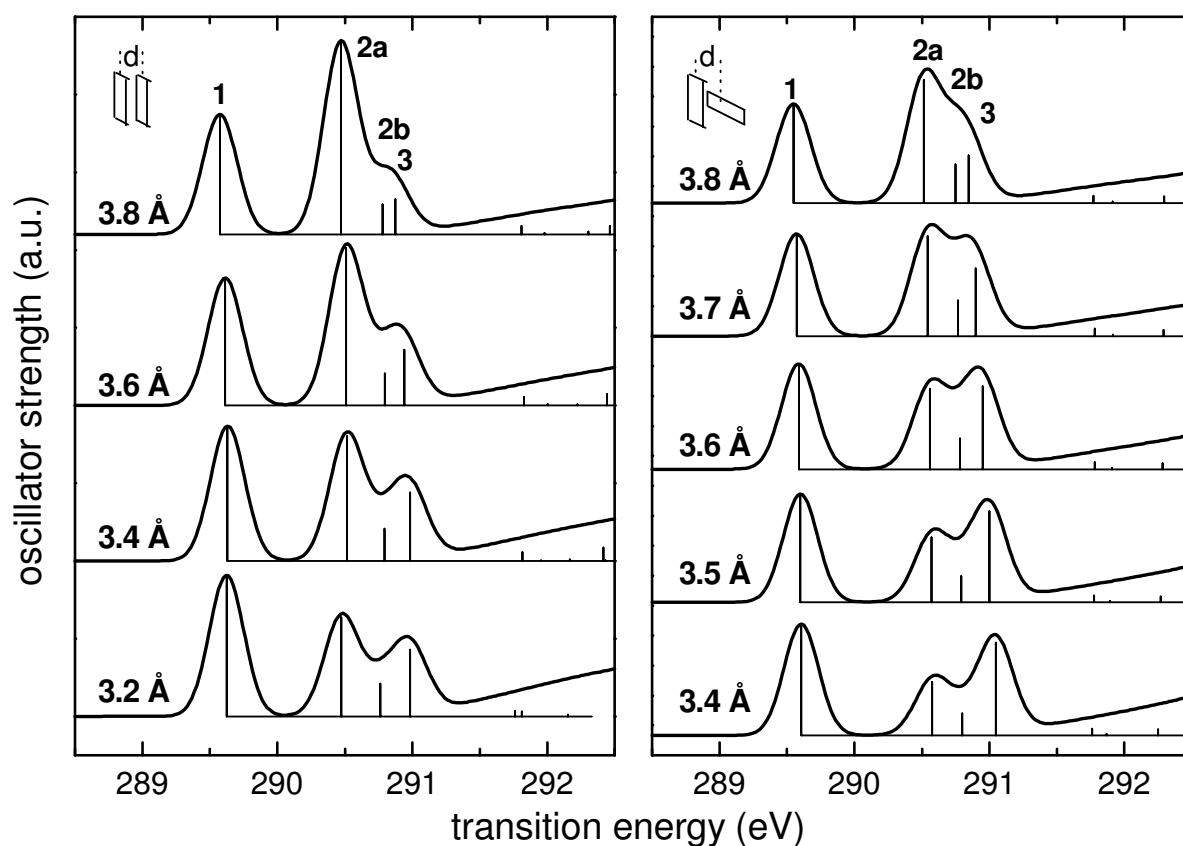


Figure 4.6.6: Calculated spectra for two butane dimers (parallel: left and perpendicular: right) and several intermolecular distances. (Plotted on a common intensity scale to aid discerning the absolute changes in intensity. Individual spectra offset for clarity.)

whereas the intensities of the resonances 1 and 3 are increased. The transition energies of the three main resonances 1, 2a, and 3 shift slightly towards higher energies for smaller separation. The transition energies and relative intensities of the four resonances 1, 2a, 2b, and 3 are summarized in Table 4.6.2 and can be compared against the experimental values for EB-37 and EB-100. The experimental data itself and the comparison to the results of the ab initio calculations lead to the conclusion, that differences in the intermolecular distances account for the observed variations in the electronic structure of all samples.

Our observations illuminate several important issues regarding the spectroscopy and the electronic and geometric structure of PE in particular and long chain alkanes in general:

- (i) Generally, Rydberg states present in small molecules are quenched in condensed systems. The degree to which that happens is still under discussion [193]. However, it seems reasonable to assume that Rydberg states will be quenched, rather than enhanced, by encroaching nearest neighbours. Since the 287.4 eV and 288.1 eV features are enhanced, in theory and experiment, in the highest density copolymers, these features can not be dominated by Rydberg character. We thus assign primarily C-H σ^* character to peaks (1) and (3). Intermediate peak (2), at 287.7 eV, gets indeed quenched and has the most Rydberg character. Our assignments are in agreement with Stöhr et al. [189] and Väterlein et al. [194], but at variance with Bagus et al. [193].

Resonance	1	2a ^{a)}	2b ^{a)}	3 ^{a)}
Symmetry in butane	A'	A''	A'	A''
Present calculation				
Parallel geometry				
Energy/eV d=3.8Å	289.58	290.47	290.78	290.88
d=3.2Å	289.63	290.47	290.77	290.99
Rel. intensity d=3.8Å	=1 ^{b)}	1.59	0.25	0.29
d=3.2Å	1.18	0.83	0.27	0.56
Crossed geometry				
Energy/eV d=3.8Å	289.55	290.52	290.75	290.85
d=3.4Å	289.60	290.58	290.80	291.05
Rel. intensity d=3.8Å	=1 ^{b)}	1.24	0.39	0.48
d=3.4Å	1.12	0.54	0.22	0.94
X α -calc. for propane[194]				
Symmetry, assignment	5a1,3s/(C-H)*	3b1, 3p	6a1,3p/(C-H)*	
Energy/eV (rel. to IP)	-3.97	-2.81	-2.57	
Experimental data				
Peak-number	(1)	(2)	(3)	
Energy/eV EB-100	287.22	287.66	288.11	
EB-37	287.32	287.70	288.11	
Rel. intensity EB-100	=1 ^{b)}	0.89	0.94	
EB-37	1.11	0.74	1.16	

Table 4.6.2: Summary of experimental and theoretical results. The labeling of resonances refers to calculations (1,2,3,4) and experiments ((1),(2),(3)).

- (ii) In deriving experimental support for a Rydberg assignment from angle dependent spectra of a thick layer of heptatriacotane, Bagus et al. performed a fit with six peaks in the 287-289 eV energy region and assumed the existence of a sizable vibrational component for the crystalline phase at an energy of 287.7 eV [193]. The spectral dependence observed in our copolymer samples with variable crystallinity excludes the existence of such a vibrational component: the higher the crystallinity in the EB sequence, the lower the spectral intensity at 287.7 eV (peak (2)). Hence, the component fitted by Bagus et al. as “crystalline” corresponds to peak (2) in our analysis: an intrinsic resonance, rather than a vibrational overtone, with the largest Rydberg character.

- (iii) The simultaneous changes, i.e. “splitting” of the $\sigma^*_{\text{C-H}}$ /Rydberg and $\sigma^*_{\text{C-C}}$ features as a function of intermolecular interaction, suggest a common or related underlying cause.
- (iv) Conformational changes do not directly cause major spectral changes. This has been previously commented on by Weiss et al. based on calculations that explored matrix effects [84]. Our conclusion that conformational effects are negligent can be drawn directly from experimental observations. The spectral changes that we observe arise from different “packing” in a solid.

4.6.4 Summary

In summary, we have developed an improved understanding of the C 1s NEXAFS spectroscopy of high molecular weight bulk ethylene-1-alkene copolymers. The experimental data cannot be explained by a conformational, or intramolecular, dependence of the electronic structure, but only through complex intermolecular interactions that enhance or quench spectral features as a function of distance. The experimental data support the assignment of dominant $\sigma^*_{\text{C-H}}$ character for the low energy features (1) and (3). Our results suggest caution in using molecular model analogues (i.e., “building-block” approach) in order to interpret NEXAFS spectra. However, they clearly show that a local electronic probe such as NEXAFS is rather sensitive to intermolecular interaction and hence to subtle differences in some polymeric materials. This effect can be put to good use. For example, the observed effect can serve as a contrast mechanism in polymer NEXAFS microscopy [183,200] and opens up a variety of very useful applications in polymer science. The morphology in polyolefin blends has already been imaged without having to resort to chemical etching or staining [201].

5 Appendix

5.1 Radiation damage study on PTCDA multilayers

One of the crucial problems the experimenter has to deal with when performing spectroscopic experiments on organic substances is the high sensitivity of macromolecules to radiation damage. Degradation of the investigated samples was observed for all kinds of organic materials, from one ring aromates via polymers to biologic tissues. This is, of course, particularly important, if the experiment includes high photon exposures of the sample, as it is the case for many modern synchrotron based methods. Especially micro-spectroscopic (e.g. STXM, see Chapter 4.6) and spectro-microscopic (e.g. SMART or PEEM) techniques are well-known to require very high photon flux densities, but also for x-ray emission spectroscopy a very high intensity of the synchrotron light is important due to the low cross section of the fluorescence decay (see Figure 2.6 in Chapter 2.2) of light atoms (carbon, oxygen, nitrogen, sulphur ..), that are the main components of organic matter.

To get a feeling for the timescale of radiation damage, that we have to expect during the NEXAFS and XPS experiments on our systems, a damage study was performed on PTCDA multilayers on Ag(111) at the U49/1-PGM beamline in 10/2001. For that purpose the undulator was set to 200 eV and the monochromator to zero order, to obtain a high flux density on the sample of about $1 \cdot 10^{15}$ photons/s \cdot mm²·100 mA. The sample was then exposed to the synchrotron light for a certain time; XPS C 1s and O 1s spectra where recorded subsequently. The resulting data is displayed are Figure 5.1.1.

The data clearly show, that radiation damage leads to a stronger decrease of the O 1s (Figure 5.1.1.b) intensity, if compared to the C 1s data (Figure 5.1.1.a). This has to be interpreted as desorption of oxygen, that is split off from the anhydride group. Furthermore, if the relative intensities of the two oxygen species in Figure 5.1.1b are compared, the stronger decrease of the peak at 532 eV clearly shows, that the double bonded oxygen species is removed from the PTCDA molecule with a relatively high cross section.

While the damage occurs, in the C 1s data (Figure 5.1.1a) a strong decrease of the anhydride carbon peak can be observed, that is due to either the complete loss of the anhydride group or to the change of the chemical environment of the anhydride carbon atoms, when the oxygen is removed from the functional group. Thus, with increasing exposure, the spectroscopic fingerprint shows a proceeding transformation of the sample towards a graphite like species.

Note, that in the normal experimental set-up with monochromatic light between 300 eV and 700 eV no signs of radiation damage could be observed on the timescale of 2-3 hours. The generally applied photon flux density of about $2 \cdot 10^{12}$ photons/s \cdot mm²·100 mA is about 3 orders of magnitude smaller than the densities used in this damage study. In addition, to completely exclude even minor influences of the synchrotron radiation in our normal experiments, the sample was routinely moved after each spectrum to minimize the local exposure.

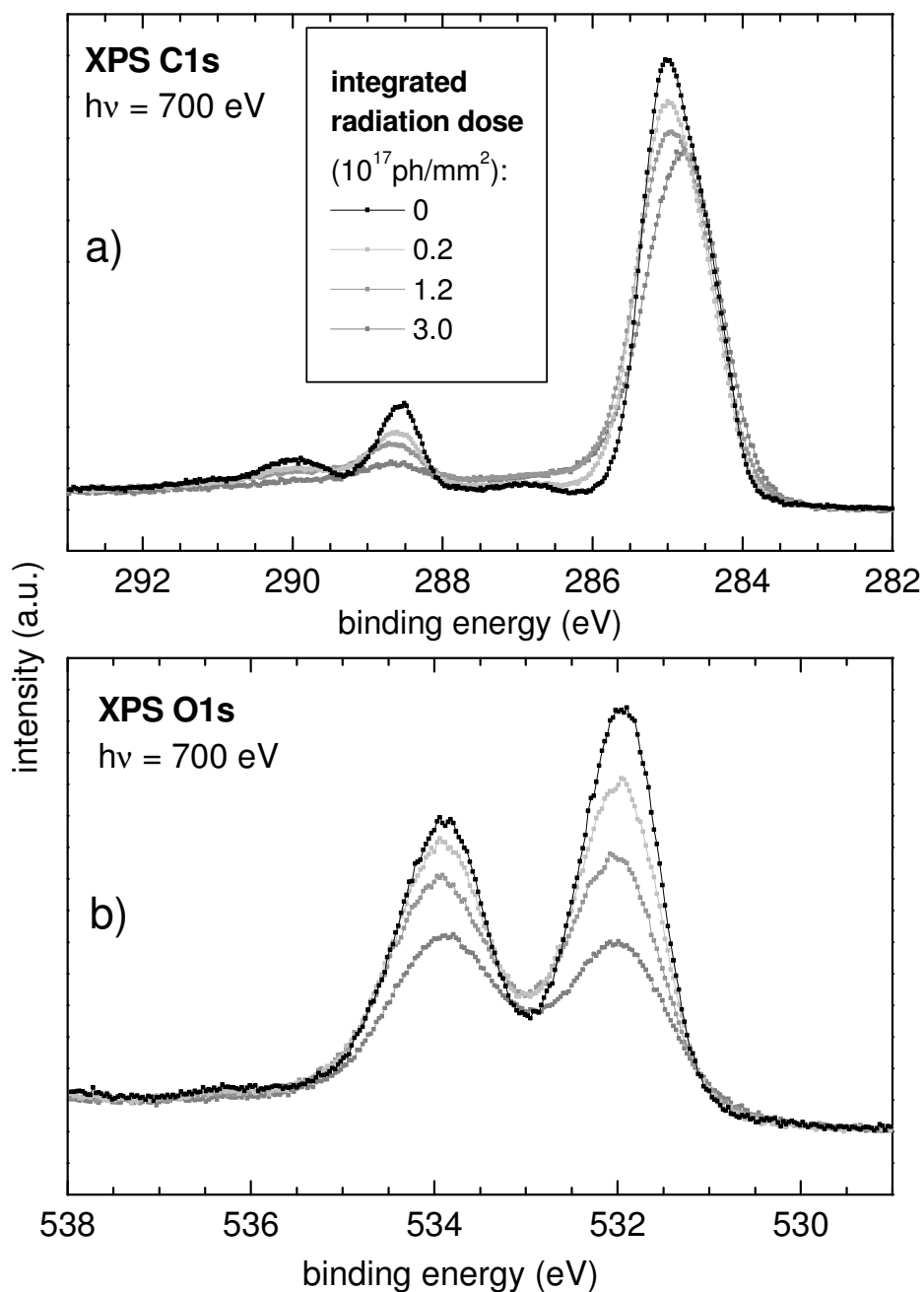


Figure 5.1.1: XPS C 1s (a) and O 1s spectra (b) of PTCDA multilayers (ca. 10 ML) on Ag(111) recorded after the sample was exposed to the denominated doses of zero order synchrotron light at the U49/1-PGM beamline. The spectra were taken with a photon energy of 700 eV and a constant analyser pass energy of 40 eV.

5.2 Calculated NEXAFS spectra

In this chapter additional calculated NEXAFS data will be presented, that were so far not published but might be helpful for future projects.

The calculations were performed with the program GSCF3 according to Chapter 2.3. The energy of the calculated spectra was aligned to fit the lowest energy NEXAFS resonance in the corresponding experimental spectrum. Note that all calculated energy scales appear stretched, which was mentioned before and is well-known for this and similar *ab initio* methods, depending on the applied basis set.

5.2.1 3,4,9,10-perylene-tetracarboxylic acid dianhydride (PTCDA)

Figure 5.2.1 shows the molecular structure of the PTCDA molecule. The distinct carbon (C1 – C7) and oxygen atoms (O1 – O2) with chemically different environment, that have to be respected in the calculations, are labelled. The high number (seven) of chemically different carbon sites in PTCDA makes an interpretation of the C K-NEXAFS data relatively complicated. The superposition of the spectra of the different core sites leads to various resonances in the calculated spectra, as can be derived from Figure 5.2.2, where the GSCF3 calculated C K-NEXAFS spectrum (bottom) is compared to the experimental data. The experimental spectrum was already presented and discussed in Chapter 4.2.3.

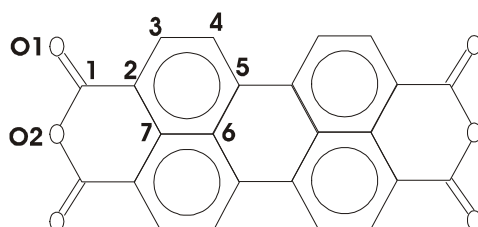


Figure 5.2.1: Structure model of the PTCDA molecule. The seven chemically different carbon atoms C1 – C7 and the two oxygen atoms O1 - O2 are labelled.

Nevertheless, the calculations can explain the most important contributions to the NEXAFS peaks, as indicated by the guidelines in Figure 5.2.2. Peak 3 and 4 (at 288 eV and 289 eV, respectively) are mainly due to C 1s \rightarrow LUMO and LUMO+1 transitions at the anhydride group carbon atom, in strong analogy to the interpretation of the anhydride molecules NTCDA and NDCA in Chapter 4.2.

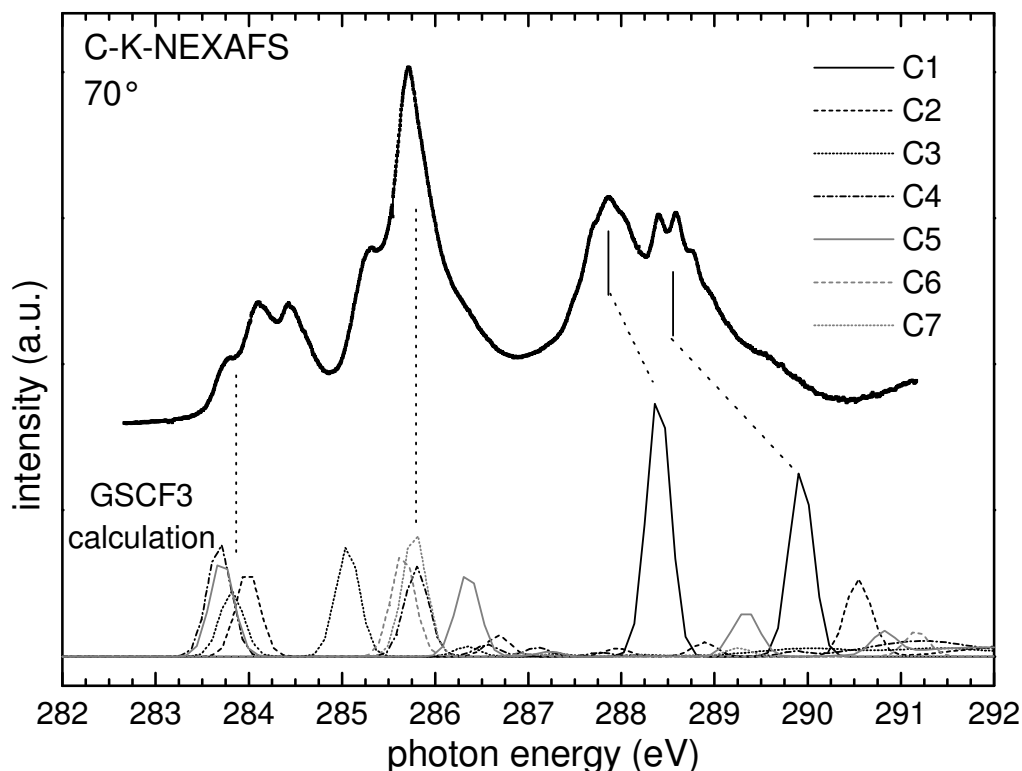


Figure 5.2.2: Calculated C K-NEXAFS data for PTCDA compared to the experimental data recorded at the UE49/1-PGM beamline at BESSY II. The spectra were recorded with grazing incidence and horizontal polarization of the synchrotron light on a PTCDA multilayer sample (ca. 10 ML).

5.2.2 Naphthalene

The molecular structure of naphthalene can be derived from Figure 5.2.3. Three chemically different carbon sites have to be considered for the calculation. The result of the GSCF3 calculation is plotted in Figure 5.2.4, together with experimental C K-NEXAFS data of condensed naphthalene multilayers on Ag(111). The spectra were recorded in 01/2002 at the U49/1-PGM beamline at BESSY II with grazing incidence of the horizontally polarised synchrotron light.

The calculation reproduces the experimental data very well and the assignment of the various

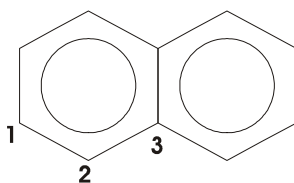


Figure 5.2.3: Structure model of the naphthalene molecule, The chemically different carbon atoms C1 – C3 distinguished in the calculation are labelled.

calculated transitions to the experimental peaks is indicated by the guidelines in Figure 5.2.4. The first experimental π^* -resonance, that shows well resolved vibronic fine structure, can thus be attributed to two $C\ 1s \rightarrow LUMO$ transitions with the core hole at the two carbon atoms with hydrogen bonds (C1 and C2, respectively).

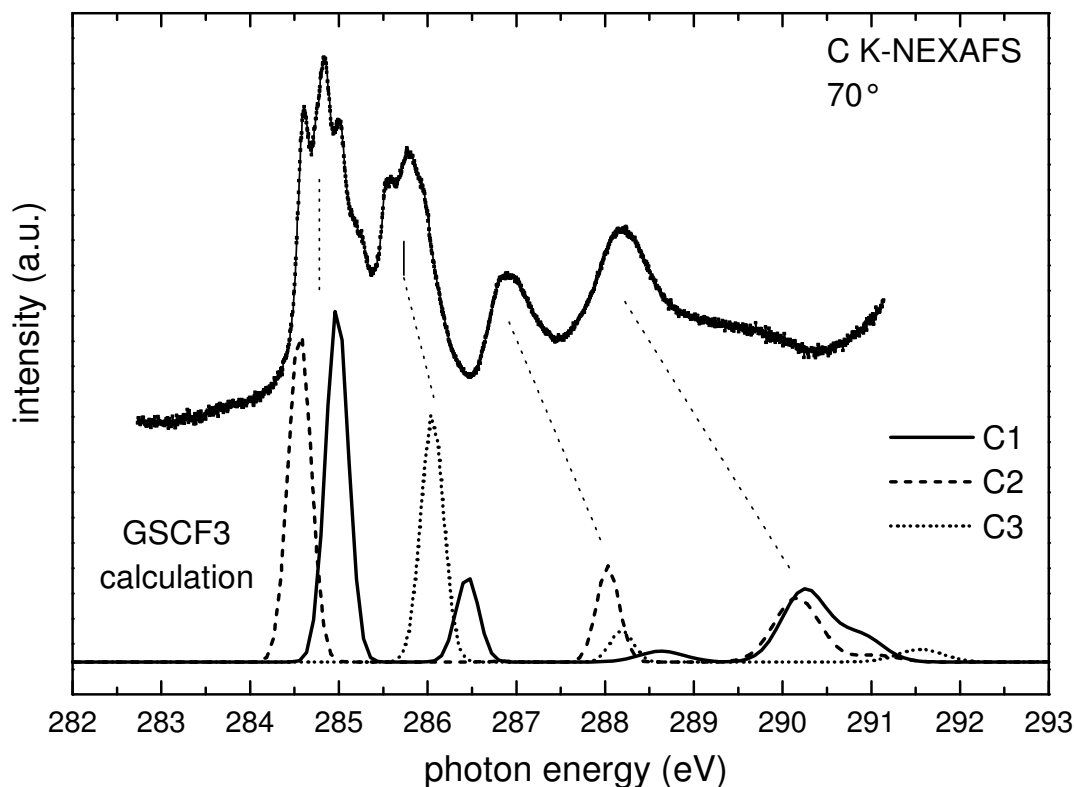


Figure 5.2.4: Calculated C K-NEXAFS data for naphthalene compared to the experimental data recorded at the UE49/1-PGM beamline at BESSY II. The spectra were recorded with grazing incidence and horizontal polarization of the synchrotron light on a naphthalene multilayer sample (ca. 20 ML).

5.2.3 Perylene

The molecular structure of perylene is plotted in Figure 5.2.5. Six chemically different carbon atoms (labelled 1-6 in Figure 5.2.5) have to be considered in the GSCF3 calculation. Figure 5.2.6 shows the *ab initio* calculated C K-NEXAFS spectrum (bottom) together with the experimental data (top). The experimental curve was recorded at the UE52/PGM beamline in 02/2003 on a multilayer film on $Al_2O_3/NiAl(111)$. The molecules were preferentially oriented upright and thus the spectrum presented in Figure 5.2.6 was recorded with grazing incidence and vertical polarisation of the synchrotron light. If the energy stretch is taken into account, the calculated data fit the experimental spectrum very well and allow the interpretation of all observed peaks, as indicated by the guidelines in Figure 5.2.6.

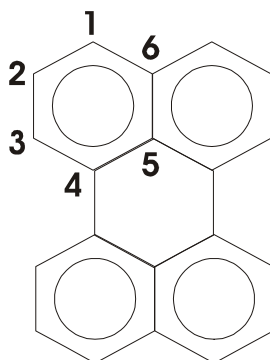


Figure 5.2.5: Structure model of the perylene molecule. The chemically different carbon atoms C1 – C6 distinguished in the calculation are labelled.

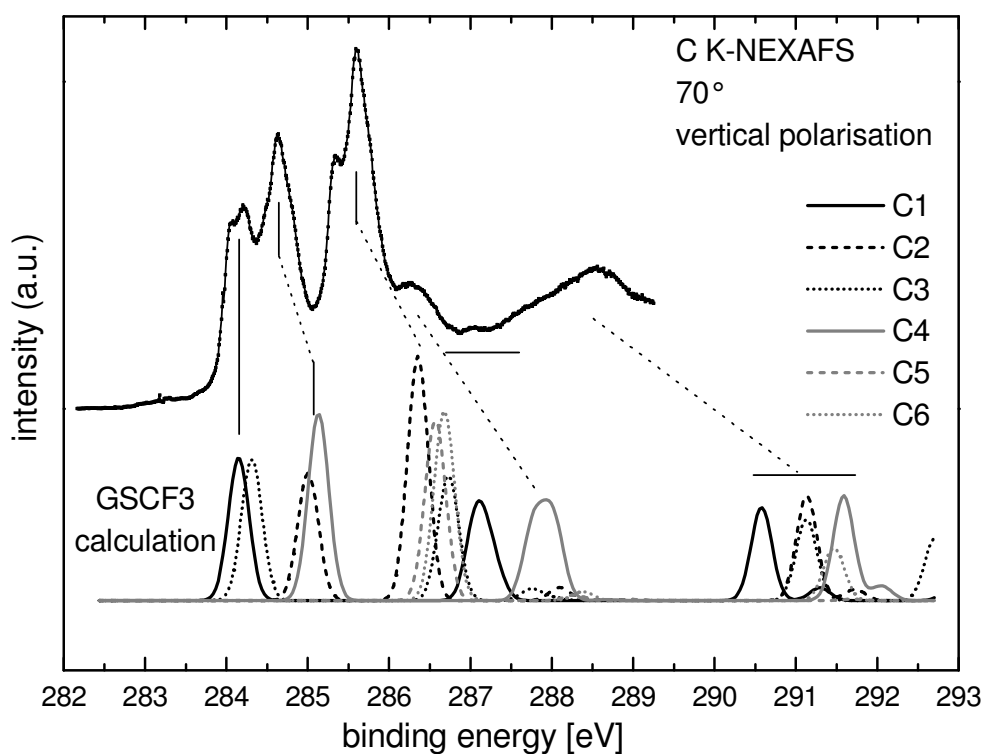


Figure 5.2.6: Calculated C K-NEXAFS data for perylene compared to the experimental data recorded at the UE52/PGM beamline at BESSY II. The spectra were recorded with grazing incidence and vertical polarization of the synchrotron light on a perylene multilayer sample with preferentially upright oriented molecules (ca. 10 ML).

5.2.4 Tetracyanochinondimethan (TCNQ)

The molecular structure of Tetracyanochinondimethan (TCNQ) is plotted in Figure 5.2.7, where also the four chemically different carbon atoms C1 – C4 are labelled. The experimental C K- and N K-NEXAFS spectra of TCNQ multilayers on Ag(111) were recorded by C. Buchberger [71] at the PM1 beamline at BESSY I in 1998. The molecules build almost

perfectly flat lying films as indicated by the strong NEXAFS dichroism in the spectra in Figure 5.2.8. The spectra are compared to GSCF3 calculated data, that are plotted underneath the corresponding experimental spectra in Figure 5.2.8. The dichroic behaviour of the TCNQ film is very well reproduced by the calculated spectra. For normal incidence of the horizontally polarised light the C K- as well as the N K-data are dominated by one π -

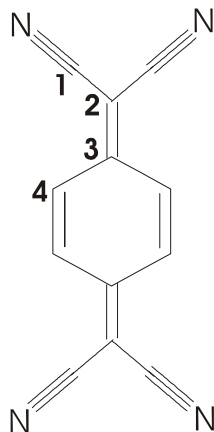


Figure 5.2.7: Structure model of the TCNQ molecule. The chemically different carbon atoms C1 – C4 distinguished in the calculation are labelled.

resonance, that can be attributed to the C-N threefold bonding. By comparison with the calculations these peaks can be assigned to C1 $1s \rightarrow$ LUMO and N $1s \rightarrow$ LUMO transitions, respectively.

Note, that NEXAFS experiments with increased energy resolution were performed at the U49/1-PGM beamline in 10/01 in order to resolve the vibronic fine structure. However, due to the much higher photon flux density of the undulator beamline compared to the dipole beamline PM1 significant radiation damage occurred on the time scale of the NEXAFS experiments, even if the smallest exit slit (10μ) and the pinhole were utilized to minimize the exposure.

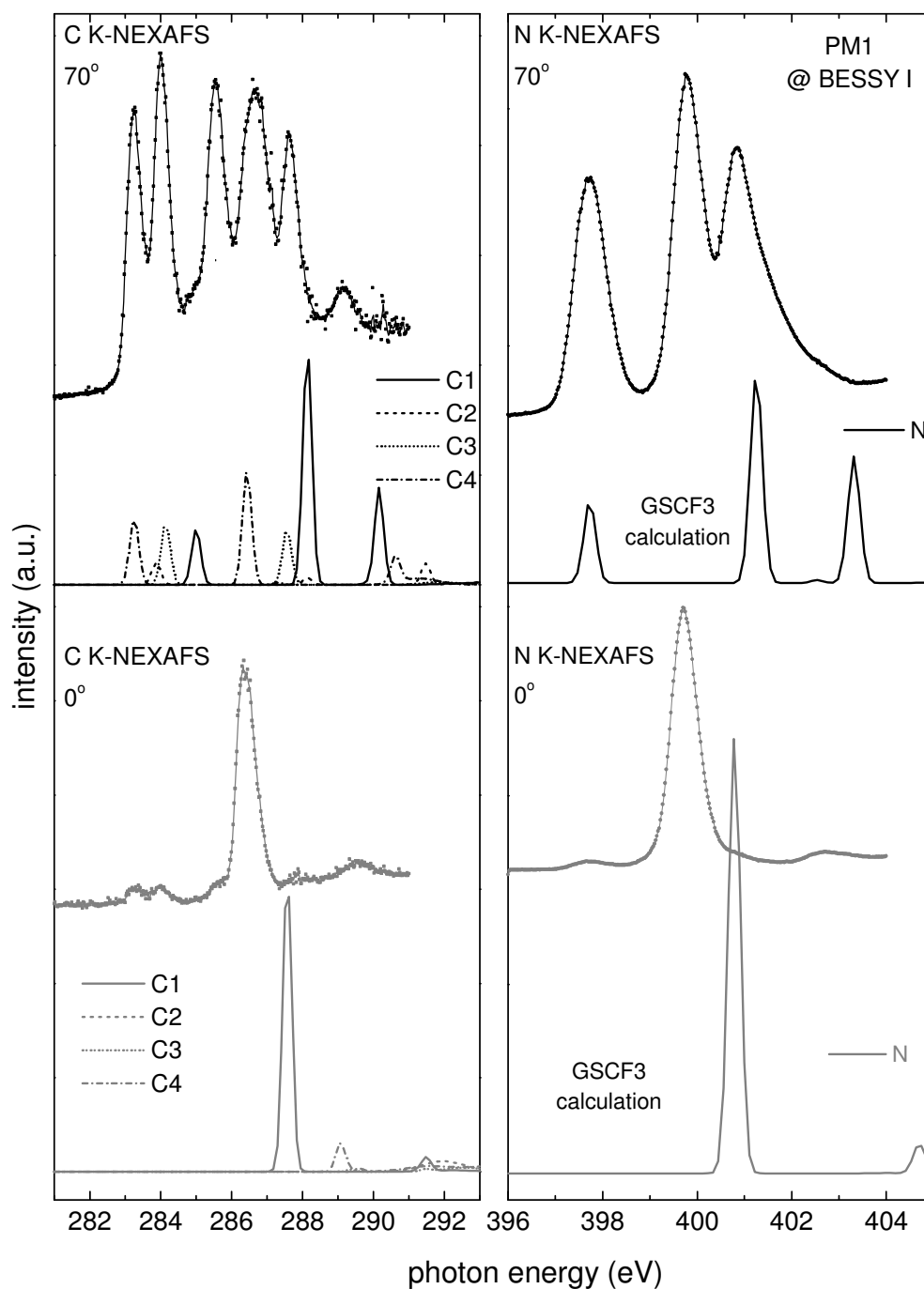


Figure 5.2.8: Calculated C K- (left) and N K-NEXAFS data (right) for the molecule TCNQ compared to experimental data (from Ref. [71]) recorded at the PM1 beamline at BESSY I. The spectra were taken with grazing (top) and normal incidence (bottom) of the synchrotron light, respectively, and the spectra reflect the respective polarisation (see text).

5.3 LEED pictures of additional NTCDA monolayer phases on Ag(111)

During the investigation of the NTCDA phase transition on Ag(111) (see Chapter 4.5) additional phases could be identified by SPA-LEED measurements. Starting with the relaxed NTCDA monolayer (see Chapter 4.4) at room temperature (RT), the sample was cooled down with approximately -10 K/s to the specified temperatures. The sample was then kept at this temperature for about 2-4 h until the LEED structures could be observed. All SPA-LEED pictures were recorded with an electron energy of 28 eV. Note, that especially the pictures at 180 K and 240 K show an extremely low signal to background ratio and can thus most probably not be detected with a common LEED apparatus and a fluorescence screen.

Between all presented phases reversible phase transitions could be demonstrated, i.e. all phases could equally well be generated by cooling from the next higher temperature phase or by heating from the next lower temperature phase.

5.3.1 220 K structure

The LEED structure displayed in Figure 5.3.1 was recorded after the relaxed NTCDA monolayer was cooled to 220 K. The picture can be explained by a super structure with the super structure matrix $\begin{pmatrix} 5 & 4 \\ 1/3 & 3 \end{pmatrix}$. The experimental data is compared to the simulated LEED

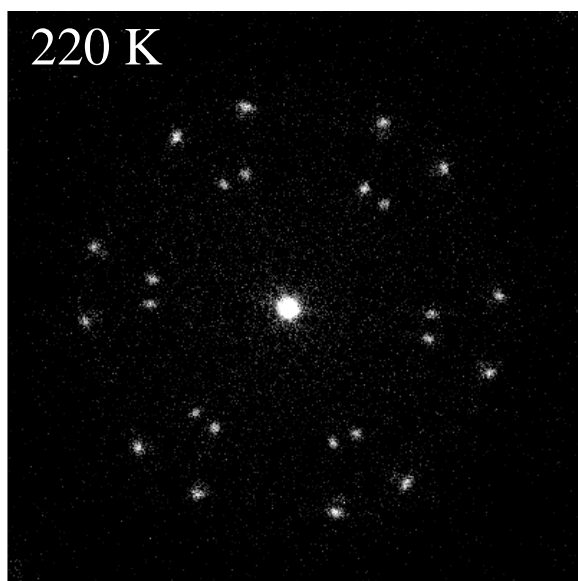


Figure 5.3.1: SPA-LEED picture recorded after the relaxed monolayer film was cooled to 220 K.

pattern in Figure 5.3.2a. The structure is in third order commensurate, and a possible real space structure is suggested in Figure 5.3.2b. In this model the molecules form rows with their long sides touching each other. The unit cell contains one molecule, and the area per molecule (i.e. the area of the unit cell) is with 100 \AA^2 considerably larger than for the relaxed monolayer at room temperature (87 \AA^2 , see Ref. [65]). Since the transition from the RT structure to the 220 K phase is completely reversible and no desorption of molecules could be demonstrated by XPS (see Chapter 4.5), this structure can only exist together with additional, more densely packed domains, that account for the lack of molecules. Since no signature of this additional phase can be observed in the LEED picture, it should be lacking of any long range order.

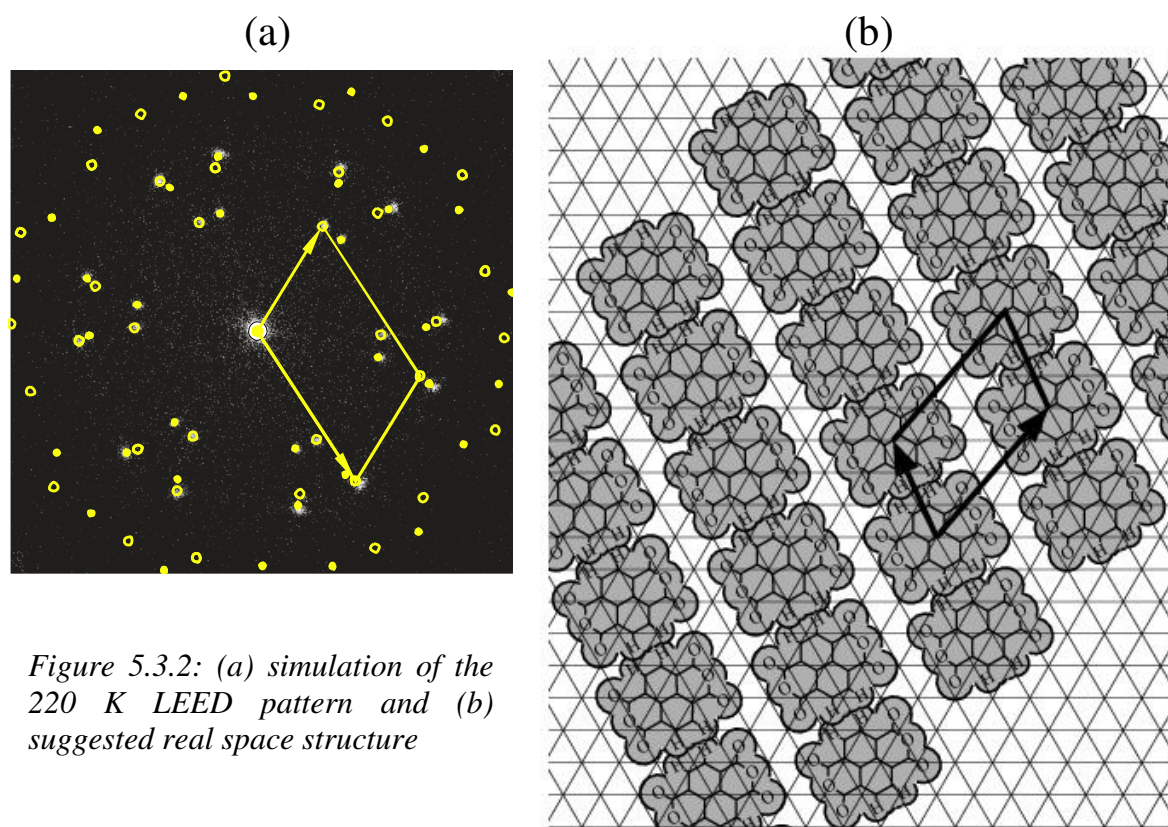


Figure 5.3.2: (a) simulation of the 220 K LEED pattern and (b) suggested real space structure

5.3.2 180 K structure

If the relaxed monolayer sample is cooled to 180 K, the LEED picture displayed in Figure 5.3.3 can be observed. Note, that the sample had to be cooled for more than four hours until the picture of Figure 5.3.3 appeared, thus indicating the long time scale of the corresponding phase transition. Only six super structure spots are visible, which are arranged in the same direction as the substrate spots. The length of the reciprocal super structure vector is a third of the substrate vector. The very low signal to background ratio and low sharpness of the spots indicates a small size and a low quantity of the ordered domains.

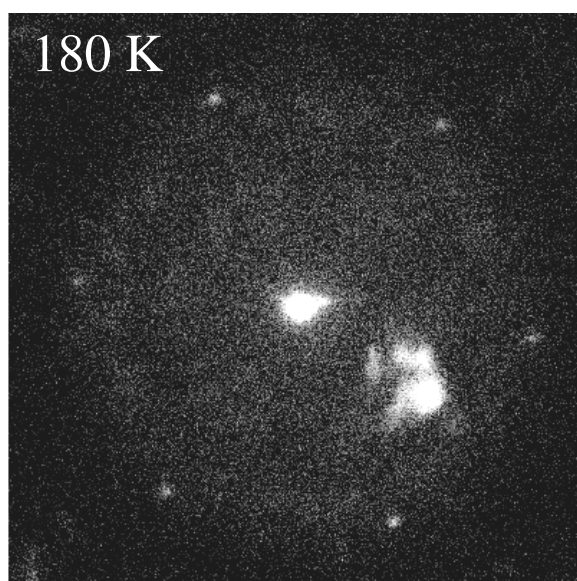


Figure 5.3.3: SPA-LEED picture recorded after the relaxed NTCDA monolayer sample was cooled to 180 K.

Finding an adequate real space structure in agreement with the information of the LEED picture is a hard task, since only one vector is defined by Figure 5.3.3. In this direction, however, the real space super structure vector is three times the Ag(111) substrate vector. The indicated distance fits very well to the minimum distance between two non-overlapping NTCDA molecules, i.e. two molecules touching with their long sides. Maybe this result

indicates that the final stage of the inverse melting process consists of several correlated pairs of NTCDA molecules.

5.3.3 240 K structure

At 240 K the LEED picture displayed in Figure 5.3.4 can be observed. The picture can be explained by a superposition of the 240 K structure with the 220 K and the 180 K structures described above. The remaining LEED signature belongs to a structure, which can be described by a $\begin{pmatrix} 4 & 1.5 \\ 0 & 5 \end{pmatrix}$ superstructure matrix. The simulated picture is compared to the experimental data in Figure 5.3.5a.

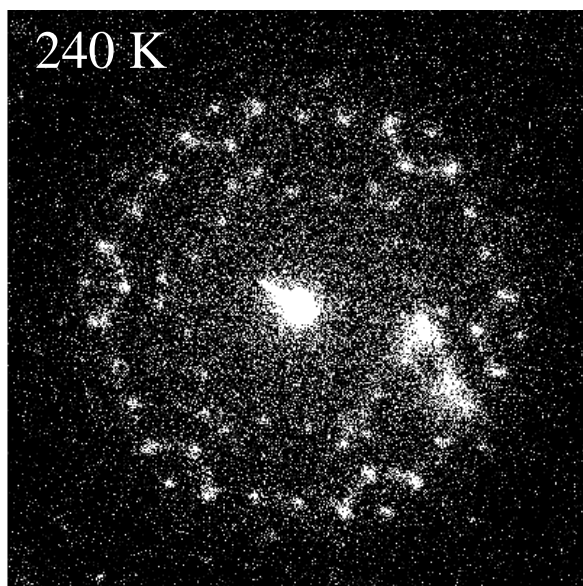


Figure 5.3.4: SPA-LEED picture recorded for the NTCDA monolayer at 240 K.

A real space model for this structure is suggested in Figure 5.3.5b. The unit cell size of 147 \AA^2 is smaller than the corresponding value for the compressed NTCDA monolayer (157 \AA^2 , see Ref. [65]), but it still allows to fit two molecules in one unit cell. The molecular arrangement displayed in Figure 5.3.5b thus represents a close packing of the NTCDA molecules, with only a very small overlap of the van-der-Waals radii.

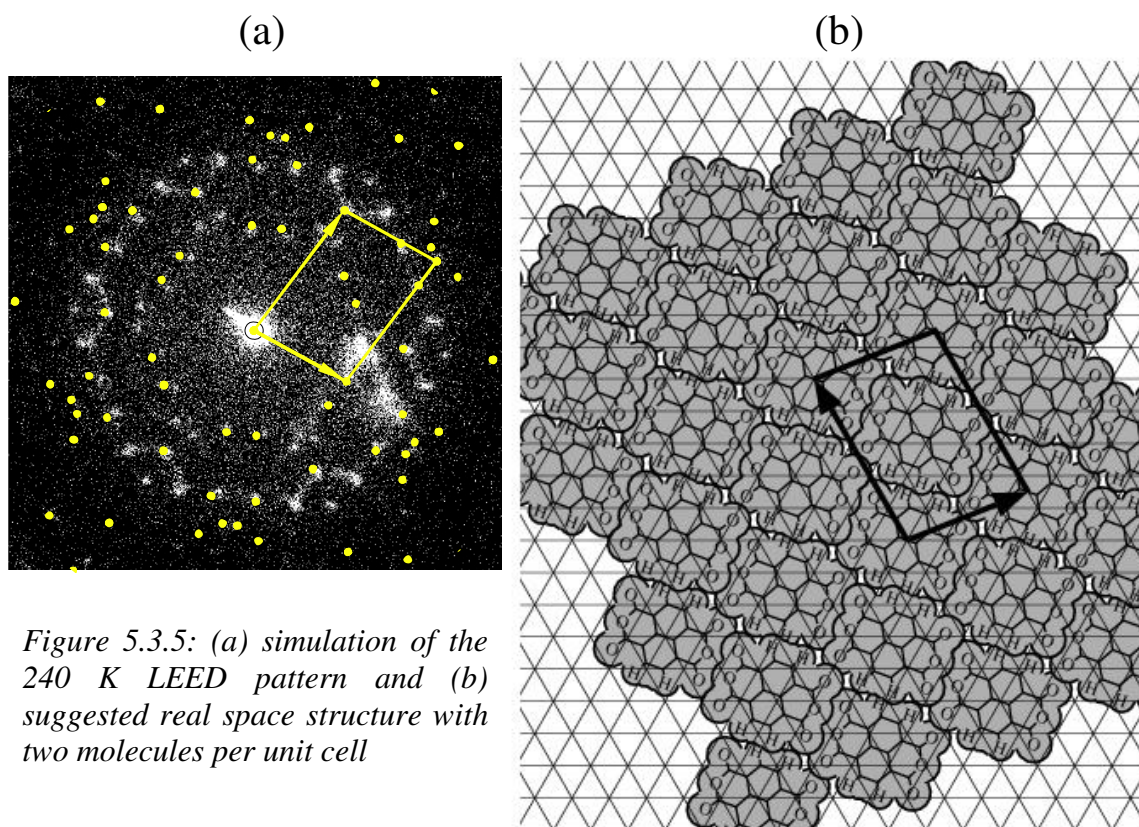


Figure 5.3.5: (a) simulation of the 240 K LEED pattern and (b) suggested real space structure with two molecules per unit cell

6 References

- [1] C. Väterlein, H. Neureiter, W. Gebauer, B. Ziegler, M. Sokolowski, P. Bäuerle, et al, *J. Appl. Phys.* 82 (1997) 3003-3013.
- [2] J. Lee, Y. Park, D.Y. Kim, H.Y. Chu, H. Lee and L.M. Do, *Appl. Phys. Lett.* 82 (2003) 173-175.
- [3] T. Dobbertin, M. Kroeger, D. Heithecker, D. Schneider, D. Metzdorf, H. Neuner, et al, *Appl. Phys. Lett.* 82 (2003) 284-286.
- [4] G. Horowitz, R. Hajlaoui and F. Kouki, *Eur. Phys. J.-Appl. Phys.* 1 (1998) 361-367.
- [5] C. Videlot, J. Ackermann, P. Blanchard, J.M. Raimundo, P. Frere, M. Allain, et al, *Adv. Mater.* 15 (2003) 306-310.
- [6] M. Hiramoto, H. Fujiwara and M. Yokoyama, *Applied Physics Letters* 58 (1991) 1062-1064.
- [7] K. Takahashi, N. Kuraya, T. Yamaguchi, T. Komura and K. Murata, *Solar Energy Materials and Solar Cells* 61 (2000) 403-416.
- [8] E. Umbach, K. Glöckler and M. Sokolowski, *Surf. Sci.* 404 (1998) 20-31.
- [9] E. Umbach and R. Fink, How to control the properties of interfaces and thin films of organic molecules? in V.M. Agranovich, G.C. La Rocca (Eds.), *International School of Physics "Enrico Fermi"*. IOS Press, Amsterdamm, 2002.
- [10] H. Inokuchi, K. Imaeda, T. Enoki, T. Mori, Y. Maruyama, G. Saito, et al, *Nature* 329 (1987) 39-40.
- [11] M. Halik, H. Klauk, U. Zschieschang, G. Schmid, W. Radlik, S. Ponomarenko, et al, *J Appl. Phys.* 93 (2003) 2977-2981.
- [12] E.E. Koch, *Phys Scripta T17* (1987) 120-136.
- [13] W.R. Salaneck, *Crc. Cr. Rev. Sol. State* 12 (1985) 267-296.
- [14] J. Stöhr, *NEXAFS Spectroscopy*, Springer, Berlin-Heidelberg-New York, 1992.
- [15] W.E.S. Unger, A. Lippitz, C. Wöll and W. Heckmann, *Fresenius Journal of Analytical Chemistry* 358 (1997) 89-92.
- [16] M. Grunze, *Phys. Scripta T49B* (1993) 711-717.
- [17] H. Ade, A.P. Smith, H. Zhang, G.R. Zhuang, J. Kirz, E. Rightor, et al, *J. Electron. Spectrosc.* 84 (1997) 53-71.
- [18] J. Stöhr and S. Anders, *IBM J. Res. Dev.* 44 (2000) 535-551.
- [19] A. Thompson, D. Attwood, E. Gullison, M. Howells, K. Kim, J. Kirz, et al, *Xray data booklet*, Berkley, CA, 2001.

-
- [20] D. Briggs and M.P. Seah, *Practical Surface Analysis by Auger and X-ray PES*, John Wiley & Sons, New York, 1983.
- [21] G. Ertl and J. Küppers, *Low Energy Electrons and Surface Chemistry*, VHC Weinheim, Weinheim, 1985.
- [22] S. Hüfner, *Photoelectron Spectroscopy, Principles and Applications*, Springer, Berlin, 1995.
- [23] H. Lüth, *Photoelectron Spectroscopy: Principles and Applications*, Springer, Berlin, 1993.
- [24] U. Höfer, Doctoral thesis, TU München, 1989.
- [25] E. Umbach, Doctoral thesis, TU München, 1980.
- [26] W. Weiss, Doctoral thesis, Universität Stuttgart, 1992.
- [27] T. Koopman, *Physica 1 (1932/1933) 104*.
- [28] K. Siegbahn, *ESCA: atomic, molecular and solid state structure by means of Electron Spectroscopy*, Almquist and Wiksells, Uppsala, 1967.
- [29] K. Siegbahn, *ESCA, Applied to Free Molecules*, North-Holland, Amsterdam, 1971.
- [30] R.P. Messmer, S.H. Lamson and D.R. Salahub, *Physical Review B 25 (1982) 3576-3592*.
- [31] H.J. Freund and E.W. Plummer, *Physical Review B 23 (1981) 4859-4878*.
- [32] J.W. Gadzuk, *Physical Review B 14 (1976) 2267-2280*.
- [33] G.E. Laramore and W.J. Camp, *Physical Review B 9 (1974) 3270-3277*.
- [34] U. Gelius, *Physica Scripta 9 (1974) 133-147*.
- [35] R. Manne, M. Karras and E. Suoninen, *Chem. Phys. Lett. 15 (1972) 34-&*.
- [36] N.V. Richardson and A.M. Bradshaw, *Symmetry and the Electron Spectroscopy of Surfaces*, Academic Press, 1981.
- [37] B.I. Lundqvist, *Physik der Kondensierten Materie 9 (1969) 236-&*.
- [38] E.W. Plummer and W. Eberhardt, *Advances in Chemical Physics 49 (1982) 533-656*.
- [39] J. Taborski, Doctoral thesis, Universität of Stuttgart, 1994.
- [40] V.F. Traven, *Frontier Orbitals and Properties of Organic Molecules*, Ellis Horwood Ltd., 1992.
- [41] T.J. Gil, C.L. Winstead, J.A. Sheehy, R.E. Farren and P.W. Langhoff, *Physica Scripta T31 (1990) 179-188*.
- [42] D.D. Vvedensky, in J.E. Inglesfield (Ed.), *Unoccupied Electronic States, Fundamentals for XANES, EELS, IPS and BIS; Topics in Applied Physics*. Springer, 1992.
- [43] J. Somers, in J.E. Inglesfield (Ed.), *Unoccupied Electronic States, Fundamentals for XANES, EELS, IPS and BIS; Topics in Applied Physics*. Springer, 1992.

-
- [44] N. Kosugi and H. Kuroda, *Chem. Phys. Lett.* 74 (1980) 490-493.
- [45] N. Kosugi, *Theor Chim Acta* 72 (1987) 149-173.
- [46] N. Kosugi and H. Kuroda, *Chem. Phys. Lett.* 94 (1983) 377-382.
- [47] J.L. Dehmer and D. Dill, *J. Chem. Phys.* 65 (1976) 5327-5334.
- [48] D. Dill and J.L. Dehmer, *Physical Review A* 16 (1977) 1423-1431.
- [49] J.C. Slater, *Quantum Theory of Molecular Solids*, McGraw-Hill, 1965.
- [50] S.G. Urquhart, A.P. Hitchcock, A.P. Smith, H. Ade and E.G. Rightor, *J. Phys. Chem. B* 101 (1997) 2267-2276.
- [51] S.G. Urquhart and H. Ade, *J. Phys. Chem. B* 106 (2002) 8531-8538.
- [52] H. Oji, R. Mitsumoto, E. Ito, H. Ishii, Y. Ouchi, K. Seki, et al, *J. Chem. Phys.* 109 (1998) 10409-10418.
- [53] M. Born and R. Oppenheimer, *Annalen der Physik* 84 (1927) 457 ff.
- [54] J. Franck, *Faraday Society* 21 (1925) 536 ff.
- [55] E.U. Condon, *Physical Review* 32 (1928) 858 ff.
- [56] L.S. Cederbaum and W. Domcke, *J. Chem. Phys.* 60 (1974) 2878-2889.
- [57] G. Herzberg, *Molecular spectra and molecular structure*, Krieger Publishing Comp., Malabar, Florida, 1991.
- [58] D.W. Turner, C. Baker and C.R. Brundle, *Molecular Photoelectron Spectroscopy*, Wiley-Interscience, London, 1970.
- [59] P.M. Morse, *Physical Review* 34 (1929) 57 ff.
- [60] R. Rydberg, *Zeitschrift für Physik* 73 (1931) 376 ff.
- [61] O. Klein, *Zeitschrift für Physik* 76 (1932) 226 ff.
- [62] A.L. Rees, *Proceedings of the Physical Society* 59 (1947) 998 ff.
- [63] M.A.V. Hove, W.H. Weinberg and C.M. Chan, *Low Energy Electron Diffraction: Experiment, Theory and Surface Structure Determination*, Springer, Berlin, 1986.
- [64] M.H. von Hoegen, *Zeitschrift für Kristallografie* 214 (1999) 1-75.
- [65] L. Kilian, *Doctoral thesis*, Universität Würzburg, 2002.
- [66] D. Gador, *Doctoral thesis*, Universität Würzburg, 1999.
- [67] U. Baston, *Doctoral thesis*, Universität Stuttgart, 1999.
- [68] H. Petersen, C. Jung, C. Hellwig, W.B. Peatman and W. Gudat, *Rev. Sci. Instrum.* 66 (1995) 1-14.
- [69] N. Martensson, P. Baltzer, P.A. Bruhwiler, J.O. Forsell, A. Nilsson, A. Stenborg, et al, *J. Electr. Spectrosc.* 70 (1994) 117-128.
- [70] H. Petersen, *Opt. Commun.* 40 (1982) 402-406.

- [71] C.T. Buchberger, Diploma thesis, Universität Würzburg, 1996.
- [72] M. Feser, M. Carlucci-Dayton, C. Jacobsen, J. Kirz, U. Neuhäusler, G. Smith, et al, in I. McNulty (Ed.), X-ray microfocusing: applications and techniques. Eds., 1998, p. 19.
- [73] B. Winn, H. Ade, C. Buckley, M. Feser, M. Howells, S. Hulbert, et al, *J. Sync. Rad.* 7 (2000) 395-404.
- [74] U. Scheithauer, G. Meyer and M. Henzler, *Surface Science* 178 (1986) 441-451.
- [75] P.A. Stevens, T.H. Upton, J. Stöhr and R.J. Madix, *Phys. Rev. Lett.* 67 (1991) 1653-1656.
- [76] A. Wuhn, J. Weckesser and C. Wöll, *Langmuir* 17 (2001) 7605-7612.
- [77] S.G. Urquhart, H. Ade, M. Rafailovich, J.S. Sokolov and Y. Zhang, *Chem. Phys. Lett.* 322 (2000) 412-418.
- [78] K. Kaznatcheyev, A. Osanna, C. Jacobsen, O. Plashkevych, O. Vahtras and H. Agren, *J. Phys. Chem. A* 106 (2002) 3153-3168.
- [79] D. Gador, C. Buchberger, R. Fink and E. Umbach, *Europhys. Lett.* 41 (1998) 231-236.
- [80] G. Hähner, M. Kinzler, C. Wöll, M. Grunze, M.K. Scheller and L.S. Cederbaum, *Phys. Rev. Lett.* 67 (1991) 851-854.
- [81] J. Hasselstrom, O. Karis, M. Weinelt, N. Wassdahl, A. Nilsson, M. Nyberg, et al, *Surface Science* 407 (1998) 221-236.
- [82] P. Väterlein, H. Dietz, J. Taborski, W. Wurth and E. Umbach, *J. Electron Spectrosc.* 78 (1996) 351-354.
- [83] P. Väterlein, T. Krause, M. Bäessler, R. Fink, E. Umbach, J. Taborski, et al, *Phys. Rev. Lett.* 76 (1996) 4749-4752.
- [84] K. Weiss, P.S. Bagus and C. Wöll, *J. Chem. Phys.* 111 (1999) 6834-6845.
- [85] A. Schöll, Y. Zou, D. Hübner, D. Gador, L. Kilian, C. Jung, et al, *Phys. Rev. Lett.* (submitted).
- [86] A. Schöll, Y. Zou, T. Schmidt, R. Fink and E. Umbach, *J. Electron Spectrosc.* 129 (2003) 1-8.
- [87] G. Kaindl, M. Domke, C. Laubschat, E. Weschke and C. Xue, *Rev. Scientific Instr.* 63 (1992) 1234-1240.
- [88] F. Eggenstein, F. Senf, T. Zeschke and W. Gudat, *Nucl. Instrum. Methods Phys. Res. Sect. A-Accel. Spectrom. Dect. Assoc. Equip.* 467 (2001) 325-328.
- [89] D. Briggs and M.P. Seah, *Practical Surface Analysis*, Wiley, 1983.
- [90] M.P. Seah and M.T. Anthony, *Surface Interface and Analysis* 6 (1984) 230.
- [91] M.R. Weiss, R. Follath, K.J.S. Sawhney and T. Zeschke, *Nucl Instrum Meth A* 467 (2001) 482-484.
- [92] F. Senf, H. Lammert, R. Follath, T. Zeschke, W. Gudat, K. Feichtinger, et al, *J Synchrotron Radiat* 5 (1998) 584-586.

-
- [93] A. Schöll, L. Kilian, Y. Zou, T. Schmidt, R. Fink and E. Umbach, (in preparation).
- [94] T. Kato, K. Yoshizawa and K. Hirao, *J. Chem. Phys.* 116 (2002) 3420-3429.
- [95] T. Kato and T. Yamabe, *J. Chem. Phys.* 117 (2002) 2324-2331.
- [96] C.T. Chen, Y. Ma and F. Sette, *Phys. Rev. A* 40 (1989) 6737-6740.
- [97] M. Coreno, M. de Simone, K.C. Prince, R. Richter, M. Vondracek, L. Avaldi, et al, *Chem. Phys. Lett.* 306 (1999) 269-274.
- [98] Y. Ma, C.T. Chen, G. Meigs, K. Randall and F. Sette, *Phys. Rev. A* 44 (1991) 1848-1858.
- [99] Y. Jugnet, F.J. Himpsel, P. Avouris and E.E. Koch, *Phys. Rev. Lett.* 53 (1984) 198-201.
- [100] H. Köppel, F.X. Gadea, G. Klatt, J. Schirmer and L.S. Cederbaum, *J. Chem. Phys.* 106 (1997) 4415-4429.
- [101] H. Rabus, D. Arvanitis, M. Domke, A. Puschmann, L. Wenzel, G. Comelli, et al, *Phys. Scripta T31* (1990) 131-136.
- [102] F.X. Gadea, H. Köppel, J. Schirmer, L.S. Cederbaum, K.J. Randall, A.M. Bradshaw, et al, *Phys. Rev. Lett.* 66 (1991) 883-886.
- [103] K.C. Prince, R. Richter, M. De Simone and M. Corone, *Surf. Rev. Lett.* 9 (2002) 159-164.
- [104] G. Remmers, M. Domke and G. Kaindl, *Phys. Rev. A* 47 (1993) 3085-3091.
- [105] Y. Ma, F. Sette, G. Meigs, S. Modesti and C.T. Chen, *Phys. Rev. Lett.* 63 (1989) 2044-2047.
- [106] C. Kolczewski, R. Püttner, O. Plashkevych, H. Agren, V. Staemmler, M. Martins, et al, *J. Chem. Phys.* 115 (2001) 6426-6437.
- [107] G. Contini, V. Carravetta, V. Di Castro, S. Stranges, R. Richter and M. Alagia, *J. Phys. Chem. A* 105 (2001) 7308-7314.
- [108] A.N. Debrito, S. Svensson, N. Correia, M.P. Keane, H. Agren, O.P. Sairanen, et al, *J. Electron Spectrosc.* 59 (1992) 293-305.
- [109] M.P. Demiranda, J.A. Beswick, P. Parent, C. Laffon, G. Tourillon, A. Cassuto, et al, *J. Chem. Phys.* 101 (1994) 5500-5514.
- [110] U. Höfer, M.J. Breitschäfer and E. Umbach, *Phys. Rev. Lett.* 64 (1990) 3050-3053.
- [111] A. Föhlisch, N. Wassdahl, J. Hasselstrom, O. Karis, D. Menzel, N. Martensson, et al, *Phys. Rev. Lett.* 81 (1998) 1730-1733.
- [112] T. Ramsvik, A. Borg, T. Worren and M. Kildemo, *Surf. Sci.* 511 (2002) 351-358.
- [113] M.R. Weiss, R. Follath, K.J.S. Sawhney, F. Senf, J. Bahrtdt, W. Frentrup, et al, *Nucl. Instrum. Meth. A* 467 (2001) 449-452.
- [114] M.L. Rocco, A. Schöll, T. Schmidt, R. Fink and E. Umbach, (in preparation).
- [115] L. Born and G. Heywang, *Z. Kristallogr.* 190 (1990) 147-152.

- [116] T. Schmidt, H. Marchetto, U. Groh, R. Fink and E. Umbach, (to be published).
- [117] K.C. Prince, M. Vondracek, J. Karvonen, M. Coreno, R. Camilloni, L. Avaldi, et al, *J. Electron Spectrosc.* 103 (1999) 141-147.
- [118] A.S. Davydov, *Theory of molecular excitons*, Plenum, New York, 1971.
- [119] M. Pope and C.E. Swenberg, *Electronic Processes in Organic Crystals*, Clarendon Press, Oxford, 1982.
- [120] C. Taliani, F. Biscarini, E. Lunedei, P. Mei, M. Muccini, M. Murgia, et al, *Int. J. Mod. Phys. B* 15 (2001) 3722-3726.
- [121] D.W. Turner, A.D. Baker, C.R. Brundle, *Molecular Photoelectron Spectroscopy*, Wiley-Interscience, London, 1970.
- [122] D. Hübner, V. Shklover, M. Sokolowski, R. Fink and E. Umbach, (in preparation).
- [123] A. Schöll, D. Hübner, T. Schmidt, S.G. Urquhart, R. Fink and E. Umbach, *Chem. Phys. Lett.* (submitted).
- [124] T.C.W. Mak and J. Trotter, *Acta Crystallographica* 16 (1963) 811-&.
- [125] S.N. Singh, M.G. Jayswal and R.S. Singh, *Current Science* 36 (1967) 624-&.
- [126] Sigma-Aldrich, FTIR spectroscopy - reference1(2), 82A.
- [127] A. Schöll, Y. Zou, D. Hübner, Th. Schmidt, R. Fink, E. Umbach, (in preparation).
- [128] A. Schöll, Y. Zou, D. Hübner, S.G. Urquhart, T. Schmidt, R. Fink, et al, (in preparation).
- [129] L. Chkoda, M. Schneider, V. Shklover, L. Kilian, M. Sokolowski, C. Heske, et al, *Chem. Phys. Lett.* 371 (2003) 548-552.
- [130] E.A. Silinsh and V. Capek, *Organic Molecular Crystals, Interaction, Localization and Transport Phenomena*, AIP Press, Woodbury, 1994.
- [131] F.S. Tautz, M. Eremitchenko, J.A. Schaefer, M. Sokolowski, V. Shklover and E. Umbach, *Phys. Rev. B* 65 (2002) art. no.-125405.
- [132] A. Schöll, M. Jung, Y. Zou, T. Schmidt, R. Fink and E. Umbach, *J. Chem. Phys.* (submitted).
- [133] V. Carravetta, G. Iucci, A. Ferri, M.V. Russo, S. Stranges, M. de Simone, et al, *Chem. Phys.* 264 (2001) 175-186.
- [134] H.J. Freund and R.W. Bigelow, *Physica Scripta* T17 (1987) 50-63.
- [135] R.W. Bigelow, K.Y. Law, D.H.K. Pan and H.J. Freund, *J. Electron Spectrosc.* 46 (1988) 1-17.
- [136] L. Yang and H. Agren, *Phys. Rev. B* 54 (1996) 13649-13655.
- [137] M. Jung, U. Bason, T. Porwol, H.-J. Freund and E. Umbach, *J. Electron. Spectrosc.* (submitted).
- [138] K. Siegbahn, *Philosophical Transactions of the Royal Society of London Series a-Mathematical and Physical Sciences* 268 (1970) 33-&.

- [139] G. Beamson, D. Briggs, High resolution XPS of organic polymers: The SCIENTA ESCA300 Database, John Wiley and Sons, England, 1992.
- [140] L. Torsi, A. Dodabalapur, N. Cioffi, L. Sabbatini and P.G. Zambonin, *Sens. Actuator B-Chem.* 77 (2001) 7-11.
- [141] Y. Hirose, A. Kahn, V. Aristov, P. Soukiassian, V. Bulovic and S.R. Forrest, *Phys. Rev. B* 54 (1996) 13748-13758.
- [142] E.V. Tsiper, Z.G. Soos, W. Gao and A. Kahn, *Chem. Phys. Lett.* 360 (2002) 47-52.
- [143] H. Ishii, K. Sugiyama, E. Ito and K. Seki, *Advanced Materials* 11 (1999) 605-+.
- [144] H. Ishii, K. Sugiyama, E. Ito and K. Seki, *Advanced Materials* 11 (1999) 972-972.
- [145] K. Seki, N. Hayashi, H. Oji, E. Ito, Y. Ouchi and H. Ishii, *Thin Solid Films* 393 (2001) 298-303.
- [146] R. Fink, D. Gador, U. Stahl, Y. Zou and E. Umbach, *Phys. Rev. B* 60 (1999) 2818-2826.
- [147] A. Schöll, Y. Zou, D. Hübner, D. Gador, L. Kilian, Th. Schmidt, R. Fink, E. Umbach, (in preparation).
- [148] R. Fink, D. Gador, U. Stahl, Y. Zou and E. Umbach, *Phys. Rev. B* 60 (1999) 2818-2826.
- [149] U. Stahl, D. Gador, A. Soukopp, R. Fink and E. Umbach, *Surf. Sci.* 414 (1998) 423-434.
- [150] A. Schöll, Y. Zou, Th. Schmidt, R. Fink and E. Umbach, *J. Phys. Chem.* (submitted).
- [151] T.A. Carlson, W.B. Dress, F.A. Grimm and J.S. Haggerty, *J. Electron Spectrosc.* 10 (1977) 147-154.
- [152] T.A. Carlson, *Annual Review of Physical Chemistry* 26 (1975) 211-233.
- [153] D.P. Spears, H.J. Fischbeck and T.A. Carlson, *J. Electron Spectrosc.* 6 (1975) 411-420.
- [154] U. Gelius, *J. Electron Spectrosc.* 5 (1974) 985-1057.
- [155] E. Umbach, *Surf. Sci.* 117 (1982) 482-502.
- [156] M.J. Breitschafter, E. Umbach and D. Menzel, *Surf. Sci.* 109 (1981) 493-511.
- [157] E. Umbach, S. Kulkarni, P. Feulner and D. Menzel, *Surf. Sci.* 88 (1979) 65-94.
- [158] J.C. Fuggle and D. Menzel, *Surf. Sci.* 79 (1979) 1-25.
- [159] J.C. Fuggle, E. Umbach, P. Feulner and D. Menzel, *Surface Science* 64 (1977) 69-84.
- [160] E. Umbach, J.C. Fuggle and D. Menzel, *J. Electron Spectrosc.* 10 (1977) 15-34.
- [161] D. Gador, Y. Zou, C. Buchberger, M. Bertram, R. Fink and E. Umbach, *J. Electron Spectrosc.* 103 (1999) 523-528.
- [162] D. Hübner, L. Kilian, A. Schöll, R. Fink and E. Umbach, (in preparation).

-
- [163] K. Hermann, P.S. Bagus, C.R. Brundle and D. Menzel, *Phys. Rev. B* 24 (1981) 7025-7040.
- [164] C.R. Brundle, P.S. Bagus, D. Menzel and K. Hermann, *Phys. Rev. B* 24 (1981) 7041-7056.
- [165] P.S. Bagus and K. Hermann, *Surf. Sci.* 89 (1979) 588-595.
- [166] K. Hermann and P.S. Bagus, *Phys. Rev. B* 16 (1977) 4195-4208.
- [167] P.S. Bagus, K. Hermann and M. Seel, *J. Vacuum Sci. & Tech.* 18 (1981) 435-452.
- [168] K. Schönhammer and O. Gunnarsson, *Solid State Commun.* 23 (1977) 691-693.
- [169] O. Gunnarsson and K. Schönhammer, *Phys. Rev. Lett.* 41 (1978) 1608-1612.
- [170] K. Schönhammer and O. Gunnarsson, *Surf. Sci.* 89 (1979) 575-587.
- [171] J.C. Fuggle and D. Menzel, *Vakuum-Technik* 27 (1978) 130-135.
- [172] A.L. Greer, *Nature* 404 (2000) 134-135.
- [173] P.M. Tedrow and D.M. Lee, *Phys. Rev.* 181 (1969) 399-&.
- [174] S. Rastogi, G.W.H. Höhne and A. Keller, *Macromolecules* 32 (1999) 8897-8909.
- [175] G. Tammann, *Kristallisieren und Schmelzen*, J.A. Barth, Leipzig, 1903.
- [176] G. Tammann, *Lehrbuch der Metallographie*, L. Voss, Leipzig, 1921.
- [177] G. Tammann, *A text book of metallography*, Chemical Catalog Co., New York, 1925.
- [178] W. Sinkler, C. Michaelsen, R. Bormann, D. Spilsbury and N. Cowlam, *Phys. Rev. B* 55 (1997) 2874-2881.
- [179] H.Y. Bai, C. Michaelsen and R. Bormann, *Phys. Rev. B* 56 (1997) 11361-11364.
- [180] L. Kilian, A. Schöll, D. Hübner, R. Fink and E. Umbach, *Science* (in preparation).
- [181] D. Gador, C. Buchberger, R. Fink and E. Umbach, *J. Electron Spectrosc.* 96 (1998) 11-17.
- [182] Y. Zou, *Doctoral thesis, Universität Würzburg*, 2003.
- [183] H. Ade and S.G. Urquhart, in T.K. Sham (Ed.), *Chemical Applications of Synchrotron Radiation*. World Scientific Publishing, 2002.
- [184] F. Gelmukhanov and H. Agren, *J. Phys. B* 28 (1995) 3699-3715.
- [185] A.P. Hitchcock, S.G. Urquhart and E.G. Rightor, *J. Phys. Chem.* 96 (1992) 8736-8750.
- [186] L.G.M. Pettersson, H. Agren, B.L. Schurmann, A. Lippitz and W.E.S. Unger, *Int. J. Quantum Chem.* 63 (1997) 749-765.
- [187] S.G. Urquhart, A.P. Smith, H.W. Ade, A.P. Hitchcock, E.G. Rightor and W. Lidy, *J. Phys. Chem. B* 103 (1999) 4603-4610.
- [188] R. Giebler, B. Schulz, J. Reiche, L. Brehmer, M. Wuhn, C. Woll, et al, *Langmuir* 15 (1999) 1291-1298.

-
- [189] J. Stöhr, D.A. Outka, K. Baberschke, D. Arvanitis and J.A. Horsley, *Phys. Rev. B* 36 (1987) 2976-2979.
- [190] A.P. Hitchcock, D.C. Newbury, I. Ishii, J. Stöhr, J.A. Horsley, R.D. Redwing, et al, *J. Chem. Phys.* 85 (1986) 4849-4862.
- [191] D.A. Outka, J. Stöhr, J.P. Rabe, J.D. Swalen and H.H. Rotermund, *Phys. Rev. Lett.* 59 (1987) 1321-1324.
- [192] T. Ohta, K. Seki, T. Yokoyama, I. Morisada and K. Edamatsu, *Physica Scripta* 41 (1990) 150-153.
- [193] P.S. Bagus, K. Weiss, A. Schertel, C. Wöll, W. Braun, C. Hellwig, et al, *Chem. Phys. Lett.* 248 (1996) 129-135.
- [194] P. Väterlein, R. Fink, E. Umbach and W. Wurth, *J. Chem. Phys.* 108 (1998) 3313-3320.
- [195] R.G. Alamo and L. Mandelkern, *Thermochimica Acta* 238 (1994) 155-201.
- [196] A. Alizadeh, L. Richardson, J. Xu, S. McCartney, H. Marand, Y.W. Cheung, et al, *Macromolecules* 32 (1999) 6221-6235.
- [197] A. Schöll, R. Fink, E. Umbach, G.E. Mitchell, S.G. Urquhart and H. Ade, *Chem. Phys. Lett.* 370 (2003) 834-841.
- [198] W.J. Hunt and W.A.I. Goddard, *Chem. Phys. Lett.* 3 (1969) 414.
- [199] N. Kosugi, E. Shigemasa and A. Yagishita, *Chem. Phys. Lett.* 190 (1992) 481-488.
- [200] H. Ade, X. Zhang, S. Cameron, C. Costello, J. Kirz and S. Williams, *Science* 258 (1992) 972-975.
- [201] G. Appel, I. Koprinarov, G.E. Mitchell, A.P. Smith and H. Ade, *Advanced Light Source Compendium of User Abstracts 2001* (2002).

Danksagung

An dieser Stelle möchte ich all jenen danken, die zum Entstehen der vorliegenden Arbeit beigetragen haben.

Prof. Dr. E. Umbach hat mir über Jahre hinweg die eigenständige wissenschaftliche Arbeit in seiner Arbeitsgruppe ermöglicht. Er hat mich dabei in viele Hinsicht unterstützt und mir in zahlreichen Diskussionen geholfen, den richtigen Weg in dem großen und komplexen Themengebiet dieser Dissertation zu finden. Dafür möchte ich mich an dieser Stelle bedanken.

Auch Prof. Dr. Rainer Fink danke ich für die jahrelange Unterstützung und Zusammenarbeit, für die vielen organisatorischen Hilfen und für das Hand anlegen bei BESSY Messzeiten.

Bei Prof. Dr. J. Geurts möchte ich mich für die Übernahme des Zweitgutachtens dieser Arbeit bedanken, bei Priv. Doz. Dr. G. Reents für seine freundliche Hilfe bei der Weiterentwicklung des Programms zur Franck-Condon Analyse und für die Übernahme der Zweitprüferrolle.

Dr. Th. Schmidt hat in vielen Bereichen zum Gelingen dieser Arbeit beigetragen, durch seine tatkräftige Unterstützung bei Messzeiten, seine Diskussionsbereitschaft und seine Offenheit, durch die ich Zugang zu seiner enormen Erfahrung im Bereich der Experimentalphysik haben durfte.

Meinen langjährigen Weggefährten Dr. Ying Zou möchte ich an dieser Stelle besonders hervorheben. Während der vielen Messzeiten bei BESSY hat es immer Spaß gemacht mit ihm zu arbeiten. Selbst wenn experimentelle Probleme und sehr wenig Schlaf die Nerven auf die Probe stellten, konnte man sich seines positiven Gemütes und seiner schier endlosen Geduld sicher sein.

Dr. Lennart Kilian hatte großen Anteil am Gelingen der SPA-LEED Messungen. Auch stammt von ihm das Programm zur Franck-Condon Analyse, das für diese Arbeit von großem Wert war.

Dominique Hübner danke ich besonders für die unzähligen selbstlosen Hilfen, v.a. bei den BESSY Messzeiten. Auch hat seine Erfahrung im Bereich der Schwingungsspektroskopie zum Gelingen dieser Arbeit beigetragen.

Prof. Dr. Harald W. Ade danke ich für die Ermöglichung des Polyethylenprojekts, die Unterstützung und die interessanten Diskussionen während meines Aufenthaltes in Raleigh.

Für die Einführung in die GSCF3 Rechenmethode und die Betreuung der Rechnungen, die für diese Arbeit durchgeführt wurden, bin ich Prof. Dr. Stephen G. Urquhart zu Dank verpflichtet. Auch in anderen Bereichen waren zahlreiche Diskussionen mit ihm sehr hilfreich. In diesem Zusammenhang möchte ich mich auch bei Prof. Dr. N. Kosugi bedanken, der mir die Benutzung der von ihm entwickelten Programme gestattete.

Dass die beiden STXM-Messzeiten in Brookhaven so erfolgreich waren ist hauptsächlich der Verdienst von Dr. Andy Winesett. Er kam in dieser Zeit kaum zum schlafen.

Dr. Bodo Richter, Helder Marchetto, Dr. Benedetta Casu und Prof. Dr. Maria Luiza Rocco haben mich bei BESSY Messzeiten unterstützt. In diesem Zusammenhang möchte ich auch der BESSY Crew, v.a. Dr. C. Jung, Dr. D. Bachelor und Dr. M. Mast, für ihre Hilfe danken.

Den restlichen Mitgliedern der Arbeitsgruppe Umbach sei mein Dank für die vielen Hilfen und das tolle Klima.

Last but not least möchte ich meiner Familie, Margot, Noah und meinen Eltern, danken. Ihrer bedingungslose Unterstützung kann ich mir jederzeit gewiss sein.

Lebenslauf

Persönliche Daten:

Name: Achim Schöll
Geburtsdatum: 21.08.1971
Geburtsort: Kirchheim/Teck
Familienstand: ledig, ein Kind (1)

Schulbildung:

1977-1981: Grundschule
1982-1990: Armin-Knab-Gymnasium Kitzingen
1990: Abitur

Universitätsausbildung:

1990-1997: Physikstudium an der
Julius-Maximilians-Universität Würzburg
1996-1997: Diplomarbeit am Institut für Experimentelle Physik II bei
Prof. Dr. E. Umbach. Thema der Arbeit: „*Koadsorption von
Kohlenmonoxid und Kalium auf Ag(110)*“
September 1997: Physik-Diplom
1998-1999: Zivildienst beim Arbeiter Samariter Bund in Würzburg
seit Juli 1999: Wissenschaftlicher Angestellter am Institut für Experimentelle
Physik II der Universität Würzburg.
Arbeit an der vorliegenden Dissertation bei Prof. Dr. E. Umbach
November 1999-
April 2000: Wissenschaftlicher Angestellter am Institute of Physics der
North Carolina State University in Raleigh, NC, USA.
Mikrospektroskopische Untersuchungen an Polymerdünnfilmen
in der Arbeitsgruppe von Prof. Dr. H. W: Ade